Institute of Engineering Surveying and Space Geodesy (IESSG)

Development of azimuth dependent tropospheric mapping functions, based on a high resolution mesoscale numerical weather model, for GNSS data processing

Etienne J. Orliac

Dipl.-Ing., EPFL, Switzerland, 2002

Thesis submitted to the University of Nottingham
for the Degree of Doctor of Philosophy

July 2009

Abstract

This thesis is dedicated to the development of two new tropospheric mapping functions for GNSS data processing, based on a high resolution mesoscale numerical weather model (NWM). NWMs have proven to be beneficiary in the processing of GNSS and VLBI data, both for deriving mapping functions and for providing a priori information such as zenith hydrostatic delay (ZHD).

The mapping functions derived here make a greater use of the NWM information than the mapping functions currently recommended by the International GNSS Service. In addition to using a single vertical profile at the site in order to derive mapping functions under the assumption of an azimuthally symmetric atmosphere, the NWM was also ray traced every thirty degrees in azimuth. This way, a complete volume of the atmosphere is sensed, and better modelling is expected if the NWM does indeed provide an accurate representation of the atmosphere, by accounting for azimuthal variations.

An emphasis was put in this thesis on assessing the mathematical models used to vertically interpolate meteorological information, as they play a key role in computing the refractivities in the ray tracing algorithm. Error sources were identified and quantified. As expected, water vapour is the major source of error. However, the results showed that the model used for the total pressure induced a systematic bias.

To derive an azimuth dependent mapping function, the Marini model traditionally used had to be left in favor of a cubic spline interpolation (CSI). This new approach was validated by comparing the performance of the new azimuthally symmetric mapping functions against the updated Vienna mapping functions (VMF1), the best mapping functions currently available. Similar positioning performances were obtained, therefore validating the CSI based approach.

The performance of new azimuth dependent mapping functions (AMF) in handling the troposphere asymmetry were compared to those obtained when estimating horizontal tropospheric gradients with an azimuthally symmetric mapping function. Results show a good agreement in the modelling of the asymmetry, and that estimating gradients is justified. The gradient solution performed better overall, although it failed for some sites, and better inter-station consistency was obtained with the AMF.

This thesis also investigated the role of the tropospheric modelling in the retrieval of the atmospheric pressure loading (APL) in GNSS data processing, which is now part of the IGS 2008 recommendations. The results show that differential height time series obtained with different tropospheric modelling can correlate with the APL signal to a level up to 0.7. In other words, the choice of tropospheric modelling strategy does greatly influence the retrieval of the APL.

Acknowledgements

First of all, I would like to thank my parents, Christine and Jean-Francois, and Curt, for their support, not least material, in the early stage of my Ph.D., and permanent encouragement.

I'm also thankful to the IESSG and its director, Prof. Terry Moore, for the opportunity that was offered to me to work there as a research assistant, for about three years and a half. My time at the IESSG has been very pleasant and rich of experiences. I deeply appreciate the help and support I received towards this from my supervisors: Prof. Alan H. Dodson, Dr. Richard M. Bingley and Dr. F. Norman Teferle. Special thanks go to Richard and Norman for always making time to go through the material I produced, or to answer the phone in the middle of the night to provide instructions for printing a poster...

I'm grateful to the EPSRC for funding the tuition fees of my Ph.D. and to the funders of the various projects that contributed to my salary when employed by the IESSG working part-time on my Ph.D.. These included: the GPS Near Real-Time system for meteorological applications, funded by the UK Met Office; the ESEAS project, supported by the European Commission; the absolute fixing of tide gauge benchmarks and land levels project funded by Defra and the Environment Agency; BIGF funded by NERC; and the SISTER project, also supported by the European Commission, for which I'm thankful to Terry Moore and Chris Hill for taking me on that project.

There are a series of people and organizations I need to acknowledge for their various contributions to this Ph.D.: The IGS overall, for the data and products made available to the GNSS community; CODE for their products and support on the Bernese software; BIGF for supplying the CGPS data in the UK; the UK Met Office and the BADC for making freely available the radiosonde and numerical weather model data used in this research. Thanks to the people at the Met Office who answered questions addressed to the BADC on various aspects of the data. Thanks also to Johannes Boehm for giving insight on the Vienna mapping functions, Tonie van Dam for providing atmospheric pressure loading time series, and Simon Williams for his CATS software.

Thanks to some of my former colleagues for the time spent out, and introducing me to the British way of life'... Special thanks to Sam and Norman for hosting dinners and parties at their places.

Many thanks to Prof. G. Elgered from Chalmers University of Technology, Sweden, for being my external examiner. His comments made on the results presented in this thesis and his insight on the topic have been very valuable to me.

I am also thankful to Prof. T. Moore, my internal examiner, for his comments made on the manuscript. They helped a lot in clarifying many points.

Finally, I must apologize to my beloved Céline, for the evenings, weekends, and days 'off' where this thesis got the priority... Most importantly, I thank her for her patience, continuous support, dedication and love.

Author's Contributions

S. L. Bradley, G. A. Milne, F. N. Teferle, R. M. Bingley, and **E. J. Orliac**. Glacial isostatic adjustment of the British Isles: New constraints from GPS measurements of crustal motion. *Geophysical Journal International*, 178(1), 14-22, 2009.

F. N. Teferle, R. M. Bingley, **E. J. Orliac**, S. P. D. Williams, P. Woodworth, D. McLaughlin, T. F. Baker, I. Shennan, G. A. Milne, and S. L. Bradley. Crustal motions in Great Britain: Evidence from continuous GPS, absolute gravity and Late Holocene sea-level data. *Geophysical Journal International*, 178(1), 23-46, 2009

R. M. Bingley, F. N. Teferle, **E. J. Orliac**, A. H. Dodson, S. D. P. Williams, D. L. Blackman, T. F. Baker, M. Riedmann, M. Haynes, N. Press, D. T. Aldiss, H. C. Burke, B. C. Chacksfield, D. Tragheim, O. Tarrant, S. Tanner, T. Reeder, S. Lavery, I. Meadowcroft, S. Surendran, J. R. Goudie, and D. Richardson. Measurement of current changes in land levels as input to long-term planning for flood risk management along the thames estuary. *Journal of Flood Risk Management*, 1(3):162–172, 2008.

E. J. Orliac, A. H. Dodson, R. M. Bingley, and F. N. Teferle. Correlation between mapping functions and atmospheric pressure loading in the processing of GNSS data. 2007. AGU Fall Meeting, San Francisco, 2007.

R. Bingley, N. Teferle, **E. Orliac**, A. Dodson, S. Williams, D. Blackman, T. Baker, M. Riedmann, M. Haynes, D. Aldiss, H. Burke, B. Chacksfield, and D. Tragheim. Measuring changes in land and sea levels: a regional study of the thames estuary and river thames. *Geomatics World*, 2007. September/October issue.

R. Bingley, N. Teferle, **E. Orliac**, A. Dodson, S. Williams, and Trevor Baker. Measuring changes in land and sea levels. *Geomatics World*, 2007. July/August issue.

F. N. Teferle, **E. J. Orliac**, and R. M. Bingley. An assessment of Bernese GPS software precise point positioning using IGS final products for global site velocities. *GPS Solutions*, 11(3):205–213, 2007.

E. J. Orliac, F. N. Teferle, R. M. Bingley, and A. H. Dodson. Total mapping function. 2007. XXIV General Assembly of the International Union of Geodesy and Geophysics, Perugia, Italy, July.

F. N. Teferle, R. M. Bingley, S. D. P. Williams, **E. J. Orliac**, A. H. Dodson, and T. Baker. A decade of tide gauge monitoring using continuous GPS and absolute gravimetry in the UK: New estimates of vertical land motion and sea-level change. 2007. XXIV General Assembly of the International Union of Geodesy and Geophysics, Perugia, Italy, July.

F. N. Teferle, **E. J. Orliac**, R. M. Bingley, and A. H. Dodson. An assessment of Bernese precise point positioning for geodetic monitoring applications. 2007. XXIV General

Assembly of the International Union of Geodesy and Geophysics, Perugia, Italy, July.

F. N. Teferle, S. Bradley, G. Milne, R. M. Bingley, and **E. J. Orliac**. Modelling the glacial isostatic adjustment of the British Isles: Constraints from continuous GPS measurements of 3-D crustal motion. 2007.

R. M. Bingley, F. N. Teferle, **E. J. Orliac**, A. H. Dodson, S. D. P. Williams, D. L. Blackman, T. F. Baker, M. Riedmann, M. Haynes, D. T. Aldiss, H. C. Burke, B. C. Chacksfield, and D. Tragheim. Absolute fixing of tide gauge benchmarks and land levels: measuring changes in land and sea levels around the coast of Great Britain and along the Thames Estuary using GPS, absolute gravimetry, persistent scatterer interferometry and tide gauges. 2007. Defra/Environment Agency Joint R&D FCERM Programme R&D Technical Report FD2319/TR, 241.

E. J. Orliac, A. H. Dodson, R. M. Bingley, and F. N. Teferle. Azimuth dependent modelling of the tropospheric delay in GNSS data processing based on a high resolution numerical weather model. *Eos Transactions*, 87(52), 2006. G11A-0001.

R. M. Bingley, F. N. Teferle, S. D. P. Williams, T. F. Baker, and **E. J. Orliac**. Combining independent geodetic measurements for studies of vertical crustal motions in the british isles. *Eos Transactions*, 87(52), 2006. G22A-01.

F. N. Teferle, R. M. Bingley, **E. J. Orliac**, S. D. P. Williams, S. L. Bradley, G. A. Milne, and I. Shennan. New estimates of three-dimensional crustal motions in the British Isles from Continuous GPS, geological evidence and glacial isostatic adjustment models. *Eos Transactions*, 87(52), 2006. G24A-03.

J. Nash, **E. J. Orliac**, A. H. Dodson, R. M. Bingley, J. Jones, and F. N. Teferle. On the use of near real-time gps inferred humidity fields for monitoring thunderstorm activity. *Eos Transactions*, 87(52), 2006. A11E-08.

E. J. Orliac, A. H. Dodson, R. M. Bingley, and F. N. Teferle. Comparison of azimuth dependent and EGNOS tropospheric mapping functions. *in proceedings of the European Navigation Conference (ENC)*, 2006. Manchester, UK, May.

E. J. Orliac, A. H. Dodson, R. M. Bingley, and F. N. Teferle. Azimuth dependent mapping functions for GNSS data processing. *Geophysical Research Abstracts*, 8, 2006. EGU06-A-08499.

E. J. Orliac, R. M. Bingley, A. H. Dodson, and F. N. Teferle. Ground-based GPS near real-time zenith path delay estimation in the uk. *Geophysical Research Abstracts*, 7, 2005. EGU05-A-09279.

E. J. Orliac, R. M. Bingley, A. H. Dodson, and F. N. Teferle. Near real-time GPS data processing: influence of ambiguity fixing on ZTD estimates. *Geophysical Research Abstracts*, 7, 2005. EGU-A-09147.

E. J. Orliac, A. H. Dodson, R. M. Bingley, and F. N. Teferle. Regional numerical

weather prediction model ray-traced mapping functions for gnss data processing. *Eos Transactions*, 86(52), 2005. G21A-1261.

A. H. Dodson, F. N. Teferle, **E. J. Orliac**, R. M. Bingley, and H. P. Kierulf. Testing Bernese precise point positioning over a five year period. *Eos Transactions*, 86(52), 2005. G21A-1258.

E. J. Orliac, R. M. Bingley, and A. H. Dodson. Near real-time neutral atmosphere zenith delay estimation: first results from a UK continuous GPS network. *Geophysical Research Abstracts*, 6, 2004. EGU04-A-04869.

E. J. Orliac, R. M. Bingley, and A. H. Dodson. An assessment of near real-time and post-processing strategies for tropospheric delay estimation from a planned CGPS network in the UK. *proceedings of Atmospheric Remote Sensing Using Satellite Navigation Systems*, 2003. Special Symposium of the URSI Joint Working Group, October, Matera, Italy.

E. J. Orliac. Modèle du retard troposphérique pour la navigation satellitaire. *Vermess. Photogramm. Kulturtech.*, 100(8):523–527, 2002.

Glossary

G_E	East gradient term, 8
G_N	North gradient term, 8
K, k	Refractivity constant, 34
L	Phase range [m], 15, 16
M	Molecular weight, [kg·kmol^{-1}], 28
N	Refractivity [ppm], 10
P	Absolute Pressure [hPa], 3
P_d	Partial pressure of dry air, 35
P_{CO_2}	Partial pressure of CO_2, 35
P_{ss}	Saturation vapour pressure at steam-point, 29
R	Universal gas constant, 28
T	Absolute Temperature [K], 3
T	Tropospheric delay [m], 15, 16
T_0	Reference temperature (= 273.16 K), 30
T_{dew}	Dew-point temperature (K), 32
U	Humidity, 3
V	Volume, [m^3], 28
Z_d	Compressibility factor for dry air, 37
Z_w	Compressibility factor for water vapour, 37
Φ	Phase range [cycle], 16
δt	Clock offset [s], 15, 16
$\delta\Phi$	Uncalibrated phase delay [cycle], 16
κ	Ionospheric effect, 15, 16
λ	Wavelength, [m], 16
ρ	Density, 27
ρ	Geometric distance [m], 15, 16
b	Carrier phase ambiguity term, 16

c	Speed of light, 15
e	Partial pressure of water vapour, 35
e_{sat_i}	Saturation vapour pressure over ice, 29
e_{sat}	Saturation vapour pressure over water, 29
f	Frequency [Hz], 15, 16
g	Gravity, 27
m_g	Gradient mapping function, 8
m_h	Hydrostatic mapping function, 8
m_w	Wet mapping function, 8
n	Integer ambiguity [cycle], 16
q	Specific humidity, 32
r	Mixing ratio, 31
3D	Three dimensional, 61
AE	Azimuthal effect, 236
AMF	Azimuth dependent Mapping Function, 11
APL	Atmospheric Pressure Loading, 12
BADC	British Atmospheric Data Center, 56
Beidou	Chinese GNSS, 1
BIGF	British Isles continuous GNSS Facility, 74
BSW50	Bernese software version 5.0, 19
C/A	Coarse/Acquisition, 22
CfA-2.2	[Davis et al., 1985] Mapping Function, 5
CGPS	Continuous GPS, 74
CIT	California Institute of Technology, 19
CODE	Center for Orbit Determination in Europe, 19
CSI	Cubic Spline Interpolation, 5
DA	Direct Access, 86
DCB	Differential Code Bias, 22
DD	Double Difference/Differencing, 19
DoY	Day of Year, 19

ECMWF European Center for Medium-Range Weather Forecasts, 6

EOP Earth Orientation Parameters, 20

Galileo European GNSS, 1

GAMIT GPS Analysis at MIT, 168

GIPSY GPS-Inferred Positioning SYstem (JPL), 19

GLONASS GLObalnaja NAvigatsionnaja Sputnikovaja Systema, 1

GMF Global Mapping Functions [Boehm et al., 2006b], 5

GNSS Global Navigation Satellite System, 1

GPS Global Positioning System (American GNSS), 1

GPST GPS Time, 15

HiRes High Resolution (RS data sampled every 2 s of ascent), 11

HIRLAM High Resolution Limited Area Model, 30

IERS International Earth Rotation and Reference Frames Service, 23

IGS International GNSS Service, 7

IMF Improved/Isobaric Mapping Function [Niell, 2000], 6

IVS International VLBI Service for Geodesy and Astrometry, 7

JPL Jet Propulsion Laboratory, CIT, 19

LP Leonid Petrov non-tidal APL model, 168

MESO UKMO High Resolution Mesoscale NWM, 3

MTT Mapping Temperature Test [Herring, 1992] Mapping Functions, 5

NASA National Aeronautics and Space Administration, 19

NCEP National Center for Environmental Prediction, 9

NMF New(/Niell) [Niell, 1996] Mapping Functions, 5

NWM Numerical Weather Model, 3

OMF Orliac Mapping Functions, 54

OMFA Azimuth dependent OMF, 217

OMFAHRT OMFA used with consistent ray traced ZHD, 233

OMFS Symmetric OMF, 167

OMFSHRT OMFS used with consistent ray traced ZHD, 167

OMFSHRTGRD OMFS used with consistent ray traced ZHD and horizontal gradients estimated daily, 233

OMFSHRTGRD06H OMFS used with consistent ray traced ZHD and horizontal gradients estimated every 6 hours, 233

OMTS 'Total' version of the OMF, 167

PC-CORA Vaisala PC-CORA File Structure, 96

PCO Phase Center Offset, 21

PCV Phase Center Variation, 21

PPP Precise Point Positioning, 10

RCP Right Circularly Polarized, 21

RH Relative Humidity (%), 33

RMS Root Mean Square, 9

RS Radiosonde, 6

SLR Satellite Laser Ranging, 2

SMF Azimuthally Symmetric Mapping Function, 11

STD Slant Total Delay, 8

TAV Troposphere Azimuthal Variability, 235

TEC Total Electron Content, 17

TVD Tonie van Dam "partially tidal" APL model, 168

UKMO UK Met Office, 56

UM Unified Model, 56

VLBI Very Long Baseline Interferometry, 2

VMF Vienna Mapping Functions [Boehm and Schuh, 2003], 5

VMF1 Updated VMF [Boehm et al., 2006a], 5

VMF1G 'Gridded version of the VMF1', 167

VMF1GRT VMF1G used with consistent ray traced ZHD, 167

WMO World Meteorological Organization, 70

WRMS Weighted RMS, 178

WVR Water Vapour Radiometer, 9

ZHD Zenith Hydrostatic Delay, 8

ZTD Zenith Total Delay, 2

ZWD Zenith Wet Delay, 8

Contents

1 Introduction **1**

1.1 Motivation and Research Goals 1

1.2 Literature Review 4

1.2.1 Troposphere Mapping Function Developments 5

1.2.2 Troposphere Asymmetry Modelling 8

1.3 Thesis Organization 10

2 Background **13**

2.1 GPS Very Brief Overview 14

2.2 GNSS Observables 15

2.2.1 Zero difference (raw) observations 15

2.2.2 Forming single difference observations 17

2.2.3 Forming double difference observations 18

2.3 Precise Point Positioning 19

2.4 Non Geophysical Effects Modelling 20

2.4.1 Phase Wind-up 20

2.4.2 Antenna Phase Center Variations 21

2.4.3 Differential Code Biases 22

2.5 Site Displacement Modelling 23

2.5.1 Earth Tides 23

2.5.2 Ocean Tide Loading 24
2.5.3 Atmospheric Pressure Loading 24
2.6 Tropospheric Modelling 25
2.6.1 The Atmosphere in Brief 25
2.6.2 The Neutral Atmosphere 26
2.6.3 Definitions 27
2.6.4 Expressing Air Moisture 29
2.6.5 Radio Refractive Index of Moist Air 33
2.6.6 Refractivity Set of Constants 35
2.6.7 Compressibility Factors 37
2.6.8 Hydrostatic Delay 37
2.6.9 Neutral Atmosphere Delay: a Definition 40
2.6.10 Modelling the Tropospheric Delay in Space Geodetic Techniques 43
2.6.11 Tropospheric Mapping Functions 43
2.7 Tropospheric gradients 51

3 Building the OMF (Orliac Mapping Functions) 54
3.1 OMF Overview 55
3.2 Three Dimensional Ray Tracing Algorithm 56
3.2.1 NWM Overview 56
3.2.2 MESO Coordinate Systems 57
3.2.3 Coordinate Transformation Between the Geographical and Equatorial Systems 59
3.2.4 Comments on the Coordinate Systems 60
3.3 Ray Tracing 61
3.3.1 Definitions 61
3.3.2 Algorithm Description 61

3.3.3 Getting the Water Vapour Pressure From P, T, and U . . 70
3.3.4 Computing Tropospheric Delays 71
3.3.5 Computing the Geometric Bending Delay 71
3.4 Selection of Elevation Angles to Ray Trace and Quality Assessment of the OMF 72
3.4.1 Quality Criteria 73
3.4.2 Direct Mapping 73
3.4.3 Interpolation Error 83
3.4.4 Linear Interpolation Error 86
3.5 Cubic Spline Interpolation Versus Marini's Model 88
3.6 Implementation of the OMF 91
3.7 Summary 92

4 Assessing the Meteorological Models 94

4.1 Introduction 95
4.2 Data Set Description 96
4.3 On the Humidity Field in Radiosonde Reports 101
4.3.1 Problematic Overview 101
4.3.2 Impact of the water vapour saturation e_{sat} formula on the computed relative humidity 102
4.3.3 Identifying the e_{sat} formula for the UK hiRes RS Sites used in this study 106
4.3.4 On the Humidity Field Formal Error in Radiosonde Reports 110
4.3.5 Interpolated Versus Measured Atmospheric State Profiles . 114
4.3.6 Models' impact in the total, hydrostatic and wet refractivities 119
4.4 Details on Pressure Layers 125
4.4.1 Strategy description 125
4.4.2 Illustration 125

4.4.3 Model performance on a pressure layer basis 129
4.4.4 Temporal variation of the models' performance 135
4.5 Model Accuracy 144
4.5.1 Methodology 144
4.5.2 Two methods for computing the zenith delays 144
4.5.3 Ray tracing of hiRes RS data, results: two ray tracing methods and seven different models to represent humidity . . . 146
4.5.4 Ray-traced ZHD versus Saastamoinen 151
4.6 Impact of the modelling error on the determination of the refractivity 154
4.7 Zenith Delay Determination: High Resolution Radiosonde versus NWM, a comparison 157
4.8 Summary 158

5 Results: Azimuthally Symmetric Mapping Functions 160
5.1 Introduction 161
5.2 Data Processing 161
5.2.1 NWM and GPS Data availability 161
5.2.2 Strategy and Solution Description 167
5.2.3 Modification of the Bernese GPS Software V5.0 169
5.2.4 Modelling of offsets in the time series 172
5.3 Atmospheric Pressure Loading 177
5.3.1 Comparison of the two Atmospheric Pressure Loading Models 179
5.3.2 Atmospheric Pressure Loading: Correcting at Observation Level versus Applying Daily Average Corrections to Daily Coordinate Estimates 190
5.4 Impact of Applying Atmospheric Pressure Loading Corrections on Positioning Performances 193
5.5 Mapping functions' Performances Analysis 194

5.5.1 Positioning Precision 194
5.5.2 On a priori zenith hydrostatic delay 202
5.5.3 Total mapping function 210
5.5.4 ZTD: GPS versus NWM 211
5.6 Summary 215

6 Results: Azimuth Dependent Mapping Functions 217
6.1 Introduction 218
6.2 Asymmetry in Mapping Functions Derived from a Numerical Weather Model 219
6.3 Positioning performances 233
6.4 Estimated Troposphere Azimuthal Variability 235
6.5 The impact of Troposphere Azimuthal Variability on ZTD Estimation 247
6.6 Summary 248

7 Correlation Between Troposphere Modelling and Atmospheric Pressure Loading 250
7.1 Introduction 251
7.2 Cross-Correlation Between Height Time Series and Atmospheric Pressure Loading 252
7.3 Cross Correlation Between Differential Height Time Series and Atmospheric Pressure Loading 254
7.3.1 Impact of the Mapping Function 254
7.3.2 A Priori Zenith Delay Impact 260
7.4 Summary 261

8 Conclusions and Recommendations for Future Work 262
8.1 Conclusions 262
8.2 Recommendations for future work 265

References **267**

9 Coordinate Time Series **276**

10 Azimuthal Asymmetry in the OMF **293**

11 APL and Differential Coordinate Time Series **304**

12 APL and Differential ZTD Time Series **307**

List of Figures

2.1 Decomposition of the homosphere according to its vertical temperature profile. Courtesy of the UK Met Office. 26
2.2 Illustration of Fermat's principle for a ray travelling from A to B through a hypothetical horizontally stratified atmosphere with four layers of constant refractivity N1 > N2 > N3 > N4 > 0. The blue line would be the line of propagation in vacuum. 41

3.1 Flow chart of how the OMF are built. 55
3.2 "Equatorial" coverage of the MESO. The grid is regular, with a node spacing of 12.3 km. The UK appears to be on the equator. . 57
3.3 Geographical coverage of the UK Met Office mesoscale unified model. Each dot represents a node of the grid originally expressed in an equatorial system. 58
3.4 The geographical coordinate system (in black) and the rotated or equatorial coordinate system (in red). Coordinate transformation between the two systems is described under Section 3.2.3. Full details can be found in [Staniforth et al., 2006]. 60
3.5 Geometrical configuration for the first steps of the ray tracing. . . 65
3.6 Determination of refractivity for an arbitrary height: illustration of interaction between an arbitrary height and geopotential heights of pressure levels on each edge of the tower. **Surface at height h1**: case where on each edge of the tower, height h is comprised between the same two pressure levels, i.e, case (i) is found four times. **Surface at height h2**: case where a mix of situations is found. In case Pressure level j is the top pressure level, a mix of three case (i) for corners cj_0, cj_2 and cj_3 and one case (ii) for corner cj_1 is found ((i) with different pressure levels if pressure level j is not the top one) 68
3.7 BIGF CGPS stations used for identifying the optimal set of elevation angles to ray trace. 74
3.8 672 azimuthal profiles of the 'wet' mapping function difference (OMF minus NMF) with respect to elevation, with 1741 ray traces (points) per profile, for CGPS stations ABER, IESG and HERS over a period composed of two weeks centered on DoYs 28 and 210 of year 2005. Black dots and bars are means and associated standard deviations computed over bins of 1 degree. 75

3.9 A selection of profiles of the 'wet' mapping function difference (OMF minus NMF) versus the elevation angle, to illustrate the various shapes the profiles can take. The selection was made out of profiles for CGPS stations ABER, IESG and HERS over a period composed of two weeks centered on DoYs 28 and 210 of year 2005. 76
3.10 Daily histograms of the number of GPS observations with respect to elevation angle for CGPS station ABER for DoYs 46, 137, 228 and 319 of year 2005. 79
3.11 Daily histograms of the number of GPS observations with respect to elevation angle for CGPS station IESG for DoYs 46, 137, 228 and 319 of year 2005. 80
3.12 Daily histograms of the number of GPS observations with respect to elevation angle for CGPS station HERS for DoYs 46, 137, 228 and 319 of year 2005. 80
3.13 Density functions from the data variability, from data distribution and for a combination of the two by simply taking the average. Purple dots are the resulting elevation angles to ray trace so that the integration of f_average between two consecutive elevation angles is constant, here equal to 5%. 82
3.14 Hydrostatic (top), wet (middle) and total (bottom) mapping function differences computed between the fitted three coefficient Marini model and CSI, over a set of 20 ray traced mapping function values. Blue dots are the average difference computed every 0.2 degree with their associated error bars (1 sigma) whereas green dots are the average residual from the least squares adjustment. . 90
3.15 OMF bilinear interpolation scheme. 91

4.1 Example of measured versus interpolated profiles. Red line is the 'observed' water vapour partial pressure whereas the blue line is the interpolated water vapour pressure. The green and black lines respectively represent the observed and interpolated absolute temperature profiles. Data were taken from hiRes RS site Albemarle (UK) on July 10, 2005, at midnight. The labelled horizontal lines represent the equivalent NWM pressure levels. At those points, by construction, measured and modelled variables coincide. 97
4.2 The five hiRes RS sites in the UK. 98
4.3 Difference between the measured relative humidity and the relative humidity calculated from the measured absolute temperature T and the reported T_{dew} computed from T and RH using the Digicora formula. 106

4.4 Difference with respect to geopotential height between T_{dew} as reported in the edited radiosonde reports and the one computed from the measured RH and T using the Digicora formula, for data available at hiRes RS site Albemarle for the time span 2001–2007 (see Table 4.2 for details on the availability). The original 2 s data was reduced to a regular sample of 0.5% (one measurement out of 200) to alleviate the plotting. 107
4.5 Effect of a ± 0.5% RH bias (top left), of a ± 0.05 K T bias (top right), and of a combined ± 0.5% RH and ± 0.05 K T bias (bottom) on the computed T_{dew}. Presented are the difference between T_{dew} as reported in the edited radiosonde reports and the one computed from the measured RH and T using the Digicora formula, for data available for hiRes RS site Albemarle for the time span 2001–2007. The original 2 s data were reduced to a regular sample of 0.5% (one measurement out of 200). 109
4.6 Error propagated on T_{dew} when calculated from the Digicora approximation formulation of T_{dew} as a function of T and RH. In the error propagation, formal errors of 0.1 K and 2% are assumed for T and RH respectively. 112
4.7 Difference between the formal error of the calculated relative humidity and the formal error of the original measurement of RH (taken here as 2%) given for a range of situations. 113
4.8 Natural and positive relative deviations in % of the interpolated profiles compared to the measured profiles of P, T, e and RH for hiRes RS site Camborne. 116
4.9 Natural and positive relative deviations in % of the interpolated profiles compared to the measured profiles P, T, e and RH, for hiRes RS site Lerwick. 117
4.10 Impact of the meteorological models used on the determination of the total refractivity. The truth being the hiRes RS measured data. A green circle means 'Model ON', and a red circle means 'Model OFF', i.e. a green circle means when the model was used instead of the measurements, whereas a red circle means when the measured data were used to compute the refractivity studied. 122
4.11 Impact of the meteorological models used on the determination of the hydrostatic refractivity. The truth being the hiRes RS measured data. A green circle means 'Model ON', and a red circle means 'Model OFF', i.e. a green circle means when the model was used instead of the measurements, whereas a red circle means when the measured data were used to compute the refractivity studied. 123

4.12 Impact of the meteorological models used on the determination of the wet refractivity. The truth being the hiRes RS measured data. A green circle means 'Model ON', and a red circle means 'Model OFF', i.e. a green circle means when the model was used instead of the measurements, whereas a red circle means when the measured data were used to compute the refractivity studied. 124
4.13 Difference between synthetic data generated using the models employed in the NWM ray-tracing and the hiRes RS data. In red: total pressure (P) difference in hPa; in green: absolute temperature (T) difference in K; and in blue: difference in the water vapour partial pressure (e) in hPa for hiRes RS site Albemarle at midday of each day closest of the 15th day of months January to June of year 2005. 127
4.14 Difference between synthetic data generated using the models employed in the NWM ray-tracing and the hiRes RS data. In red: total pressure (P) difference in hPa; in green: absolute temperature (T) difference in K; and in blue: difference in the water vapour partial pressure (e) in hPa for hiRes RS site Albemarle at midday of each day closest of the 15th day of months July to December of year 2005. 128
4.15 Total pressure P error (hPa) versus pressure layer (mean) height (left plot) and pressure layer thickness (right plot), as the difference between synthetic data generated using the models employed in the NWM ray-tracing and the hiRes RS data: <synthetic-measured> for all five hiRes RS sites in the UK over years 2004, 2005 and 2006 only. 133
4.16 Absolute temperature T error (K) versus pressure layer (mean) height (left plot) and pressure layer thickness (right plot), as the difference between synthetic data generated using the models employed in the NWM ray-tracing and the hiRes RS data: <synthetic-measured> for all five hiRes RS sites in the UK over years 2004, 2005 and 2006 only. 133
4.17 Water vapour partial pressure e error (mb) versus pressure layer (mean) height (left plot) and pressure layer thickness (right plot), as the difference between synthetic data generated using the models employed in the NWM ray-tracing and the hiRes RS data: <synthetic-measured> for all five hiRes RS sites in the UK over years 2004, 2005 and 2006 only. 134
4.18 Relative humidity RH error (%) versus pressure layer (mean) height (left plot) and pressure layer thickness (right plot), as the difference between synthetic data generated using the models employed in the NWM ray-tracing and the hiRes RS data: <synthetic-measured> for all five hiRes RS sites in the UK over years 2004, 2005 and 2006 only. 134

4.19 Time series of the daily total pressure P (hPa) average error (and 1 sigma error bars) with respect to pressure layers for hiRes RS site Albemarle over year 2005. By error is meant the difference between synthetic data generated using the models employed in the NWM ray-tracing and the hiRes RS data. 136
4.20 Time series of the daily absolute temperature T (K) average error (and 1 sigma error bars) with respect to pressure layers for hiRes RS site Albemarle over year 2005. By error is meant the difference between synthetic data generated using the models employed in the NWM ray-tracing and the hiRes RS data. 137
4.21 Time series of the daily water vapour partial pressure e (hPa) average error (and 1 sigma error bars) with respect to pressure layers for hiRes RS site Albemarle over year 2005. By error is meant the difference between synthetic data generated using the models employed in the NWM ray-tracing and the hiRes RS data. Actually, e is not observed but derived from other quantities. 138
4.22 Time series of the daily relative humidity RH (%) average error (and 1 sigma error bars) with respect to pressure layers for hiRes RS site Albemarle over year 2005. By error is meant the difference between synthetic data generated using the models employed in the NWM ray-tracing and the hiRes RS data. Actually, RH is observed but the one used here was derived from other quantities (T and T_{dew}). 139
4.23 Time series of the daily total pressure P (hPa) average error (and 1 sigma error bars) with respect to pressure layers for hiRes RS site Camborne over year 2005. By error is meant the difference between synthetic data generated using the models employed in the NWM ray-tracing and the hiRes RS data. 140
4.24 Time series of the daily absolute temperature T (K) average error (and 1 sigma error bars) with respect to pressure layers for hiRes RS site Camborne over year 2005. By error is meant the difference between synthetic data generated using the models employed in the NWM ray-tracing and the hiRes RS data. 141
4.25 Time series of the daily water vapour partial pressure e (hPa) average error (and 1 sigma error bars) with respect to pressure layers for hiRes RS site Camborne over year 2005. By error is meant the difference between synthetic data generated using the models employed in the NWM ray-tracing and the hiRes RS data. Actually, e is not observed but derived from other quantities. 142

4.26 Time series of the daily relative humidity RH (%) average error (and 1 sigma error bars) with respect to pressure layers for hiRes RS site Camborne over year 2005. By error is meant the difference between synthetic data generated using the models employed in the NWM ray-tracing and the hiRes RS data. Actually, RH is observed but the one used here was derived from other quantities (T and T_{dew}). 143
4.27 Error propagated on the total refractivity N (ppm) for the different pressure levels. A priori sigma for P, T, and e (assumed independent) were previously determined (Table 4.9) and are reproduced in brackets on each plot. 156

5.1 Six hourly (top) and daily (bottom) NWM data availability for the period January 2003 to October 2006. 164
5.2 Station selection for testing the new OMF mapping functions, as a tradeoff between GPS and NWM data availability and geographic distribution. 165
5.3 Combined daily data availability (based on NWM and GPS data availability). Numbers on the right hand side are the number of full days per station. 166
5.4 Default BSW50 GNSS observation elevation weighting function (red curve) versus the (normalized) weighting function used in Tregoning and Herring [2006] (blue curve). 170
5.5 Example offset selection for CGPS station LIVE. **Left plot**: all potential global offsets induced by changes in product generation, local offsets due to hardware changes (receiver/antenna) and visually identified offsets included. **Right plot**: only offsets identified as significant included. Green bars represent "global" offsets (from product generation). Light grey bars represent receiver changes. Pink bars represent antenna changes. Black bars are simultaneous receiver plus antenna changes. Orange bars indicate where an offset was not attributed to a hardware change nor a change in the processing strategy of the analysis center who generated the products but was manually added. Yellow areas are bad periods which were taken away from the analysis. Black lines represent (broken) linear variations whereas white on red lines (East and North) and white on green (Up) represent (broken) linear plus annual plus semi-annual signals as estimated using MLE using respectively all offsets (left) and selected only (right) offsets. 175

5.6 Example offset selection for CGPS station NOTT. **Left plot**: all potential global offsets induced by changes in product generation, local offsets due to hardware changes (receiver/antenna) and visually identified offsets included. **Right plot**: only offsets identified as significant included. Green bars represent "global" offsets (from product generation). Light grey bars represent receiver changes. Pink bars represent antenna changes. Black bars are simultaneous receiver plus antenna changes. Orange bars indicate where an offset was not attributed to a hardware change nor a change in the processing strategy of the analysis center who generated the products but was manually added. Yellow areas are bad periods which were taken away from the analysis. Black lines represent (broken) linear variations whereas white on red lines (East and North) and white on green (Up) represent (broken) linear plus annual plus semi-annual signals as estimated using MLE using respectively all offsets (left) and selected only (right) offsets. 176
5.7 APL induced displacement time series predicted by the two models LP (top row) and TVD (middle row), for the North, East and Up components at two CGPS stations: CAMB and IESG, and the difference between them, taken as LP minus TVD (bottom row). . 181
5.8 RMS in mm of the predicted APL induced displacement by the TVD model (top left), the LP model (top right) and the difference <LP minus TVD> (bottom), for the north component. RMS were computed over a 7 years period. Colour and size of the squares are according the magnitude of the RMS. 185
5.9 RMS in mm of the predicted APL induced displacement by the TVD model (top left), the LP model (top right) and the difference <LP minus TVD> (bottom), for the east component. RMS were computed over a 7 years period. Colour and size of the squares are according the magnitude of the RMS. 186
5.10 RMS in mm of the predicted APL induced displacement by the TVD model (top left), the LP model (top right) and the difference <LP minus TVD> (bottom), for the up component. RMS were computed over a 7 years period. Colour and size of the squares are according the magnitude of the RMS. 187
5.11 Power spectrum densities of the APL induced displacement for the North, East and Up component as computed for CGPS station CAMB for the TVD model (left) and LP model (right). 188
5.12 Power spectrum densities of the APL induced displacement for the North, East and Up component as computed for CGPS station IESG for the TVD model (left) and LP model (right). 189

5.13 Example of time series of the difference in mm in the vertical positions obtained after daily correction for the APL minus positions obtained when processing data corrected at the observation level for APL. All time series shown were obtained using the NMF mapping functions and standard a priori ZHD. 192
5.14 (Part 1 out of 4) Daily height comparisons between 7 different tropospheric modelling strategies over a 3.8 year period. Common level is the average height of the solution in abscissa. 198
5.15 (Part 2 out of 4) Daily height comparisons between 7 different tropospheric modelling strategies over a 3.8 year period. Common level is the average height of the solution in abscissa. 199
5.16 (Part 3 out of 4) Daily height comparisons between 7 different tropospheric modelling strategies over a 3.8 year period. Common level is the average height of the solution in abscissa. 200
5.17 (Part 4 out of 4) Daily height comparisons between 7 different tropospheric modelling strategies over a 3.8 year period. Common level is the average height of the solution in abscissa. 201
5.18 Example of time series of the difference in the vertical position of CGPS station HERS obtained with different mapping functions, as indicated on the top right of each plot. No APL corrections were applied. In red: differential vertical position in mm; In blue: differential 6 hourly ZTD in mm; In black: pressure variation in hPa; and in green: predicted radial induced APL displacement in mm. 204
5.19 Example of time series of the difference in the vertical position of CGPS station CAMB obtained with different mapping functions, as indicated on the top right of each plot. No APL corrections were applied. In red: differential vertical position in mm; In blue: differential 6 hourly ZTD in mm; In black: pressure variation in hPa; and in green: predicted radial induced APL displacement in mm. 205
5.20 Impact on height estimate (mm) of the error in the a priori ZHD introduced (cm) in the GPS data processing. In blue: CGPS station PMTG. Slope and intercept were computed excluding PMTG. . . 207
5.21 Impact on height estimate (mm) of the error in the estimated surface pressure introduced (hPa) in the GPS data processing when computing the a priori ZHD. In blue: CGPS station PMTG. Slope and intercept were computed excluding PMTG. 207
5.22 Error in the a priori ZHD (cm) computed using the Saastamoinen [1972] model with respect to the error in the surface pressure (hPa). 208
5.23 Sensitivity in mm/hPa of the inferred height to the error in the surface pressure used to compute the a priori ZHD plotted against the orthometric height of station (m). 208

5.24 Sensitivity in mm/hPa of the inferred height to the error in the surface pressure used to compute the a priori ZHD. Black squares: orthometric height of the station. 209
5.25 Comparison of the total mapping function versus the usual pair of hydrostatic and wet mapping function (with ray traced a priori ZHD). Differential coordinates in red and differential ZTD in blue. 212
5.26 Mean offsets of the 6 hourly ZTD difference <GPS-NWM> computed over samples of size 106,000 to 108,000. NMF: red square; GMF: purple stars; OMFS: blue circles; OMFSHRT: blue triangle; VMF1G: black circle; and VMF1GRT: black triangles. Error bars were left out for clarity but are about 14 mm. 215

6.1 Slant atmospheric delay difference for CGPS station ABER between the azimuth dependent mapping function OMFA and the NMF at 5 degrees elevation for a standard ZHD of 2300 mm (left column) and ZWD 100 mm (right column) for 26 July, 2006. . . . 220
6.2 Slant atmospheric delay difference for CGPS station ABER between the azimuth dependent mapping function OMFA and the NMF at 5 degrees elevation for a standard ZHD of 2300 mm (left column) and ZWD 100 mm (right column) for 28 July, 2006. . . . 221
6.3 Slant atmospheric delay difference for CGPS station IESG between the azimuth dependent mapping function OMFA and the NMF at 5 degrees elevation for a standard ZHD of 2300 mm (left column) and ZWD 100 mm (right column) for 26 July, 2006. 222
6.4 Slant atmospheric delay difference for CGPS station IESG between the azimuth dependent mapping function OMFA and the NMF at 5 degrees elevation for a standard ZHD of 2300 mm (left column) and ZWD 100 mm (right column) for 28 July, 2006. 223
6.5 Time series of the hydrostatic mapping functions asymmetry at 5 degrees elevation for CGPS station IESG. Time series are plotted every 60 degrees (although ray-traced every 30 degrees) for clarity. 227
6.6 Time series of the hydrostatic mapping functions asymmetry at 5 degrees elevation for CGPS station HERS. Time series are plotted every 60 degrees (although ray-traced every 30 degrees) for clarity. 228
6.7 Time series of the wet mapping functions asymmetry at 5 degrees elevation for CGPS station IESG. Time series are plotted every 60 degrees (although ray-traced every 30 degrees) for clarity. 229
6.8 Time series of the wet mapping functions asymmetry at 5 degrees elevation for CGPS station HERS. Time series are plotted every 60 degrees (although ray-traced every 30 degrees) for clarity. 230
6.9 Time series of the total mapping functions asymmetry at 5 degrees elevation for CGPS station IESG. Time series are plotted every 60 degrees (although ray-traced every 30 degrees) for clarity. 231

6.10 Time series of the total mapping functions asymmetry at 5 degrees elevation for CGPS station HERS. Time series are plotted every 60 degrees (although ray-traced every 30 degrees) for clarity. 232
6.11 Four months time series of the tropospheric asymmetry at 5 degrees elevation and on different azimuths at CGPS station IESG. Red: estimated using azimuth dependent mapping functions; Blue: estimated using 6 hourly horizontal tropospheric gradients. 238
6.12 Four months time series of the tropospheric asymmetry at 5 degrees elevation and on different azimuths at CGPS station HERS. Red: estimated using azimuth dependent mapping functions; Blue: estimated using 6 hourly horizontal tropospheric gradients. 239
6.13 Four months time series of the tropospheric asymmetry at 5 degrees elevation and on different azimuths at CGPS station NSTG. Red: estimated using azimuth dependent mapping functions; Blue: estimated using 6 hourly horizontal tropospheric gradients. 240
6.14 Amplitude and phase of the annual signal found in the azimuthal tropospheric asymmetry evaluated at 5 degrees elevation for the north (top) and south (bottom) directions. Red: using the azimuth dependent OMF; Green: estimating horizontal gradients. 244
6.15 Amplitude and phase of the annual signal found in the azimuthal tropospheric asymmetry evaluated at 5 degrees elevation for the east (top) and west (bottom) directions. Red: using the azimuth dependent OMF; Green: estimating horizontal gradients. 245
6.16 Time series of vertical coordinate (red) and ZTD (blue) difference based on different gradient estimation approaches for CGPS station IESG over year 2004. 248

7.1 Average cross-correlations between the predicted atmospheric pressure loading induced displacements and height time series computed over a set of CGPS 27 stations in the UK. Error bars represent the standard deviation associated with the plotted value (only represented for the first solution plotted for clarity, as rather constant over the different solutions). 253
7.2 Average cross-correlations between the predicted atmospheric pressure loading induced displacements and differential height time series computed over a set of 27 CGPS stations in the UK. Error bars represent the standard deviation associated with the plotted value (only represented for the first solution plotted, for clarity, as rather constant over the different solutions). 255

7.3 Average cross-correlations between the predicted atmospheric pressure loading induced displacements and differential height time series computed over a set of 27 CGPS stations in the UK with OMFS_OFF as the reference solution. Error bars represent the standard deviation associated with the plotted value (only represented for the first solution plotted, for clarity, as rather constant over the different solutions). Only solutions with standard a priori ZHD considered. 256
7.4 Average cross-correlations between the predicted atmospheric pressure loading induced displacements and differential height time series computed over a set of 27 CGPS stations in the UK with OMFSHRT_OFF as the reference solution. Error bars represent the standard deviation associated with the plotted value (only represented for the first solution plotted, for clarity, as rather constant over the different solutions). Only solutions with ray traced a priori ZHD considered. 257
7.5 Differential height time series for CGPS station HERS. From top to bottom: GMF minus NMF, OMFS minus NMF, OMTS minus NMF, OMTS minus OMFS, and VMF1GRT minus VMF1G. Plotted on the same scale are the vertical displacement induced by atmospheric pressure loading as predicted by two models: in green a model run by T. van Dam (pers. comm.) and in light gray by aplo [Petrov, 2008]. No artificial offset was introduced. 258
7.6 Differential ZTD time series for CGPS station HERS. Top left: GMF minus NMF; Top right: OMFS minus NMF; Middle left: OMTS minus NMF; Middle right: OMTS minus OMFS; Bottom: VMF1GRT minus VMF1G. Plotted on the same scale are the vertical displacement induced by atmospheric pressure loading as predicted by two models: in green a model run by T. van Dam (pers. comm.) and in light gray by aplo [Petrov, 2008]. No artificial offset was introduced. 259
7.7 Average cross-correlations between the predicted atmospheric pressure loading induced displacements and differential height time series computed over a set of 27 CGPS stations in the UK with OMFSHRT_OFF as the reference solution. Error bars represent the standard deviation associated with the plotted value (only represented for the first solution plotted, for clarity, as rather constant over the different solutions). Only solutions with ray traced a priori ZHD considered. 260

9.1 Example offset selection for CGPS station ABER. **Left plot**: all potential global offsets induced by changes in product generation, local offsets due to hardware changes (receiver/antenna) and visually identified offsets included. **Right plot**: only offsets identified as significant included. Green bars represent "global" offsets (from product generation). Light grey bars represent receiver changes. Pink bars represent antenna changes. Black bars are simultaneous receiver plus antenna changes. Orange bars indicate where an offset was not attributed to a hardware change nor a change in the processing strategy of the analysis center who generated the products but was manually added. Yellow areas are bad periods which were taken away from the analysis. Black lines represent (broken) linear variations whereas white on red lines (East and North) and white on green (Up) represent (broken) linear plus annual plus semi-annual signals as estimated using MLE using respectively all offsets (left) and selected only (right) offsets. 277
9.2 Same as Figure 9.1 for CGPS stations ABYW (top) and BARK (bottom). Left: all offsets; right: selected offsets. 278
9.3 Same as Figure 9.1 for CGPS stations CAMB (top) and CARL (bottom). Left: all offsets; right: selected offsets. 279
9.4 Same as Figure 9.1 for CGPS stations COLC (top) and DARE (bottom). Left: all offsets; right: selected offsets. 280
9.5 Same as Figure 9.1 for CGPS stations EDIN (top) and GLAS (bottom). Left: all offsets; right: selected offsets. 281
9.6 Same as Figure 9.1 for CGPS stations HERS (top) and IESG (bottom). Left: all offsets; right: selected offsets. 282
9.7 Same as Figure 9.1 for CGPS stations INVE (top) and IOMS (bottom). Left: all offsets; right: selected offsets. 283
9.8 Same as Figure 9.1 for CGPS stations KING (top) and LEED (bottom). Left: all offsets; right: selected offsets. 284
9.9 Same as Figure 9.1 for CGPS stations LERW (top) and LIVE (bottom). Left: all offsets; right: selected offsets. 285
9.10 Same as Figure 9.1 for CGPS stations LOWE (top) and MORP (bottom). Left: all offsets; right: selected offsets. 286
9.11 Same as Figure 9.1 for CGPS stations NEWC (top) and NEWL (bottom). Left: all offsets; right: selected offsets. 287
9.12 Same as Figure 9.1 for CGPS stations NOTT (top) and NPLD (bottom). Left: all offsets; right: selected offsets. 288
9.13 Same as Figure 9.1 for CGPS stations NSTG (top) and OSHQ (bottom). Left: all offsets; right: selected offsets. 289
9.14 Same as Figure 9.1 for CGPS stations PERS (top) and PMTG (bottom). Left: all offsets; right: selected offsets. 290
9.15 Same as Figure 9.1 for CGPS stations SHEE (top) and SUNB (bottom). Left: all offsets; right: selected offsets. 291

9.16 Same as Figure 9.1 for station THUR. Left: all offsets; right: selected offsets. 292

10.1 Slant atmospheric delay difference for CGPS station GLAS between the azimuth dependent mapping function OMF_AZI and the NMF at 5 degrees elevation for a standard ZHD of 2300 mm (left column) and ZWD 100 mm (right column) for 26 July, 2006. 294
10.2 Slant atmospheric delay difference for CGPS station GLAS between the azimuth dependent mapping function OMF_AZI and the NMF at 5 degrees elevation for a standard ZHD of 2300 mm (left column) and ZWD 100 mm (right column) for 28 July, 2006. 295
10.3 Slant atmospheric delay difference for CGPS station IOMS between the azimuth dependent mapping function OMF_AZI and the NMF at 5 degrees elevation for a standard ZHD of 2300 mm (left column) and ZWD 100 mm (right column) for 26 July, 2006. 296
10.4 Slant atmospheric delay difference for CGPS station IOMS between the azimuth dependent mapping function OMF_AZI and the NMF at 5 degrees elevation for a standard ZHD of 2300 mm (left column) and ZWD 100 mm (right column) for 28 July, 2006. 297
10.5 Slant atmospheric delay difference for CGPS station LERW between the azimuth dependent mapping function OMF_AZI and the NMF at 5 degrees elevation for a standard ZHD of 2300 mm (left column) and ZWD 100 mm (right column) for 26 July, 2006. . . . 298
10.6 Slant atmospheric delay difference for CGPS station LERW between the azimuth dependent mapping function OMF_AZI and the NMF at 5 degrees elevation for a standard ZHD of 2300 mm (left column) and ZWD 100 mm (right column) for 28 July, 2006. . . . 299
10.7 Slant atmospheric delay difference for CGPS station NEWL between the azimuth dependent mapping function OMF_AZI and the NMF at 5 degrees elevation for a standard ZHD of 2300 mm (left column) and ZWD 100 mm (right column) for 26 July, 2006. . . . 300
10.8 Slant atmospheric delay difference for CGPS station NEWL between the azimuth dependent mapping function OMF_AZI and the NMF at 5 degrees elevation for a standard ZHD of 2300 mm (left column) and ZWD 100 mm (right column) for 28 July, 2006. . . . 301
10.9 Slant atmospheric delay difference for CGPS station NSTG between the azimuth dependent mapping function OMF_AZI and the NMF at 5 degrees elevation for a standard ZHD of 2300 mm (left column) and ZWD 100 mm (right column) for 26 July, 2006. . . . 302
10.10 Slant atmospheric delay difference for CGPS station NSTG between the azimuth dependent mapping function OMF_AZI and the NMF at 5 degrees elevation for a standard ZHD of 2300 mm (left column) and ZWD 100 mm (right column) for 28 July, 2006. . . . 303

11.1 Differential height time series for CGPS station ABER. From top to bottom: GMF minus NMF, OMFS minus NMF, OMTS minus NMF, OMTS minus OMFS, and VMF1GRT minus VMF1G. Plotted on the same scale are the vertical displacement induced by atmospheric pressure loading as predicted by two models: in green a model run by T. van Dam (pers. comm.) and in light gray by aplo, L. Petrov's package available from url. No artificial offset was introduced. 305
11.2 Differential height time series for CGPS station IESG. From top to bottom: GMF minus NMF, OMFS minus NMF, OMTS minus NMF, OMTS minus OMFS, and VMF1GRT minus VMF1G. Plotted on the same scale are the vertical displacement induced by atmospheric pressure loading as predicted by two models: in green a model run by T. van Dam (pers. comm.) and in light gray by aplo, L. Petrov's package available from url. No artificial offset was introduced. 306

12.1 Differential ZTD time series for CGPS station ABER. Top left: GMF minus NMF; Top right: OMFS minus NMF; Middle left: OMTS minus NMF; Middle right: OMTS minus OMFS; Bottom: VMF1GRT minus VMF1G. Plotted on the same scale are the vertical displacement induced by atmospheric pressure loading as predicted by two models: in green a model run by T. van Dam (pers. comm.) and in light gray by aplo, L. Petrov's package available from url. No artificial offset was introduced. 308
12.2 Differential ZTD time series for CGPS station HERS. Top left: GMF minus NMF; Top right: OMFS minus NMF; Middle left: OMTS minus NMF; Middle right: OMTS minus OMFS; Bottom: VMF1GRT minus VMF1G. Plotted on the same scale are the vertical displacement induced by atmospheric pressure loading as predicted by two models: in green a model run by T. van Dam (pers. comm.) and in light gray by aplo, L. Petrov's package available from url. No artificial offset was introduced. 309

List of Tables

2.1 Atmospheric Composition (from [USSA, 1976], [Gleuckauf, 1951] and [Salby, 1995], *Only the most relevant constituents are shown. Constituents missing from the original table are:* O_3, CH_4, N_2O, CO, NO, $CFC-11$ *and* $CFC-12$) 27
2.2 "*Best available*" and "*best average*" refractivity constants as identified and computed by Rüeger [2002]. 36
2.3 Coefficients of the Niell [1996] Hydrostatic Mapping Function (nmfh2.0) 48
2.4 Coefficients of the Niell [1996] Wet Mapping Function (nmfw2.0) . 48
2.5 Parameters c_0, c_{10}, c_{11}, and Ψ needed for the computation of c in the hydrostatic VMF1 mapping function. 50

3.1 NWM cell nodes indices. 62
3.2 Ray tracing integration step increments according to the height, [Rocken et al., 2001] 64
3.3 Approximate corresponding starting elevation angles to the quantified outgoing ones, in degrees. Starting elevation angles were found by averaging corresponding values of the outgoing ones over the range [outgoing - 0.25, outgoing + 0.25 degrees] to encompass different meteorological situations. 83
3.4 Statistics of the difference between a regular grid of mapping function correction generated using cubic spline interpolation from data sets of 1741 points and 20 points. Interpolated values are compared every 0.01 degree of outgoing elevation with a sample of more than 10 million elevation angles considered. 84
3.5 Equivalent absolute range errors incurred when using a regular grid of mapping function correction generated using cubic spline interpolation form data sets of 1741 points and 20 points with an a priori zenith hydrostatic delay of 2.3 metres and zenith wet delay of 0.2 metre. The values given in millimetres and were computed with a sample of more than 10 million elevation angles. 85
3.6 Mapping function errors propagated on the range at selected elevation angles for CGPS station IESG on DoY 210 of 2005. Values given in millimetres. 85
3.7 Statistics on the linear interpolation error with respect to the grid spacing used to interpolate the mapping function. 87

3.8 Statistics on the equivalent range error of the linear interpolation error with respect to the grid spacing used to interpolate the mapping function. 87

4.1 Coordinates of the five hiRes RS sites in the UK. 99
4.2 Monthly data availability for the five hiRes RS sites in the UK for the period January 2001 to March 2007 inclusive. 100
4.3 Published range of operation, resolution, accuracy and lag of RS meteorological measurements. 101
4.4 Statistics on the difference between measured relative humidity and relative humidity calculated from the reported RS dew point temperature, using the HIRLAM saturation water vapour pressure function and the Wexler one. Values given in [%]. 104
4.5 Statistics on the absolute and relative difference between water vapour pressure computed using the HIRLAM saturation water vapour pressure function and the Wexler one. The last column indicates the effective sample size on which the average relative difference was computed as situations with zero humidity had to be removed. So numbers with an effective sample size much smaller than the original sample should be treated with care. 105
4.6 Means and associated standard deviations for the *natural* deviations of the interpolated profiles compared to measured profiles of P, T, e and RH for all five hiRes RS sites. Values are given in %. 118
4.7 Means and associated standard deviations for the *positive* deviations of the interpolated profiles compared to measured profiles of P, T, e and RH for all five hiRes RS sites. Values are given in %. 119
4.8 Details on model performance on a pressure layer basis as the average and standard deviation of the difference between synthetic data generated using the models employed in the NWM ray-tracing and the hiRes RS data: <synthetic-measured> for all five hiRes RS sites in the UK. The NWM data was interpolated to the RS measurement time. 130
4.9 Overall model performance on a pressure layer basis as the average and standard deviation of the difference between synthetic data generated using the models employed in the NWM ray-tracing and the hiRes RS data: <synthetic-measured> for all five hiRes RS sites in the UK over years 2004, 2005 and 2006 only. 131
4.10 Average height in metres of equivalent NWM pressure levels. The heights were computed using 5 years of data from all five hiRes RS sites in the UK. Right hand column indicates the average thickness in metres of the pressure layers defined as the part of the atmosphere comprised between two consecutive pressure levels. . . 132
4.11 Statistics on the difference on the zenith delays ray-traced from hiRes RS data and extracted standard data. The difference was taken as <Standard-Hires>. All numbers are given in mm. 148

4.12 Mean offsets and associated standard deviations of the difference between the integrated ZHD and one computed using Saastamoinen [1972], using hiRes RS data and corresponding standard data. All values are given in mm. Radiosonde profiles were extended assuming a dry atmosphere in hydrostatic equilibrium, hence the null correction term. 153
4.13 Statistics (mean and associated standard deviation) of the difference between zenith delays derived from the NWM and the hiRes RS data. 158

5.1 Description of the different tropospheric modelling strategies used in the study. 167
5.2 Selection of changes in the CODE processing strategy that were considered to potentially impact time series of estimated coordinates and/or ZTDs (extracted from Table 2 in Hugentobler et al. [2005]). 173
5.3 Statistics on the difference between published APL predicted displacements for available UK sites from the NASA APL loading service and the ones produced locally running aplo@Petrov, L. Values given in mm. 180
5.4 Amplitude A (mm) and phase ϕ (deg) of the annual and semi-annual components of the atmospheric pressure loading induced displacement computed from the TVD and LP APL models over a 7 year period. Details are given on a station by station basis for the radial component only and averages plus associated standard deviation for horizontal and radial components. 184
5.5 Weighted RMS (mm) for the vertical component of site time series obtained using 16 combinations of tropospheric modelling strategies and atmospheric pressure loading correction schemes. (Functional model: linear regression plus annual and semi-annual signals. Stochastic model is white noise plus Flicker noise.) 193
5.6 Weighted RMS (mm) for the north, east and up components obtained for 7 different tropospheric modelling strategies and vertical offset to the NMF_OFF solution. (Functional model: linear regression plus annual and semi-annual signals; Stochastic model: combination of white noise plus Flicker noise; Offsets in time series: selected only) 195
5.7 Statistics for the difference <GPS - NWM> for 6 hourly ZTD estimated from GPS and the ones ray traced from NWM. Data from site PMTG excluded. 212

6.1 Characteristic of the signal found in the azimuth dependent hydrostatic mapping function (modelled as white noise only and solving for an offset plus linear trend plus seasonal variations), averaged over all 30 sites. Values (and associated standard deviation) are given for an elevation angle of 5 degrees and a nominal hydrostatic zenith delay of 2300 mm. 226
6.2 Same as Table 6.1 but for the azimuth dependent wet mapping function and a nominal wet zenith delay of 100 mm. 226
6.3 Same as Table 6.1 but for the azimuth dependent total mapping function and a nominal total zenith delay of 2400 mm. 226
6.4 Weighted RMS (mm) for the north, east and vertical components for 10 different tropospheric modelling strategies and mean vertical offset to OMFS_OFF solution. (Functional model: linear regression plus annual and semi-annual signals; Stochastic model: combination of white noise plus Flicker noise; Offsets in time series: selected only.) 234
6.5 Average amplitude and RMS of the northern and southern tropospheric asymmetry, estimated using both AMF and gradients, and their difference for 30 CGPS stations in the UK. Values are given for an elevation of 5 degrees. 242
6.6 Average amplitude and RMS of the eastern and western tropospheric asymmetry, estimated using both AMF and gradients, and their difference for 30 CGPS stations in the UK. Values are given for an elevation of 5 degrees. 243
6.7 Bias and standard deviation of the difference between ZTD estimated using the azimuth dependent OMF mapping function and ZTD estimated using the symmetric OMF with and without gradients, for 30 CGPS stations in the UK over a 3.8 year period. . . 249

Chapter 1

Introduction

1.1 Motivation and Research Goals

Global Navigation Satellite Systems (GNSS), like the American Global Positioning System (GPS), or GLONASS, the Russian one (and upcoming systems like Galileo in Europe or Beidou in China) are mainly known for their capability to provide real-time navigation information, like position, velocity, acceleration and time. These GNSS (principally GPS so far) have also led to the development of a new variety of geodetic applications, notably in geodynamics and atmospheric sensing. GNSS are all weather proof systems operating continuously with data acquisition and processing possible up to 50 Hz. The efficiency of such systems and their relatively low cost have led to ground networks being developed and rapidly spreading all around the world. For example, Japan now has a network of twelve hundred sites used in the monitoring of seismic activities.

All GNSS data collected near the surface of the Earth are affected by the propagation of the GNSS signals through the atmosphere. From an electromagnetic wave propagation point of view, the atmosphere can be divided in two parts: the lower one, roughly below 50 kilometres height, is named the neutral at-

mosphere and is non-dispersive (neutral); above, and up to 1000 kilometres, is the ionosphere, which is dispersive, at least for the L-Band, to which all GNSS frequencies belong. This thesis addresses some specific aspects of the modelling and the sensing of the lower, neutral part of the atmosphere, referred to as the troposphere in the context of GNSS, with all systems affected in a similar fashion by this non dispersive medium.

Ultimately the research work in this thesis was dedicated to the study of troposphere asymmetry. The study of this started more than three decades ago with the work of Gardner [1976] on Satellite Laser Ranging (SLR). In these early studies, tropospheric asymmetry was handled by estimating a pair of gradients on top of the usually modelled zenith path delay, the delay that would be imposed on a satellite at the zenith, with the gradients accounting for the horizontal linear change of the refractive index. Such early publications on the importance of parametrization of gradients to account for atmospheric asymmetry were acknowledged for example by MacMillan [1995] or Davis et al. [1993] for Very Long Baseline Interferometry (VLBI) and Bar-Sever et al. [1998] for GPS. When modelling zenith total delay (ZTD), the hydrostatic component (see [Davis et al., 1985]) is usually introduced as a priori information, computed from meteorological data collected in situ or predicted by a model, and a correction for the non-hydrostatic part being estimated. Other a priori information that comes into the treatment of space geodetic data are mapping functions. Mapping functions define the ratio of the atmospheric effect experienced at a certain elevation angle when compared to the one that would be experienced in the zenith direction. As it is mathematically impossible to estimate all together a slant delay for each observable, they are all assumed to relate to the same zenithal quantity, via the mapping function. With today's mapping functions, azimuthal symmetry is always assumed. The zenithal

quantity is then either assumed to be constant over a certain period of time, or to exhibit certain properties, either functional, where it is assumed to vary linearly with time (as implemented for example in the Bernese GPS Software [Dach et al., 2007]), or stochastic, where it is usually treated as the realization of a random walk process.

The last decade has witnessed the increasing availability of another source of information revealed to be useful in the treatment of space geodetic data: numerical weather models (NWM). In short, these are a representation of the atmosphere for a certain area, varying in scale from local to global models. In a NWM the physics of the atmosphere is represented, real meteorological information is assimilated, and simulation (prediction or re-analysis) is performed. The results of this process that are of interest to the research work in this thesis are the three dimensional grids of total pressure (P), absolute temperature (T) and humidity (U), as these three quantities are necessary to compute the refractive index of the atmosphere. The NWM allows for a three dimensional representation of the Earth's atmosphere refractive index, enabling ray-tracing in order to derive useful information for the processing of GNSS data.

The knowledge of the true refractivity of the atmosphere along the path of an observed signal would allow the processing of GNSS data as atmospheric free quantities. Clearly, such a knowledge is not available. Instead, the best, but inevitably imperfect, representations of the atmosphere are those available from a NWM. They are at the core of current GNSS research, and particularly the one used throughout the research work in this thesis (MESO, the UK Met Office High Resolution Mesoscale NWM) is a high resolution one, with a spatial grid of about 12.5 km.

The ultimate aim of the research work for this thesis can be summarized by the question: **Can such a high resolution numerical weather model be used to define azimuth dependent mapping functions that can improve state of the art tropospheric modelling and estimation in GNSS data processing**? To answer this question, the following objectives were set in order to derive and test a series of azimuthally symmetric and azimuth dependent tropospheric mapping functions:

- Develop and validate a three-dimensional ray-tracing algorithm.
- Develop and validate a new "model" for the mapping functions (the one traditionally employed [Marini, 1972] was found to be inadequate when trying to fit it to mapping function values obtained from the three dimensional ray tracing of the NWM).
- Assess and compare the performances of the derived mapping functions with traditional and standard modelling, in particular the retrieval of the asymmetry, when compared to simple gradient estimation.
- Investigate the correlation between the derived (azimuthally symmetric and azimuth dependent) mapping functions and atmospheric pressure loading.

1.2 Literature Review

This literature review is split into two parts. The first one concentrates on tropospheric mapping function developments, whereas the second one is dedicated to troposphere asymmetry modelling in space geodetic techniques.

1.2.1 Troposphere Mapping Function Developments

The most common model used for describing the variation of the ratio of the slant delay at a certain elevation angle to the zenith delay was derived by Marini [1972]. This model, a truncated expansion in $1/\sin(\epsilon)$, assumes the neutral atmosphere to be symmetric around the station. Some variants have been proposed and used, with respect to the degree of the expansion (usually 3, but sometimes 2 or 4 have been employed) and a normalization of the model to get a value of 1.0 at the zenith. To deal with the issue of asymmetrical atmosphere, a new approach was developed for the research work in this thesis, which uses a cubic spline interpolation (CSI) carried out on a limited set of mapping ratios at selected elevations, obtained through the ray-tracing of a high resolution NWM.

According to Mendes [1999], most of the mapping functions currently used can be categorized in three different families: (*i*) the ones based on quartic profile, developed by Hopfield [1969]; (*ii*) the ones based on the Marini model [Marini, 1971], [Marini, 1972]; and (*iii*) a smaller group based on the expansion of the cosecant law (including [Saastamoinen, 1973] mapping functions). Marini's model, which assumes spherical symmetry, is undoubtedly the preferred model nowadays and is used notably in the CfA-2.2 [Davis et al., 1985], MTT [Herring, 1992], NMF [Niell, 1996], VMF [Boehm and Schuh, 2003], VMF1 [Boehm et al., 2006a], and the GMF [Boehm et al., 2006b] approaches. Also adopted in all current mapping functions is the normalization at zenith proposed by Herring [1992].

Instead of trying to review mapping functions by types or input model, a more chronological approach is chosen here. The different mapping functions can be seen as belonging to two groups: the ones before the publication of the Niell Mapping Functions (NMF), and the ones after. Considering Table 3.6 in [Mendes, 1999], with the exception of the Black and Eiser [1989], Chao [1972], Chao [1974]

and Moffett [1973] mapping functions, which depend on nothing else but elevation, all others rely on some kind of meteorological surface data as input, whereas, for NMF, Niell [1996] defined mapping functions that were dependent on the location and time of year, and were valid anywhere, and anytime, still providing an overall similar level of precision and accuracy to the best mapping functions relying on in-situ meteorological input, such as the MTT or the Ifadis mapping functions [Mendes, 1999].

In the research work in this thesis, only the NMF and mapping functions published after the NMF were considered. After meaning, basically, NWM based mapping functions. These started with the Improved/Isobaric Mapping Function (IMF) developed by Niell [2000]. The geopotential height 200 hPa was found to correlate well with radiosonde (RS) profile, ray-traced, hydrostatic mapping functions at 5 degree elevation and thus was taken as input to the new mapping function, so-called isobaric. For the wet, coefficients were derived from the ray-tracing of vertical profiles at the site. A factor of two improvement was obtained in both precision and accuracy for the hydrostatic, whereas a 25% improvement was obtained for the wet mapping function. However these were for coefficients derived from the radiosonde profiles, and not from the gridded data, and thus should be taken as the maximum improvement reachable, as vertical profiles interpolated from the grid are not expected to match the (true) profile provided by the radiosonde.

In Boehm and Schuh [2003] the Vienna Mapping Functions (VMF) were introduced. These are based on the full ray-tracing of the European Center for Medium-Range Weather Forecasts (ECMWF) operational analysis data and come in two flavors: rigorous and fast. The rigorous approach determines all three coeffi-

cients for the hydrostatic and wet mapping functions from a set of ten (according to [Boehm and Schuh, 2003]) ray-traced elevations using least-squares. As ray-tracing is rather time consuming, a fast approach was developed where only a ray-trace at a low elevation (3.3 degrees) is needed. Information is then borrowed from both the NMF and IMF, and only the a coefficients remain to be found. Boehm and Schuh [2004] found the VMF (and the IMF) to improve VLBI baseline length repeatability by 10% and 5% in two different campaigns (IVS-R1 and IVS-R4 respectively) when compared to NMF. An upgrade of the VMF was then proposed in Boehm et al. [2006a], where new values for the hydrostatic coefficients b and c were derived and the concept of a total mapping function was also discussed. These new mapping functions were then called the VMF1. The improvement regarding the baseline length repeatability was "small, but significant". However, the main improvement in the new coefficients determination came from the cancelling of systematic effects in the old ones when close to the equator and at high latitudes, where mean station heights could be affected by up to 4 mm [Boehm et al., 2006a]. There are now two distributions of the VMF1: at specific International GNSS Service (IGS) sites or on grids (the latter having been tested by Kouba [2008]).

To take full advantage of a NWM it needs to be ray-traced at a site location, which is not realistic for most users. To overcome this situation, Boehm et al. [2006b] published the Global Mapping Function (GMF). This has the convenience of the NMF, as only location and time are necessary as input, but coefficients (still for the three-term continued fraction used in the NMF) were derived from a global NWM (ECMWF). Coefficients were computed on a 15 $\times$ 15 degrees grid of monthly mean profiles over 36 months, and have a time, latitude and longitude dependency. Amplitude and phase of the GMF coefficients found on the grid

were then expanded into spatial spherical harmonics coefficients. The GMF are, therefore, purely parametric mapping functions. However, unlike the NMF, which are based on a limited set of radiosonde profiles, they are based on NWM data with global coverage and overall wider spatial and temporal coverage. The result being that when compared to NMF, a "significantly smaller bias for the hydrostatic" is observed and a better precision is obtained [Boehm et al., 2006b].

1.2.2 Troposphere Asymmetry Modelling

Several authors have shown the benefit of including a parametrization for the troposphere's asymmetry in space geodetic data processing such as Chen and Herring [1997] and MacMillan [1995] for VLBI, and Bar-Sever et al. [1998] for GPS. Instead of having only a zenith delay parameter estimated, two further horizontal gradient parameters are estimated. The general model (e.g. McCarthy and Petit [2003]) can be described as:

$$STD = m_h(\epsilon)ZHD + m_w(\epsilon)ZWD + m_g(\epsilon)[G_N \cos(\alpha) + G_E \sin(\alpha)] \qquad (1.1)$$

where STD is the slant total delay; ZHD and ZWD are the zenith hydrostatic and wet delays; ϵ and α are the elevation and azimuth angles of the observed incoming signal; m_h, m_w, and m_g are the hydrostatic, wet and gradient mapping functions respectively; and G_N and G_E are the north and east direction gradient terms to be estimated on top of the ZWD, which is strictly speaking a correction to the usually introduced a priori ZHD. That is, three parameters are set for estimation: ZWD, G_N and G_E, whereas ZHD, m_h, m_w, and m_g come as a priori information. The parametrization offered in the literature for estimated gradients vary mainly in the gradient mapping function m_g.

Gardner [1977] found (at optical frequencies) gradients of several centimetres at 10 degree elevation. Compared to GPS or VLBI, the contribution of water vapour to atmospheric refraction at optical frequencies is small, so that a single (total) mapping function can be used [Mendes et al., 2002]. MacMillan [1995] reported wet gradients with spatial scales of less than 10 km and temporal ones of less than one hour and Bar-Sever et al. [1998] reported agreement with water vapour radiometer (WVR) derived gradients down to timescales of 15 min. Whereas, hydrostatic gradients have much larger spatial and temporal time scales, in the region of 100 km and days respectively [Gardner, 1976], [Gardner, 1977], [MacMillan, 1995].

Chen and Herring [1997] found good agreement between predicted gradients inferred from three dimensional NCEP atmospheric data and the ones inferred from VLBI data (gradients up to 30 mm at 10° elevation), concluding that this could be used to "compute globally the expected gradient signals", and they found the parametrization of gradients to improve the RMS scatters of estimated quantities (7.4 mm versus 11.6 mm for the height component), provided a cut-off angle of no less than 10 degrees was used. However, they noted a defect in their model with the assumption that "the atmospheric refractivity can be expressed as a linear function of horizontal distance from the site", which could lead to a horizontal position error of 5 mm.

MacMillan [1995] reported daily average gradient effects of up to 50 mm at 7 degrees elevation. The estimation of gradients in his VLBI data processing brought baseline length repeatability improvement of 1 to 8 mm in a root-sum square sense. Bar-Sever et al. [1998] brought the gradient modelling used by MacMillan [1995] into GPS data processing and compared gradient solutions to the JPL

routine solutions. To estimate gradients a selected subset of the IGS stations (37 out of 150) were processed with the elevation angle cut-off lowered from 15 to 7 degrees and improvements of 15 and 20% were obtained in the horizontal and radial site position repeatabilities (18.5% in 3-D position). However, Bar-Sever et al. [1998] found GPS, when compared to WVR, to be underestimating the wet gradients' magnitude by about 60%, although the direction was properly sensed with their "crude treatment of the hydrostatic delay over contiguous 12-hour intervals". Closer to this thesis (as GPS data were processed with same GPS software package, Bernese [Dach et al., 2007], but with a different processing technique, as the authors used double difference data whereas zero difference data were used in this thesis) Meindl et al. [2004] found a 1.5 times improvement factor in the horizontal but less in the vertical ($\sim$12%) when estimating gradients. They also found the RMS errors of the gradients to be much reduced by including low elevation (down to 3 degrees) data, with a reduction by a factor of three.

1.3 Thesis Organization

Chapter 2 reviews the theoretical background that lies behind the research work in this thesis. It is limited to the work presented here and is not intended to be exhaustive. The background information covers some essential properties of the atmosphere as a propagation for electromagnetic waves of the band in which all GNSS signals belong, with an emphasis on refractivity (N) models. Then, the very basics of GPS are presented. It is implicitly assumed that it applies for all GNSS. When some differences occur (e.g. in some places for GLONASS), they are highlighted. After the presentation of the GPS observable, the so called Precise Point Positioning (PPP) (after [Zumberge et al., 1997]) processing technique is described, with some specific reference to its implementation in the software

used ([Dach et al., 2007]) to process all the data the results in this thesis stem from.

Chapter 3 describes the building of the new azimuthally symmetric or azimuth dependent mapping functions (SMF and AMF). The three dimensional ray-tracing algorithm used to ray-trace MESO (the UK Met Office high resolution Mesoscale NWM) is described and details of the validation tests carried out are given. Assessment of this new approach to represent the mapping function is made, together with the identification of the best set of elevation angles to be ray-traced as a tradeoff between computer resource, mapping function error and observed data distribution.

Chapter 4 provides an assessment of the ray-tracing performances by comparing ray-traced quantities from the NWM to those inferred from high resolution (HiRes) radiosonde (RS) data. By running the same ray-tracing algorithm in the zenith direction, these HiRes RS data are a unique opportunity to analyze and quantify the NWM errors, assuming the RS data provide a true vertical profile of the lower atmosphere. Ultimately, integrated quantities such as ZTD are compared to those inferred from GPS data.

Chapter 5 analyzes the performances of the developed SMF and compares them to other existing SMF currently used in GNSS data processing. All the processing of this chapter and the following two was carried out using the Bernese GPS Software package [Dach et al., 2007] and the PPP technique only.

Chapter 6 analyzes the performances of the developed AMF and compares them to the use of SMF with horizontal tropospheric gradients estimated, to handle tropospheric asymmetry. The main differences between the two approaches are

described.

The final results chapter, Chapter 7 highlights the correlation between different mapping functions and the Atmospheric Pressure Loading (APL) effect, principally with respect to the more modern mapping functions based on a NWM instead of generic meteorological models.

Finally, Chapter 8 summarizes the findings of the research, makes some recommendations and proposes ways to carry on and extend this research work.

Chapter 2

Background

This chapter gives the essential theoretical background to understand the GPS data processing carried out to obtain the results presented in this thesis. It starts with the description of GPS/GNSS observables and the models involved in the so-called Precise Point Positioning processing technique. Then follows a brief description of the neutral atmosphere. Emphasis is put on the determination of the refractive index, the determination of the neutral atmosphere delay and its modelling in GPS/GNSS data processing.

2.1 GPS Very Brief Overview

The GPS is generally presented to be made of three segments: the space segment, the control segment, and the user segment. The space segment consists of a constellation of about 24 satellites, spread over 6 orbital planes inclined at 55° to the equatorial plane. All GPS satellites transmit continuously on two radio frequencies L1 and L2, with frequencies of respectively f_{L1} = 1575.42 MHz and f_{L2} = 1227.60 MHz. A third frequency (L5) is just beginning to be available at the time of the writing but is not considered in this work. The signal structure is the following [Misra and Enge, 2001]:

- Carrier: radio frequency sinusoidal signal with frequency of f_{L1} or f_{L2}
- Ranging code: impressed on the carrier by phase shifting (by half a cycle). It allows the receiver to compute the signal transit time.
- Navigation data, among which, ephemeris, clock offset parameters and satellite health status.

The control segment is basically in charge to maintain the space segment by monitoring satellites' health, controlling their orbits, compute prediction for the ephemerides and clocks, and uploading them to the satellites so that they can be retransmitted to the user segment in the navigation data, and by maintaining the GPS time mainly.
The user segment can be thought of anyone (or anything) using a GPS receiver.

2.2 GNSS Observables

2.2.1 Zero difference (raw) observations

A receiver, by aligning a duplicate of the code received from a satellite, is able to determine the transit time τ for a signal emitted by a satellite to reach the receiver. The pseudo-range P is defined by $P = \tau \times c$, where c is the speed of light. The quantity P differs from the true range ρ by several biases: satellite and receivers clock offsets to the GPS time (GPST), ionosphere and neutral atmosphere delays principally. For a satellite i, a receiver m, and a frequency band k, the pseudo-range writes as (following [Blewitt, 1989] for example):

$$P^i_{m,k} = \rho^i_m + c\left(\delta t_m - \delta t^i\right) - \frac{\kappa^i_m}{f_k^2} + T^i_m \tag{2.1}$$

$$= \varrho^i_m - \frac{\kappa^i_m}{f_k^2} \tag{2.2}$$

where $P^i_{m,k}$ is the code pseudo-range observation, ρ^i_m is the geometric range between the receiver (phase center of the antenna) at reception time and the satellite at emission time; δt_m and δt^s the receiver and satellite clock offsets to GPST; κ^i_m and T^i_m are the ionospheric and tropospheric effects; λ_k and f_k are the wavelength and frequency of the carrier; Noise and multipath are not explicitly written and ϱ^i_m is then the lumped sum of the geometric range plus clock offsets and tropospheric delay.

A far more precise measurement than the pseudo-range is the carrier-phase one. It is the difference between the phase of the receiver generated signal and the one receiver from the satellite. As opposed to the pseudo-range, it is ambiguous by an amount $b^i_{m,k}$ called the phase ambiguity. The model for the carrier-phase

writes as (see also e.g. [Larson and Levine, 1999]):

$$
\begin{aligned}
L^i_{m,k} &= -\lambda_k \Phi^i_{m,k} && (2.3)\\
&= \rho^i_m + c\left(\delta t_m - \delta t^i\right) - \frac{\kappa^i_m}{f_k^2} + T^i_m + \lambda_k b^i_{m,k} && (2.4)\\
&= \varrho^i_m - \frac{\kappa^i_m}{f_k^2} + \lambda_k b^i_{m,k} && (2.5)\\
& && (2.6)
\end{aligned}
$$

where $L^i_{m,k}$ is the phase range in metres and $\Phi^i_{m,k}$ is the carrier-phase in cycles.

The carrier-phase ambiguity term is composed of three parts:

$$b^i_{m,k} = n^i_{m,k} + \delta\Phi^i_k + \delta\Phi_{m,k} \tag{2.7}$$

where $n^i_{m,k}$ is the integer ambiguity and $\delta\Phi^i_k$ and $\delta\Phi_{m,k}$ are (non-integer) uncalibrated phase delays in the satellite and receiver. $\delta\Phi_{m,k}$ is common to all satellites observed by a receiver [Blewitt, 1989], and identical for similar receivers [Ge et al., 2008], and these offsets are stable to better than a nanosecond [Blewitt, 1989]. Those uncalibrated phase delays prevent the resolution of the integer ambiguities [Ge et al., 2008] when the data is processed in a zero difference mode, such as Precise Point Positioning (PPP), see Section 2.3.

Following [Bassiri and Hajj, 1993], the GPS observables can be rewritten as follows (dropping sub- and superscripts for the receiver and satellite):

$$P_k = \varrho + \frac{q}{f_k^2} + \frac{s}{f_k^3} \tag{2.8}$$

$$L_k = \varrho + n_k\lambda_k - \frac{q}{f_k^2} - \frac{1}{2}\frac{s}{f_k^3} \tag{2.9}$$

where ϱ is the geometrical range plus clock offsets and tropospheric delay; and q and s are the ionospheric effects, where q is a parameter that only depends on the Total Electron Content (TEC) whereas s is related to the effect induced by the Earth's magnetic field. To deal with the (dispersive) ionosphere, GPS was specifically designed to emit on two different frequencies. For dual-frequency receivers, the so-called ionosphere-free linear combination (L3) can be obtained as a combination of L1 and L2 measurements (either phase or code):

$$L_3 = \frac{f_1^2}{f_1^2 - f_2^2} L_1 - \frac{f_2^2}{f_1^2 - f_2^2} L_2 \tag{2.10}$$

The combination eliminates the first order ionosphere effect but higher order effects remain. Two other major drawbacks of the L_3 observable are the level of noise, which is about three times that of the L1 observable, and the loss of the integer nature of the carrier phase ambiguity. The magnitude of the first-order signal group delay/phase advance is of 1-50 m whereas the second-order one is about 1000 times smaller [Kedar et al., 2003]. However, not modelling the second order ionospheric "*can alias into artificial diurnal, seasonal and inter-annual station motions*" and cause a latitude-dependent position shift up to 0.5 cm [Kedar et al., 2003].

2.2.2 Forming single difference observations

Assuming the same satellite i is observed by two receivers m and n, one can form the between-receivers single difference phase observation $\Delta\Phi^i_{m,n,k}$ as:

$$\Delta L^i_{m,n,k} = L^i_{m,k} - L^i_{n,k} \tag{2.11}$$

$$= \Delta\rho^i_{m,n} + c\,\Delta\delta t_{m,n} - \frac{\Delta\kappa^i_{m,n}}{f_k^2} + \Delta T^i_{m,n} + \Delta n^i_{m,n,k} + \Delta\delta\Phi_{m,n,k} \tag{2.12}$$

where Δ denotes the single difference (or between-receivers) operator. The single difference essentially eliminates the satellite clock offset δt^i and the satellite uncalibrated phase delay $\delta\Phi^i_k$. Similarly, the pseudo-range single difference is given by:

$$\begin{aligned} \Delta P^i_{m,n,k} &= P^i_{m,k} - P^i_{n,k} && (2.13) \\ &= \Delta\rho^i_{m,n} + c\,\Delta\delta t_{m,n} + \frac{\Delta\kappa^i_{m,n}}{f_k^2} + \Delta T^i_{m,n} && (2.14) \end{aligned}$$

2.2.3 Forming double difference observations

Assuming that the two receivers m and n now observe a second satellite j, one can form a double difference phase observation $\nabla\Delta L^{i,j}_{m,n,k}$, as the difference between the single differences $\Delta L^i_{m,n,k}$ and $\Delta L^j_{m,n,k}$ formed on each satellite i and j:

$$\begin{aligned} \nabla\Delta L^{i,j}_{m,n,k} &= \Delta L^i_{m,n,k} - \Delta L^j_{m,n,k} && (2.15) \\ &= \nabla\Delta\rho^i_{m,n} - \frac{\nabla\Delta\kappa^i_{m,n}}{f_k^2} + \nabla\Delta T^i_{m,n} + \nabla\Delta n^{i,j}_{m,n,k} && (2.16) \end{aligned}$$

where ∇ denotes the double difference (or between-satellites) operator. The double differencing eliminates the receivers' clock errors and the receivers' uncalibrated phase delays. A important point here is that the double difference phase ambiguity is now an integer, contrary to the zero and single difference measurements. Similarly, the pseudo-range double difference is given by:

$$\begin{aligned} \nabla\Delta P^{i,j}_{m,n,k} &= \Delta P^i_{m,n,k} - \Delta P^j_{m,n,k} && (2.17) \\ &= \nabla\Delta\rho^i_{m,n} + \frac{\nabla\Delta\kappa^i_{m,n}}{f_k^2} + \nabla\Delta T^i_{m,n} && (2.18) \end{aligned}$$

2.3 Precise Point Positioning

The Precise Point Positioning (PPP) technique was developed at NASA Jet Propulsion Laboratory (JPL) [Zumberge et al., 1997] and until recently was associated mainly with the JPL GPS-Inferred Positioning SYstem (GIPSY) software. However, the Bernese software version 5.0 (BSW50), is also able to produce PPP solutions [Dach et al., 2007]. An assessment of the BSW50 PPP compared to a GIPSY PPP solution (in particular) is offered in [Teferle et al., 2007]. Over a period of 5 years, the authors found the north (N), east (E) and up (U) daily position differences are characterized by means and standard deviations of 2.2±4.8, 0.6±7.9 and 4.8±17.3 mm respectively.

The observables in PPP are the phase and code ionosphere-free linear combination of the L1 and L2 observations. In double differencing (DD) (see e.g.[Misra and Enge, 2001]), both the transmitter and receiver clock offsets cancel out. In PPP, where undifferenced data are used, the approach is different as precise satellite clock offsets are introduced a priori. That is, they must be estimated prior to the PPP run. Usually, this is done by processing, in DD mode, a global network, so that all satellite clock offsets can be estimated simultaneously and consistently.

At the core of the PPP concept lies the fact that satellite clock offsets are introduced exactly as estimated for certain epochs (e.g. IGS clock products used to have a 15 min time resolution but are now 5 min; the Center for Orbit Determination in Europe (CODE) since DoY 095 of 2004, for the final product, also provides a 30 seconds high precision clock product [IGS Mail 4913, 2004]). The nature of the clock products therefore limits the overall processing rate.

As mentioned in Dach et al. [2007], utmost consistency between the different

products (clocks, orbits and Earth Orientation Parameters (EOP)), must be observed to achieve optimal PPP solutions. Also, the models used in the generation of products should then be employed in the PPP processing (so, in this work, only CODE products were used as these are generated using BSW50).

Estimated in the PPP run are receiver clock offsets, coordinates, and troposphere parameters, with the datum being the one of the orbits and clocks. For a mathematical description of the PPP technique see e.g. [Kouba and Heroux, 2001].

Compared to DD, PPP is much faster as the data is processed on a single station basis; however, the presence of uncalibrated phase delays [Blewitt, 1989] makes carrier phase ambiguity resolution difficult. Some (networked) strategies have been developed to overcome this limitation, e.g. Ge et al. [2008] resolved zero difference carrier phase ambiguities and obtained an improvement of 27% in the repeatability of the east component (the non-fixing of the ambiguities mainly affects the east component, due the north-south ground tracks of GPS satellites at the equator in the Earth fixed reference frame [Remondi, 1985], [Blewitt, 1989]). Apart from carrier phase ambiguity resolution, other effects that require proper modelling are described in the following two sections.

2.4 Non Geophysical Effects Modelling

2.4.1 Phase Wind-up

Phase wind-up was discussed in [Wu et al., 1993] where a correction was proposed for crossed-dipole type antenna. The phase measurement being the angle between

the instantaneous electromagnetic field direction and a reference direction at the antenna, and due to the right circularly polarized (RCP) nature of the GPS signal, a change in orientation of either the receiver or satellite antenna will impact the measured phase. The phase wind-up effect is composed of two parts one geometrical, and another linked to the attitude of the satellite. The BSW50 package, since November 2006, allows for full modelling of this effect; furthermore, the later part of the effect can be fully absorbed by satellite clock corrections [Dach et al., 2007].

2.4.2 Antenna Phase Center Variations

Transmitting time between the satellite and receiver antennas refers to their instantaneous electrical phase centers, and not the physical phase centers of the antennas, nor, for the satellite (transmitter), the center of mass to which orbits refer to. The difference depends on the frequency and the elevation and azimuth angles of the tracked signal and is usually decomposed into two parts: a mean Phase Center Offset (PCO) plus an elevation and azimuth (depending on the product) Phase Center Variation (PCV). Antennas have to be calibrated to derive PCV tables. Furthermore, for a given antenna, calibration values change with the use of a radome[1] and its type.

Receiver Antenna Phase Center

According to Dach et al. [2007], relative station height error can reach 10 cm if PCVs are not accounted for. Until November 2006 [IGS Mail 5438, 2006], relative receiver PCVs were used, which were obtained by calibrating receiver antennas relative to a reference antenna, the AOAD/M_T (Allen Osborne Associates Dorne Margolin T), assumed to have zero PCV (see [Mader, 1999]). For short baselines,

[1] Cover for the antenna that protects it from the environmental effects.

this assumption was acceptable but not for longer baselines, where a satellite is seen at different elevation angles by the receiver antennas at the two ends of the baseline. Absolute receiver PCVs were proposed as early as 1994 by calibrating antennas in anechoic chambers [Schupler et al., 1994]. However, because a significant scale change of 15 ppb ([Schmid and Rothacher, 2003]) was found in global network processing when switching from relative to absolute PCVs, these were, as mentioned earlier, only introduced by the IGS in November 2006.

Satellite Antenna Phase Center

Schmid and Rothacher [2003] and Schmid et al. [2007] (and references therein) underlined the fact that satellite antenna PCOs used in common practice and recommended by the IGS at the time were inaccurately known, or even properly identified (to which frequency the PCOs were referring to). However, since then, a set of absolute satellite antenna PCOs and PCVs, consistent with the absolute receiver PCOs and PCVs from robot calibration was derived in Schmid et al. [2007], and are now part of the IGS recommendations.

2.4.3 Differential Code Biases

Except for the latest block IIR-M satellites which now provide L2 C/A (or L2C) code measurements, GPS satellites transmit only L1 C/A (C1) plus L1P (P1) and L2P (P2) code measurements, and receivers measure C1 plus a combination of the following: (i) P1, (ii) P2 and, (iii) X2 == C1 + (P2-P1) [Dach et al., 2007] (or [Schaer and Steigenberger, 2006]). Differential Code Biases (DCBs) originate in the different tracking technologies of receivers. The issue appeared to be discussed within the IGS when a uniform Rogue-TurboRogue network started to switch to a mixed network with newer technology. For details, see [IGS Mail 2320, 1999]. Following Dach et al. [2007], the C1, P1 and P2 biases can be denoted B_{C1}, B_{P1},

and B_{P2} but as these biases can only be estimated in a differential sense, there are two DCBs: (i) $B_{P_1} - B_{P_2} = P_{P_1-P_2}$ and (ii) $B_{P_1} - B_{C_1} = P_{P_1-C_1}$. By IGS convention, data has to be made consistent with the P1/P2 L3 (itself absolutely biased by $\frac{f_1^2}{f_1^2-f_2^2}B_{P_1} - \frac{f_2^2}{f_1^2-f_2^2}B_{P_2}$). Therefore, only $B_{P_1-C_1}$ DCBs need be applied.

2.5 Site Displacement Modelling

A physical reference point on the Earth's crust is subject to various displacements that originate in the Earth's interaction with other celestial bodies. Only a very brief overview is offered here. The reader is referred to the International Earth Rotation and Reference Frames Service (IERS) Conventions for more in depth detailing and referencing. In short, the models described below relate the regularized position of the reference points to their instantaneous position (McCarthy and Petit [2003])

2.5.1 Earth Tides

The crust of the Earth, albeit a rigidity twice that of steel, undergoes periodic movement due to the attraction effect caused by gravitational bodies, the moon and the sun principally. According to Vanicek and Krakiwsky [1982], if the contribution of the Moon to the tidal potential is 1, the one of the Sun is of 0.4618, whereas the most contributing body following is Venus, with a relative contribution of 0.000054 only. A procedure is given in the McCarthy and Petit [2003] for computing solid Earth tide displacement to correct for instantaneous position. The displacement can vary up to 40 cm in 6 hours [Baker et al., 1995]. Because the geometric scale is in the order of 1000 km, the effect can be largely ignored in differential techniques over baseline lengths well below 1000 km. However, for PPP, it must be accounted for, always.

A permanent tide also exists and is removed by convention. Furthermore, the Earth's pole tide effect must also be modelled, as it can reach 2.5 cm in the radial component [McCarthy and Petit, 2003].

2.5.2 Ocean Tide Loading

The previous section concentrated on the Earth's crust response to combined gravitational pulls of the moon and the sun. The water mass, or oceans, also respond to the gravitational effect, in a dynamical way. Tidal harmonics have periods that range from half a day to half a year with complicated (amplitude) spatial variations [Baker et al., 1995]. The total displacement is the sum of several tidal harmonics of known frequency, each of them representing an astronomical motion [Penna and Baker, 2002]. For a particular location, each tidal harmonic is characterized by amplitude and phase, the amplitude being time independent. Currently, the main part of the displacement is represented using a set of 11 tidal harmonics. They are split into three classes according to their period: semi-diurnal, diurnal and long-term, the long term periods varying between 13.66 and 182.62 days. The coefficients used in this thesis were from the FES2004 model [Lyard et al., 2006], and were computed according to [Scherneck, 1991] and made available through the online OTL service provider from Chalmers University (http://www.oso.chalmers.se/∼loading) maintained by M.S. Bos and H.-G. Scherneck.

2.5.3 Atmospheric Pressure Loading

Darwin [1882] showed that the Earth's (as an elastic body) crust was deforming with variation of the pressure. This displacement can be as large as 20 mm in the vertical component and 3 mm in the horizontal ones [Petrov and Boy, 2004]. The computation of the atmospheric pressure loading (APL) at a given site requires

the convolution of a global pressure field and the Earth's gravitational field. Such computation is given in Petrov and Boy [2004] and routines are available from L. Petrov's website at `http://gemini.gsfc.nasa.gov/aplo` where time series of APL for VLBI and IGS GNSS sites are also available.

2.6 Tropospheric Modelling

2.6.1 The Atmosphere in Brief

For a natural or artificial space geodetic signal to reach a receiver in the vicinity of the Earth's crust, it has to propagate through the gaseous shell of the the Earth, the atmosphere. As a propagation medium for L-band electromagnetic waves, it can be split into two parts. The part closer to the Earth, spanning about 50 km height, is the neutral troposphere and the focus of this thesis. Above that the atmosphere is ionized and dispersive and this work assumes that this effect is taken care of with the use of dual-frequency measurement, hence, it is not discussed further in what follows.

There are various way to "decompose" the atmosphere, among them, are its chemical composition or its temperature profile. According to the former one, the part below 100 km, called the homosphere, is uniform and has well mixed main constituents (e.g. [Wallace and Hobbs, 1977]). Above this is the heterosphere. If the vertical profile of temperature of the atmosphere is used as a discriminant factor, Figure 2.1 is obtained.

Following Iribarne and Godson [1973], the atmosphere's constituents can be grouped into three categories: dry air, water substance, and aerosols. Table 2.1 is reproduced from Salby [1995].

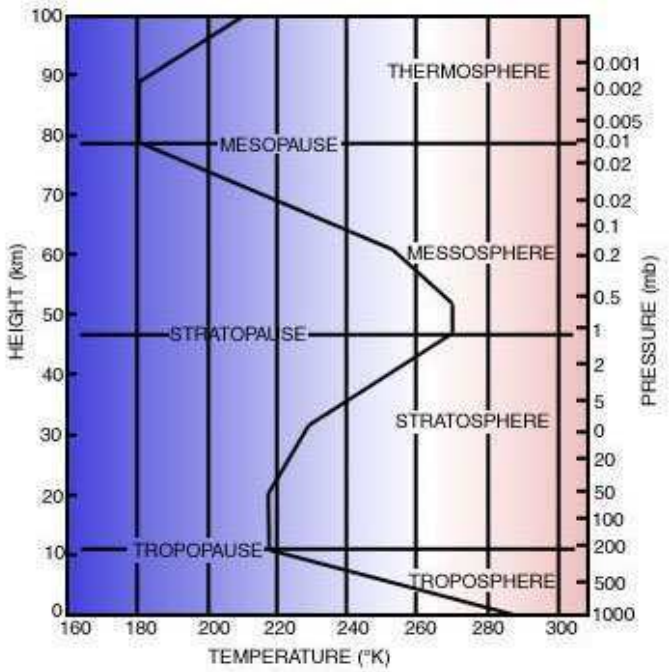

Figure 2.1: Decomposition of the homosphere according to its vertical temperature profile. Courtesy of the UK Met Office.

2.6.2 The Neutral Atmosphere

As mentioned before, the neutral atmosphere is that part of the atmosphere that roughly extends from the surface to an altitude of about 50 km. From Figure 2.1 it includes the troposphere and the stratosphere. The troposphere is the first 7-18 km, depending on the latitude, season and weather patterns (see [Mendes, 1999] and references therein for more details). It contains 80% of the atmospheric mass (e.g. [Wallace and Hobbs, 1977]) and almost all of the atmospheric water. The temperature in the standard troposphere decreases linearly with height at a rate of 6.5°C/km (e.g. [USSA, 1976]). The troposphere and the stratosphere are separated by a layer called the tropopause. The bottom part has a constant temperature (up to 20 km, see Figure 2.1), and then a positive gradient of +1.0°C/km up to 32 km, followed by a sharper positive gradient of 2.8°C/km up to 47 km ([USSA, 1976]), the altitude of the so called stratopause which delimits

Table 2.1: Atmospheric Composition (from [USSA, 1976], [Gleuckauf, 1951] and [Salby, 1995], *Only the most relevant constituents are shown. Constituents missing from the original table are:* O_3, CH_4, N_2O, CO, NO, $CFC-11$ *and* $CFC-12$)

Constituent	Molar Weight kg/kmol	Tropospheric mixing ratio	Vertical distribution (mixing ratio)	Controlling processes
		Dry Air		
N_2	28.0134	0.78084	Homogeneous	Vertical mixing
O_2	31.9988	0.209476	Homogeneous	Vertical mixing
Ar	39.948	0.00934	Homogeneous	Vertical mixing
CO_2	44.00995	314-345 ppmv	Homogeneous	Vertical mixing; production by surface and anthropogenic processes
N_e	20.183	0.00001818		
H_e	4.0026	0.00000524		
K_r	83.30	0.00000114		
X_e	131.30	0.000000087		
		Water Vapour		
H_2O	18.0152	$\leq$0.030	Decreases sharply in troposphere; increases in stratosphere; Higly variable	Evaporation, condensation, transport; production by CH4 oxidation

the stratosphere from the next layer, the mesosphere.

2.6.3 Definitions

Hydrostatic Equilibrium

Consider a vertical column of unity cross section; z the height coordinate. The hydrostatic equilibrium (or balance) states that the weight of the layer comprised between the two pressure levels of heights z and $z + dz$ is equal to the difference of pressure dp between those two layers:

$$dp = -\rho g dz \tag{2.19}$$

where ρ is the density and g the gravity. It is Newton's second law applied to the vertical, in the absence of motion. Even in the presence of motion this equation remains valid but not for 'deep convective towers and other small-scale

phenomena' where hydrostatic equilibrium may be violated by strong vertical accelerations [Salby, 1995].

Ideal (or Perfect) Gas (e.g [Bueche, 1986])

An ideal gas is a gas that obeys Boyle's and Charles' laws, its state observes the following:

$$PV = nRT \tag{2.20}$$

the well known equation of state where P is the absolute pressure [Pa], V the volume [m^3], n the number of moles of the gas, $R = 8.314472$ [$JK^{-1}mol^{-1}$] the universal gas constant, and T the absolute temperature [K]. n relates to its molecular weight M [$kg{\cdot}kmol^{-1}$] as:

$$n = \frac{m}{M} \tag{2.21}$$

where m is the mass of the gas [kg] contained in volume V.
The specific gas constant R^* of a gas is

$$R^* = \frac{R}{M} \tag{2.22}$$

For a mix of gases contained in V of total pressure P, Dalton's law states that

$$P = \sum_i P_i \tag{2.23}$$

where P_i is the partial pressure of each constituent of the mix.

So follows the definition of the mean specific gas constant and molecular weight for the mix:

$$R_m = \frac{\sum_i m_i R_i}{m} \tag{2.24}$$

$$M_m = \frac{\sum_i n_i M_i}{n} \tag{2.25}$$

2.6.4 Expressing Air Moisture

Saturation Vapour Pressure e_{sat}

The saturation water vapour pressure over water e_{sat} is defined as the water vapour pressure "when in a state of neutral equilibrium with a plane surface of pure water at the same temperature" [Byers, 1959]. Over a plane surface of ice, sublimation takes place instead of evaporation and condensation [Haltiner and Martin, 1957], and the saturation water vapour is with respect to ice and is labelled e_{sat_i}. Saturation vapour pressure is the maximal water vapour pressure a volume at a certain temperature T can hold before water vapour will start coexisting with water or ice. $e_{sat}(T)$ is a complicated solution of the Clausius-Clapeyron equation. Various analytical expression exist for e_{sat}; only the ones which were used in this thesis are given below.

- **Modified Goff-Gratch** [Goff and Gratch, 1946], [Goff, 1957]

$$\begin{aligned} e_{sat} = \quad P_{ss} \times 10 \exp \quad & (10.79586 \times (1 - \frac{T_0}{T}) - 5.02808 \times \log_{10} \frac{T}{T_0} \\ & +1.50474 \times 10^{-4} \times (1 - 10 \exp(-8.29692 \times (\frac{T}{T_0} - 1.0))) \\ & +0.42873 \times 10^{-3} \times (10 \exp(4.76955 \times (1.0 - \frac{T_0}{T})) - 1.0) \\ & -2.2195983) \end{aligned} \tag{2.26}$$

where P_{ss} is the saturation vapour pressure at steam-point and equals 1013.25 hPa, T is the absolute temperature in K, and T_0 is the temperature

at triple point of water and equals 273.16 K.

$$\begin{aligned} e_{sat_i} = \quad P_{ss} \times 10 \exp \quad & (-9.096936 \times (T_0/T - 1.0) \\ & -3.56654 \times \log_{10}(\frac{T_0}{T}) \\ & +0.876817 \times (1.0 - \frac{T}{T_0}) \\ & -2.2195983) \end{aligned} \tag{2.27}$$

- **Digicora** e.g. [Haase et al., 2003]

$$e_{sat} = R_2 \exp\left[R_3 \frac{T - T_0}{T - R_4}\right] \tag{2.28}$$

where $R_2 = 611.21$ Pa, $R_3 = 17.502$ K, $R_4 = 32.19$ K, and T_0=273.16 K.

- **HIRLAM** [Sass et al., 1999]

It uses the same formulation as the Digicora but the constants are refined.

$$e_{sat} = R_2 \exp\left[R_3 \frac{T - T_0}{T - R_4}\right] \tag{2.29}$$

where $R_2 = 610.78$ Pa, $T_0 = 273.16$ K, $R_{3_{ice}} = 21.875$ K, $R_{3_{liquid}} = 17.269$ K, $R_{4_{ice}} = 7.66$ K, $R_{4_{liquid}} = 35.86$ K, "*with the ice constants being used below −15 degrees Celcius and the liquid constants above freezing, and a gradual change, linear in T, from the ice constants to the liquid constants from the −15 to +0 degrees Celcius interval*" [Haase et al., 2003].

- **Wexler** ([Wexler, 1976], [Wexler, 1977])

$$
\begin{aligned}
e_{sat_w} = 0.01 \times \exp \quad [\quad & 2.858487 \ln(T) \\
& - 2991.2729/T^2 - 6017.0128/T \\
& + 18.87643854 \\
& - 0.028354721\ T + 1.7838301.10^{-5}\ T^2 \\
& - 8.4150417.10^{-10}\ T^3 \\
& + 4.4412543.10^{-13}\ T^4\ ]
\end{aligned} \tag{2.30}
$$

$$
\begin{aligned}
e_{sat_i} = 0.01 \times \exp \quad [\quad & 0.69186510 \ln(T) \\
& - 5865.3696/T \\
& + 22.24103300 \\
& + 1.3749042.10^{-2}\ T - 3.4031775.10^{-5}\ T^2 \\
& + 2.6967687.10^{8}\ T^3\ ]
\end{aligned} \tag{2.31}
$$

Mixing Ratio r

The mixing ratio (r) ([g/g] or [g/kg]) is defined as 'the mass of water vapour m_w contained in a mixture with a unit mass of dry air m_d' [Byers, 1959].

$$
r = \frac{m_w}{m_d} \tag{2.32}
$$

equivalently:

$$
r = \frac{\rho_w}{\rho_d} = \frac{\frac{e}{R_w T}}{\frac{P-e}{R_d T}} = \epsilon \frac{e}{P-e} \tag{2.33}
$$

with ϵ defined as:

$$\epsilon = \frac{R_d}{R_w} \tag{2.34}$$

The saturation mixing ratio r_s is the mixing ratio at saturation.

Specific Humidity q

Specific humidity (q) is defined as the ratio of mass of water vapour m_w to the mass of moist air m:

$$q = \frac{m_w}{m} \tag{2.35}$$

or equivalently, as per r:

$$q = \epsilon \frac{e}{P - (1 - \epsilon)e} \tag{2.36}$$

The mixing ratio and the specific humidity relate to each other via:

$$q = \frac{r}{1 + r} \tag{2.37}$$

Dew-point Temperature T_{dew}

The dew-point temperature (T_{dew}) is defined as the temperature at which a parcel of moist air must be cooled down, keeping the pressure and mixing ratio constant (see above), so that the air becomes saturated. T_{dew} a direct measure of the water vapour pressure:

$$e = e_{sat}(T_{dew}) \tag{2.38}$$

Relative Humidity RH

Relative humidity (RH) is defined (List [1966], Mendes [1999]), as the ratio of the mixing ratio r to the saturation mixing ratio r_s, and is usually expressed in %:

$$RH(\%) = 100\frac{r}{r_s} \tag{2.39}$$

RH is commonly approximated by:

$$RH(\%) \approx 100\frac{e}{e_{sat}} \tag{2.40}$$

Relative Humidity With Respect to Ice U

The ratio [%] of the actual mixing ratio to the ice saturation mixing ratio at the same temperature and pressure. The relative humidity with respect to ice is always greater than the relative humidity with respect to water, except at 0°C where the two are equal.

2.6.5 Radio Refractive Index of Moist Air

Debye [1929] studied the polarizability of non-polar and polar molecules subjected to an electric field, and concluded that polarizability is composed of two effects: one is the distortion of all molecules, whereas the second one is caused by an "orientation effect exerted upon polar molecules" [Bean and Dutton, 1966]. For an external field with frequency less than 100 GHz, Debye [1929] gives for the polarization P of polar molecules:

$$P(\omega) = \frac{\epsilon - 1}{\epsilon + 2}\frac{M}{\rho} = \frac{4\,\pi\,N}{3}\left[\alpha_0 + \frac{\mu^2}{3\,k\,T}\right] \tag{2.41}$$

where: $\omega = 2\pi f$ and f is the frequency of the external field,
ϵ is the dielectric constant,
M is the molecular weight,
ρ density of the liquid,
N is the Avogadro's number,
α_0 is the average polarizability of the molecules in the liquid, assuming no interaction between molecules
μ is the permanent dipole moment,
T is the absolute temperature,
k is Boltzmann's constant.

which reduces for non-polar molecules (no permanent dipole $\mu = 0$) to:

$$\frac{\epsilon - 1}{\epsilon + 2}\frac{M}{\rho} = \frac{4\,\pi\,N\alpha_0}{3} \tag{2.42}$$

well approximated by

$$\epsilon - 1 \approx \frac{\rho}{M}\,4\,\pi\,N\,\alpha_0 \tag{2.43}$$

for gases at low pressures [Bean and Dutton, 1966]. Assuming the gas is ideal

$$\epsilon - 1 \approx K_1'\frac{P}{T} \tag{2.44}$$

where K_1' a constant. Similarly, for polar gases

$$\epsilon - 1 \approx \frac{\rho}{M}\,4\,\pi\,N\left[\alpha_0 + \frac{\mu^2}{3\,k\,T}\right] \tag{2.45}$$

which results for ideal gases in

$$\epsilon - 1 \approx K_2'\frac{P}{T}\left(A + \frac{B}{T}\right) \tag{2.46}$$

Using Dalton's law, the polarizability of moist air is given by

$$\epsilon - 1 = K'_{11}\frac{P_d}{T} + K'_{21}\frac{e}{T}\left(A + \frac{B}{T}\right) + K'_{12}\frac{P_{CO_2}}{T} \tag{2.47}$$

where P_d is the partial pressure of dry air, e the one of water vapour, and P_{CO_2} the one of CO_2. Still following Bean and Dutton [1966] development, from the refractive index (n) which is by definition

$$n = \sqrt{\mu\epsilon} \tag{2.48}$$

where μ is the permeability and for air is nearly equal to 1.0. The refractivity (N) is approximated by

$$N = (n-1)10^6 = K'_1\frac{P_d}{T} + K_2\frac{e}{T} + K_3\frac{e}{T^2} + K_4\frac{P_c}{T} \tag{2.49}$$

Equation 2.49 can be reduced to the commonly used three coefficient form

$$N = (n-1)10^6 = K_1\frac{P_d}{T} + K_2\frac{e}{T} + K_3\frac{e}{T^2} \tag{2.50}$$

by adjusting the dielectric constant of dry air to the one of dry air plus CO_2.

2.6.6 Refractivity Set of Constants

The main challenge with the formulation of refractivity N (see Eq. 2.50 above) is the determination of its set of constants, K_1, K_2 and K_3, which is still an ongoing research topic, with published values actively discussed over time. Here, it is just emphasized that according to Hill et al. [1982], Thayer's published values, widely used in radio geodesy (as per e.g. [Mendes, 1999] or [Rüeger, 2002]), should not be used as they are partially based on optical data. In this thesis, it was decided

to use the "*best average*" values computed by Rüeger [2002] (from previously published values), which are presented in Table 2.2 along with, for comparison, the "*best available*" values identified by Rüeger [2002]. The average values and their associated uncertainties are weighted means based as follows:

K'$_1$ [Birnbaum et al., 1951], [Essen and Froome, 1951], [Zieman, 1952], [Gabriel, 1952], [Essen, 1953], [Jansinski & Berry, 1954][2], [Battaglia et al., 1957], [Boudouris, 1958][2], [Newell and Baird, 1965], [Liebe et al., 1977]

K$_2$ **&** **K**$_3$ [Stranathan, 1935],[Groves and Sugden, 1935], [Hurdis and Smyth, 1942], [Birnbaum and Chatterjee, 1952], [Boudouris, 1958][2].

K$_4$ [Essen and Froome, 1951], [Heineken and Bruin, 1954], [Boudouris, 1963], [Newell and Baird, 1965], [Liebe et al., 1977].

Table 2.2: "*Best available*" and "*best average*" refractivity constants as identified and computed by Rüeger [2002].

Constant	*"best available"*		*"best average"*
K'_1 [K/hPa]	77.674 ±0.013	[Newell and Baird, 1965]	77.6681 ±0.0094
K_2 [K/hPa]	71.97 ±10.5	[Boudouris, 1963]	71.2952 ±1.3
K_3 [K^2/hPa]	375406 ±3000	[Boudouris, 1963]	375463 ±760
K_4 [K/hPa]	133.484 ±0.022	[Newell and Baird, 1965]	133.480 ±0.022
K_1 [K/hPa]	77.691 ±0.013	Assuming 300 ppm CO_2. See below for derivation	77.6848 ±0.0094

where the K1 value can be obtained from the following equality

$$K_1 \frac{P_d}{T} = K'_1 \frac{P_{d-c}}{T} + K_4 \frac{P_c}{T} \tag{2.51}$$

For temperatures between -50°C and +40°C, total pressure between 187 and 1013.25 hPa, partial water vapour pressure between 0 and 27 hPa and frequencies

[2]Not referenced in Rüeger [2002]

between 1 Hz and 30 GHz, [Rüeger, 2002] quotes an accuracy, of "an equivalent equation" from [Boudouris, 1963], for N of 0.5% when computed using the "best available" constants. For the "best average", the accuracy is 0.012% (0.02%) of N_d and 0.15% of N_w [Rüeger, 2002]. Note that the concentration of CO_2 in the atmosphere is about 385 ppm in 2009 according to Tans [2009].

2.6.7 Compressibility Factors

Following Owens [1967], Thayer [1974] proposed the use of compressibility factors Z_d and Z_w to account for the departure from assumed ideal gas behavior. So Equation 2.50 becomes:

$$N = K_1 \frac{P_d}{T} Z_d^{-1} + K_2 \frac{e}{T} Z_w^{-1} + K_3 \frac{e}{T^2} Z_w^{-1} \tag{2.52}$$

where

$$Z_d^{-1} = 1 + P_d \left(57.90 \times 10^{-8} - \frac{9.4581 \times 10^{-4}}{T} + \frac{0.25844}{T^2} \right) \tag{2.53}$$

$$Z_w^{-1} = 1 + e \left(1 + 3.7 \times 10^{-4} e \right) \times \left(-2.37321 \times 10^{-3} + \frac{2.23366}{T} - \frac{710.792}{T^2} + \frac{7.75141 \times 10^4}{T^3} \right) \tag{2.54}$$

which are the original formulations by Owens [1967] (not those rearranged by Thayer [1974]). Their use is though questionable and it was suggested that the equation of refractivity for general use in geodesy should be free of compressibility factors [Rüeger, 2002].

2.6.8 Hydrostatic Delay

Davis et al. [1985] rearranged the refractivity equation into:

$$N = k_1 R_d \rho + k_2' \frac{e}{T} Z_w^{-1} + k_3 \frac{e}{T^2} Z_w^{-1} \tag{2.55}$$

where ρ is the total mass density

$$\rho = \rho_d + \rho_w \tag{2.56}$$

and

$$k_2' = k_2 - k_1 \frac{R_d}{R_w} = k_2 - k_1 \frac{M_w}{M_e} \tag{2.57}$$

stemming from the rearrangement of the first two terms of Eq. 2.50 using the equation of state for the dry and wet components:

$$\begin{aligned} k_1 \frac{P_d}{T} Z_d^{-1} + k_2 \frac{e}{T} Z_w^{-1} &= k_1 R_d \rho_d + k_2 R_w \rho_w & (2.58) \\ &= k_1 R_d \rho + k_2' \frac{e}{T} Z_w^{-1} & (2.59) \end{aligned}$$

Davis et al. [1985] underline the fact that the first term of Eq. 2.55 does not depend on the wet/dry mixing ratio, but instead on the total density only. Integrating this term with respect to height, with hydrostatic equilibrium condition assumed, leads to the so called zenith hydrostatic delay ZHD:

$$ZHD = 10^{-6} k_1 R_d g_m^{-1} P_0 \tag{2.60}$$

where g_m is defined by Davis et al. [1985] as

$$g_m = \frac{\int_0^\infty \rho(z) g(z) dz}{\int_0^\infty \rho(z) dz} \tag{2.61}$$

which "nearly represents the acceleration due to gravity at the center of mass of the vertical column" and writes, as [Saastamoinen, 1972], as

$$g_m = 9.8062\,(1 - 0.00265cos(2\Phi) - 0.00031H_c) \tag{2.62}$$

where Φ is the latitude of the site and H_c the height (in km) of the center of mass of the vertical column, which is given by [Saastamoinen, 1972] as

$$H_c = 0.9H + 7.3 \tag{2.63}$$

where H is the height of the site (in km) above the geoid.

The impact of the a priori ZHD on geodetic solutions was studied by Tregoning and Herring [2006]. The authors showed that unless sufficiently accurate hydrostatic a priori zenith delays are used, errors in height and zenith total delays are caused. This comes from the fact that the dry and wet mapping functions at low elevation angles are different enough for the estimated wet component not to be able to 'catch up' on the error introduced by the a priori hydrostatic part, if it is too different from the truth. The wet mapping function does usually relate the estimated quantities to the observables, as the partial derivative of the ZTD with respect to the phase; the hydrostatic component being completely a priori information.

Mismodeling comes from the estimate of the pressure used to compute the a priori ZHD [Tregoning and Herring, 2006]. Ideally this pressure would be measured by a calibrated sensor collocated with the processed site. Usually, as these are not available, a standard model is used, that depends on a mean seal level pressure adjusted to the height of the site. Errors of several tens of hPa are there-

fore possible. Such pressure information can also be interpolated from NWM data (e.g. [Boehm et al., 2007]). Tregoning and Herring [2006] found errors in the vertical coordinate of -0.19±0.01 mm per hPa error in the estimate of the ground pressure used to compute the a priori ZHD for processing with a cut-off angle of 7 degrees.

2.6.9 Neutral Atmosphere Delay: a Definition

Starting with Fermat's principle formulation from [Born and Wolf, 1999]:
"*The principle of Fermat, known also as the principle of the shortest optical path, asserts that the optical length*

$$\int_{P_1}^{P_2} n\, ds \tag{2.64}$$

of an actual ray between two points P_1 and P_2 is shorter than the optical length of any other curve which joins these points and which lies in a certain regular neighborhood of it".

In this section, the way the neutral atmosphere or tropospheric total delay can be computed is examined, assuming that the refractive index is known anywhere along the path. The refractive index is greater than unity and is generally higher at lower altitude. For normal conditions at sea level, $n \approx 1.000320$, that is $N \approx 320$ [ppm]. For a review of some refractivity models, see e.g. Mendes [1999]. The denser the medium of propagation, the slower the propagation is. As Fermat's principle of *least time* encompasses refraction, from which *Snell's law* can be derived, not only is the radio wave propagation slower in the neutral atmosphere, but it also bends, so that less time is spent by the signal in denser layers (by penetrating it in a direction closer to the normal of that layer, leading to a shorter path) at the cost of spending more time in less dense parts by deviating from the normal. Figure 2.2 illustrates that concept.

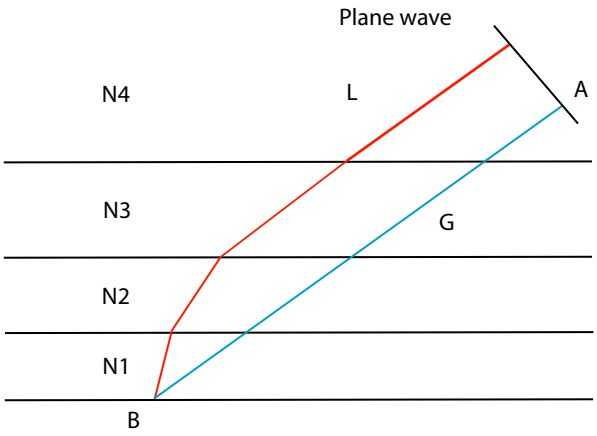

Figure 2.2: Illustration of Fermat's principle for a ray travelling from A to B through a hypothetical horizontally stratified atmosphere with four layers of constant refractivity N1 > N2 > N3 > N4 > 0. The blue line would be the line of propagation in vacuum.

As the energy travels at the group velocity $v = c/n$ along the path [Born and Wolf, 1999; Misra and Enge, 2001] Equation 2.64 can be rewritten as:

$$\int_{P_1}^{P_2} n \, ds = c \int_{P_1}^{P_2} dt \tag{2.65}$$

where c is the velocity of light. The quantity L

$$L = \int_{P_1}^{P_2} n \, ds \tag{2.66}$$

is the electromagnetic path length as opposed to the geometric (i.e. straight) path G, the path that would be travelled by the ray in vacuum

$$G = \int_{P_1}^{P_2} (n =)1 \, ds \tag{2.67}$$

On Fig. 2.2, L would be the red path and G the blue path.

The neutral atmospheric delay T is defined as the difference between L and G:

$$T = \int_{P_1}^{P_2} n \, ds - \int_{P_1}^{P_2} ds \tag{2.68}$$

The reader should keep in mind that the two integrals don't integrate along the same path, therefore:

$$T \neq \int_{P_1}^{P_2} (n-1) \, ds \tag{2.69}$$

The quantity T can then be written as

$$T = \int_{P_1}^{P_2} (n-1) \, ds_{ray} + \left[\int_{P_1}^{P_2} ds_{ray} - \int_{P_1}^{P_2} ds_{vac} \right] \tag{2.70}$$

where it is made use of two different integration variables ds_{vac} and ds_{ray} to underline the fact that the first term of the square bracket expression refers to the actual path whereas the second refers to the virtual case of vacuous atmosphere. The square bracket expression is purely geometric and evaluates the geometrical delay (also know as the ray bending), that is, the excess path length travelled when going from P1 to P2 following the path used by the ray in a real atmosphere compared to the geometrical path. The first term is the delay due to the slower speed of propagation, due to a refractive index greater or equal to unity. Mendes [1999] for example refers to it as the excess path delay.

To summarize, what will be referred to as the "neutral atmosphere delay" or "tropospheric delay" in the following, will encompass the two contributions: excess path delay and geometric delay.

2.6.10 Modelling the Tropospheric Delay in Space Geodetic Techniques

The common model for handling the neutral atmosphere delay in space geodetic techniques is given e.g by [McCarthy and Petit, 2003] as:

$$STD = m_h(\epsilon)ZHD + m_w(\epsilon)ZWD + m_g(\epsilon)\left[G_N cos(\alpha) + G_E sin(\alpha)\right] \qquad (2.71)$$

where	ϵ	...	Elevation angle
	α	...	Azimuth angle
	STD	...	Slant Total Delay
	ZHD	...	Zenith Hydrostatic Delay
	ZWD	...	Zenith Wet Delay
	$m_h(\epsilon)$	...	Hydrostatic mapping function
	$m_w(\epsilon)$	...	Non-hydrostatic or "wet" mapping function
	$m_g(\epsilon)$	...	Gradient mapping function

ZHD is usually introduced as a priori information (see 2.6.8) and the ZWD (erroneous naming for what is a correction upon the introduced ZHD) and, if included, the two gradient terms G_N and G_E are then estimated. The gradients terms are now commonly estimated and ought to account for atmospheric asymmetries.

The following section investigates the mapping functions in more details.

2.6.11 Tropospheric Mapping Functions

Chao Mapping Function

The Chao [1972] mapping function was based on Marini's expansion, with only two coefficients and with a "tangent" instead of a "sine" in the second term to

make the mapping function unity at zenith:

$$m(\varepsilon) = \frac{1}{\sin(\varepsilon) + \frac{a}{\tan(\varepsilon) + b}} \tag{2.72}$$

CfA-2.2: Davis et al. Mapping Function

In order to "*achieve subcentimeter accuracy at 5 degrees elevation*", Davis et al. [1985] borrowed the form adopted by Chao [1972] (see above) but added a third term to it:

$$m(\varepsilon) = \frac{1}{\sin(\varepsilon) + \frac{a}{\tan(\varepsilon) + \frac{b}{\sin(\varepsilon) + c}}} \tag{2.73}$$

The authors mention however that errors of 1 to 2 mm can be expected for elevation angles ranging form 20 to 60 degrees because of the "tan" term not converging quickly enough towards $\sin(\varepsilon)$. Down to 5 degrees, the CfA-2.2 was able to model the delay to within 3 mm and with an RMS deviation of less than 1.5 mm Davis et al. [1985]. The CfA-2.2 mapping function depends on the total pressure at the surface, the partial pressure of water vapour at the surface, the temperature at the surface, the tropospheric temperature lapse rate and the the height of the tropopause. The derived set of formulas for computing a and b (c being held fixed at a value of -0.0090) are not reproduced here as the CfA-2.2 is not used in the results presented in this thesis.

MTT: Herring Mapping Functions

The MTT mapping functions were developed by Herring [1992] based on the ray tracing of atmospheres at 10 locations in the United States (close to VLBI stations) were temperature and water vapour profiles were obtained from radiosondes [Herring, 1992]. They need a single meteorological input: the surface temperature

at the site.

The model adopted from the mapping function was a normalized three term Marini's $\sin(\epsilon)$ expansion used for mapping both the hydrostatic and the wet components:

$$m_{h,w}(\varepsilon) = \frac{1 + \dfrac{a_{h,w}}{1 + \dfrac{b_{h,w}}{1 + c_{h,w}}}}{\sin(\varepsilon) + \dfrac{a_{h,w}}{\sin(\varepsilon) + \dfrac{b_{h,w}}{\sin(\varepsilon) + c_{h,w}}}} \tag{2.74}$$

where, for the hydrostatic:

$$\begin{aligned} a_h &= [1.2320 + 0.0139\cos(\phi) - 0.0209H_s + 0.00215(T_s - 10)] \times 10^{-3} \\ b_h &= [3.1612 + 0.1600\cos(\phi) - 0.0331H_s + 0.00206(T_s - 10)] \times 10^{-3} \\ c_h &= 71.244 - 4.293\cos(\phi) - 0.149H_s - 0.0021(T_s - 10)] \times 10^{-3} \end{aligned}$$

and for the wet:

$$\begin{aligned} a_h &= [0.583 + 0.011\cos(\phi) - 0.052H_s + 0.0014(T_s - 10)] \times 10^{-3} \\ b_h &= [1.402 + 0.102\cos(\phi) - 0.101H_s + 0.0020(T_s - 10)] \times 10^{-3} \\ c_h &= 45.85 - 1.91\cos(\phi) - 1.29H_s - 0.015(T_s - 10)] \times 10^{-3} \end{aligned}$$

with ϕ the latitude of the site, H_s the height of the site in km and T_s the surface temperature in °C [Herring, 1992]. Herring reported typical RMS differences between ray traced and mapped delays at 5 degrees to be 30 mm for the hydrostatic and 10 mm for the wet.

New(/Niell) Mapping Functions (NMF)

Since their publication by Niell [1996], NMF have been undoubtedly the most used mapping functions in space geodetic data analysis, although they have now been superseded by generic NWM based mapping functions (like the GMF or the VMF1, see below). The form adopted by Niell [1996] for his mapping functions is the one defined by Herring [1992] (Equation 2.74). They are developed upon

the USSA profiles of temperature and relative humidity. Although all the information is relative to the northern hemisphere, the derived mapping functions are also valid for the southern hemisphere by assuming that the two hemisphere are "antisymmetric in time".

Niell [1996] states that mapping functions depending on surface temperature like the Davis et al. [1985] (CfA), Lanyi [1984], Ifadis [1986], and Herring [1992] (MTT) are ultimately limited in accuracy by this dependence, because the boundary layer has much more variability in temperature. See Niell [1996] for details. Instead, Niell [1996] says that a global mapping function should be based on properties of the whole atmosphere (global profiles) and be latitude dependent; the USSA as a basis for developing the new mapping functions is then justified. An obvious drawback is that this kind of source of information is incapable of reflecting specific time and location atmospheric state. That is the NMF are based on climatology instead of in situ meteorology.

Two sets of coefficients tabulated at the same latitudes for which the USSA profiles are available were derived allowing interpolation for any location and time. Tables 2.3 and 2.4 contains those coefficients for respectively the hydrostatic and wet mapping functions whereas Equation 2.75 indicates how to compute any hydrostatic coefficients (a, b and c) for any latitude and time. Note: for the wet, only a linear interpolation on the latitude is needed.

To compute the values of the hydrostatic coefficients a, b and c for a latitude ϕ between two tabulated ϕ_i and ϕ_j values as given in Table 2.3, at a specific time t (in UT days), the values of a,b, and c first need to be computed at ϕ_i and ϕ_j as:

$$p(\phi_{i,j}, t) = p_{avg_{i,j}} + p_{amp_{i,j}}(\phi_{i,j})\ cos\left(2\pi \frac{t - T_0}{365.25}\right) \tag{2.75}$$

where $T_0 = 28.0$ [day] (it corresponds to the average coldest day of the year). Then a linear interpolation between $p(\phi_i, t)$ and $p(\phi_j, t)$ is performed to find the value of p at the desired ϕ.

A height correction then needs to be applied to the hydrostatic value, depending on the height above sea level of the observing point:

$$\frac{dm(\varepsilon)}{dh} = \frac{1}{sin(\varepsilon)} - f(\varepsilon, a_{ht}, b_{ht}, c_{ht}) \tag{2.76}$$

where ε is the elevation angle, a_{ht}, b_{ht}, and c_{ht} are constant parameters (reproduced in Table 2.3), and f is the mapping function in the form given by Equation 2.74. The correction $\Delta m(\varepsilon)$ to be added to $m(\varepsilon)$ is:

$$\Delta m(\varepsilon) = \frac{dm(\varepsilon)}{dh} H \tag{2.77}$$

where H is the height above sea level.

Isobaric Mapping Functions (IMF)

Niell [2000] published new mapping functions based on NWM data. The hydrostatic is based solely on the 200 mb geopotential height. This last one was found to be correlated with the radiosonde derived hydrostatic mapping function at 5 degrees. As per the NMF [Niell, 1996], a three coefficients normalized Marini's model ([Marini, 1972], [Herring, 1992]) is used. A global assessment of the IMF was carried out by [Vey et al., 2006].

Vienna Mapping Functions (VMF)

The VMF [Boehm and Schuh, 2004] are based on the full ray-tracing of a NWM, namely the ECMWF one. Full ray-tracing means ray-tracing from the site for

Table 2.3: Coefficients of the Niell [1996] Hydrostatic Mapping Function (nmfh2.0)

	Latitude				
Coefficient	15°	30°	45°	60°	75°
			Average		
a	1.2769934e-3	1.2683230e-3	1.2465397e-3	1.2196049e-3	1.2045996e-3
b	2.9153695e-3	2.9152299e-3	2.9288445e-3	2.9022565e-3	2.9024912e-3
c	62.610505e-3	62.837393e-3	63.721774e-3	63.824265e-3	64.258455e-3
			Amplitude		
a	0.0	1.2709626e-5	2.6523662e-5	3.4000452e-5	4.1202191e-5
b	0.0	2.1414979e-5	3.0160779e-5	7.2562722e-5	11.723375e-5
c	0.0	9.0128400e-5	4.3497037e-5	84.795348e-5	170.37206e-5
			Height Correction		
a_{ht}			2.53e-5		
b_{ht}			5.49e-3		
c_{ht}			1.14e-3		

Table 2.4: Coefficients of the Niell [1996] Wet Mapping Function (nmfw2.0)

	Latitude				
Coefficient	15°	30°	45°	60°	75°
a	5.8021897e-4	5.6794847e-4	5.8118019e-4	5.9727542e-4	6.1641693e-4
b	1.4275268e-3	1.5138625e-3	1.4572752e-3	1.5007428e-3	1.7599082e-3
c	4.3472961e-2	4.6729510e-2	4.3908931e-2	4.4626982e-2	5.4736038e-2

which the mapping functions are to be determined up to the upper limit of the neutral atmosphere. The model to be fitted is the Marini [1972] one as formulated by Herring [1992]. Paths for ten initial elevation angles are ray-traced, from 3.3 degrees to zenith, the lowest one corresponding to an outgoing elevation angle of about 3.0 degrees. That's for the rigorous approach. A fast determination is also available for the a coefficients, based on a single ray-trace at 3.3 degrees. Predefined formulas are used in conjunction to get the b and c coefficients, the hydrostatic ones being taken from the IMF, and the wet ones from the NMF. Six hourly coefficients are made available by the Institute of Geodesy and Geophysics (IGG) of the Technical University of Wien [Boehm, 2008 (last accessed July 5, 2009)]. In a reprocessing of VLBI data, about 75% of baselines had their length repeatability improved when using the VMF (fast) instead of the NMF, with an an improvement comprised between 5 and 11% depending on the VLBI campaign. At the time, improvement over the IMF were not obvious.

(Updated) Vienna Mapping Functions (VMF1)

Boehm et al. [2006a] proposed updated b and c coefficients for the hydrostatic VMF based on one year of the ECMWF ERA-40 data set. On a 156 points grid, using monthly values for epochs 00, 06, 12 and 18, ten (starting) elevations were ray traced and corresponding discrete mapping functions computed. The usual three coefficients Marini's model was fitted by least squares for each of the (156x12x4) profiles and residual were found to be in general below 0.5 mm. The b coefficient was found to be constant and equal to 0.0029. The procedure was then repeated with b held to its newly defined value and c was found to be:

$$c = c_0 + \left[\left(\cos(\left(\frac{\mathrm{DoY} - 28}{365} 2\pi + \Psi \right) + 1 \right) \frac{c_{11}}{2} + c_{10} \right] (1 - \cos(\phi)) \qquad (2.78)$$

where c_0, c_0, c_0, and Ψ are given in Table 2.5. The b and c for the wet are kept from the original. The c coefficient is no longer symmetric with respect to the equator and has a time and latitude dependency. Compared to VMF, [Boehm et al., 2006a] mention a constant change in station height of up to 2 mm at the equator and seasonal variations between 4 mm and 0 mm at the poles, with VLBI baseline length repeatability slightly improved. Boehm [2008 (last accessed July 5, 2009)] is an excellent starting point for the Vienna mapping functions in general and related products, where either site or gridded values for the VMF1 can be obtained. An assessment of the gridded VMF1 can be found in [Kouba, 2008].

Table 2.5: Parameters c_0, c_{10}, c_{11}, and Ψ needed for the computation of c in the hydrostatic VMF1 mapping function.

Hemisphere	c_0	c_{10}	c_{11}	Ψ
Northern	0.062	0.001	0.005	0
Southern	0.062	0.002	0.007	π

Global Mapping Functions (GMF)

The GMF published by Boehm et al. [2006b] are based on the VMF1 parameters but are aimed to be used like the NMF. Monthly mean profiles of pressure, temperature, and humidity from the 40 years reanalysis project (ERA40) of the ECMWF were used on a global 15 $\times$ 15 degrees grid to derive the a parameters, a_h and a_w for the hydrostatic and wet mapping functions respectively. b and c are taken from VMF1 (see 2.6.11). Three years of data were used to this end. For each one of the 312 grid points, a parametric form similar to [Niell, 1996] (annual sinusoidal) was fitted to the 36 samples long time series of a coefficients:

$$a = a_0 + A \cdot \cos\left(\frac{\mathrm{DoY} - 28.0}{365.0} \cdot 2\pi\right) \tag{2.79}$$

where a_0 is the mean value and A the amplitude of the signal. Those two parameters were then expanded into spatial spherical harmonic coefficients of degree 9:

$$a_0 = \sum_{n=0}^{9} \sum_{m=0}^{n} P_{nm} \sin(\phi) \left[A_{nm} \cos(m\lambda) + B_{nm} \sin(m\lambda) \right] \tag{2.80}$$

Grids for the the coefficients P, A and B can be found at [Boehm, 2008 (last accessed July 5, 2009)].

The difference between the monthly values and their parametric representation in Equation 2.79 has a maximum standard deviation of 8 mm of equivalent height error for the hydrostatic, increasing from equator to higher latitude, and 3 mm for the wet, at the equator [Boehm et al., 2006b].

2.7 Tropospheric gradients

To the knowledge of the author, Gardner [1977] was first to develop a model to account for a non spherically symmetric atmosphere. To do so, Gardner [1977] developed a two term expression to correct for the error introduced by horizontal gradients. In a previous publication ([Gardner, 1976]) Gardner evaluated the impact of such gradients on pulsed laser ranging measurements. He estimated that a RMS error approaching 3 cm was introduced for a satellite near 10 degrees elevation. The reader should keep in mind that the magnitude of the delay depends on the frequency of the signal of the ranging system. The first term is a 'Marini and Murray-type correction' (see [Marini and Murray, 1973]) whereas the second term accounts for the gradient effects. For the gradient correction computation, horizontal gradient of surface temperature and pressure were needed (inferred from surrounding meteorological stations).

In modern GPS data processing, atmospheric gradients can be introduced as unknowns in the least squares procedures and be estimated along other site specific parameters like the zenith total delay. For example, Herring [1992] proposed to "tilt" the atmosphere. The asymmetric contribution L_{az} to the total tropospheric delay can then be written as:

$$L_{az} = m_g(\epsilon) \times (G_N \cos\alpha + G_E \sin\alpha) \tag{2.81}$$

where the gradient mapping function m_g was defined as :

$$m_g(\epsilon) = \frac{1}{\sin\epsilon \tan\epsilon + 0.0032} \tag{2.82}$$

G_N and G_E are two parameters representing the north-south and east-west gradients, α and ϵ the azimuth and and elevation angle of a signal, and the 0.0032 constant was empirically determined.

A similar approach was implemented in the Bernese GPS Software (BSW50, Dach et al. [2007]). A full derivation of the gradient estimation implementation is detailed in Meindl et al. [2004]. The horizontal gradients contribution L_{az} was written as:

$$L_{az} = \frac{\partial f}{\partial z} \times (G_N \cos\alpha + G_E \sin\alpha) \tag{2.83}$$

where f is the mapping function used to map the estimated zenithal tropospheric correction (the misleading "ZWD" parameter). In the Bernese software, this will usually be the NMF Wet.

Equations 2.81 and 2.83 only differ by the gradient mapping function used, and this is general to most gradient estimation formulations actually in use in space

geodetic techniques. McCarthy and Petit [2003] mentions difference up 50% between the different m_g at 5 degrees elevation. On top of the two gradient mapping functions already presented, MacMillan [1995] proposed m_g to be written as $m_g = m(\epsilon)cot(\epsilon)$ where $m(\epsilon)$ is the "mapping function that gives the dependence of the delay on ϵ" (either the hydrostatic or the wet).

Chapter 3

Building the OMF (Orliac Mapping Functions)

This chapter details the development of the new azimuth dependent (and azimuthally symmetric) mapping functions, referred to in this thesis as OMF. The OMF are based on the 3D ray tracing a high spatial resolution numerical weather model. It starts with the description of the three dimensional ray tracing algorithm developed to this end. A strategy for selecting an optimal set of elevation angles to ray trace, as a tradeoff between accuracy and processing power is presented and assessed. Then, the accuracy of the mapping functions themselves is analyzed. Contrary to all current mapping functions the azimuth dependent OMF is free of the assumption that the atmosphere is spherically symmetric around the station.

3.1 OMF Overview

The flow chart below outlines the way the OMF are built, on each azimuth. Section 3.6 describes the way the OMF can be computed for any pair of azimuth and elevation angles.

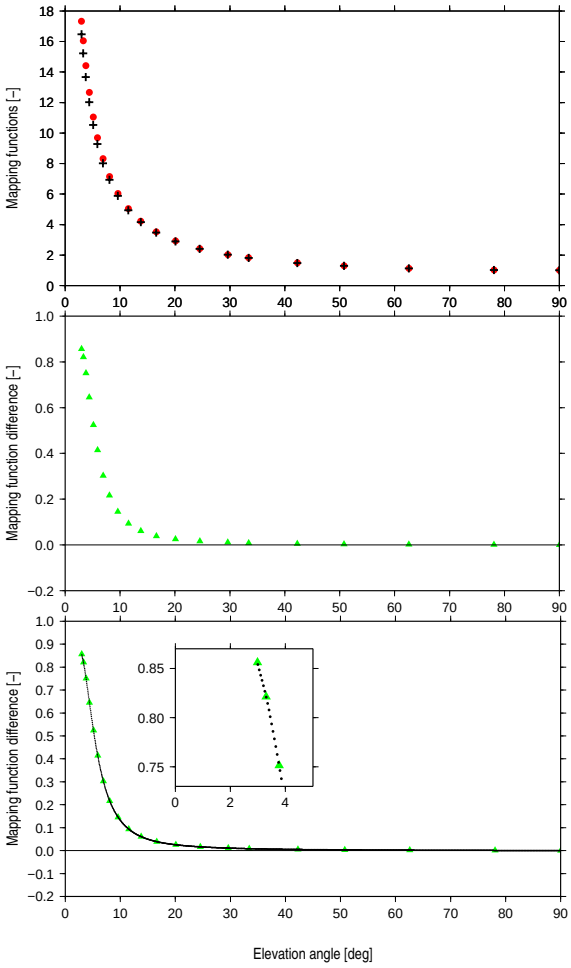

Step 1: The NWM is ray traced to obtain discrete values of mapping functions at certain elevation angles (red dots). The corresponding NMF values are computed (black crosses).

Step 2: The difference ray traced minus NMF mapping function is computed.

Step 3: Using a cubic spline interpolation, a fine regular grid of mapping function coefficients (every 0.05 degrees)is generated that will allow linear interpolation between consecutive values.

Figure 3.1: Flow chart of how the OMF are built.

3.2 Three Dimensional Ray Tracing Algorithm

3.2.1 NWM Overview

The numerical weather model used in this study is the UK Met Office (UKMO) Unified Model (UM). The mesoscale version of the UKMO UM was used and is labelled MESO throughout this work. The global one is not considered here but could be the basis for global azimuth dependent mapping functions. The UM is a non-hydrostatic model (i.e. it does not simply assume that the atmosphere is in hydrostatic equilibrium). For details on the model's formulation see Staniforth et al. [2006]. Only relevant facts are reported here with respect to the implementation of the ray tracing algorithm used to derive the OMF.

The MESO is composed of 13 pressure levels: 1000, 950, 850, 700, 500, 400, 300, 250, 200, 150, 100, 70 and 30 mb. On these pressure levels, three data sets were used to derive the hydrostatic, wet and total refractivities at any point of a ray:

1. *Geopotential height*,
2. *Temperature*,
3. *Relative humidity with respect to ice*.

Four different outputs are available from the British Atmospheric Data Center (BADC): (*i*) Analysis field on model levels, (*ii*) Analysis field on pressure levels, (*iii*) Prediction field on model levels, (*iv*) Prediction field on pressure levels. Only the analysis fields on pressure levels were used in this work. The analysis field can be seen as the product to use for high accuracy post-processing of space geodetic data whereas the prediction fields would be the ones to use for any real-time and near real-time GNSS applications.

3.2.2 MESO Coordinate Systems

The model output coordinate system is a rotated system where the pole position, expressed in the geographical system, is 37.5 degrees north and 177.5 degrees east. It is roughly equivalent to moving the UK down to the equator or bringing the equator below the UK. The result of the operation is that a regular grid, in terms of latitude and longitude spacing translates into an almost regular grid on the ground than it would do at the latitude of the UK. The rotated system is presented in Figure 3.2 and the geographical system in Figure 3.3.

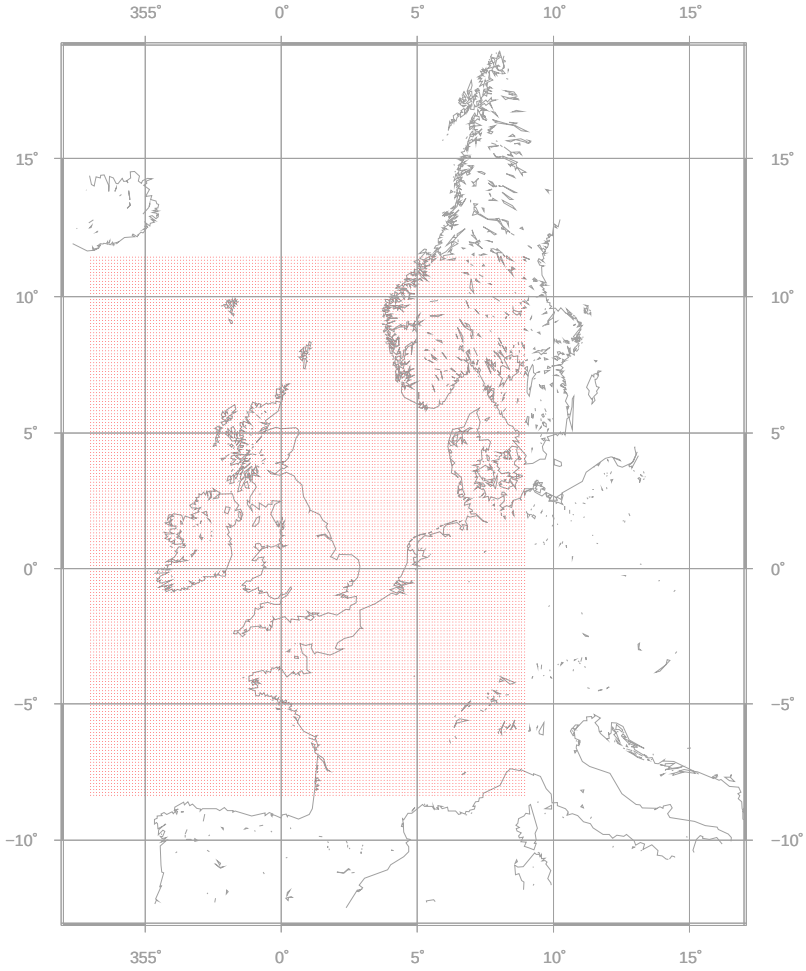

Figure 3.2: "Equatorial" coverage of the MESO. The grid is regular, with a node spacing of 12.3 km. The UK appears to be on the equator.

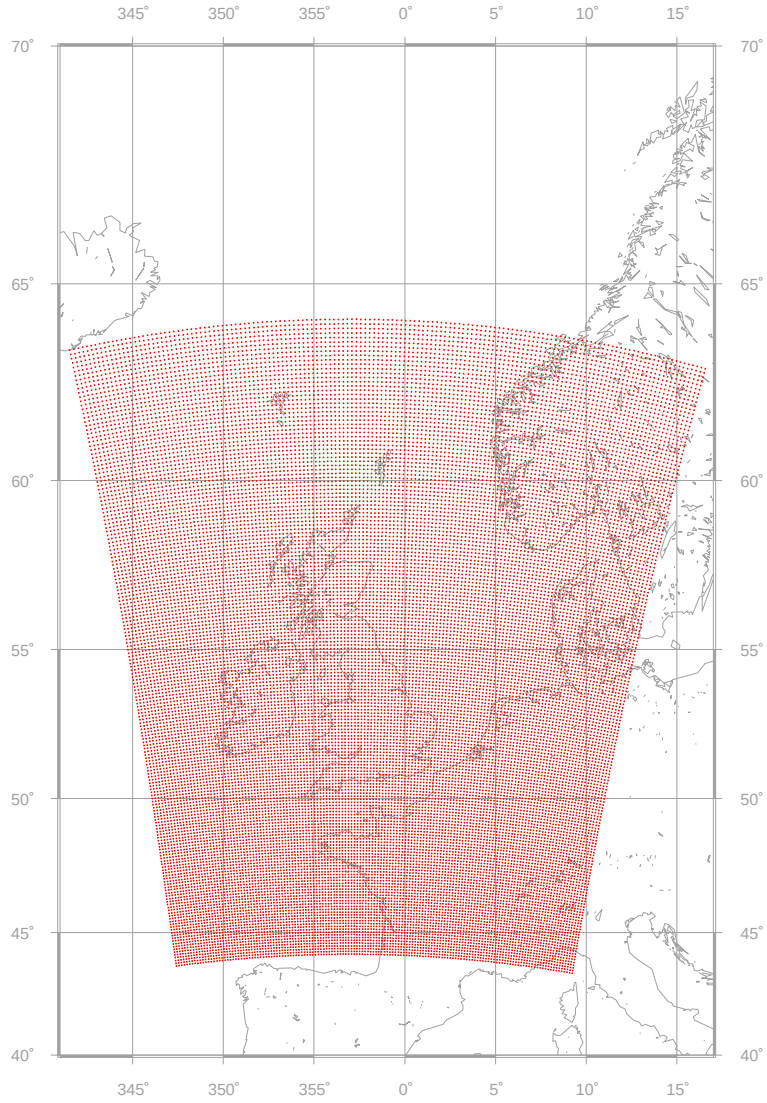

Figure 3.3: Geographical coverage of the UK Met Office mesoscale unified model. Each dot represents a node of the grid originally expressed in an equatorial system.

The equatorial grid clearly has a regular spacing of 0.11 degree (≈12.3 km), both in longitude and latitude. The south-west corner is located at (353.00°,-8.36°) and the north-east corner at (8.96°, 11.44°). The grid has 146 x 181 nodes. Whereas, as a result of a coordinate transformation, the geographical grid is clearly not regular.

3.2.3 Coordinate Transformation Between the Geographical and Equatorial Systems

The transformation is taken from Staniforth et al. [2006] (where the reader can refer to for further details on the model in general and the transformation in particular).

For a point P with coordinates (λ, ϕ) are, in the geographical system, the equatorial (or rotated as per in Staniforth et al. [2006]) system is defined by:

1. Its origin being located at (λ_{rot_0}, ϕ_{rot_0})

2. Its polar axis being in the plane define by the meridian λ_{rot_0}.

See Figure 3.4 for illustration. P, expressed in the equatorial system, has the coordinates (Λ, Φ) that relate to (λ, ϕ) as follows:

$$\cos\Phi\cos\Lambda = \cos\phi\cos(\lambda-\lambda_{rot0})\cos\phi_{rot0}+\sin\phi\sin\phi_{rot0} \quad (3.1)$$

$$\cos\Phi\sin\Lambda = \cos\phi\sin(\lambda-\lambda_{rot0}) \quad (3.2)$$

$$\sin\Phi = \sin\phi\cos\phi_{rot0}-\cos\phi\cos(\lambda-\lambda_{rot0})\sin\phi_{rot0} \quad (3.3)$$

The reverse transformation that gives the geographical coordinates (λ, ϕ) of a point P, given coordinates (Λ, Φ) in the equatorial system is:

$$\cos\phi\cos(\lambda-\lambda_{rot0}) = \cos\Phi\cos\Lambda\cos\phi_{rot0}-\sin\Phi\sin\phi_{rot0} \quad (3.4)$$

$$\cos\phi\sin(\lambda-\lambda_{rot0}) = \cos\Phi\sin\Lambda \quad (3.5)$$

$$\sin\phi = \sin\Phi\cos\Phi_{rot0}+\cos\Phi\cos\Lambda\sin\phi_{rot0} \quad (3.6)$$

As mentioned in Staniforth et al. [2006] these two sets of equations must be used with care as 3.1 leads unambiguously to Φ whereas both 3.2 and 3.3 (giving respectively the cosine and the sine of Λ) are needed to determine to which quadrant

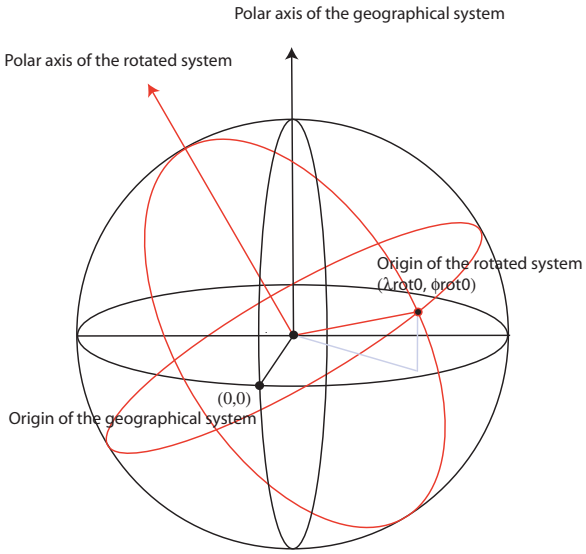

Figure 3.4: The geographical coordinate system (in black) and the rotated or equatorial coordinate system (in red). Coordinate transformation between the two systems is described under Section 3.2.3. Full details can be found in [Staniforth et al., 2006].

Λ belongs to. Idem for the second set of equations (3.4 - 3.6).

3.2.4 Comments on the Coordinate Systems

The fact that the MESO data is not expressed in a geographical system complicated the implementation of the ray tracing algorithm as the transformation between the two systems doesn't conserve directions and orientation. It is obvious that the implementation would have been easier on a regular grid. Quoted from Staniforth et al. [2006]: "*There are two good reasons for what might seem at first sight a perverse manoeuvre*":

1. It avoids numerical complications around the poles

2. A quasi uniform grid is obtained from points with regular longitude and

latitude distribution.

3.3 Ray Tracing

This section details the implementation of the ray-tracing algorithm. The initial conditions are: (i) a starting point P_0 of geographical coordinates $(\lambda_0, \phi_0, r_0$ or $h_0)$ and geocentric coordinates (X_0, Y_0, Z_0), (ii) an arrival azimuth angle a_0 and (iii) elevation angle e_0. The output are hydrostatic and wet delays, bending effect and the outgoing (geometrical) elevation angle. The organization of this section reflects the actual implementation of the OMF by the author.

3.3.1 Definitions

Cell: The NWM grid nodes are indexed starting from the bottom left corner of the grid set up to be (0, 0). Then, indices are positively incremented when moving in northern and eastern directions. By cell is meant the region defined by four adjacent points of the NWM grid output c_0, c_1, c_2 and c_3 whose indices are defined in Table 3.1. The indices of a cell node are taken as the ones of its lower left corner.

Tower: By tower it is meant here the volume defined by four radii originating from the Earth's center and passing through the four nodes of a cell, when considering only the part above the Earth's surface, see Figure 3.6 later.

3.3.2 Algorithm Description

The two dimensional algorithm was taken from [Boehm and Schuh, 2003] but enhanced to be three dimensional (3D), that is, it is also dependent on the starting

Table 3.1: NWM cell nodes indices.

Point	North index	East index
c_0	nc_0	ec_0
c_1	$nc_0 + 1$	ec_0
c_2	$nc_0 + 1$	$ec_0 + 1$
c_3	nc_0	$ec_0 + 1$

azimuth angle, and not solely on the starting elevation angle. The input of the 3D ray tracing algorithm are the geographical coordinates of the site and the arrival (seen as starting by the algorithm) azimuth and elevation angles of the signal. In brief, the ray-tracing itself is performed in the geographical coordinate system, whereas the meteorological information is accessed in the equatorial system, as in the geographical system it is not straightforward, if possible, to identify to which cell (or tower) a points belongs to.

The steps undertaken in the algorithm are below:

Step 1 The geographical coordinates (λ_0, ϕ_0) of the starting point P_0 are transformed into equatorial (Λ_0, Φ_0) ones (see Section 3.2.3).

Step 2 As the equatorial grid is almost regular (and assumed perfectly regular in the following), it is straightforward to determine to which cell of the grid the point belongs to, which is hardly feasible in the geographical system, hence this necessary pass from one system to the other! The longitude and latitude indices (I, J) of the cell are computed as follows:

$$I = int(\Lambda / gridRes) \tag{3.7}$$

$$J = int(\Phi / gridRes) \tag{3.8}$$

where $int()$ is the integer operand and $gridRes$ is the longitudinal and latitudinal resolution of the equatorial grid (0.11 degree or 12.3 km). This gives

the location of the base of the "tower" which P belongs to.

Step 3 Using Table 3.1, the indices of the remaining three corners of the cell to which P_0 belongs to are obtained; the coordinates of each corner, in both coordinate systems are then computed (see 3.2.3).

Step 4 The following geocentric cartesian coordinate system is defined: (i) Earth's center as origin (the Earth is assumed to be spherical), (ii) z axis defined by $\overrightarrow{OP_0}$, and (iii), the x axis is so that the tangent to the signal at P_0 lies in the plan $(\overrightarrow{z}, \overrightarrow{x})$. This system is referred to as the *rotated* system hereafter, in opposition to the conventional geocentric system, where (x_i, y_i, z_i) are the coordinates of any integration point in the rotated system, and (X_i, Y_i, Z_i) the coordinates of the same point in the conventional geocentric system.

P_0 is therefore defined by:

$$x_{i=0} = x_0 = 0.0 \tag{3.9}$$

$$y_{i=0} = y_0 = 0.0 \tag{3.10}$$

$$z_{i=0} = z_0 = r_i \tag{3.11}$$

$$\epsilon_{i=0} = \epsilon_0 = \epsilon_0 \tag{3.12}$$

$$\tag{3.13}$$

Step 5 Using Table 3.2 (from [Rocken et al., 2001]) get the next geometrical height (radial distance) r_j which defines the next integrating point P_j. The length of the segment $s_i = [P_i, P_{j=i+1}]$, is given by:

$$s_i = -r_i \sin(\epsilon_i) + \sqrt{r_j^2 - r_i^2 cos(\epsilon_i)^2} \tag{3.14}$$

Equation 3.14 is a solution of the second order polynomial obtained in triangle (OP_0P_1) (see figure 3.5 for the geometrical configuration) in which the cosine rule gives us:

$$r_j^2 = r_i^2 + s_i^2 - 2r_i s_i \cos(\pi/2 + \epsilon) \tag{3.15}$$

Rearranged as a second order polynomial:

$$s_i^2 + s_i(2r_i \sin\epsilon) + (r_i^2 - r_j^2) = 0 \tag{3.16}$$

The coordinates of P_j, in the rotated geocentric system, are then given by:

$$\begin{aligned} x_j &= x_i + s_i \cos\epsilon_i \\ y_j &= y_i + 0.0 \\ z_j &= z_i + s_i \sin\epsilon_i \end{aligned} \tag{3.17}$$

Step 6 Transform $(x_j,\ y_j,\ z_j)$ to the geographic (i.e. spherical) system. To do so, first transform the coordinates from the rotated geocentric to the conventional geocentric where the coordinates of $P_j = (X_i, Y_i, Z_i)$ are converted into spherical coordinates $P_j = (\lambda_i, \phi_i, r_i)$.

Table 3.2: Ray tracing integration step increments according to the height, [Rocken et al., 2001]

Height range [km]	Integration increment [m]
0-2	10
2-6	20
6-16	50
16-36	100
36-80	500

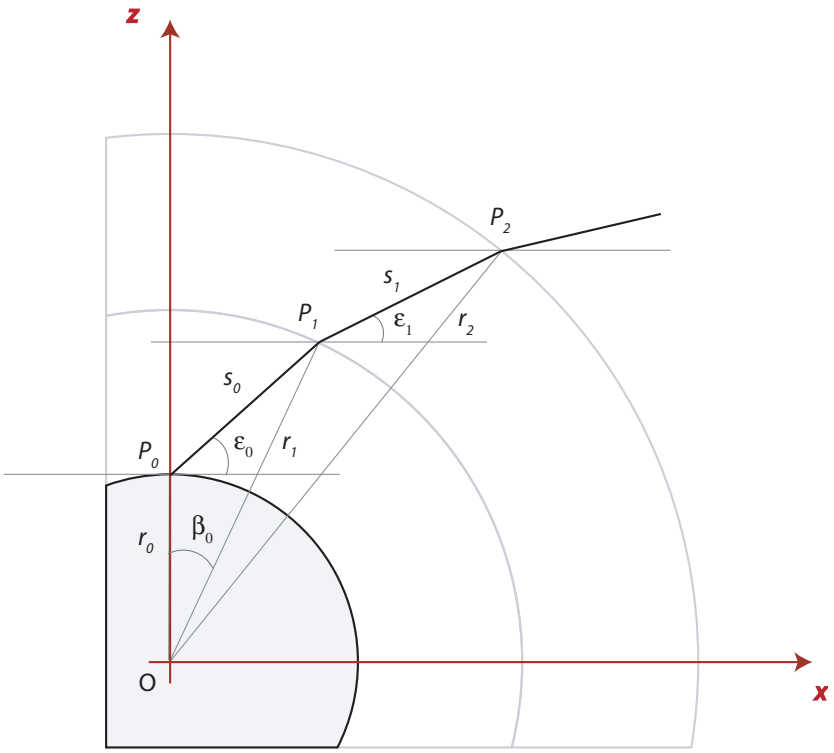

Figure 3.5: Geometrical configuration for the first steps of the ray tracing.

Coordinate Transformation Between the Rotated Geocentric and the Geocentric Systems

With λ_0 and ϕ_0 the longitude and latitude of P_0 and α_0 the azimuth of the incoming signal, the transformation between the rotated geocentric and (conventional) geocentric system of a point $P_i = (x_i, y_i, z_i)$ writes as:

$$\begin{pmatrix} X_i \\ Y_i \\ Z_i \end{pmatrix} = R_1 \cdot R_2 \cdot R_3 \begin{pmatrix} x_i \\ y_i \\ z_i \end{pmatrix} \tag{3.18}$$

where:

$$R_1 = \begin{pmatrix} \cos\lambda_0 & -\sin\lambda_0 & 0 \\ \sin\lambda_0 & \cos\lambda_0 & 0 \\ 0 & 0 & 1 \end{pmatrix} \tag{3.19}$$

$$R_2 = \begin{pmatrix} \sin\phi_0 & 0 & -\cos\phi_0 \\ 0 & 1 & 0 \\ \cos\phi_0 & 0 & \sin\phi_0 \end{pmatrix} \tag{3.20}$$

$$R_3 = \begin{pmatrix} -\cos\alpha_0 & -\sin\alpha_0 & 0 \\ \sin\alpha_0 & -\cos\alpha_0 & 0 \\ 0 & 0 & 1 \end{pmatrix} \tag{3.21}$$

with (X_i, Y_i, Z_i) the coordinates of P_i in the (conventional) geocentric system.

Coordinate Conversion Between the Geocentric and Geographic (Spherical) Systems

The geocentric coordinates of P (X_i, Y_i, Z_i) relate to the geographic (in our case spherical) coordinates (λ, ϕ, r) via:

$$r = \sqrt{X_i^2 + Y_i^2 + Z_i^2} \tag{3.22}$$

$$\cos\phi = \frac{Z}{r} \tag{3.23}$$

$$\cos\lambda = \frac{X}{r\sin\phi} \tag{3.24}$$

$$\sin\lambda = \frac{Y}{r\sin\phi} \tag{3.25}$$

(ϕ is unambiguously determined whereas λ needs to be worked out from both its sine and the cosine)

Step 7 Identify the pressure levels on each branch of the towers to which point P_j's cell nodes belong to. They can be different although in the majority of cases, similar pressure levels will be identified.

At this stage the coordinates of P_j are know in the equatorial system. The height is known, but, the four edges of the corresponding tower (see Section 3.3.1) are successively scanned to find out whether:

1. h is comprised between two consecutive pressure levels, and which ones,
2. h is above the highest pressure level,
3. h is below the lowest pressure level.

In some cases, for heights h close to geopotential heights, the cases on the four edges might be a mix of (i) and (ii) or (iii), and even though h might lie between two consecutive levels on each edge, those two consecutive levels might not be the same. It happens when the height is close to the geopotential height of a pressure level, but the PL height is different on each edge of the tower. Figure 3.6 illustrates some of those cases.

Step 8 Derive the meteorological information at an arbitrary height, from the readings made at the appropriate pressure level(s). The structure follows the cases enumerated under Step 7.

Case (i) h is comprised between two consecutive pressure levels, labelled PL_i and PL_j. On each edge, on the two pressure levels, the information as given in the output file of the NWM, that is, the temperature in Kelvin, the total pressure in hectopascal, the relative humidity over ice and the geopotential height of the pressure level, is read. Dropping the index for the edge, on each edge are then available:

GH_i, GH_j Geopotential heights of pressure level i and j respectively

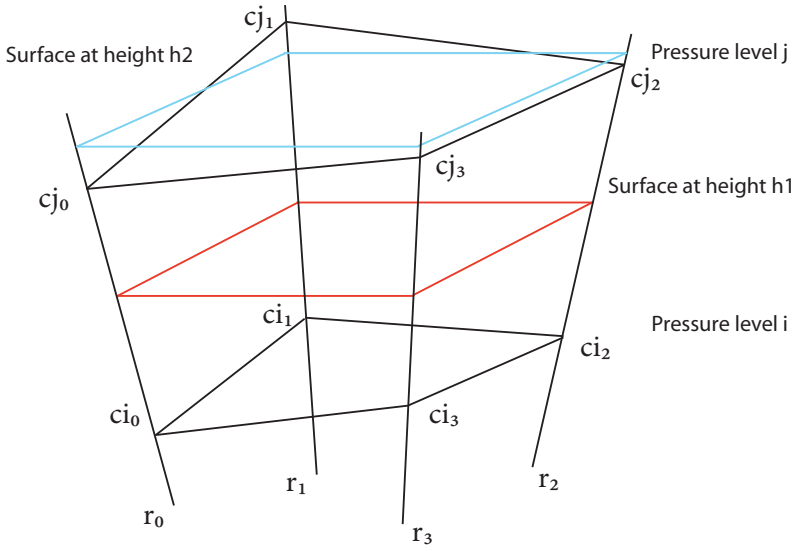

Figure 3.6: Determination of refractivity for an arbitrary height: illustration of interaction between an arbitrary height and geopotential heights of pressure levels on each edge of the tower. **Surface at height h1**: case where on each edge of the tower, height h is comprised between the same two pressure levels, i.e, case (i) is found four times. **Surface at height h2**: case where a mix of situations is found. In case Pressure level j is the top pressure level, a mix of three case (i) for corners cj_0, cj_2 and cj_3 and one case (ii) for corner cj_1 is found ((i) with different pressure levels if pressure level j is not the top one)

T_i, T_j Temperatures of pressure level i and j respectively

U_i, U_j Relative humidities over ice of pressure level i and j respectively

P_i, P_j Total pressures of pressure level i and j respectively.

In order to compute the refractivity, the water vapour pressure is needed, and is derived from P, T and U, as described in Subsection 3.3.3.

In the implementation, a cursor is set on the 8 corners of the volume that contains the point P ($c_{i0..3}$ and $c_{j0..3}$ on Figure 3.6) and the values of P, T and e on each of those is kept in memory as long as the point doesn't not get out of that volume.

On each edge, are defined $\delta h = h - GH_i$ and $\Delta h = GH_j - GH_i$. The following models for P, T and e variations with height were adopted from [Boehm and Schuh, 2003]:

$$\begin{aligned} P(h) &= P(GH_i) \times \exp\left(\frac{\delta h}{\alpha_P}\right) \\ T(h) &= T(H_i) + \alpha_T \times \delta h \\ e(h) &= e(H_i) \times \exp\left(\frac{\delta h}{\alpha_e}\right) \end{aligned} \tag{3.26}$$

where:

$$\alpha_P = \frac{\Delta h}{\log\left(\frac{P_j}{P_i}\right)},\ \alpha_T = \frac{T_j - T_i}{\Delta h}\ and\ \alpha_e = \frac{\Delta h}{\log\left(\frac{e_j}{e_i}\right)}$$

Case (ii) h is below the lowest pressure level. Then the coefficients α_P,α_T and α_e are computed from the first and second pressure levels above the surface. Then P, T, and e are extrapolated from the first pressure level.

Case (iii) h is above the highest pressure level. Then the coefficients α_P,α_T and α_e are computed from the second to the last and last pressure levels above the surface. Then P, T, and e are extrapolated from the last pressure level. For the temperature, above 50 km height, a standard profile is used instead as otherwise it wouldn't reflect the mean temperature variations.

Step 9 Compute refractive indices on each node of P_j's with P, T, and e being available from Step 8, it now possible to compute the corresponding hydrostatic, wet and total refractivities $N_{h0..3}$, $N_{w0..3}$, and $N_{t0..3}$ using the

relationships by Davis et al. [1985]:

$$N_h = k_1 \times \rho \times R_d \tag{3.27}$$

$$N_w = k_2^{'} \frac{e}{T} \times Z_w^{-1} + k_3 \frac{e}{T^2} \times Z_w^{-1} \tag{3.28}$$

$$N_t = N_{hyd} + N_{wet} \tag{3.29}$$

Step 10 Compute the refractivity at P using a bilinear interpolation. Assuming that for any point P, of height h, the refractivity of the cell nodes are known, the refractivity at P is computed, in the equatorial system, using a bilinear interpolation. Weights in the bilinear interpolation are normalized, so that the sum of the four is always exactly one, to cover the case of a non-perfectly rectangular cell, as assumed and requested in the bilinear interpolation.

Step 11 Get next point P' height and apply Snell's law at P to compute coordinates of P' and start again with Step 1. Loop through until the maximum height is reached.

3.3.3 Getting the Water Vapour Pressure From P, T, and U

The parameters P and T can be interpolated directly. As a measure of the humidity (U), the relative humidity RH with respect to ice is provided in the NWM data, however the refractivity formula (see Subsection 2.6.5) needs the water vapour pressure e as input. In this thesis, it was decided to interpolate on e (several schemes were tested in Section 4.5.3), therefore the RH had to be turned into e, a step that requires the determination of the saturation water vapour pressure e_{sat}. This was obtained using the modified Goff-Gratch formulation (see Subsection 2.6.4), the WMO reference formula. The ray-tracing algorithm was

implemented so that, although the data set is called "relative humidity with respect to ice", for temperature above zero degree Celcius, the saturation water vapour pressure is computed over water instead of over ice in order to derive the water vapour pressure needed to compute the refractivity.

3.3.4 Computing Tropospheric Delays

On each iteration of the ray tracing algorithm, two points, P_i and P_{i+1} define a segment s_i for which the hydrostatic, wet and total refractivities N_{h_i}, N_{w_i} and N_{t_i}, and $N_{h_{i+1}}$, $N_{w_{i+1}}$ and $N_{t_{i+1}}$ are known. The hydrostatic, wet and total tropospheric delays on s_i (again determined by heights h_i and h_{i+1}), denoted dL_i, are computed as:

$$dL_i = (1 - 10^{-6}) \frac{N_i + N_{i+1}}{2} \times s_i \tag{3.30}$$

where corresponding refractivities are used for computing the hydrostatic, wet or total delay.

To get the (zenithal or slant) delays L, dL_i needs to be computed and integrated from the height of the site until the maximum height is reached:

$$L = \sum_{h_{site}}^{h_{max}} dL_i \tag{3.31}$$

3.3.5 Computing the Geometric Bending Delay

The geometric bending delay was computed following Boehm and Schuh [2003]:

$$L_{geo} = \sum_{h_{site}}^{h_{max}} \left[s_i \left(1 - \cos \left(e_i - e_{i+2} \right) \right) \right] \tag{3.32}$$

3.4 Selection of Elevation Angles to Ray Trace and Quality Assessment of the OMF

For any azimuth and elevation angle, the value of the corresponding mapping function has to be computed. For a set of ray traced mapping function values, two situations can arise: (*i*) a model is fitted to those values (being generally continuous on the range of elevation angles considered in the GNSS data processing) or (*ii*), direct mapping is used (on the ray traced values or on an augmented set of ray traced values as presented below).

In mapping functions like the NMF, IMF, VMF, VMF1 or GMF, azimuthal symmetry is assumed, that is, for any pair of azimuth and elevation angles, the only information used to derive the mapping function was the vertical atmospheric profile at the station (from either radiosondes or a numerical weather model). In such a case, the continuous fraction in 1/sin(e) developed by Marini is remarkably adapted to describe the variation of the mapping function according to the elevation angle. Adopting a similar model for the OMF on each azimuth, appeared to be clearly unsatisfactory - or impossible - and lead to gross errors; fitting the Marini model to the OMF ray traced values was generally fine for the hydrostatic mapping function but hardly for the wet. The best that could be obtained for the wet, in terms of least-squares success, was to set two of the three coefficients (b and c) to the values predicted by the wet NMF; even with constraining b and c, the a posteriori sigma of the fit was far worse than the precision needed. This is attributed to the fact that the ray traced values don't come from the vertical profile of refractivity at the site, a condition assumed in the development of the Marini model, but instead from the three dimensional representation of the atmosphere.

A *direct mapping* approach was chosen instead and is likely to be the only suitable option able to handle the variability of the atmosphere and consequently of the mapping functions.

3.4.1 Quality Criteria

First, the desired accuracy (assuming the ray tracing gives us the truth) that needs to be obtained has to be defined. A rule of thumb ([Niell, 1996], [Chen and Herring, 1997], [Boehm et al., 2006a]) says that the error in the vertical is between one third and one fourth of the error of the mapping function at the lowest elevation observed in terms of equivalent range correction. So, if a maximum mapping function induced error in the vertical of 1 mm is allowed, the mapping function error budget is of 3–4 mm maximum.

3.4.2 Direct Mapping

When developing the OMF, it was soon realized that it was much more efficient to model the variation of the ray traced mapping functions over a reference or 'base' mapping function, at least for direct mapping when using a cubic spline interpolation (CSI) scheme to interpolate in between ray traced values. In this work, the base mapping functions used were the Niell mapping functions [Niell, 1996]. The hydrostatic mapping function serves as a base for both the OMF hydrostatic and the OMF total, whereas the NMF wet serves as a base for the OMF wet only. That is to say, the OMF can, in a way, be seen as a correction for the NMF. As detailed below the interpolation scheme chosen was the CSI for its flexibility, smoothness and above all, the fact that interpolated values don't exceed the values of the data set used for the interpolation, so it is contained by the ray tracing itself.

The first thing that had to be determined was the number of elevation angles to

ray trace on each azimuth. It has to be optimized with respect to three criteria: (*i*) the quality of the representation of the variation made out of this limited number of elevations; (*ii*) the number of points to be ray traced is limited by the processing time and capabilities available; (*iii*) the error made when interpolating on this ray traced set of values has to be acceptable. To reach these objectives a reference data set was created.

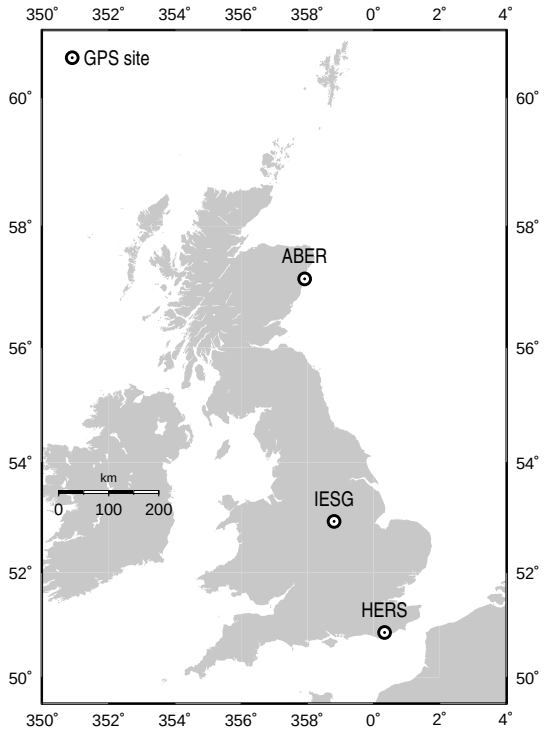

Figure 3.7: BIGF CGPS stations used for identifying the optimal set of elevation angles to ray trace.

Reference Data Set

Although only data above 5 degrees elevation angle are available for most of the BIGF continuous GPS (CGPS) stations, the interpolation scheme was assessed for elevations between 3 degrees and zenith. Three stations were considered (see Figure 3.7): ABER, IESG and HERS. The time span composed of two weeks:

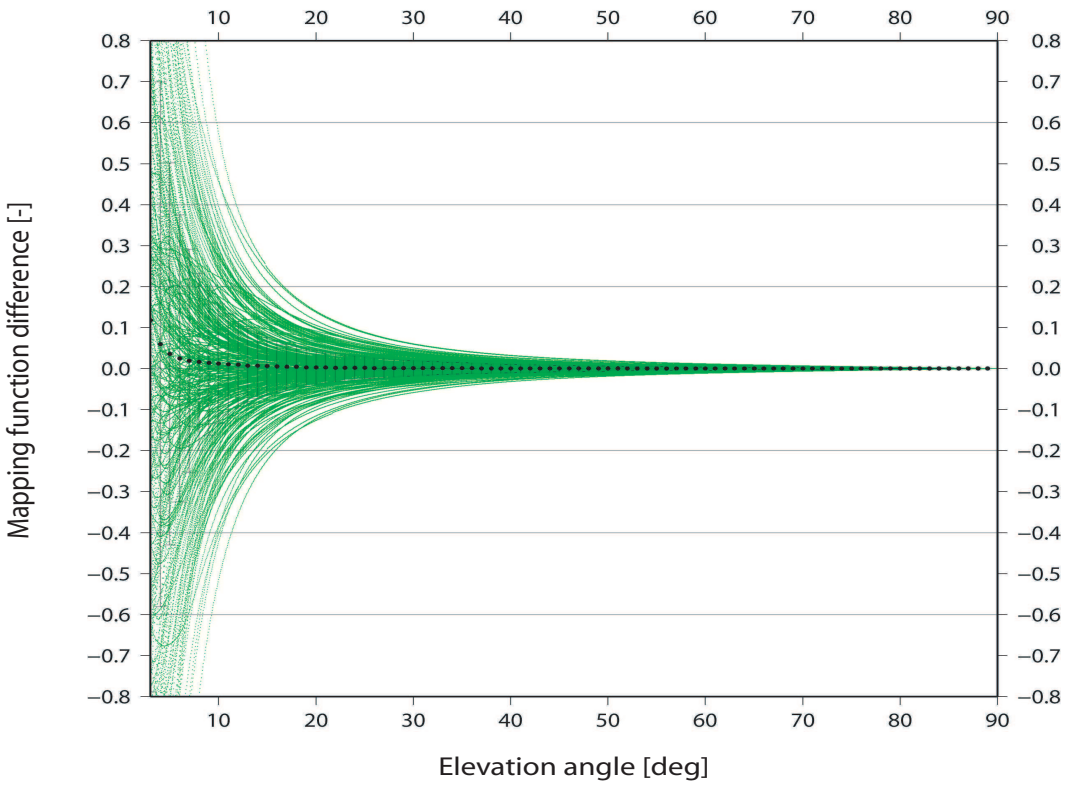

Figure 3.8: 672 azimuthal profiles of the 'wet' mapping function difference (OMF minus NMF) with respect to elevation, with 1741 ray traces (points) per profile, for CGPS stations ABER, IESG and HERS over a period composed of two weeks centered on DoYs 28 and 210 of year 2005. Black dots and bars are means and associated standard deviations computed over bins of 1 degree.

the first week centered on DoY 28 of 2005 and the second centered on DoY 210 of 2005, DoY 28 being considered as an extreme in NMF. The atmosphere was ray traced on 8 different azimuths (every 45 degrees from 0 degree North) and on every 0.05 degree elevation, 4 times a day. Hence a total of 1344 (3 sites $\times$ 14 days $\times$ 4 times per day $\times$ 8 azimuths per site) azimuthal profiles were obtained with 1741 ($\frac{90.0-3.0}{0.05}+1$) points each, that is, a total of about 2.34 million ray traces were performed. Such a data set is expected to cover a wide range of different meteorological situations for the British Isles and to be a representative sample of a more ideal data set that would cover a whole year (at least). Figure 3.8

shows all wet profiles along with average and associated standard deviations on elevation bins of one degree, whereas Figure 3.9 gives a selection of profiles only to highlight the different shapes the profile can take that the mapping function model, in the end, must be able to represent.

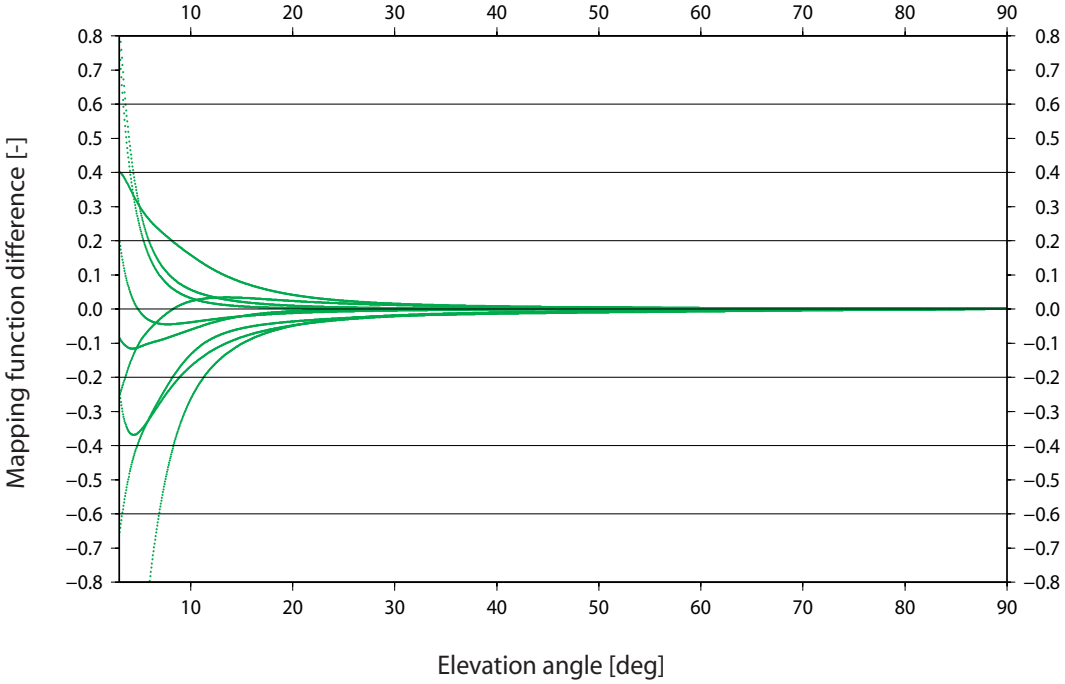

Figure 3.9: A selection of profiles of the 'wet' mapping function difference (OMF minus NMF) versus the elevation angle, to illustrate the various shapes the profiles can take. The selection was made out of profiles for CGPS stations ABER, IESG and HERS over a period composed of two weeks centered on DoYs 28 and 210 of year 2005.

Selection of Elevation Angles to Ray Trace

As mentioned above, it is important to properly select a set of elevation angles to be ray traced that is large enough to represent well enough most of the situations and small enough so that the time spent on ray tracing is acceptable in a productive environment. The number of elevation angles to be ray traced was determined by the processing power available: with a maximum of 20 considered feasible (see Chapter 5) for producing mapping functions for 30 stations over the

UK for a maximum period of 4 years. The remaining question was then how to distribute the elevations over the range of interest. To answer this, two criteria were considered:

- The first criterion was the variability of the difference with respect to the elevation angle. The standard deviation around the mean of the difference, computed on bins of one degree in elevation angle here, is an appropriate estimator of that variability. On Figure 3.8, plotted in black, are the mean and the standard deviation of the difference: OMF minus NMF, for bins of elevation angle of one degree. The distribution of the variability between the lowest elevation and the zenith should be directly reflected in the selection of the data set. Note that in this artificial data set, the distribution of the data (outgoing elevation angles) is almost constant between the lowest and highest elevation (by taking elevation angles every 0.05 degree) which is not representative of the real data distribution (see below). To conclude, it can be postulated that the distribution of the standard deviation could be taken as the distribution of the elevation angles to ray trace if the the data were uniformly distributed over the range of observations.

- A second criterion, as discussed in Niell [2001] and Niell and Petrov [2003], is that the (systematic) error propagated into position or baseline length from a bias in the mapping function is not simply related to the lowest angle observed/processed but more precisely to the distribution of the data processed. Obviously, and contrary to what is assumed above, the distribution of the data with respect to the elevation angle is not quite uniform; hence, the real data distribution will be the second criterion considered in this work.

So, generally speaking, the density of the ray traced elevation angles should be determined by the variability of the mapping function differences and the real data distribution of the elevation angles over a day (the azimuthal distribution is not considered here). The challenge then is to find a way to combine those two distributions so that the combined distribution is optimal with respect to GPS data processing. It is implicitly assumed here that no weighting scheme is applied on the the GPS data in the least-squares estimation although, contrary to VLBI, GNSS signals are subject to multipath, and it is generally wise to reduce the weight of lower elevation angle data.

As the BIGF stations do not record observations below 5 degrees elevation angle, some data were simulated. The goal of the simulation is to assess whether or not a general distribution can be assumed for the reasons exposed earlier for the second criterion to be considered in the determination of the optimal set of elevations to be ray traced. For that, 4 days equally separated over year 2005 were chosen (day of week 2 of GPS weeks 1310, 1323, 1336 and 1349). The simulation was performed for the same stations used to create the ray tracing reference data set (ABER, IESG and HERS in the UK). Based on the simulated data, two things were assessed:

1. The variation of the distribution, for a given station, over time

2. The variation of the distributions between (remote) stations.

From there, it should be possible to judge if a general distribution of the GPS observations with respect to the elevation angle can be considered suitable. Because the repeat time of the constellation, from the observer point of view, is on average 247 seconds less per day [Agnew and Larson, 2007], two consecutive days observe about 99.71% of an identical constellation. To re-observe the same constellation at the same time of a day, an observing site has to wait approximatively 350 days,

almost a year. Between two consecutive days of the four selected days here, the offset is about 6 hours and 16 minutes. The offset between the first and third days or between the second and fourth days should be a close indicator of the maximum difference between the daily constellations that can be observed by the same site.

Figures 3.10, 3.11, and 3.12, present the daily data distributions for the 3 stations over the 4 days considered. It shows that for a station, at a few percent level of variation, the daily distribution of the data with respect to the elevation angle, can reasonably be taken as constant over time. To assess whether or not the distribution can be taken as constant over the UK, for each station, the average distribution over the 4 days is considered. Then a reference distribution is created by averaging all 12 daily distributions.

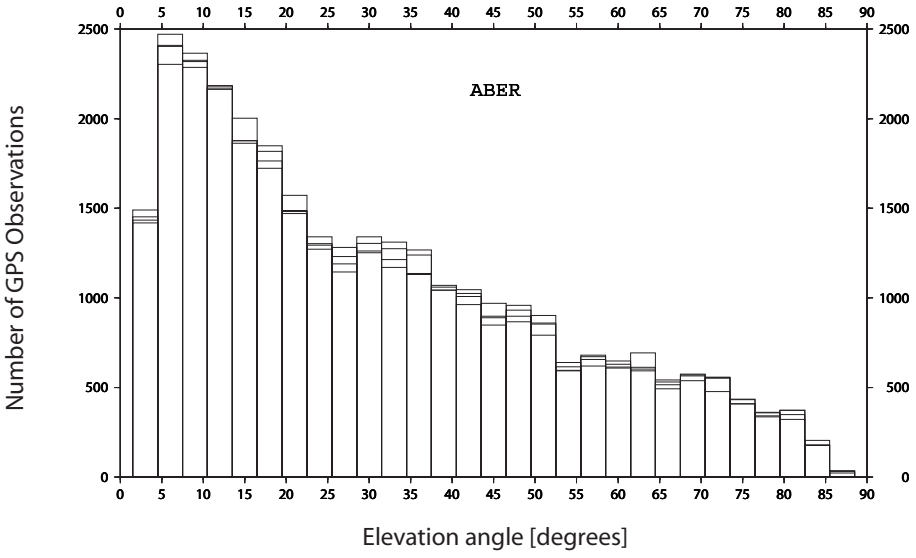

Figure 3.10: Daily histograms of the number of GPS observations with respect to elevation angle for CGPS station ABER for DoYs 46, 137, 228 and 319 of year 2005.

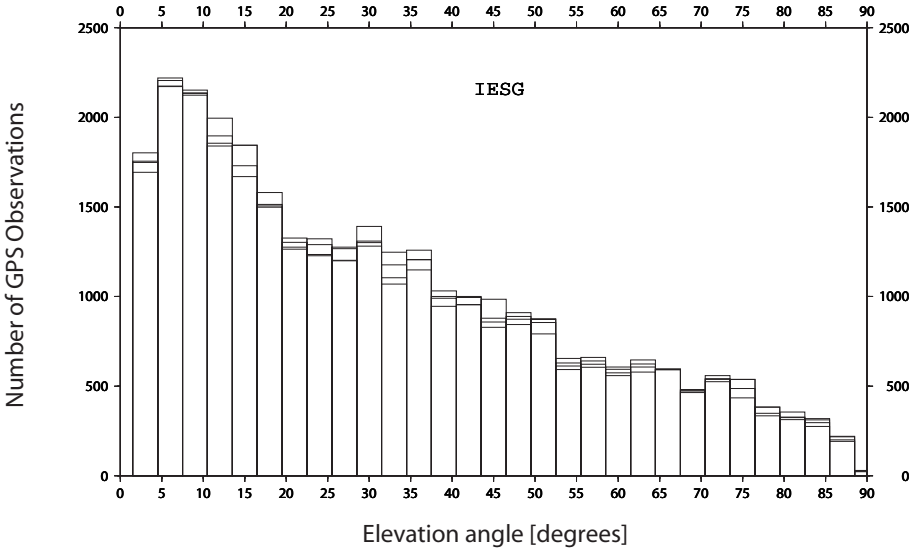

Figure 3.11: Daily histograms of the number of GPS observations with respect to elevation angle for CGPS station IESG for DoYs 46, 137, 228 and 319 of year 2005.

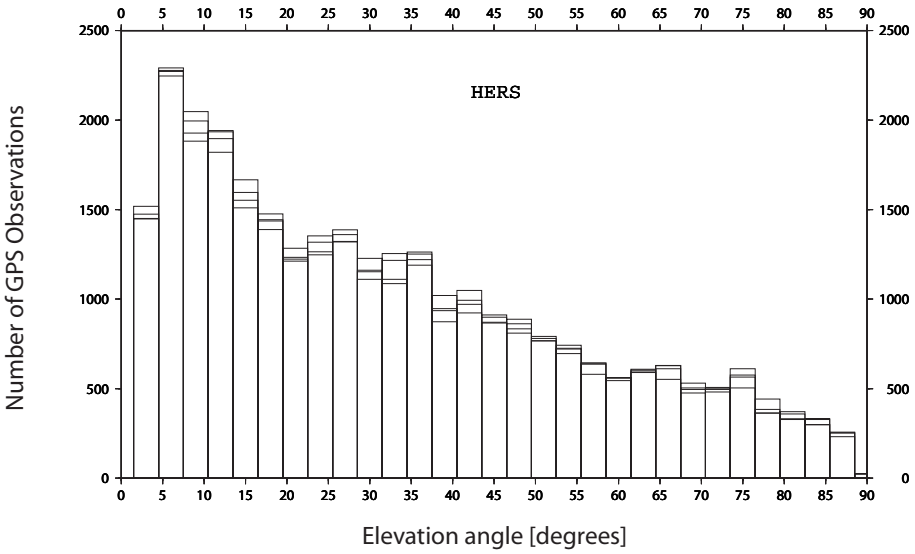

Figure 3.12: Daily histograms of the number of GPS observations with respect to elevation angle for CGPS station HERS for DoYs 46, 137, 228 and 319 of year 2005.

Those results show that taking the average distribution as constant over time and space in the UK is very acceptable.

The next section shows how the two distributions obtained from the two criteria that were considered, variability of the difference OMF minus NMF and real data distribution, are combined together to obtain what will be referred hereafter as the '*combined distribution*', denoted f_{comb}. From the combined distribution, and the maximum number of elevation angles to ray-trace (20, see above) it will then be possible to choose the points to form an optimal data set.

Combining the Two Distributions

A simple way to combine the the two discrete distributions could be to weight each distribution and define f_{comb} as the sum of the weighted individual density functions so that the function f_{comb} can be effectively considered as the density function of the elevation angle to ray trace. If a maximum m points has to be distributed, the following criterion can be used to compute the distance between two points, starting either from the lowest elevation or the zenith:

$$\int_{e_i}^{e_j} f_{comb}(e) \leqslant 1/m \tag{3.33}$$

where e is the elevation angle, e_i and e_j are two consecutive elevation angles with $i \in [1..m-1]$ and $j = i + i \in [2..m]$, and e_1 being the lowest elevation angle to be considered, 3 degrees here.

From the data distribution, two discreet density functions are created (with bins of 0.1 degree of elevation). They are presented in Figure 3.13. The red curve is the average density function and was used together with Equation 3.33 to find what will be considered, with respect to the considerations made earlier, as optimal.

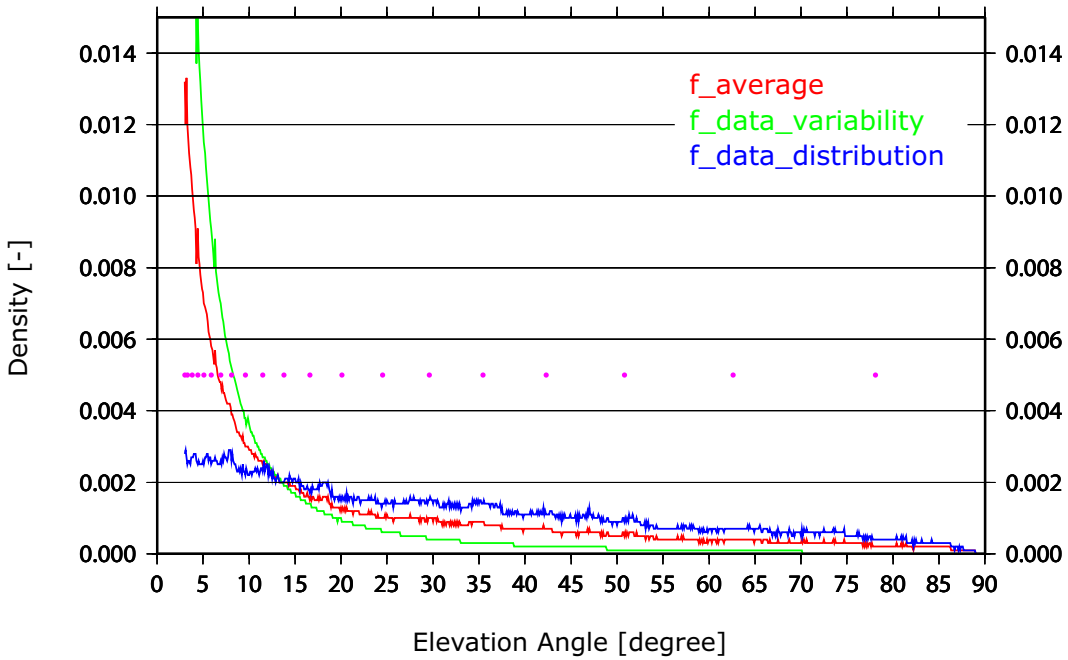

Figure 3.13: Density functions from the data variability, from data distribution and for a combination of the two by simply taking the average. Purple dots are the resulting elevation angles to ray trace so that the integration of f_average between two consecutive elevation angles is constant, here equal to 5%.

The outgoing elevation angles are: 3.0, 3.3, 3.8, 4.4, 5.1, 5.9, 6.9, 8.1, 9.6, 11.5, 13.8, 16.6, 20.1, 24.5, 29.6, 35.4, 42.3, 50.8, 62.6 and 78.1 degrees (zenith is ray traced in a previous run only one time per numerical weather model output and per station).

Ray Bending

To get the corresponding starting elevation angles, as input to the ray tracing algorithm, the empirical relationship between the starting and outgoing elevation over the same period must be used.

This is known as ray bending. To get representative starting elevation angles, the values of the starting elevation angles corresponding to the range of outgoing

Table 3.3: Approximate corresponding starting elevation angles to the quantified outgoing ones, in degrees. Starting elevation angles were found by averaging corresponding values of the outgoing ones over the range [outgoing - 0.25, outgoing + 0.25 degrees] to encompass different meteorological situations.

Outgoing elevation angle [deg]	Starting elevation angle [deg]	Outgoing elevation angle [deg]	Starting elevation angle [deg]
3.0	3.25	13.8	13.85
3.3	3.55	16.6	16.65
3.8	4.00	20.1	20.15
4.4	4.60	24.5	24.55
5.1	5.30	29.6	29.65
5.9	6.05	35.4	35.45
6.9	7.05	42.3	42.30
8.1	8.20	50.8	50.80
9.6	9.70	62.6	62.60
11.5	11.60	78.1	78.10

elevation angles [outgoing-0.25; outgoing+0.25 degree] were averaged. The reason is the variability of the meteorological conditions that lead, for the same starting elevation angle, to different outgoing elevation angles. For higher elevations, the variability is less, so the corresponding starting elevations are modulo 0.05 degree, due to the construction of the data set. The precision obtained here is not so critical though for the ray tracing process. Table 3.3 contains the elevation angles to ray-trace and this data set can be considered as optimal with respect to the processing power available and the data distribution.

3.4.3 Interpolation Error

To evaluate the error made in the interpolation based on a limited set of ray traced values (see previous section), a fine grid of values generated from the ray-tracing of 1741 elevations and from the ray-tracing of 20 elevations, as identified before, were compared. The fine grid is created for every 0.01 degree of outgoing elevation

by cubic spline interpolation (CSI), for 8 consecutive days centered on DoY 210 of 2005 (DoY 206 to 213 inclusive), 4 times a day, on 12 different azimuth, for 3 CGPS stations: ABER, HERS and IESG, that is more than 10 million values considered (less actually compared due to incomplete NWM data). This way, the impact on the CSI itself can be assessed. The second thing to determine is the minimum grid spacing needed to get an acceptable error on the linear interpolation made in between.

Table 3.4 gives the statistics of the differences between the corrections given by two different CSI: the first one is based on the full set of (1741) elevation angles whereas the second one is based on the optimal 20 elevations only. The statistics are given for the hydrostatic, wet and total mapping function corrections. Tables 3.5 and 3.6 give the equivalent range error for different elevation angles, assuming the maximum amplitude errors are committed at those angles.

Overall, to ray-trace only 20 elevations angles is very satisfactory and it is clear from Tables 3.4, 3.5 and 3.6 that it generates a regular grid which, at the sub millimetre level, is the same as that generated from 1741 elevation angles.

Table 3.4: Statistics of the difference between a regular grid of mapping function correction generated using cubic spline interpolation from data sets of 1741 points and 20 points. Interpolated values are compared every 0.01 degree of outgoing elevation with a sample of more than 10 million elevation angles considered.

Solution	Minimum	Maximum	Average	Standard deviation
HYD	-2.652e-04	2.425e-04	8.104e-08	1.316e-05
WET	-1.243e-02	8.203e-03	-1.085e-06	1.737e-04
TOT	-5.253e-04	9.238e-04	1.017e-07	2.355e-05

Table 3.5: Equivalent absolute range errors incurred when using a regular grid of mapping function correction generated using cubic spline interpolation form data sets of 1741 points and 20 points with an a priori zenith hydrostatic delay of 2.3 metres and zenith wet delay of 0.2 metre. The values given in millimetres and were computed with a sample of more than 10 million elevation angles.

Solution	Minimum	Maximum	Average	Standard deviation
HYD	-0.61	0.56	0.000	0.030
WET	-2.49	1.64	-0.000	0.035
TOT	-1.31	2.31	0.000	0.059

Table 3.6: Mapping function errors propagated on the range at selected elevation angles for CGPS station IESG on DoY 210 of 2005. Values given in millimetres.

Solution	El. angle	NMF value	Minimum	Maximum	Average	St. dev.
	3.0	14.605	-0.042	0.038	0.000	0.002
	5.0	10.116	-0.060	0.055	0.000	0.003
	7.0	7.642	-0.080	0.073	0.000	0.004
HYD	10.0	5.549	-0.110	0.101	0.000	0.005
	15.0	3.799	-0.161	0.147	0.000	0.008
	30.0	1.993	-0.306	0.280	0.000	0.015
	60.0	1.154	-0.528	0.483	0.000	0.026
	3.0	16.389	-0.152	0.100	-0.000	0.002
	5.0	10.742	-0.231	0.153	-0.000	0.003
	7.0	7.917	-0.314	0.207	-0.000	0.004
WET	10.0	5.656	-0.440	0.290	-0.000	0.006
	15.0	3.833	-0.649	0.428	-0.000	0.009
	30.0	1.996	-1.245	0.822	-0.000	0.017
	60.0	1.154	-2.153	1.421	-0.000	0.030

3.4.4 Linear Interpolation Error

To finally get the value of the mapping function, a linear interpolation is performed on a grid created using the CSI on the set of ray traced elevation angles. The grid is an augmentation of the set of values obtained by ray-tracing and is regular in terms of outgoing elevation angles. Now that the number of elevation angles to ray trace is determined, the spacing of the regular grid needs to be determined as well in order to keep the linear interpolation error acceptable.

A very thin grid could be created. However, the OMF is implemented so that every time a mapping function has to be computed, the modified BSW50 reads the corresponding thin grid files (two of them because of the linear interpolation in time). Direct access (DA) files are used instead of looping over ASCII files for obvious reasons of time efficiency. Knowing the spacing of the grid to interpolate on and the azimuth spacing use in the ray tracing, the index of the records to be used can be computed and read directly from the file. However, the conversion from an ASCII file to a DA file is rather time consuming, so this step needed some optimization as well.

The strategy to determine how thin the augmented regular grid should be was based on using CSI to generate grids of different spacing. Then, assuming it should represent an average worse case scenario, considering three consecutive elevation angles, the value in between the first one and third one is compared to the average value of the first one and the the third one. The comparison was made for elevation angles ranging from 3 to 90 degrees elevation. Table 3.7 summarizes the series of tests conducted and the results obtained.

Table 3.7: Statistics on the linear interpolation error with respect to the grid spacing used to interpolate the mapping function.

MF	Grid spacing [degree]	Sample size	Bias [-]	Std. dev. [-]	Min. [-]	Max. [-]
HYD	0.50	128712	-1.42e-05	8.16e-05	-1.69e-03	1.25e-03
	0.10	646536	-5.49e-07	3.58e-06	-8.47e-05	8.86e-05
	0.05	1293816	-1.37e-07	9.00e-07	-2.22e-05	2.32e-05
WET	0.50	128712	1.64e-05	3.22e-03	-1.17e-01	1.31e-01
	0.10	646536	8.35e-07	1.44e-04	-5.93e-03	7.71e-03
	0.05	1293816	2.07e-07	3.63e-05	-1.56e-03	2.03e-03
TOT	0.50	128712	-9.64e-05	5.23e-04	-1.19e-02	5.44e-03
	0.10	646536	-4.12e-06	2.28e-05	-6.41e-04	3.47e-04
	0.05	1293816	-1.03e-06	5.73e-06	-1.68e-04	9.13e-05

For clarity, Table 3.7 is translated into a range equivalent error assuming ZHD of 2300 mm, a ZWD of 200 mm and ZTD of 2500 mm and presented in Table 3.8. From here it can be seen that to keep the error at the sub millimetre level in all situations, a grid of 0.05 degree is necessary. Overall, the error shall be considered as non significant with such a grid.

Table 3.8: Statistics on the equivalent range error of the linear interpolation error with respect to the grid spacing used to interpolate the mapping function.

MF	Grid spacing [degree]	Sample size	Bias [mm]	Std. dev. [mm]	Min. [mm]	Max. [mm]
HYD	0.50	128712	-3.26e-02	1.88e-01	-3.89e+00	2.87e+00
	0.10	646536	-1.26e-03	8.24e-03	-1.95e-01	2.04e-01
	0.05	1293816	-3.16e-04	2.07e-03	-5.10e-02	5.33e-02
WET	0.50	128712	3.28e-03	6.45e-01	-2.34e+01	2.61e+01
	0.10	646536	1.67e-04	2.88e-02	-1.19e+00	1.54e+00
	0.05	1293816	4.14e-05	7.26e-03	-3.11e-01	4.05e-01
TOT	0.50	128712	-2.41e-01	1.31e+00	-2.97e+01	1.36e+01
	0.10	646536	-1.03e-02	5.69e-02	-1.60e+00	8.68e-01
	0.05	1293816	-2.56e-03	1.43e-02	-4.21e-01	2.28e-01

3.5 Cubic Spline Interpolation Versus Marini's Model

The model proposed by Marini [1972] was developed to describe the variation of the mapping function with respect to the elevation angle for a given vertical atmospheric profile at a station (atmosphere assumed to be horizontally stratified). Agreement with ray traced standard atmosphere was found to be below 0.3% at elevations down to 1 degree. Using a three dimensional ray tracing algorithm (as per the one used to derive the OMF), the conditions for which this model was derived may not be valid anymore. The meteorological information doesn't come solely from the vertical direction at the station but instead is read along the path. Furthermore, the restrictions of the model became clear when trying to fit it to three dimensional ray traced sets of mapping function values on specific azimuths, particulary for the wet part, as the least squares fitting appeared impossible or of inacceptable quality. The CSI was, therefore, adopted in place of the inadequate Marini's model but in doing this what is needed, is a comparison of the two, to decide which one out performs the other.

To compare the two approaches the case of an hypothetical azimuthally symmetric atmosphere was considered. Based on the 20 elevation angles ray traced, Marini's model (in the form proposed by Herring [1992]) was fitted with a set of three coefficients and a CSI was then performed to generate a comparing regular grid of 0.2 degree outgoing elevation angle spacing. The two mapping functions were compared between 3 and 90 degrees elevation. For each elevation and each epoch (limited in the case by the numerical weather model data availability) the differences were computed as CSI minus fitted Marini. On each elevation, the corresponding average and associated standard deviation were then computed (for

about 1100 samples). The results are plotted on Figure 3.14 for one year of data for the wet, hydrostatic and total mapping functions (CGPS station IESG over the year 2005). The differences themselves do not tell us which approach is better than the other. To decide, the final residuals of the least squares adjustment are also examined. Note that the comparison is not perfect as the least squares residuals are computed over the outgoing elevation angle, which is obviously not constant for a fixed starting elevation angle; the spread of the outgoing elevation angles depending on the variability of the meteorological conditions over the year. By grouping the residuals on outgoing elevation angles rounded at the first digit level this situation is overcome (e.g. all residuals for outgoing elevations angle $]\epsilon - 0.05,\epsilon + 0.05[$ are considered to compute statistics on ϵ). A couple of low elevation angles with respectively 1 and 9 samples (out of a total of 26334) were removed. Those 10 samples being probably due to extreme conditions leading to a refraction greater than 0.05 degree and the size of the samples on those two elevations being far too small to be of any significance.

From the results, two important points can be made:

1. The difference, in terms of equivalent range delays, is, for each case, always below 1 mm.

2. The difference seen between the fitted three coefficient Marini model and the CSI approach is completely explained by the least square residuals.

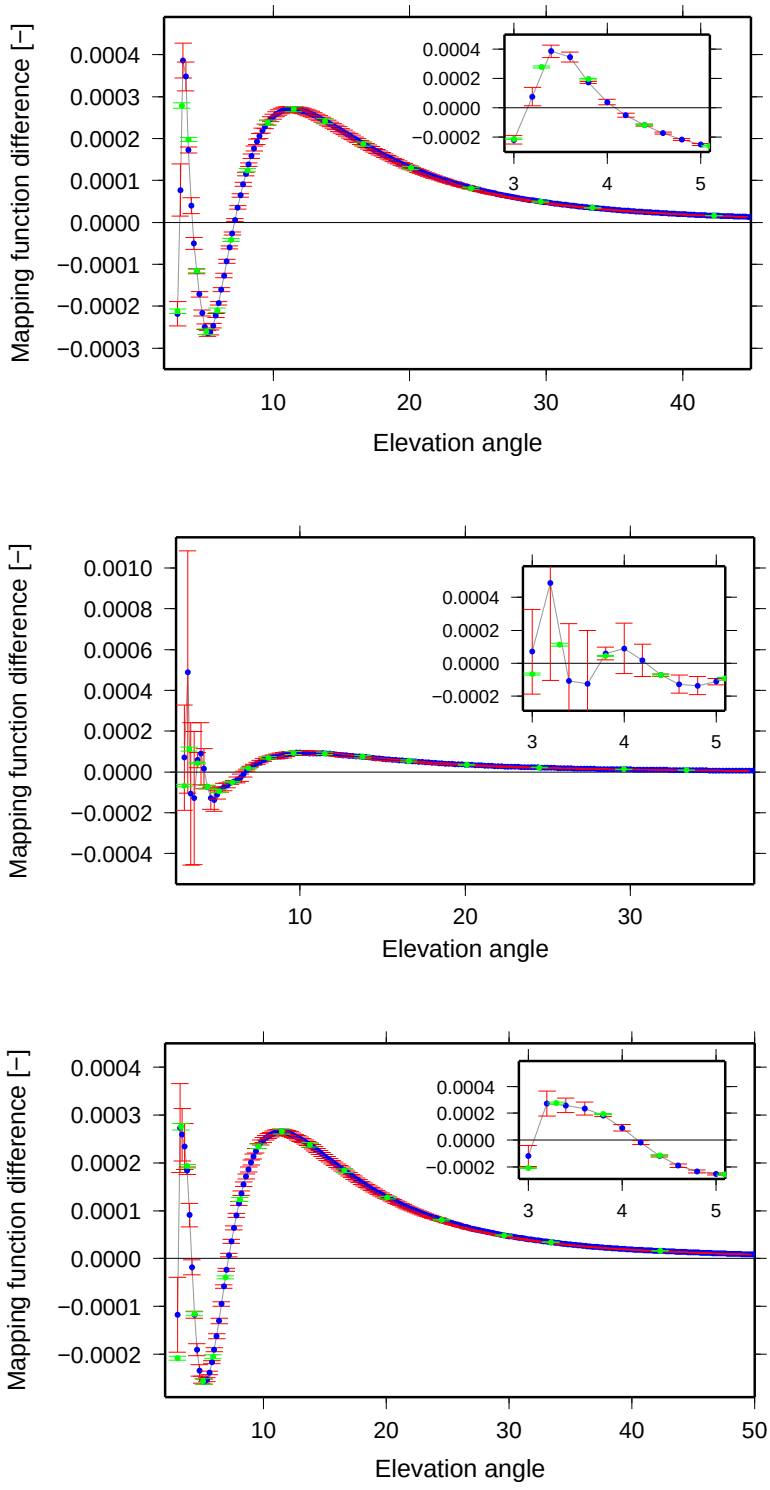

Figure 3.14: Hydrostatic (top), wet (middle) and total (bottom) mapping function differences computed between the fitted three coefficient Marini model and CSI, over a set of 20 ray traced mapping function values. Blue dots are the average difference computed every 0.2 degree with their associated error bars (1 sigma) whereas green dots are the average residual from the least squares adjustment.

3.6 Implementation of the OMF

The implementation of the OMF was done via "direct mapping", which is the determination of the mapping function value not by fitting a model to the ray traced values but by interpolating directly between the ray traced values, or an augmented set of ray traced values, as proposed in this work. Direct mapping was used because no suitable model was found to be able to fit for all azimuthal ray traced sets of mapping functions. The direct mapping implemented for this thesis is a very straightforward one, and simply uses linear interpolations both on the azimuth and the elevation angle, as exposed below.

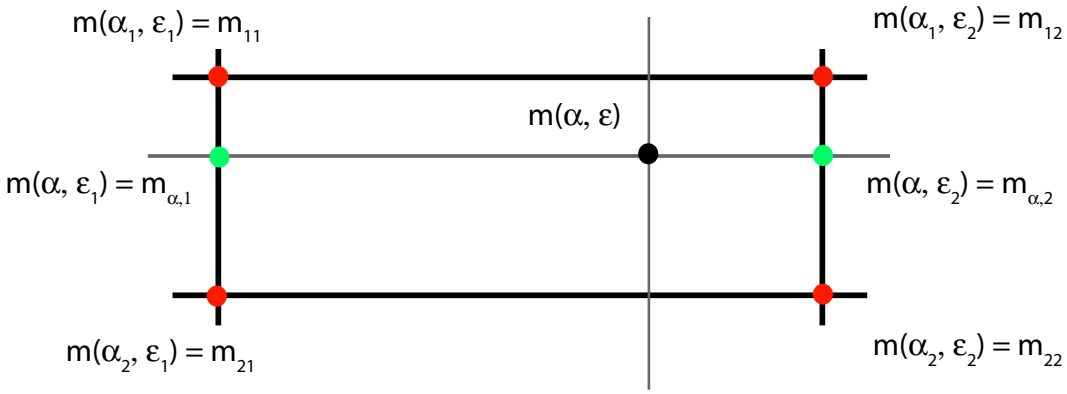

Figure 3.15: OMF bilinear interpolation scheme.

To compute the corresponding mapping function for an azimuth α lies between the ray traced azimuths α_1 and α_2 (with α_i for now taken every 30°, starting in the Northern direction) and that our elevation angle ε lies between the two ray traced elevation angles ε_1 and ε_2, the values of the mapping functions at those points are defined as follows: $m(\alpha_1, \varepsilon_1) = m_{11}$, $m(\alpha_1, \varepsilon_2) = m_{12}$, $m(\alpha_2, \varepsilon_1) = m_{21}$, and $m(\alpha_2, \varepsilon_2) = m_{22}$. The situation is depicted on Figure 3.15.

To determine $m(\alpha, \varepsilon)$ the values $m_{\alpha,1}$ and $m_{\alpha,2}$ are interpolated first, that is the

interpolated values at azimuth α and elevation angles ε_1 and ε_2:

$$m_{\alpha,1} = m_{11} + (m_{21} - m_{11}) * r_{az} \tag{3.34}$$

$$m_{\alpha,2} = m_{12} + (m_{22} - m_{12}) * r_{az} \tag{3.35}$$

where r_{az} and r_{el} are the azimuth and elevation ratios defined as:

$$\begin{aligned} r_{az} &= \frac{\alpha - \alpha_1}{\alpha_2 - \alpha_1} \\ r_{el} &= \frac{\varepsilon - \varepsilon_1}{\varepsilon_2 - \varepsilon_1} \end{aligned} \tag{3.36}$$

then, $m(\alpha, \varepsilon)$ is obtained:

$$m(\alpha, \varepsilon) = m_{\alpha,1} + (m_{\alpha,2} - m_{\alpha,1}) \cdot r_{el} \tag{3.37}$$

The derivatives with respect to the azimuth and the elevation angle are also computed (according to the implementation of the BSW50 (`$LG/NMFDRY.f` and `$LG/NMFWET.f`), the derivative with respect to the elevation angle $\frac{dm(\alpha,\varepsilon)}{d\varepsilon}$ is needed due to the magnitude of the term:

$$\frac{dm(\alpha, \varepsilon)}{d\varepsilon} = (m_{\alpha,2} - m_{\alpha,1}) \cdot \frac{dr_{el}}{d\varepsilon} = \frac{m_{\alpha,2} - m_{\alpha,1}}{\varepsilon_2 - \varepsilon_1} \tag{3.38}$$

3.7 Summary

In this chapter was described several important aspects of the derivation of the OMF mapping functions, symmetric and asymmetric. These are summarized below:

- A major aspect of the OMF is the way they are built: a NWM is ray traced in order to derive corrections to a 'base' mapping function, for efficiency,

instead of directly deriving the mapping functions themselves.

- The set of elevation angles to ray trace was carefully selected, based on real GPS data distribution over the UK, and as a tradeoff between computer resources and mapping function error.

- CSI was employed in place of the usually Marini model, and this new approach to interpolate the mapping function on the elevation angle was assessed.

- The UK Met Office Mesoscale Unified Model (MESO) was introduced, as the NWM used as input to the derivation of the OMF mapping functions.

- The steps for the three dimensional ray tracing algorithm developed were presented and its implementation described.

Chapter 4

Assessing the Meteorological Models

This chapter offers an assessment of the performance of the models used by the author in the ray-tracing of the numerical weather model to derive new mapping functions. High resolution radiosonde data are used as it represents a unique opportunity to compare real measurements over a vertical profile with ones obtained using models over standard data (NWM pressure levels). This way, the impact of each quantity on the determination of the refractivities and integrated delays, and the performance of the models used (and further ones tested for comparison) could be assessed.

4.1 Introduction

Chapter 2 introduced the models used to interpolate and extrapolate the meteorological data needed to compute the refractivities at integrating points from a finite set of values. Comparing vertical profiles augmented from the NWM pressure levels and those from high resolution (hiRes) radiosonde (RS) data (RS data sampled every 2 s of ascent) at a location reveals two/three obvious type of problems that will affect the comparison of the two:

- There is a discrepancy between the two data sources (e.g. they should give, for a given point, epoch and field, the same value, but don't).
- The choice of the model to represent the vertical variation of a meteorological state (P, T and U) is inadequate. Indeed, even if between two adjacent pressure levels where perfect agreement is exhibited between the two data sources (NWM and hiRes RS), the NWM interpolated values won't agree with the hiRes RS measured ones unless the model is able to fully represent the real behavior seen in the hiRes RS measured data.
- The third type of problem is a combination of the first two.

To investigate these points, hiRes RS data available at five different sites (see Figure 4.2) in the UK was used. Between adjacent pressure levels, the quality of interpolation models for meteorological states is studied: the hiRes RS data are compared to data interpolated from *standard* RS data (standard RS data is defined in here as RS data at standard NWM pressure levels). To this end, several models for the humidity (U) field were tested.

Figure 4.1 shows an example of a measured and interpolated profile for the water vapour partial pressure e and the absolute temperature T for RS site Albemarle on DoY 200 of 2005. The red profile is based on the hiRes measurements.

The blue and black profiles were interpolated from data at pressure levels similar to the ones supplied in the the UK mesoscale model. Those levels are represented by the horizontal gray lines. A perfect representation is obviously not expected, however, it is crucial to assess the general quality of the models to evaluate their impact on the ray traced tropospheric delays and furthermore, the derived mapping functions. The main point of this chapter is to figure out wether or not they introduce any bias in the solutions, and if so, to bring a quantification for those. First, a description of the data set used to this end is given in the following section.

4.2 Data Set Description

As said in the preamble, the hiRes RS data is a unique opportunity to test the behavior of the meteorological models used in this study. It was thereby assumed that the physics in the numerical weather model represents well enough the truth that the radiosondes are assumed to provide. To test that hypothesis is beyond the scope of this work. The hiRes RS data was from UK sites only as this was the only region covered by the NWM. Figure 4.2 shows the locations of the five hiRes RS sites available in the UK. They are operated by the UK Met Office and the data were obtained via the British Atmospheric Data Center (BADC, `http://badc.nerc.ac.uk/home/index.html`). Information about their location is summarized in Table 4.1[1]. To assess the performance of a model used in the ray tracing algorithm and to compare the NWM to RS in terms of meteorological data sources, exactly those coordinates were introduced in the ray tracing, so exact collocation is assumed. It was thereby assumed that exactly those coordinates were used in the NWM data assimilation scheme.

[1]The default resolution (2 decimal places for lat/long and nearest metre for height above mean sea level) of the coordinates is the one from the PC-CORA files. More precise coordinates are quoted when available from the WMO website.

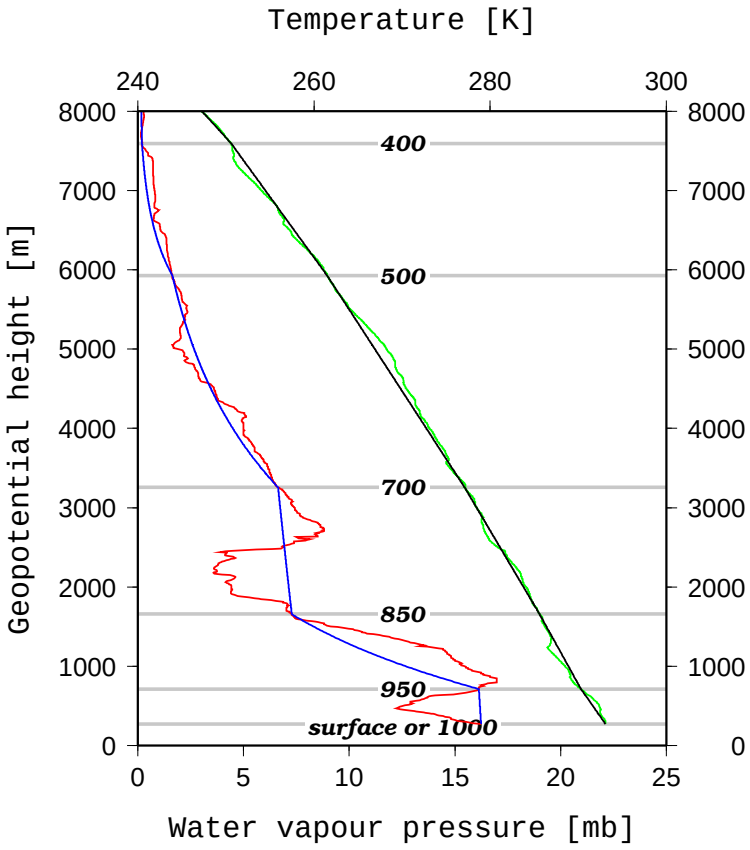

Figure 4.1: Example of measured versus interpolated profiles. Red line is the 'observed' water vapour partial pressure whereas the blue line is the interpolated water vapour pressure. The green and black lines respectively represent the observed and interpolated absolute temperature profiles. Data were taken from hiRes RS site Albemarle (UK) on July 10, 2005, at midnight. The labelled horizontal lines represent the equivalent NWM pressure levels. At those points, by construction, measured and modelled variables coincide.

To assess the meteorological models, only the regular profiles at 11 am and 11 pm are used, although sometimes those two profiles are completed with more launches to cover special events. At the time of writing, the data availability as provided on the BADC web site was not up to date, but it is included here for completeness. All data available from 2001 to 2007 (inclusive) were considered. Table 4.2 provides the main figures on the data availability detailed by site and month. Although only Lerwick and Watnall were available dur-

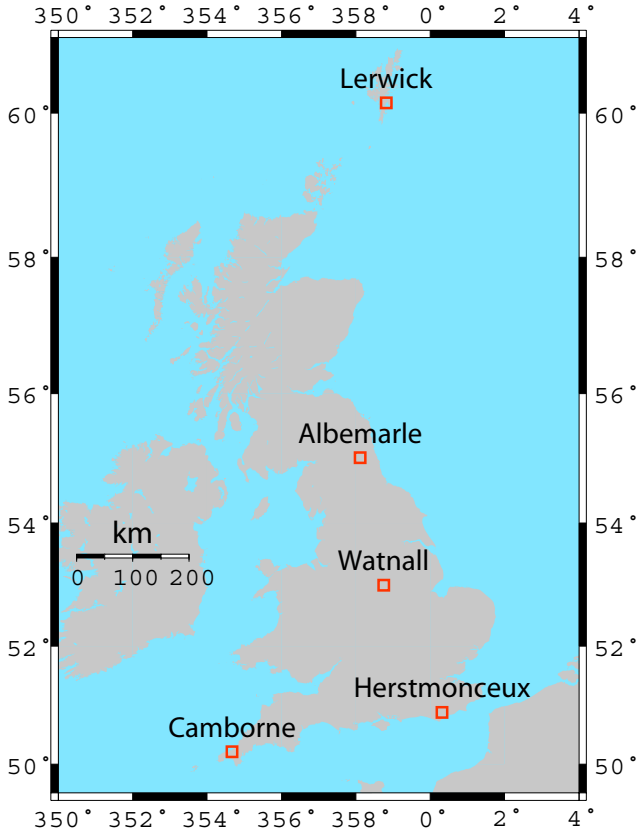

Figure 4.2: The five hiRes RS sites in the UK.

ing 2001, the data available were used. Generally speaking, the availability is very good. There are missing data but not enough to significantly affect the results presented here. The statistics given in Table 4.2 only consider launches that took place at either 1100 or 2300 UTC so the numbers might be different from the ones published on the BADC web site (http://badc.nerc.ac.uk/data/rad-highres/status.html) where every launch is accounted for. Since April 2002, all the RS sites appear to have launches twice a day only, whereas up to four launches were performed before that date (assuming all are available from BADC). As the statistics on the availability here are only given for hours 11 and 23 UTC of each days, there are approximatively 60 launches a month. This allowed the comparison to be consistent over the full period considered for the NWM ray tracing and GPS data processing. Table 4.3 provides statistics on

the accuracy and precision of the RS measurements. The raw data are in the PC-CORA format. For a full description of the format see Vaisala [1998] or visit `http://badc.nerc.ac.uk/data/rad-highres/pc-coradata.html` for general information. Only the information of the met variables involved in the present work are reproduced here in Table 4.3.

To represent the humidity, it had to be decided wether to interpolate directly on e computed from the relative humidity on each pressure layer, or on a more adequate meteorological quantity such as the relative humidity (RH) or the specific humidity (q) for example, and then convert the interpolated value to e, needed for the computation of the wet refractivity and density. The determination of the humidity field is of prime interest as it is known to be the most difficult to represent. So error in the modelling itself should be kept minimal. RS reports do not usually contain the measured RH but instead the derived dew point temperature T_{dew}. This could be due to the fact that T_{dew} is used in the production of tephigrams.

Table 4.1: Coordinates of the five hiRes RS sites in the UK.

Radiosonde site	ID	Latitude [deg]	Longitude [deg]	Orthometric height [m]	Geoid height [m]	Ellipsoid height [m]
Albemarle	albe	52.02	−1.88	141	50.574	191.574
Camborne	camb	50.218	−5.329	88	53.344	141.344
Herstmonceux	hers	50.89	0.319	54	45.052	99.052
Lerwick	lerw	60.139	−1.183	82	49.665	131.665
Watnall	watn	53.005	−1.250	117	49.201	166.201

Table 4.2: Monthly data availability for the five hiRes RS sites in the UK for the period January 2001 to March 2007 inclusive.

Year	Month	Potential number of profiles	Albermale Nb. of profiles	Albermale Avail. %	Camborne Nb. of profiles	Camborne Avail. %	Herstmonceux Nb. of profiles	Herstmonceux Avail. %	Lerwick Nb. of profiles	Lerwick Avail. %	Watnall Nb. of profiles	Watnall Avail. %
2001	jan	62	0	0	0	0	0	0	61	98	29	46
	feb	56	0	0	0	0	0	0	55	98	26	46
	mar	62	0	0	0	0	0	0	62	100	31	50
	apr	60	0	0	0	0	0	0	60	100	57	95
	may	62	0	0	0	0	0	0	62	100	58	93
	jun	60	0	0	0	0	0	0	58	96	57	95
	jul	62	0	0	0	0	0	0	61	98	58	93
	aug	62	0	0	0	0	0	0	62	100	61	98
	sep	60	0	0	0	0	0	0	60	100	49	81
	oct	62	0	0	0	0	0	0	62	100	58	93
	nov	60	0	0	0	0	0	0	60	100	56	93
	dec	62	0	0	1	1	1	1	62	100	60	96
2002	jan	62	0	0	62	100	61	98	62	100	61	98
	feb	56	0	0	56	100	51	91	56	100	55	98
	mar	62	48	77	60	96	51	82	59	95	57	91
	apr	60	2	3	59	98	58	96	60	100	56	93
	may	62	51	82	61	98	57	91	62	100	58	93
	jun	60	58	96	60	100	54	90	60	100	55	91
	jul	62	62	100	61	98	61	98	61	98	59	95
	aug	62	59	95	62	100	56	90	61	98	57	91
	sep	60	57	95	57	95	57	95	60	100	54	90
	oct	62	62	100	62	100	60	96	61	98	60	96
	nov	60	59	98	60	100	58	96	60	100	54	90
	dec	62	56	90	61	98	53	85	62	100	60	96
2003	jan	62	59	95	61	98	58	93	62	100	58	93
	feb	56	55	98	54	96	54	96	53	94	54	96
	mar	62	60	96	62	100	61	98	61	98	58	93
	apr	60	56	93	59	98	55	91	60	100	53	88
	may	62	58	93	61	98	59	95	62	100	60	96
	jun	60	60	100	57	95	54	90	60	100	56	93
	jul	62	62	100	62	100	58	93	62	100	61	98
	aug	62	61	98	62	100	55	88	62	100	59	95
	sep	60	60	100	60	100	55	91	59	98	57	95
	oct	62	60	96	61	98	61	98	62	100	59	95
	nov	60	55	91	59	98	58	96	60	100	54	90
	dec	62	61	98	61	98	55	88	61	98	58	93
2004	jan	62	50	80	60	96	56	90	62	100	59	95
	feb	58	55	94	57	98	54	93	54	93	57	98
	mar	62	59	95	62	100	53	85	60	96	60	96
	apr	60	56	93	56	93	55	91	59	98	58	96
	may	62	60	96	58	93	58	93	62	100	60	96
	jun	60	59	98	59	98	56	93	59	98	53	88
	jul	62	60	96	61	98	56	90	62	100	60	96
	aug	62	61	98	61	98	1	1	62	100	58	93
	sep	60	60	100	58	96	59	98	60	100	59	98
	oct	62	57	91	61	98	56	90	59	95	57	91
	nov	60	47	78	57	95	29	48	59	98	57	95
	dec	62	56	90	61	98	60	96	61	98	58	93
2005	jan	62	59	95	62	100	54	87	58	93	57	91
	feb	56	55	98	55	98	51	91	53	94	54	96
	mar	62	61	98	62	100	60	96	60	96	61	98
	apr	60	59	98	60	100	59	98	59	98	45	75
	may	62	61	98	60	96	56	90	62	100	27	43
	jun	60	58	96	59	98	56	93	57	95	52	86
	jul	62	58	93	60	96	59	95	60	96	59	95
	aug	62	60	96	62	100	47	75	55	88	61	98
	sep	60	57	95	58	96	48	80	59	98	60	100
	oct	62	55	88	61	98	56	90	60	96	57	91
	nov	60	53	88	59	98	56	93	59	98	55	91
	dec	62	57	91	62	100	61	98	62	100	59	95
2006	jan	62	56	90	61	98	44	70	60	96	59	95
	feb	56	54	96	46	82	50	89	55	98	47	83
	mar	62	61	98	58	93	51	82	59	95	62	100
	apr	60	51	85	58	96	54	90	59	98	55	91
	may	62	61	98	59	95	61	98	62	100	55	88
	jun	60	57	95	57	95	54	90	58	96	54	90
	jul	62	57	91	57	91	57	91	60	96	62	100
	aug	62	59	95	59	95	60	96	61	98	59	95
	sep	60	56	93	58	96	51	85	56	93	57	95
	oct	62	60	96	61	98	46	74	57	91	60	96
	nov	60	55	91	59	98	52	86	60	100	19	31
	dec	62	59	95	60	96	46	74	60	96	56	90
2007	jan	62	59	95	60	96	58	93	59	95	60	96
	feb	56	56	100	53	94	53	94	54	96	55	98
	mar	62	34	54	57	91	60	96	59	95	49	79
TOTAL		4562	3429	75	3735	81	3414	74	4475	98	4125	90

Fortunately, the binary data from the digicora equipment does contain the measured RH so allowed for a detailed comparison between raw measured RH values and the ones computed from the usually reported T and T_{dew} values. The following section (4.3) investigates the level of agreement between the measured and the reported (or computed or backed up) RH value, as this directly influences the wet and total refractivities determination.

Table 4.3: Published range of operation, resolution, accuracy and lag of RS meteorological measurements.

	Range of operation	Resolution	Accuracy	Lag
Pressure [hPa]	3.0 – 1060.0	0.1	0.5	-
Temperature [°C]	-90.0 – 60.0	0.1	0.2	< 2.5 s
Relative humidity [%]	0 – 100	1.0	2.0	< 1.0 s

4.3 On the Humidity Field in Radiosonde Reports

4.3.1 Problematic Overview

As mentioned earlier, RS reports do not usually contain the measured RH value, but instead, the measured T and the computed T_{dew}. As stated in Vedel et al. [2001], a precise conversion of (RH, T) to T_{dew} requires the precise knowledge on the $e_{sat}(T)$ function. This step is required to either compute e or q for example in order to derive the density of moist air and its refractive index. Furthermore, Vedel et al. [2001] indicate that the real e_{sat} is very complicated, that approximate formulae are often used in RS ground equipment, and that the approximate formula is likely to be site specific. Therefore, recovering the real, measured RH requires the knowledge of the e_{sat} used to compute the reported T_{dew}. However, this knowledge is not (always) available. Vedel et al. [2001] found a difference of

2.3 ± 1.0 mm in the ray-tracing of ZTD when using two different e_{sat} functions, a precise one from the HIRLAM model (Equation 2.29), and the one used in the Digicora equipment (Equation 2.28), as the most widespread equipment in Europe.

4.3.2 Impact of the water vapour saturation e_{sat} formula on the computed relative humidity

In this section, the magnitude of the difference between the measured relative humidity (RH_m) and one (RH_b), calculated from the reported T and T_{dew} using two different e_{sat} formulae, is quantified in order to estimate its impact on the determination of the refractivity N. To this end the following data set was created: the data from the five hiRes RS sites in the UK were used on (geopotential) height steps of 500 metres from ground up to about 17 km where the average measured relative humidity becomes lower than 5%. On each step were computed the mean and standard deviation of the difference. The calculated relative humidity was computed using the HIRLAM saturation water vapour pressure function and another one from Wexler (See Section 2.6.4).

The results are presented in Table 4.4 where it can be seen that there is a striking difference between the two formulae. Both formulae produce values of relative humidity generally inferior to the measured ones, however the Wexler formula produces a bias up to -3.1% whereas the HIRLAM formula limits the negative bias to -0.6%. The associated standard deviation is generally 2 to 3 times smaller in magnitude for HIRLAM than for Wexler. Also, the individual differences can, for Wexler, have an amplitude up to 6.3% when HIRLAM differences are all below 2.3%, which is within expectation. It also interesting to note that Wexler performs worse at lower altitudes contrary to HIRLAM.

To get a picture of the absolute impact, the relative humidity was converted to water vapour pressure, and a new table similar to Table 4.4 was produced and labelled as Table 4.5. Table 4.5 reveals that the choice of the formula to compute the saturation water vapour pressure is of great importance if one has to work with the water vapour pressure (or specific humidity). The absolute difference induced for example when choosing Wexler over HIRLAM is maximum between 1950 and 6250 metres height, with positive biases that would ultimately lead to overestimation of integrated values such as the wet delays.

Table 4.4: Statistics on the difference between measured relative humidity and relative humidity calculated from the reported RS dew point temperature, using the HIRLAM saturation water vapour pressure function and the Wexler one. Values given in [%].

Height	Sample	Average RH	Using HIRLAM e_{sat}				Using Wexler e_{sat}			
m	size	%	ave	std	min	max	ave	std	min	max
250	1101	77.1	0.0	0.4	-0.9	1.0	-0.1	0.5	-3.4	1.0
750	1534	78.2	0.0	0.4	-1.0	0.9	-0.3	0.8	-5.4	0.9
1250	1508	74.7	0.0	0.4	-1.0	1.0	-0.7	1.2	-6.2	1.0
1750	1535	66.7	0.0	0.4	-1.1	1.0	-1.4	1.7	-6.2	1.0
2250	1512	58.3	-0.0	0.4	-1.1	1.0	-2.0	1.8	-6.3	1.0
2750	1511	51.7	-0.0	0.4	-1.0	1.2	-2.5	1.8	-6.3	1.1
3250	1517	49.7	-0.0	0.3	-1.2	1.0	-2.9	1.7	-6.3	0.9
3750	1512	44.9	-0.1	0.3	-1.1	1.0	-3.0	1.5	-6.1	1.0
4250	1528	45.5	-0.1	0.3	-1.0	1.0	-3.2	1.4	-6.3	0.4
4750	1510	42.8	-0.1	0.3	-1.2	1.0	-3.2	1.3	-6.2	0.4
5250	1466	44.0	-0.1	0.4	-1.1	1.0	-3.1	1.2	-6.0	0.3
5750	1561	42.3	-0.1	0.4	-1.2	1.0	-3.0	1.0	-6.0	0.3
6250	1419	44.0	-0.2	0.4	-1.2	1.1	-3.0	1.0	-5.8	1.0
6750	1558	42.2	-0.2	0.4	-1.4	0.9	-3.0	0.9	-4.9	0.1
7250	1427	43.8	-0.2	0.4	-1.2	0.9	-3.0	0.8	-4.8	0.0
7750	1535	40.8	-0.3	0.4	-1.5	0.9	-3.1	0.8	-4.7	0.0
8250	1421	41.9	-0.3	0.4	-1.4	0.9	-3.1	0.7	-4.6	-0.3
8750	1500	39.5	-0.4	0.4	-1.4	0.7	-3.0	0.8	-4.5	-0.1
9250	1394	38.5	-0.4	0.4	-1.7	0.8	-3.0	0.8	-4.5	0.0
9750	1459	35.9	-0.5	0.4	-1.7	0.6	-2.9	0.9	-4.6	0.0
10250	1427	34.1	-0.5	0.4	-1.7	0.7	-2.8	0.9	-4.5	0.0
10750	1405	29.9	-0.6	0.4	-1.8	0.6	-2.6	1.1	-4.4	0.0
11250	1449	27.2	-0.6	0.4	-2.2	0.4	-2.5	1.1	-4.5	0.0
11750	1423	22.4	-0.6	0.5	-2.1	0.4	-2.3	1.2	-4.4	0.0
12250	1411	19.3	-0.6	0.5	-2.2	0.4	-2.1	1.2	-4.4	0.0
12750	1469	15.1	-0.5	0.5	-2.3	0.4	-1.8	1.2	-4.3	0.0
13250	1420	12.5	-0.4	0.5	-2.3	0.4	-1.6	1.2	-4.5	0.0
13750	1477	10.0	-0.4	0.4	-2.0	0.4	-1.4	1.1	-4.3	0.0
14250	1425	8.5	-0.4	0.4	-2.4	0.4	-1.3	1.1	-4.1	0.0
14750	1443	7.1	-0.3	0.4	-1.9	0.4	-1.2	1.0	-4.3	0.0
15250	1419	6.9	-0.4	0.4	-2.0	0.4	-1.1	1.0	-4.1	0.0
15750	1396	6.0	-0.3	0.4	-2.2	0.4	-1.0	0.9	-4.2	0.0
16250	1411	6.0	-0.3	0.4	-2.3	0.3	-1.0	0.9	-4.4	0.0
16750	1349	5.4	-0.3	0.4	-2.1	0.3	-0.9	0.9	-4.2	0.0
17250	1403	5.7	-0.3	0.4	-2.2	0.4	-0.9	0.9	-4.2	0.0
17750	1336	5.0	-0.3	0.4	-2.1	0.4	-0.9	0.8	-4.1	0.0

Table 4.5: Statistics on the absolute and relative difference between water vapour pressure computed using the HIRLAM saturation water vapour pressure function and the Wexler one. The last column indicates the effective sample size on which the average relative difference was computed as situations with zero humidity had to be removed. So numbers with an effective sample size much smaller than the original sample should be treated with care.

Height	Sample	Average RH	Average e	e difference (hPa)				Relative difference in e(%)		
(m)	size	(%)	(hPa)	ave	std	min	max	ave	std	sample
250	1101	77.1	8.83	0.01	0.02	-0.00	0.18	0.2	0.6	1101
750	1534	78.2	7.47	0.02	0.05	-0.00	0.26	1.1	4.3	1534
1250	1508	74.7	5.91	0.05	0.07	-0.00	0.26	2.8	6.9	1508
1750	1535	66.7	4.41	0.09	0.09	0.00	0.26	6.8	10.9	1535
2250	1512	58.3	3.24	0.13	0.09	0.00	0.26	11.3	13.5	1512
2750	1511	51.7	2.34	0.15	0.08	0.00	0.26	17.0	16.0	1511
3250	1517	49.7	1.80	0.16	0.07	0.00	0.26	20.3	15.7	1517
3750	1512	44.9	1.30	0.16	0.07	0.00	0.26	26.5	17.3	1512
4250	1528	45.5	1.01	0.16	0.07	0.01	0.26	29.2	16.3	1528
4750	1510	42.8	0.71	0.14	0.07	0.01	0.26	34.7	16.5	1510
5250	1466	44.0	0.55	0.13	0.07	0.00	0.26	37.8	16.2	1466
5750	1561	42.3	0.38	0.11	0.07	0.00	0.26	43.3	16.5	1561
6250	1419	44.0	0.29	0.10	0.06	0.00	0.26	46.8	16.4	1419
6750	1558	42.2	0.20	0.07	0.05	0.00	0.25	52.3	16.5	1558
7250	1427	43.8	0.14	0.06	0.04	0.00	0.21	56.3	16.5	1427
7750	1535	40.8	0.09	0.04	0.03	0.00	0.19	63.4	17.3	1535
8250	1421	41.9	0.06	0.03	0.03	0.00	0.15	68.0	19.0	1420
8750	1500	39.5	0.04	0.02	0.02	0.00	0.12	74.9	20.6	1500
9250	1394	38.5	0.03	0.02	0.01	0.00	0.09	79.6	21.3	1391
9750	1459	35.9	0.02	0.01	0.01	0.00	0.06	84.8	24.6	1448
10250	1427	34.1	0.01	0.01	0.01	0.00	0.05	89.0	29.9	1408
10750	1405	29.9	0.01	0.01	0.00	0.00	0.03	93.0	33.2	1349
11250	1449	27.2	0.00	0.00	0.00	0.00	0.02	98.1	39.1	1359
11750	1423	22.4	0.00	0.00	0.00	0.00	0.02	95.5	43.8	1267
12250	1411	19.3	0.00	0.00	0.00	0.00	0.02	98.1	47.7	1185
12750	1469	15.1	0.00	0.00	0.00	0.00	0.03	96.8	51.1	1135
13250	1420	12.5	0.00	0.00	0.00	0.00	0.02	90.9	56.2	1027
13750	1477	10.0	0.00	0.00	0.00	0.00	0.02	89.5	55.0	946
14250	1425	8.5	0.00	0.00	0.00	0.00	0.02	79.3	59.3	785
14750	1443	7.1	0.00	0.00	0.00	0.00	0.01	73.4	60.1	692
15250	1419	6.9	0.00	0.00	0.00	0.00	0.02	70.6	57.0	582
15750	1396	6.0	0.00	0.00	0.00	0.00	0.02	64.5	60.7	489
16250	1411	6.0	0.00	0.00	0.00	0.00	0.02	64.8	58.3	419
16750	1349	5.4	0.00	0.00	0.00	0.00	0.01	68.8	55.4	342
17250	1403	5.7	0.00	0.00	0.00	0.00	0.02	69.3	57.4	335
17750	1336	5.0	0.00	0.00	0.00	0.00	0.01	68.5	53.9	278

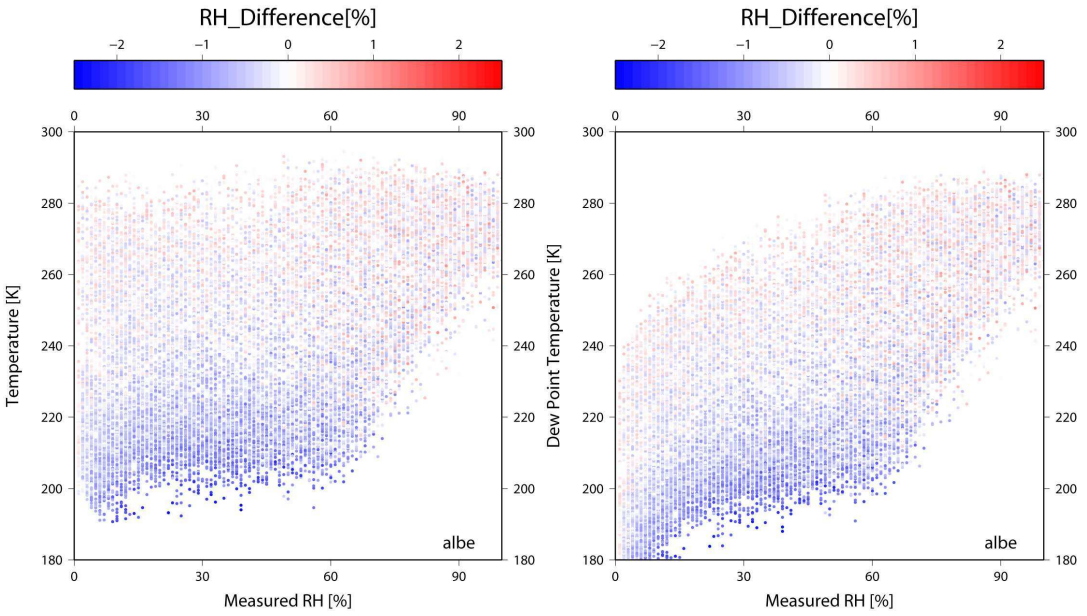

(a) RH difference on T

(b) RH difference on Tdew

Figure 4.3: Difference between the measured relative humidity and the relative humidity calculated from the measured absolute temperature T and the reported T_{dew} computed from T and RH using the Digicora formula.

Figure 4.3 shows the distribution of the error committed on the computed RH with respect to T or T_{dew} and the true (measured) RH when using the Digicora formula as observed on the data set described previously. There is a tendency for the error to be consistently (negatively) high for cold conditions, with no clear dependency on the relative humidity itself.

4.3.3 Identifying the e_{sat} formula for the UK hiRes RS Sites used in this study

The author was not able to obtain unambiguous information with respect to which e_{sat} formula(e) had been in use for the RS profiles used in this work. However, the binaries downloaded from BADC do contain the raw RH. Not only does this allow for a direct comparison between measured and computed RH, but this also makes room for testing the suitability of the most likely candidate e_{sat}

formula (the Digicora one) as the one effectively used at the RS sites which will later be the basis of a comparison between ray-traced profiles from RS and NWM.

Both the raw and edited humidity information is given as the measured RH with a precision of 1%. Having the usually reported T_{dew} and the measured RH available allowed for the reported T_{dew} to be compared to the one that can be derived from RH and T using the Digicora [Vaisala, 1998] formula. Figure 4.4 clearly shows that differences exist (apparent vertical lines are due to the precision of the values). There are two patterns, with generally higher differences at higher elevations, and differences varying between -3 and + 2 [K].

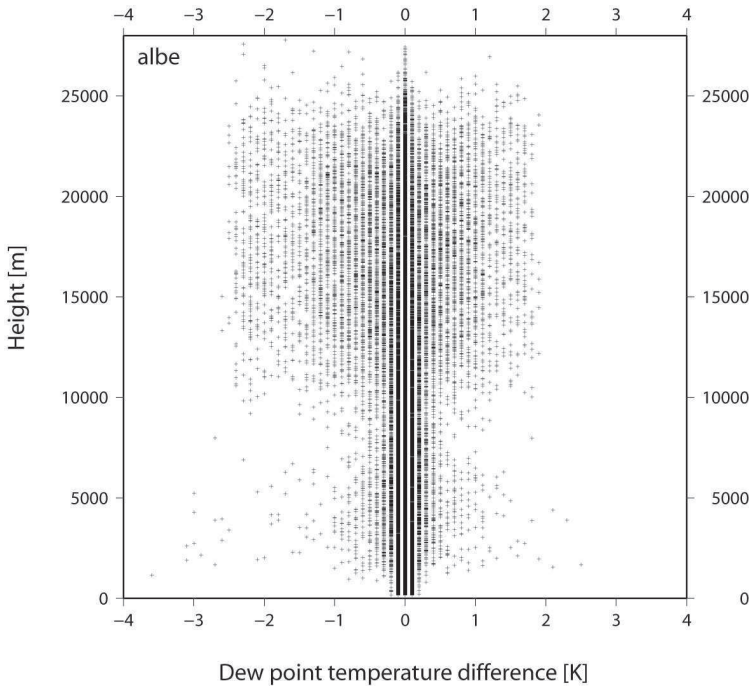

Figure 4.4: Difference with respect to geopotential height between T_{dew} as reported in the edited radiosonde reports and the one computed from the measured RH and T using the Digicora formula, for data available at hiRes RS site Albemarle for the time span 2001–2007 (see Table 4.2 for details on the availability). The original 2 s data was reduced to a regular sample of 0.5% (one measurement out of 200) to alleviate the plotting.

If indeed the Digicora formula was used, then the difference would lie in the way either one or both of the two measurements RH and T were used. An obvious candidate would be rounding effect i.e., that T_{dew} is not computed from the reported measurements with their published precision but with a higher one. To prove the point, the RH measurements (which have a 1% resolution) were biased by +0.5% and -0.5% before computing T_{dew}. The resulting differences are plotted with the plain red dots on the top left plot of Figure 4.5 whereas the observed differences are plotted as black crosses. As one can see, they form a nice envelope to the differences T_{dew} reported minus T_{dew} computed. However, there are still differences which lie outside of this envelope, which could be due to the combined effect of rounding made on the absolute temperature as well. The effect that rounding of T would have on the derived T_{dew} is presented on the top right plot of Figure 4.5 where is plotted the difference in the computed T_{dew} when the measured absolute temperature T of precision 0.1 K is biased by +0.05 and −0.05 K.

Eight different combinations of maximum biases on RH and T were then considered which are: {0.0, +0.05}, {0.0, −0.05}, {+0.5, +0.05}, {+0.5, 0.00}, {+0.5, −0.05}, {−0.5, +0.05}, {−0.5, 0.00} and {−0.5, −0.05}. The results are presented on the bottom plot of Figure 4.5. They make a strong case of whether the reported dew point temperature is indeed computed from relative humidity and absolute temperature measurements which are not rounded at the published precisions as all the observed differences are within the limits obtained with all maximum biases simulated. However, the Digicora documentation [Vaisala, 1998] does not give such information. The second, obvious, possible explanation for the observed differences between reported T_{dew} and the computed one, i.e. that a different formula than the Digicora is used, can be safely discarded based on the results presented above.

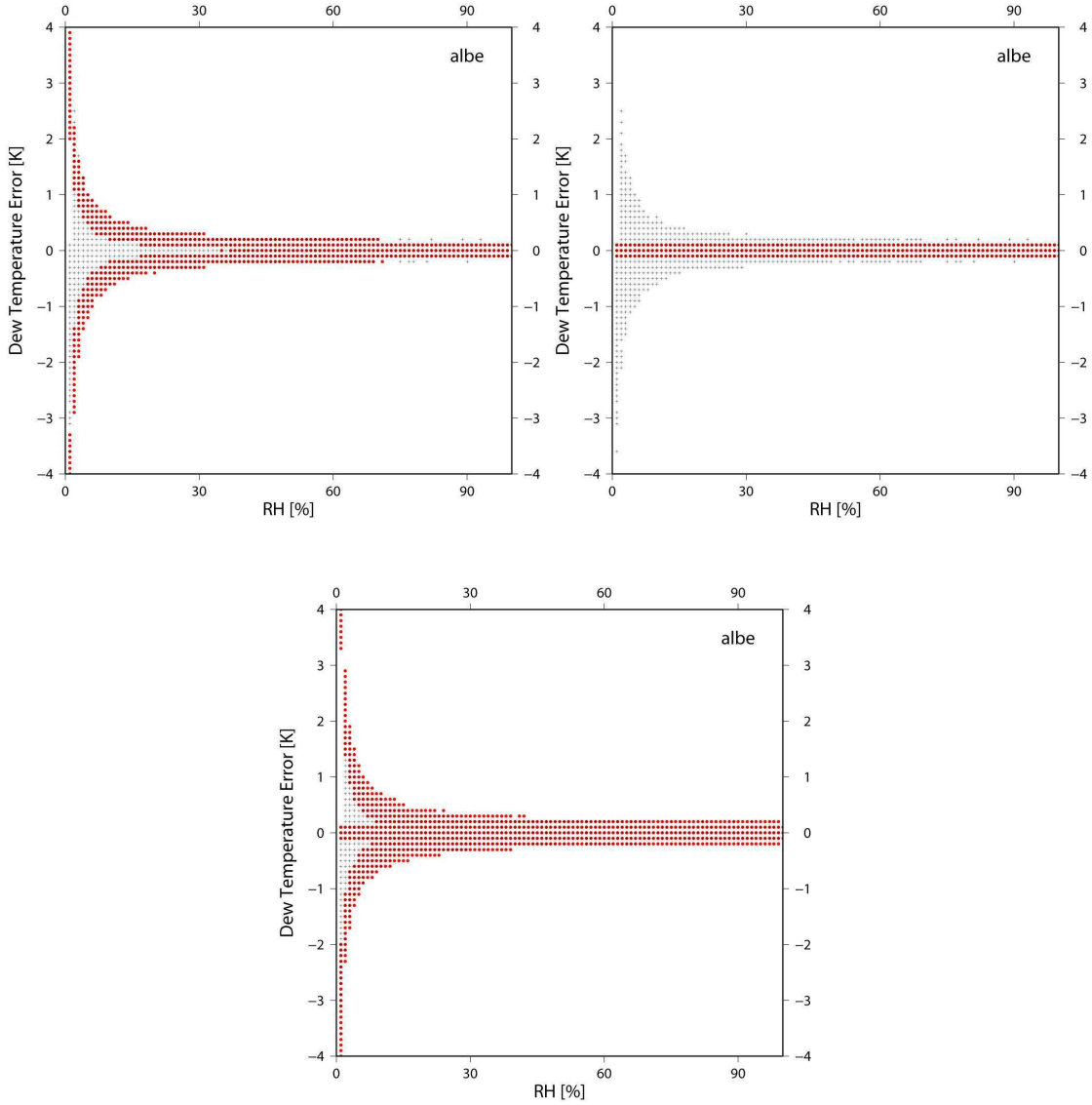

Figure 4.5: Effect of a ± 0.5% RH bias (top left), of a ± 0.05 K T bias (top right), and of a combined ± 0.5% RH and ± 0.05 K T bias (bottom) on the computed T_{dew}. Presented are the difference between T_{dew} as reported in the edited radiosonde reports and the one computed from the measured RH and T using the Digicora formula, for data available for hiRes RS site Albemarle for the time span 2001–2007. The original 2 s data were reduced to a regular sample of 0.5% (one measurement out of 200).

4.3.4 On the Humidity Field Formal Error in Radiosonde Reports

What is of interest to this study is the impact of P, T, and U on the computation of the the refractivities. In a first step is examined the influence of T and RH measurements on the determination of e that is needed to compute the refractivity. T and RH are measured by two different sensors and will be assumed to be uncorrelated. Having the direct measurements of the relative humidity would simplify the error propagation model as it avoids to introduce correlation with the T and T_{dew}. The question of whether the estimated one, if indeed based on more precise estimates of T and T_{dew} is more accurate and precise than the reported one can be asked. However, as it seems (e.g. [Vedel et al., 2001]) that usually the dew temperature instead of the measured, but yet not reported, relative humidity is available, the error propagation models were derived starting with the pair T, T_{dew} for the determination of the humidity field.

Following the notes of Vedel et al. [2001], the Digicora software computes T_{dew} from the RH and T measurements using the following relationship, an approximation of the more accurate water vapour saturation pressure e_{sat} expression:

$$T_{dew} = \frac{2 \cdot T \cdot K(RH,T)}{T \cdot \ln \frac{100}{RH} + 2 \cdot K(RH,T)} \tag{4.1}$$

where

$$K(RH,T) = 15 \cdot \ln \frac{100}{RH} - 2.0 \cdot (T - 273.15) + 2711.5 \tag{4.2}$$

F^T, the transition matrix, is built as:

$$F^T = [\frac{dT_{dew}}{dT}, \frac{dT_{dew}}{dRH}]; \tag{4.3}$$

with:

$$\frac{\partial}{\partial T}T_{dew} = \frac{2\left(15\ln\left(\frac{100}{H_p}\right) - 2T + 3257.80\right) - 4T}{T\ln\left(\frac{100}{H_p}\right) + 30\ln\left(\frac{100}{Hp}\right) - 4T + 6515.60} - \frac{2T\left(15\ln\left(\frac{100}{Hp}\right) - 2T + 3257.80\right)\left(\ln\left(\frac{100}{Hp}\right) - 4\right)}{\left(T\ln\left(\frac{100}{H_p}\right) + 30\ln\left(\frac{100}{Hp}\right) - 4T + 6515.60\right)^2}$$

$$\frac{\partial}{\partial RH}T_{dew} = -\frac{30T}{RH_{\%}\left(T\ln\left(\frac{100}{H_p}\right) + 30\ln\left(\frac{100}{Hp}\right) - 4T + 6515.60\right)} - \frac{2T\left(15\ln\left(\frac{100}{Hp}\right) - 2T + 3257.80\right)\left(-\frac{T+30}{RH_{\%}}\right)}{\left(T\ln\left(\frac{100}{H_p}\right) + 30\ln\left(\frac{100}{Hp}\right) - 4T + 6515.60\right)^2}$$

and the covariance matrix of the observables $C_{T,RH_{\%}}$ (the published accuracy of the relative humidity is 1-2%; it is assumed here that the formal error is 2% RH):

$$C_{T,RH_{\%}} = \begin{bmatrix} \sigma_T^2 & 0 \\ 0 & \sigma_{RH_{\%}}^2 \end{bmatrix} = \begin{bmatrix} 0.01 & 0 \\ 0 & 4 \end{bmatrix} \tag{4.4}$$

Figure 4.6 presents the variation of the propagated error on T_{dew} when computed from the Digicora approximate formulation of water vapour saturation pressure over a range of combinations of temperature and relative humidity. The propagated error, on the range of conditions presented here, varies between 0.26 and 2.91 K. Generally speaking, the dryer and the warmer the air is, the larger the error. It is important to note that this error is actually present in the T_{dew} provided in the radiosonde reports.

So, when using the reported T_{dew} to compute the relative humidity, that error should be accounted for. To avoid this issue, [Vedel et al., 2001] proposed to first undo what is done by Digicora, that is to use Eq. 4.5 to get back to the measured

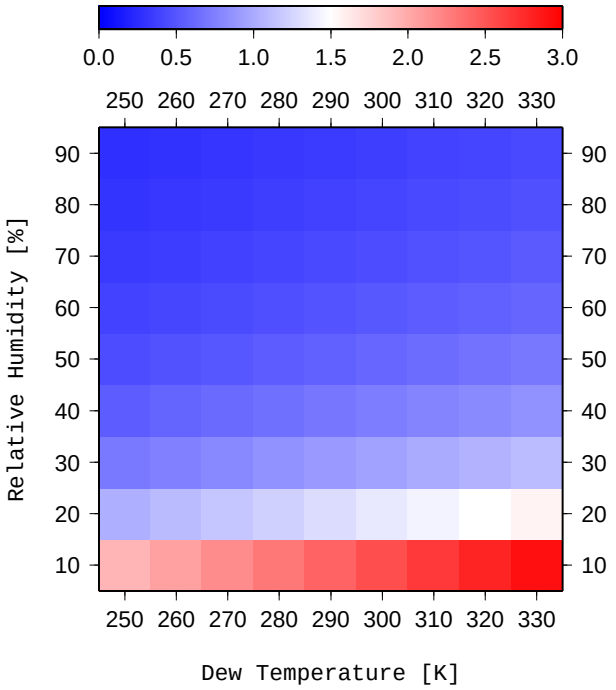

Figure 4.6: Error propagated on T_{dew} when calculated from the Digicora approximation formulation of T_{dew} as a function of T and RH. In the error propagation, formal errors of 0.1 K and 2% are assumed for T and RH respectively.

relative humidity. Note that the e_{sat} formulation is site specific, and furthermore, rounding effects cannot be ruled out.

The invert writes as follows:

$$\begin{aligned} RH(T, T_{dew}) &= \frac{100}{\exp\left(-\dfrac{-4\,T_{dew}\,T + 6515.6\,T_{dew} + 4\,T^2 - 6515.6\,T}{T_{dew}\,T + 30\,T_{dew} - 30\,T}\right)} \\ &= \frac{100}{\exp\left(-\dfrac{f_1}{f_2}\right)} \end{aligned} \tag{4.5}$$

where f_1 and f_2 are defined as:

$$\begin{aligned} f_1 &= -4\,T_{dew}\,T + 6515.6\,T_{dew} + 4\,T^2 - 6515.6\,T \\ f_2 &= T_{dew}\,T + 30\,T_{dew} - 30\,T \end{aligned} \tag{4.6}$$

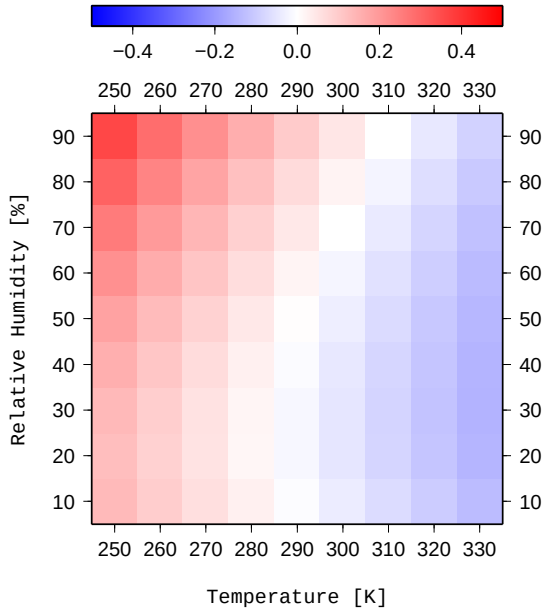

Figure 4.7: Difference between the formal error of the calculated relative humidity and the formal error of the original measurement of RH (taken here as 2%) given for a range of situations.

The partial derivatives of RH, with respect to T_{dew} and T_s can be written as:

$$\begin{aligned}
\frac{\partial RH}{\partial T_{dew}} &= -\left(\frac{4T - 6515.6}{f_2} + \frac{f_1(30+T)}{f_2^2}\right) \times RH(T, T_{dew}) \\
\frac{\partial RH}{\partial T} &= -\left(\frac{4T_{dew} - 8T + 6515.6}{f_2} + \frac{f_1(T_{dew}-30)}{f_2^2}\right) \times RH(T, T_{dew})
\end{aligned}$$

One thing that needs to be assessed is the 'cost' in term of accuracy of doing those two operations. Using a T_{dew} that contains the propagated error from the T and RH measurements, however, does not guarantee that the formal error of the calculated RH is the same as formal error of the measurement. To this end, the T_{dew} previously determined and associated error are used to recompute the RH error. The result is a formal error ranging between 1.9% and 2.4% compared to the original 2%. Figure 4.7 gives more details. Overall, it seems to be reasonable to take an overall error of 2% for whichever RH measurement is used.

4.3.5 Interpolated Versus Measured Atmospheric State Profiles

To assess the performance of each meteorological model over a profile and over time for P, T, RH and e, the integrals of the (natural) difference <model-measurements> and absolute (or positive) difference <|model-measurements|> were estimated. Ultimately, the integrated values of the refractivities (hydrostatic, wet and total) along a path are of interest to the GPS processing using either NWM ray-traced a priori zenith delay and/or mapping functions. However, the results presented here aim to help identify and understand the limitations and errors of such an approach.

An absolute measure of the difference was evaluated using the following integral:

$$A_{V,abs} = \int_{h_b}^{h_t} |V_{interpolated} - V_{measured}| \, \partial h \tag{4.7}$$

where h_b is the bottom height of the considered profile, that is, geopotential height at the surface or of the 1000 mb pressure level, h_t the geopotential height of the top level of the considered profile and V stands for one state variable (P, T, RH or e). The following expression of N, as an evaluation of A, can then be written as:

$$N_{V,abs} = \sum_{j=0}^{k-1} \frac{D_j + D_{j+1}}{2} \cdot \Delta h \tag{4.8}$$

where $D_j = |V_{interpolated_j} - V_{measured_j}|$, i.e. the difference between interpolated and measured data at (radiosonde measurement) height level j, which should provide a close approximation of A (which assumes continuous profiles) as the data is sampled every two seconds of ascension ($\approx$ every 10 m).

As a measure of the relative difference R expressed in %, is taken:

$$A_{V,abs,rel} = \frac{A_{V,abs}}{\int_{h_b}^{h_t} V_{measured}\,\partial h} \cdot 100 \tag{4.9}$$

which is approximated by M, given by:

$$M_{V,abs} = \frac{N_{V,abs}}{\sum_{j=0}^{k-1} \frac{V_{measured_j} + V_{measured_{j+1}}}{2} \cdot \Delta h} \tag{4.10}$$

For the natural differences, the quantities defined above for the absolute differences write as:

$$A_{V,nat} = \int_{h_b}^{h_t} (V_{interpolated} - V_{measured})\,\partial h \tag{4.11}$$

$$N_{V,nat} = \sum_{j=0}^{k-1} \frac{D_j + D_{j+1}}{2} \cdot \Delta h \tag{4.12}$$

where $D_j = (V_{interpolated_j} - V_{measured_j})$ and

$$A_{V,nat,rel} = \frac{A_{V,nat}}{\int_{h_b}^{h_t} V_{measured}\,\partial h} \cdot 100 \tag{4.13}$$

which is approximated by $M_{V,nat,rel}$, given by:

$$M_{V,nat,rel} = \frac{N_{V,nat}}{\sum_{j=0}^{k-1} \frac{V_{measured_j} + V_{measured_{j+1}}}{2} \cdot \Delta h} \tag{4.14}$$

Being interested in assessing the integrated performances of individual models in a first instance, it can be argued that it is more suitable not to employ the positive integral here, although the results will have to be treated with care as an integrated difference of zero will not necessarily imply a perfect match of the model to the data on each integration step of the evaluation of $A_{V,abs}$ and $A_{V,rel}$. A couple of sets of plots presented as Figures 4.8 and 4.9 show the deviations in

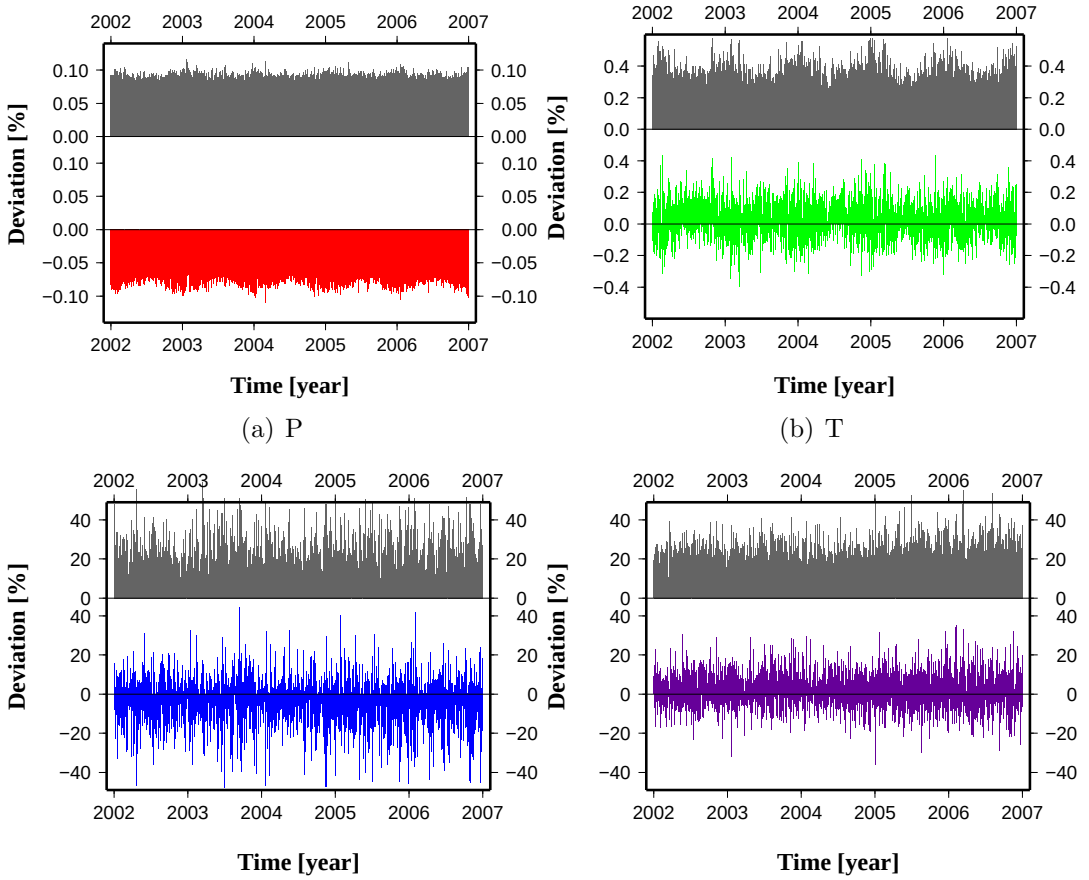

(a) P (b) T

(c) e (d) RH

Figure 4.8: Natural and positive relative deviations in % of the interpolated profiles compared to the measured profiles of P, T, e and RH for hiRes RS site Camborne.

% of the interpolated profiles compared to the measured ones for two RS sites, namely Camborne and Lerwick. As the deviations are computed over normalized integrals, the values obtained for the different state variables can be compared directly and therefore should allow us to decide which model performs best and which performs worst (regardless of their importance on the computed refractivity, at least for now). Biases and standard deviations of the differences for all stations are presented in Table 4.6 for the natural difference and Table 4.7 for the positive one.

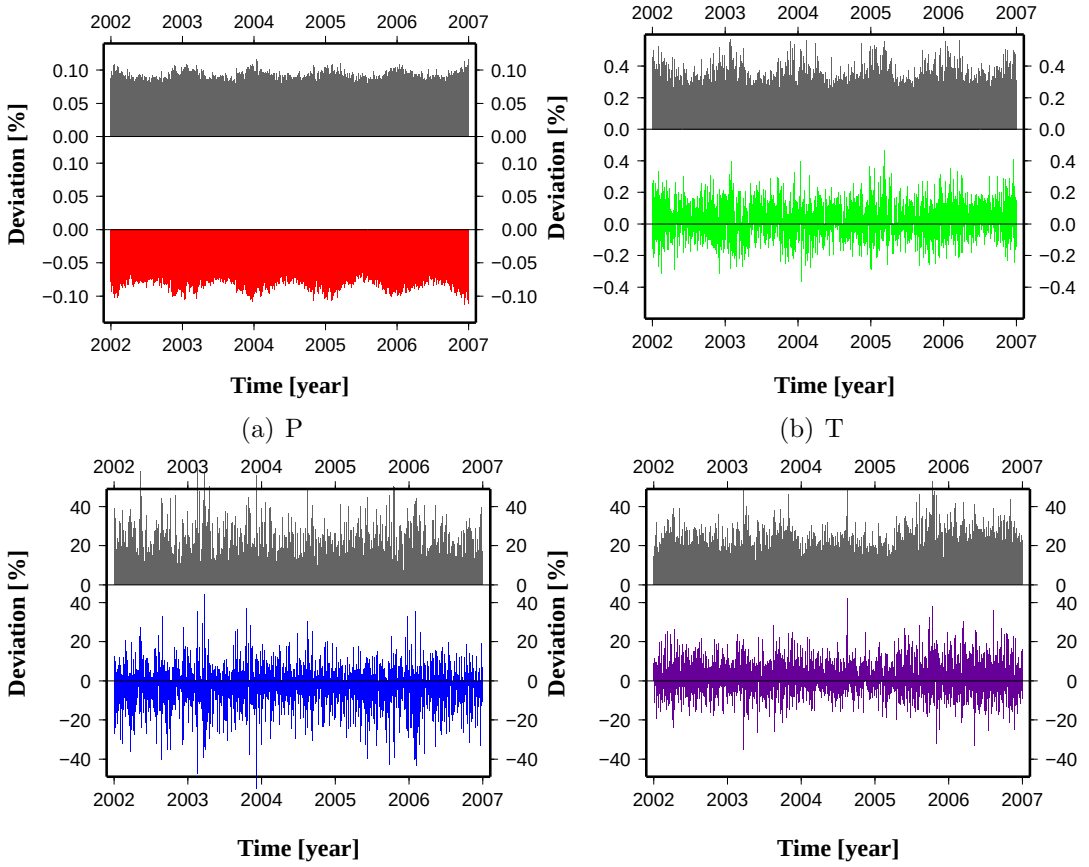

(a) P (b) T

(c) e (d) RH

Figure 4.9: Natural and positive relative deviations in % of the interpolated profiles compared to the measured profiles P, T, e and RH, for hiRes RS site Lerwick.

As can be seen, P exhibits a permanent negative deviation with a magnitude in the order of 0.08% and present an annual cycle with an amplitude of about 0.01% and a phase close to zero, that is, the model generally performs worse during winter. The fact that the *positive* deviation has an amplitude generally greater than the amplitude of the *natural* deviation implies that the model does not underestimate the measurement along all the profile but does on most of it, in a proportion that would approximated by the positive ratio of the natural deviation and the positive one.

The T model also exhibits a seasonal tendency in its performances with an

overestimation of T in summertime and and underestimation in wintertime, with relative deviation of up to $\pm 0.2\%$. Although from the natural deviation it could not be said that the model performs best in summer or winter; this is rather clear from the absolute relative difference that the models is better adapted to summer conditions than the ones founds in winter.

Time series for the natural relative values of RH don't indicate a clear seasonal tendency of the model's performance whereas the absolute ones do, indicating lower performance during summertime. However, high deviations are observed for the ideal profile, with values up to 20% for the natural deviation and up to 30% for the positive one.

The picture is harder to draw for e where high variations (both relative and absolute) appear to occur rather randomly during the year.

Table 4.6: Means and associated standard deviations for the *natural* deviations of the interpolated profiles compared to measured profiles of P, T, e and RH for all five hiRes RS sites. Values are given in %.

	Number of	P		T		e		RH	
Site	profiles	av.	std	av.	std	av.	std	av.	std
albe	3240	−0.076	0.0094	0.014	0.11	−3.4	9.0	1.5	7.4
camb	3540	−0.074	0.0092	0.026	0.11	−3.9	10.0	1.8	8.0
hers	3183	−0.075	0.0087	0.018	0.10	−3.3	9.8	1.8	7.7
lerw	3561	−0.076	0.0100	0.025	0.10	−3.0	8.9	1.3	7.5
watn	3316	−0.076	0.0090	0.021	0.11	−3.5	9.4	1.6	7.9

Table 4.7: Means and associated standard deviations for the *positive* deviations of the interpolated profiles compared to measured profiles of P, T, e and RH for all five hiRes RS sites. Values are given in %.

	Number of	P		T		e		RH	
Site	profiles	av.	std	av.	std	av.	std	av.	std
albe	3240	0.086	0.0075	0.30	0.073	14	8.5	16	7.1
camb	3540	0.086	0.0071	0.31	0.070	16	9.2	18	7.6
hers	3183	0.086	0.0073	0.30	0.067	15	8.8	17	6.9
lerw	3561	0.085	0.0081	0.29	0.067	13	8.5	16	7.3
watn	3316	0.086	0.0074	0.30	0.072	15	8.8	17	7.4

4.3.6 Models' impact in the total, hydrostatic and wet refractivities

Now is examined the impact of the models on the vertical profiles derived for the total (Figure 4.10), hydrostatic (Figure 4.11) and wet (Figure 4.12) refractivities, still evaluating the natural and positive relative deviation from the measured profile, taken as the true atmospheric states. The impact is assessed for all combinations possible by using either the measured data or the interpolated data, for all possible combinations between P, T and e. This way it is really possible to assess the impact onto the refractivity profiles of each model individually, or the combined effect of two of them or the three of them altogether.

Note: on all plots of Figures 4.10 to 4.12, a green circle means 'Model ON', and a red circle means 'Model OFF', that is, when the model was used instead of the measurements, a green circle is used, and a red one if the measured data were used to compute the refractivity studied.

Total refractivity

From Figure 4.10 it is obvious that the model used for P has the least impact on the computed total refractivity (N_{tot}), with induced positive deviation from the 'truth' of less than 0.1% (see also Figure 4.11). However, the bias is systematically negative, that is, the modelled refractivity appears to be always below its true value. Because of this systematic effect on N_{tot}, there is room for improvement on the model used for P.

The impact of T is 3–4 times greater than P, for the absolute impact. However, the model for T does not exhibit any systematic effect on N_{tot}. Furthermore, because the amplitude of the natural deviation is generally lower than the one of the absolute (or positive) one, it clearly indicates that a profile will most likely have pressure layers with overestimation and others with underestimation. The model for T can be thought as satisfactory as the mean of the natural deviation induced on N_{tot} does not show any significant bias.

The greatest impact on N_{tot} is undoubtedly coming from the modelling of e with deviation of up to 2% in summer times and lows of 0.5% in winter times, with a clear seasonal trend. Also, the imperfection of the model shows up in the systematic underestimation of N_{tot} where the seasonal signal is less pronounced but still present.

Hydrostatic refractivity

On top of comments made for the total refractivity, highlighted here is the real quasi independence of the determination of the hydrostatic refractivity N_{hyd} from e, which model as a maximum impact of 0.02% on the determination of N_{hyd}, which is far below the impact of the P and T models which have respective

positive impacts in the order of 0.1% and 0.25% in the determination of the N_{hyd} (and N_{tot}, see below).

Wet refractivity

With no surprise it is found that the error in the determination of N_{wet} stems from the model employed for humidity, in this case e, with a general systematic underestimation and a seasonal signal that indicates a less systematic error in summer times when humidity is generally greater.

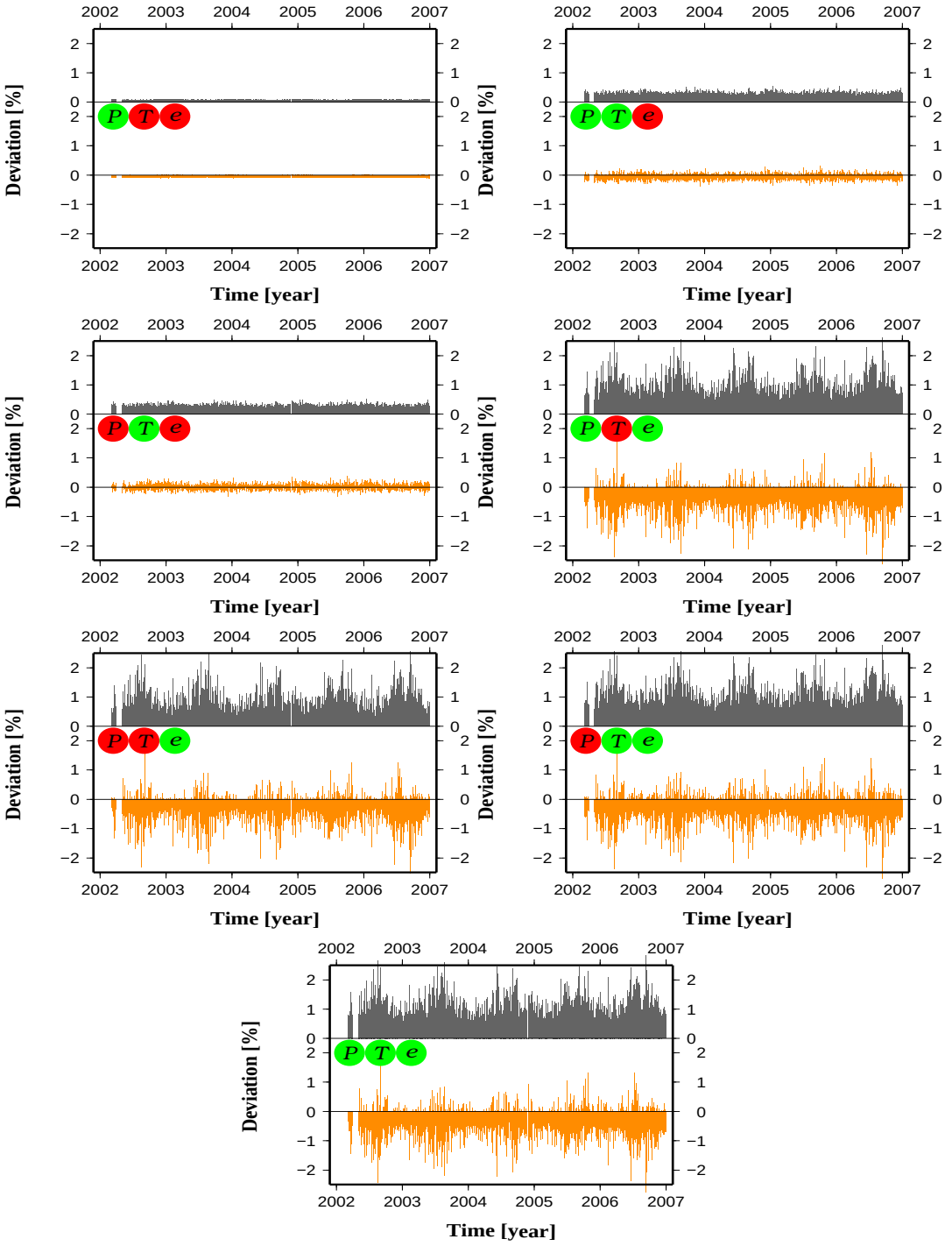

Figure 4.10: Impact of the meteorological models used on the determination of the total refractivity. The truth being the hiRes RS measured data. A green circle means 'Model ON', and a red circle means 'Model OFF', i.e. a green circle means when the model was used instead of the measurements, whereas a red circle means when the measured data were used to compute the refractivity studied.

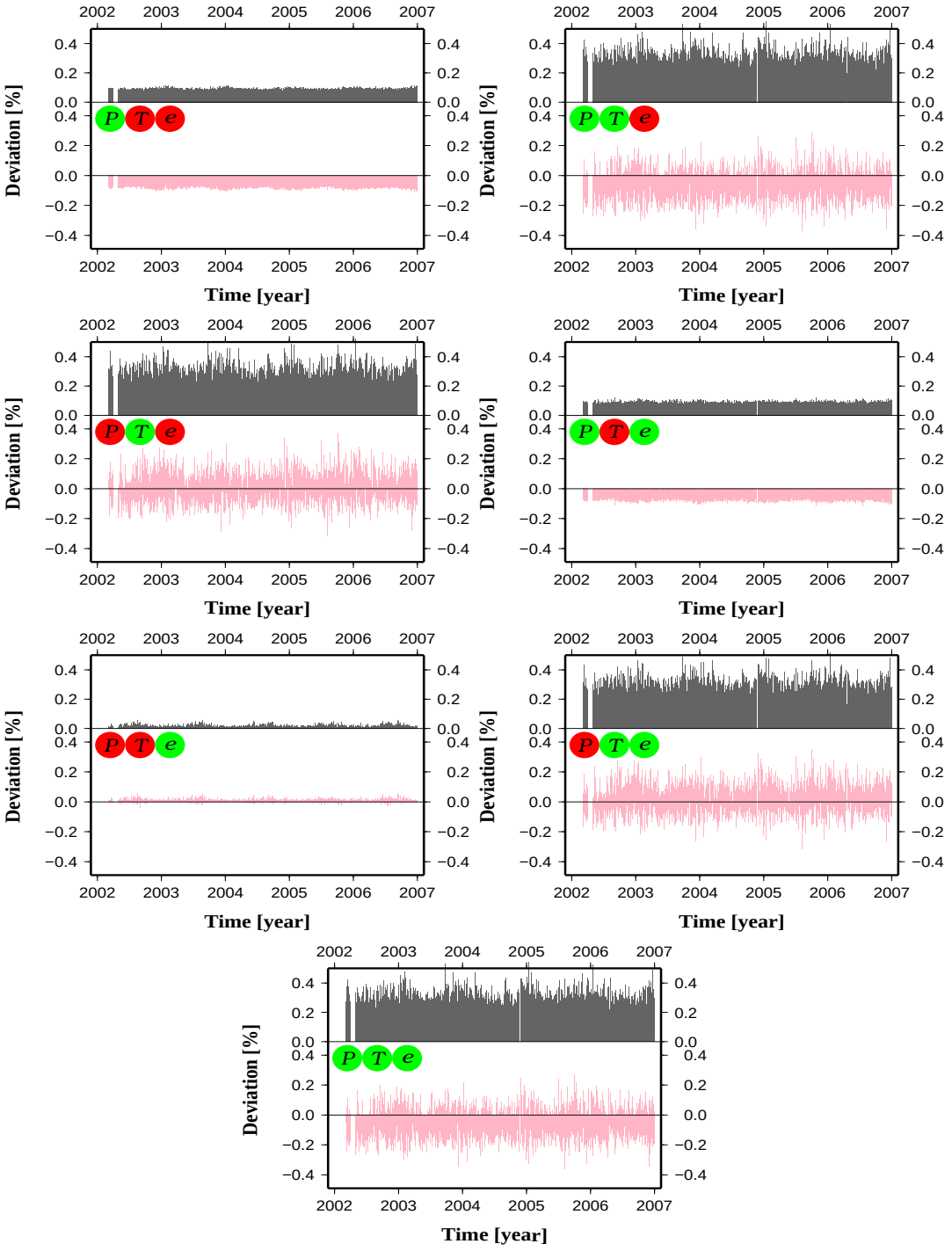

Figure 4.11: Impact of the meteorological models used on the determination of the hydrostatic refractivity. The truth being the hiRes RS measured data. A green circle means 'Model ON', and a red circle means 'Model OFF', i.e. a green circle means when the model was used instead of the measurements, whereas a red circle means when the measured data were used to compute the refractivity studied.

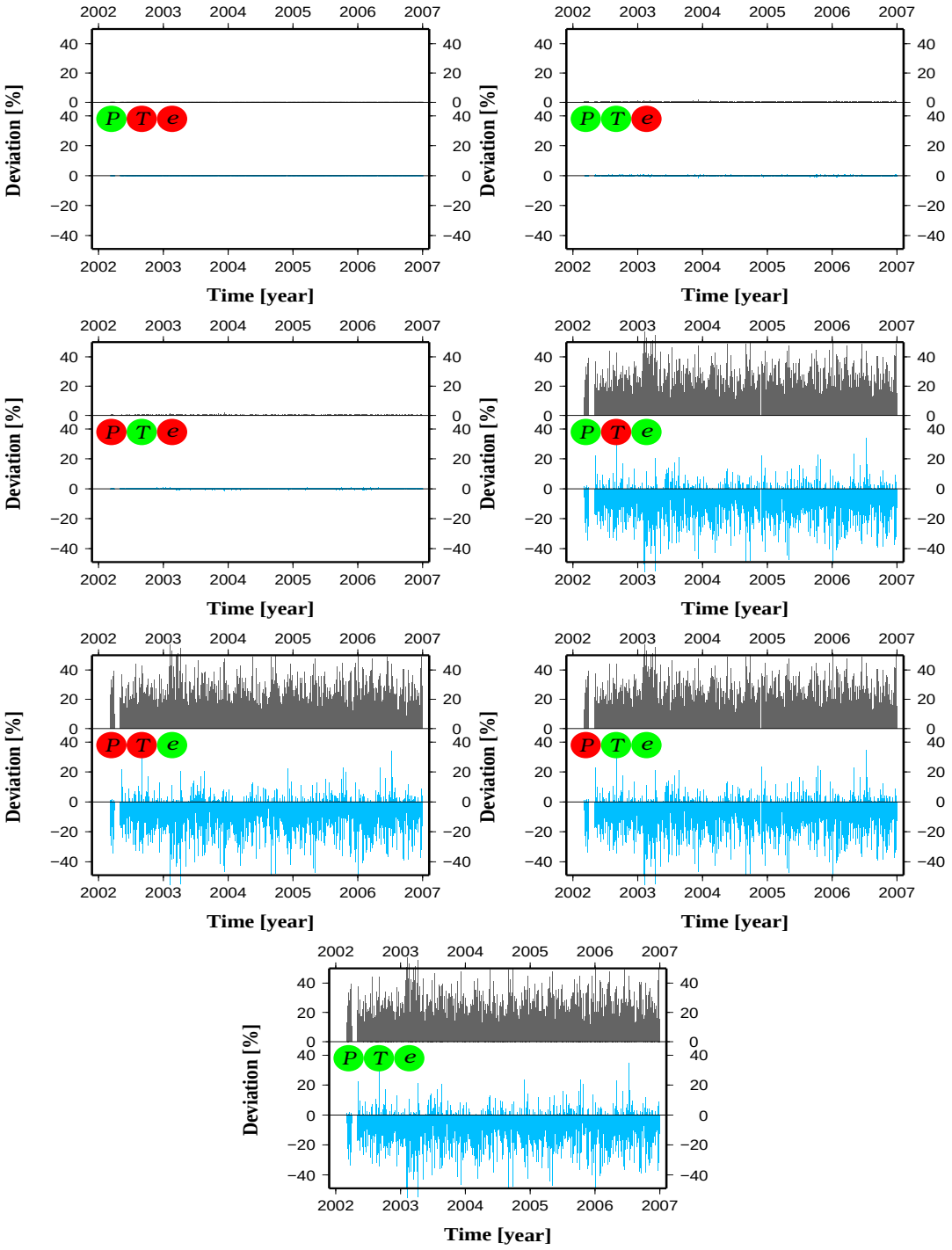

Figure 4.12: Impact of the meteorological models used on the determination of the wet refractivity. The truth being the hiRes RS measured data. A green circle means 'Model ON', and a red circle means 'Model OFF', i.e. a green circle means when the model was used instead of the measurements, whereas a red circle means when the measured data were used to compute the refractivity studied.

4.4 Details on Pressure Layers

In this section is examined the performance of a model for the quantities needed to compute the refractivity, that is, P, T, and e but this time looking at what happens on each pressure layer (by pressure layer is meant the layer comprised between two successive pressure levels and again, strictly speaking, e is not a measured quantity but derived from other measurements). In the following subsections, are derived some useful numbers on the quality of the models on a pressure layer basis, which are used in an error propagation to assess the impact of the model's inaccuracy on the refractivity determination.

4.4.1 Strategy description

From the hiRes RS data is extracted the standard levels data (see Subsection 3.2.1). Between two consecutive pressure levels (or surface pressure and 1000 hPa) synthetic data were generated corresponding to the measured data. In this way, the model performance for meteorological variables can be directly assessed by forming the difference <synthetic-measured>. Biases and 1-sigma error were computed on a pressure layer basis, although the sample size on which they are estimated varies greatly between two layers, depending on the height spacing of the two pressure levels considered.

4.4.2 Illustration

In a first place is presented an illustration of the problem investigated below on Figures 4.13 and 4.14 with a snapshot of the vertical profiles of the differences in P, T, and e on height for RS site Albemarle taken at midday on the 15th of each month of year 2005 (or the closest day when the 15th was not available). These figures nicely illustrate the limitations of the modelling, as expected. Note that

the discussion here only focuses on the models themselves, and does not include the error between the NWM values of pressure level and the truth.

From Figures 4.13 and 4.14 it looks like there is a systematic underestimation of P at heights below 10 km with an error larger at the middle of each pressure layer and looking like hyperboles. The thickness of the line is due to the precision of the measured pressure of 0.1 mb. Above 10 km (roughly) the match between synthetic and measured pressure is much better although the effect of the model can still be seen.

Errors in the temperature can easily reach several K. However, contrary to the total pressure, no systematic bias can be observed and errors seem to appear with similar magnitude over the entire range of altitude.

The known high variability of e and its difficulty to be be properly modelled is nicely shown on those figures. Although e is not measured but derived from other measurements (T and RH), for clarity, the one computed every 2 s from real measurements is referred to as 'measured'. Errors in the computation of e induced from errors in the measurements themselves and formula approximations are therefore ignored. They were studied earlier on in this chapter. Absolute errors of several hPa are not rare and can lead to relative errors up to 80% at any height. On the positive side is the random aspect of the discrepancy between model and reality.

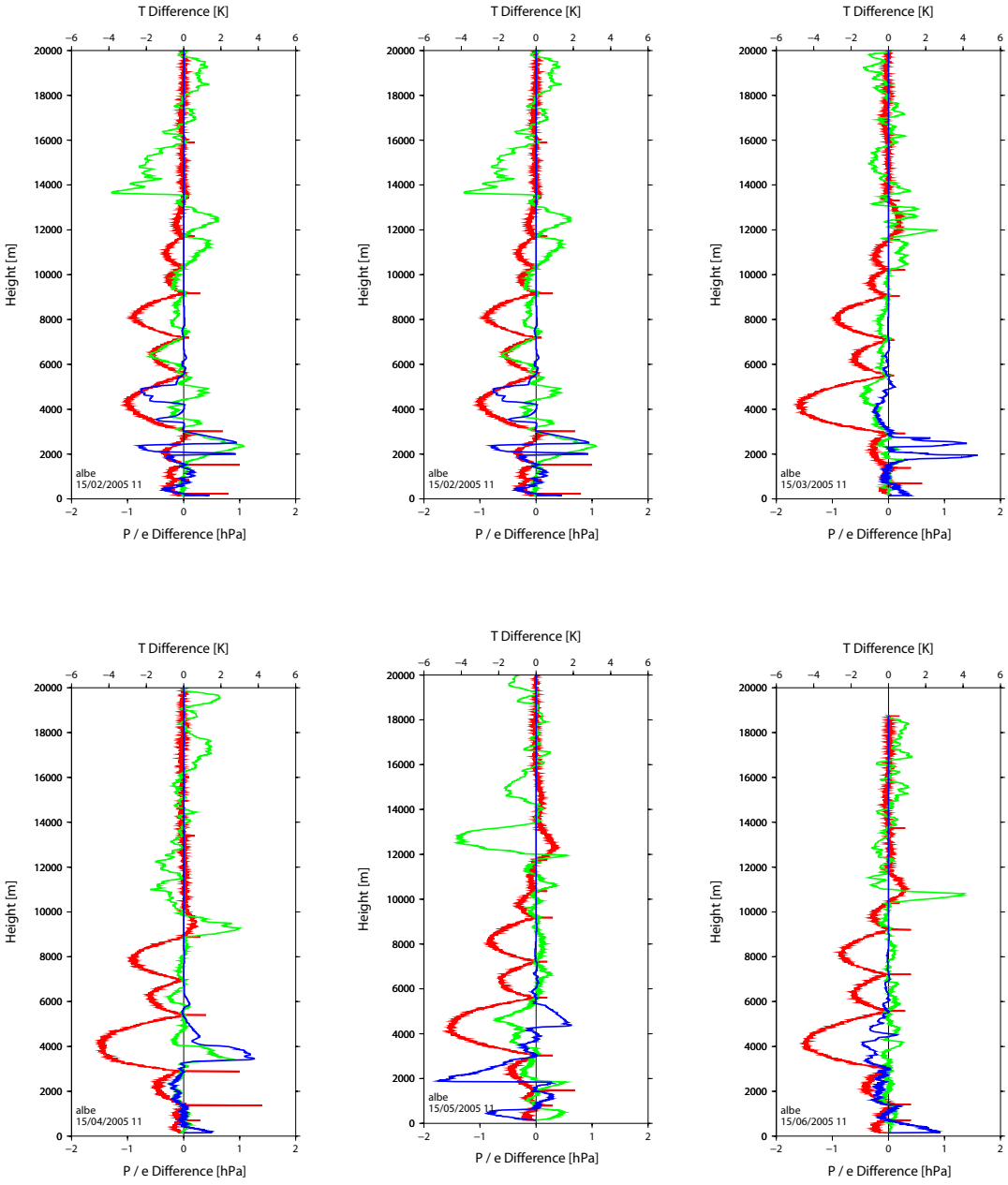

Figure 4.13: Difference between synthetic data generated using the models employed in the NWM ray-tracing and the hiRes RS data. In red: total pressure (P) difference in hPa; in green: absolute temperature (T) difference in K; and in blue: difference in the water vapour partial pressure (e) in hPa for hiRes RS site Albemarle at midday of each day closest of the 15th day of months January to June of year 2005.

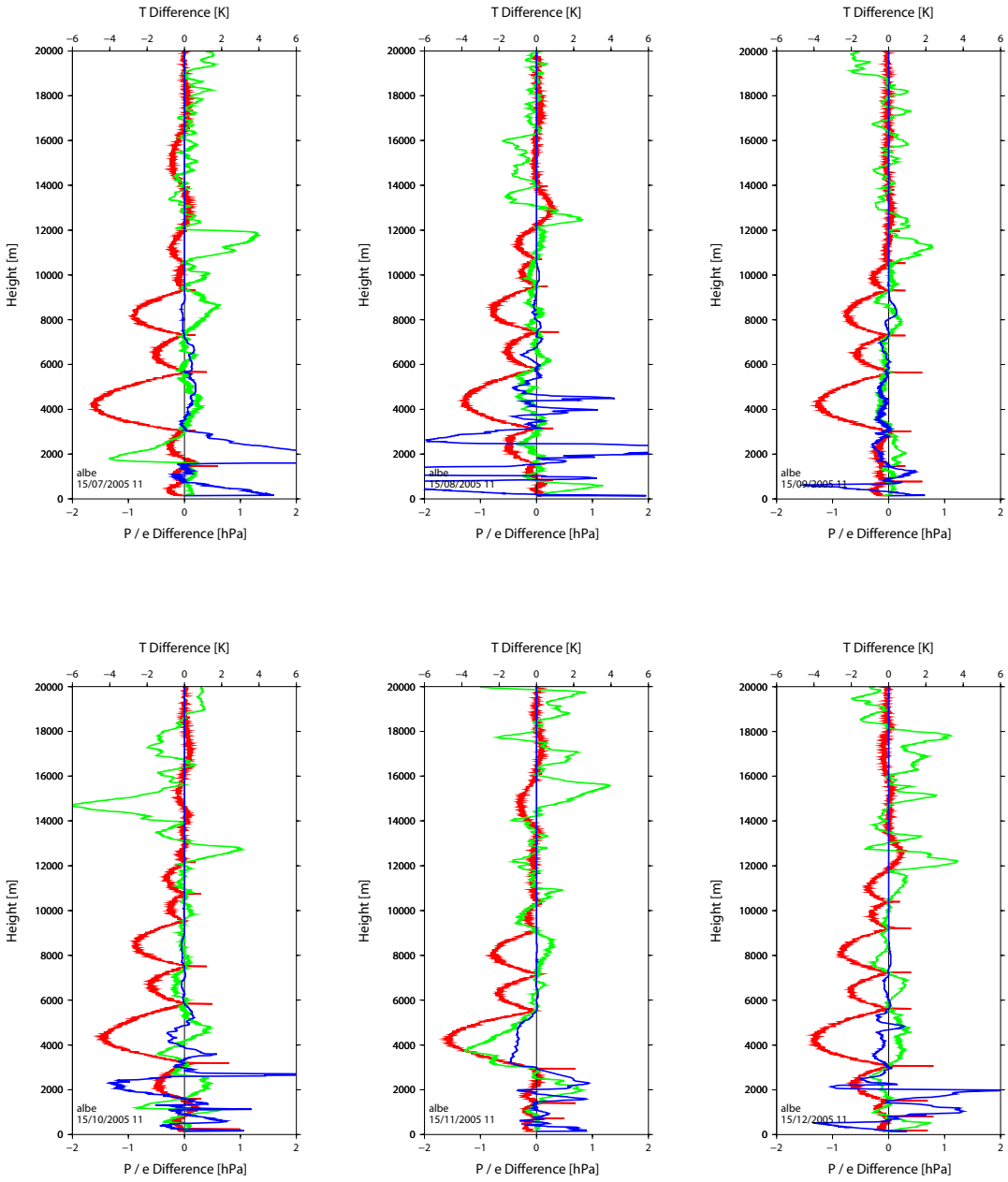

Figure 4.14: Difference between synthetic data generated using the models employed in the NWM ray-tracing and the hiRes RS data. In red: total pressure (P) difference in hPa; in green: absolute temperature (T) difference in K; and in blue: difference in the water vapour partial pressure (e) in hPa for hiRes RS site Albemarle at midday of each day closest of the 15th day of months July to December of year 2005.

4.4.3 Model performance on a pressure layer basis

An analysis of the performance of the models was conducted on a pressure layer basis, again, in the vertical direction only as no three dimensional real data are available. In a first approximation the ratio of the error of a corresponding slant delay (assuming an azimuthally symmetric atmosphere) to the zenithal error is given by the mapping function coefficient(s). Table 4.8 details the findings for each pressure layer, at 11 am and 11 pm, and this for each of the five hiRes RS sites. For day and night times, no major differences exist between the stations, and models perform equivalently during daytime and nighttime. It means that the numbers can be safely averaged over the full data set. Those numbers are presented in Table 4.9. Looking at the data with a 'uniform' distribution would discard the eventuality that the biases and spread of the difference is linked to the sampling they're computed on. As Table 4.10 shows, the average spacing between two consecutive levels varies between 383 and 5274 m, i.e., samples of 1 against 13.8 if vertical ascent with constant speed is assumed. However, samples are large enough to be considered as robust and the numbers representative.

Table 4.9 highlights the problem with the systematic total pressure underestimation at all pressure levels (except maybe 200 hPa, close to zero). The bias reaches greater than 1 hPa for the pressure layer 700–500 hPa which the thickest low level pressure layer, with a thickness of about 2566 m according to Table 4.10. However, plots in Figure 4.15 show that the model error is more correlated to the height at which the interpolation is performed than the thickness of the layer it was performed on, and that the underestimation of the total pressure is most at a bulk centered around a height of 5 km.

Looking at the left plot on Figure 4.16 reveals the broken line behavior of the error induced by the model, with a negative trend for the bias on the first three

Table 4.8: Details on model performance on a pressure layer basis as the average and standard deviation of the difference between synthetic data generated using the models employed in the NWM ray-tracing and the hiRes RS data: <synthetic-measured> for all five hiRes RS sites in the UK. The NWM data was interpolated to the RS measurement time.

Pressure layer (hPa) inf	sup	P error (hPa) av ± std	T error (K) av ± std	e error (hPa) av ± std	RH error (%) av ± std	P error (hPa) av ± std	T error (K) av ± std	e error (hPa) av ± std	RH error (%) av ± std	Sample size
ALBE		11 am				11 pm				
70	30	-0.00 0.04	0.06 1.03	0.00 0.00	-0.0 0.3	0.00 0.04	0.06 1.00	-0.00 0.00	0.0 0.3	568777
100	70	-0.01 0.05	0.05 1.06	0.00 0.00	0.0 0.3	-0.01 0.05	0.02 1.02	0.00 0.00	0.1 0.3	344277
150	100	-0.02 0.07	-0.03 1.13	0.00 0.00	0.6 1.3	-0.03 0.07	-0.04 1.14	0.00 0.00	0.8 1.6	410607
200	150	0.02 0.10	-0.10 1.44	0.00 0.00	0.7 3.1	0.02 0.10	-0.14 1.39	0.00 0.00	0.9 3.6	294504
250	200	-0.04 0.13	0.48 1.21	0.00 0.00	-0.3 3.7	-0.04 0.13	0.46 1.18	0.00 0.00	-0.3 4.1	225026
300	250	-0.12 0.11	0.23 0.66	0.00 0.00	-0.2 4.2	-0.12 0.11	0.24 0.65	0.00 0.00	-0.2 4.7	189030
400	300	-0.50 0.27	0.15 0.75	-0.00 0.03	-0.4 8.5	-0.50 0.27	0.16 0.83	0.00 0.03	-0.3 9.9	317771
500	400	-0.38 0.20	-0.06 0.50	-0.00 0.10	0.0 10.2	-0.39 0.19	-0.08 0.51	-0.00 0.10	0.0 10.9	263121
700	500	-1.02 0.51	-0.30 0.81	0.01 0.44	1.3 15.2	-1.02 0.51	-0.29 0.86	0.00 0.49	1.3 16.5	424430
850	700	-0.33 0.23	-0.18 0.99	0.09 0.93	1.8 16.0	-0.34 0.23	-0.14 1.00	0.10 0.91	1.6 15.7	258274
950	850	-0.08 0.10	0.11 0.69	-0.01 0.65	-0.9 8.6	-0.07 0.10	-0.03 0.66	-0.01 0.66	-0.2 8.5	154787
1000	950	-0.11 0.11	0.33 0.73	0.24 0.67	0.2 7.0	-0.06 0.10	-0.43 0.91	0.04 0.64	2.4 7.3	64512
CAMB		11 am				11 pm				
70	30	0.00 0.04	0.08 1.02	0.00 0.00	-0.0 0.3	0.01 0.04	0.09 1.01	0.00 0.00	0.0 0.2	906036
100	70	-0.00 0.05	0.05 0.97	0.00 0.00	0.1 0.4	-0.00 0.04	0.04 0.97	0.00 0.00	0.1 0.4	416044
150	100	-0.03 0.07	-0.08 1.10	0.00 0.00	0.8 1.5	-0.03 0.07	-0.06 1.11	0.00 0.00	0.9 1.9	481687
200	150	0.02 0.10	0.00 1.49	0.00 0.00	0.6 3.5	0.02 0.10	-0.04 1.45	0.00 0.00	0.7 4.4	327138
250	200	-0.07 0.13	0.53 1.11	0.00 0.00	-0.4 3.8	-0.07 0.13	0.52 1.10	0.00 0.00	-0.5 4.7	249210
300	250	-0.14 0.11	0.19 0.56	0.00 0.00	-0.1 4.4	-0.14 0.10	0.17 0.56	0.00 0.00	-0.1 5.3	212943
400	300	-0.52 0.26	0.07 0.64	-0.00 0.03	-0.2 9.2	-0.52 0.26	0.05 0.65	0.00 0.03	-0.1 10.3	350930
500	400	-0.38 0.19	-0.09 0.47	-0.00 0.11	0.1 10.6	-0.39 0.19	-0.09 0.49	-0.00 0.12	0.3 11.5	286064
700	500	-1.02 0.50	-0.30 0.81	0.01 0.49	1.2 15.6	-1.01 0.50	-0.29 0.82	0.01 0.55	1.3 16.9	460575
850	700	-0.32 0.22	-0.22 0.97	0.12 1.03	2.3 15.8	-0.32 0.22	-0.23 1.03	0.14 1.11	2.5 17.3	286421
950	850	-0.07 0.10	0.12 0.73	-0.01 0.88	-1.0 10.4	-0.07 0.10	0.03 0.74	0.02 0.89	-0.3 10.4	169178
1000	950	-0.10 0.10	0.26 0.60	0.01 0.74	-1.4 7.2	-0.09 0.10	-0.15 0.80	-0.01 0.88	0.5 8.8	77861
HERS		11 am				11 pm				
70	30	0.00 0.04	0.08 1.02	-0.00 0.00	-0.0 0.3	0.01 0.04	0.05 0.99	0.00 0.00	0.0 0.2	626970
100	70	-0.01 0.04	0.04 0.97	0.00 0.00	0.1 0.3	-0.01 0.04	0.03 0.97	0.00 0.00	0.1 0.3	348278
150	100	-0.03 0.07	-0.06 1.09	0.00 0.00	0.7 1.4	-0.03 0.07	-0.04 1.09	0.00 0.00	0.9 1.6	414004
200	150	0.03 0.10	-0.05 1.46	0.00 0.00	0.7 3.2	0.02 0.10	-0.09 1.44	0.00 0.00	0.9 3.9	298645
250	200	-0.06 0.13	0.52 1.13	0.00 0.00	-0.4 3.3	-0.06 0.13	0.53 1.12	0.00 0.00	-0.6 4.3	228818
300	250	-0.13 0.11	0.21 0.61	0.00 0.00	-0.2 4.2	-0.13 0.10	0.20 0.57	0.00 0.00	-0.2 4.7	193021
400	300	-0.52 0.26	0.07 0.63	-0.00 0.03	-0.3 8.9	-0.52 0.26	0.06 0.63	-0.00 0.03	-0.1 9.9	323705
500	400	-0.39 0.19	-0.09 0.48	-0.00 0.11	0.3 10.3	-0.39 0.20	-0.09 0.49	0.00 0.12	0.2 11.0	267319
700	500	-1.02 0.50	-0.30 0.79	0.02 0.49	1.9 15.8	-1.02 0.51	-0.29 0.83	0.02 0.52	1.5 16.4	425755
850	700	-0.33 0.22	-0.19 1.00	0.11 0.97	2.0 16.0	-0.33 0.23	-0.13 0.98	0.11 1.06	1.6 16.4	260147
950	850	-0.08 0.10	0.08 0.68	0.00 0.83	-0.7 9.7	-0.08 0.10	-0.00 0.63	0.01 0.80	-0.1 9.0	153647
1000	950	-0.11 0.10	0.28 0.62	-0.08 0.66	-2.1 6.8	-0.07 0.10	-0.33 0.88	0.05 0.82	1.4 8.3	71975
LERW		11 am				11 pm				
70	30	-0.01 0.04	0.08 0.90	-0.00 0.00	-0.0 0.3	-0.00 0.04	0.07 0.89	-0.00 0.00	0.0 0.2	1052990
100	70	-0.02 0.04	0.01 0.85	0.00 0.00	0.0 0.3	-0.02 0.04	0.02 0.82	0.00 0.00	0.1 0.3	495845
150	100	-0.03 0.07	-0.06 0.96	0.00 0.00	0.5 1.2	-0.03 0.07	-0.04 0.93	0.00 0.00	0.5 1.3	578936
200	150	0.02 0.09	-0.21 1.20	0.00 0.00	0.9 3.2	0.02 0.09	-0.22 1.19	0.00 0.00	1.0 3.7	400171
250	200	-0.01 0.12	0.39 1.25	0.00 0.00	-0.0 4.1	-0.01 0.12	0.36 1.19	0.00 0.00	-0.1 4.5	302877
300	250	-0.09 0.12	0.32 0.75	0.00 0.00	-0.3 4.4	-0.09 0.12	0.30 0.74	0.00 0.00	-0.3 4.8	253574
400	300	-0.48 0.27	0.22 0.82	0.00 0.02	-0.4 8.6	-0.48 0.27	0.25 0.84	0.00 0.02	-0.5 9.7	416657
500	400	-0.38 0.20	-0.05 0.48	-0.00 0.08	-0.1 10.1	-0.39 0.20	-0.05 0.49	-0.00 0.09	-0.1 11.3	337086
700	500	-1.03 0.51	-0.24 0.79	0.00 0.37	1.1 15.4	-1.02 0.51	-0.27 0.81	0.01 0.40	1.7 16.7	547904
850	700	-0.35 0.23	-0.14 0.88	0.04 0.74	1.3 15.5	-0.35 0.23	-0.14 0.89	0.06 0.80	1.8 16.7	336059
950	850	-0.08 0.10	0.06 0.64	0.01 0.59	-0.5 8.9	-0.08 0.10	0.02 0.63	0.00 0.62	-0.4 9.2	202807
1000	950	-0.09 0.10	0.24 0.73	0.10 0.66	-0.5 7.9	-0.08 0.10	-0.13 0.76	0.02 0.61	0.8 8.0	88596
WATN		11 am				11 pm				
70	30	-0.00 0.04	0.09 1.05	-0.00 0.00	-0.0 0.2	0.00 0.04	0.09 1.01	0.00 0.00	-0.0 0.2	722290
100	70	-0.01 0.05	0.07 1.02	0.00 0.00	0.1 0.3	-0.01 0.05	0.05 0.97	0.00 0.00	0.1 0.3	419062
150	100	-0.03 0.07	0.00 1.13	0.00 0.00	0.7 1.4	-0.03 0.07	-0.04 1.11	0.00 0.00	0.8 1.7	504738
200	150	0.02 0.10	-0.05 1.47	0.00 0.00	0.7 3.5	0.02 0.10	-0.09 1.41	0.00 0.00	0.8 4.2	363165
250	200	-0.05 0.13	0.50 1.20	0.00 0.00	-0.2 3.8	-0.05 0.13	0.47 1.18	0.00 0.00	-0.4 4.6	278092
300	250	-0.12 0.11	0.23 0.65	0.00 0.00	-0.3 4.3	-0.12 0.11	0.23 0.64	0.00 0.00	-0.2 5.0	233009
400	300	-0.51 0.27	0.10 0.70	-0.00 0.03	-0.1 9.0	-0.51 0.27	0.11 0.72	-0.00 0.03	-0.3 10.1	392099
500	400	-0.39 0.19	-0.08 0.48	-0.00 0.11	-0.2 10.4	-0.39 0.19	-0.08 0.50	-0.00 0.11	-0.1 11.2	326083
700	500	-1.02 0.51	-0.31 0.85	0.02 0.48	1.7 15.9	-1.02 0.51	-0.31 0.84	0.01 0.51	1.5 16.9	518511
850	700	-0.33 0.23	-0.18 1.04	0.10 0.98	1.9 16.4	-0.33 0.22	-0.15 1.01	0.08 0.99	1.3 16.5	315706
950	850	-0.08 0.10	0.10 0.69	-0.02 0.70	-1.0 9.0	-0.07 0.10	0.00 0.68	-0.02 0.73	-0.5 9.2	188531
1000	950	-0.11 0.10	0.34 0.66	0.15 0.71	-0.7 7.0	-0.07 0.10	-0.28 0.81	0.06 0.66	1.7 7.7	83465

Table 4.9: Overall model performance on a pressure layer basis as the average and standard deviation of the difference between synthetic data generated using the models employed in the NWM ray-tracing and the hiRes RS data: <synthetic-measured> for all five hiRes RS sites in the UK over years 2004, 2005 and 2006 only.

Pressure layer (hPa)		P error (hPa)	T error (K)	e error (hPa)	RH error (%)		Sample size
inf	sup	av ± std	av ± std	av ± std	av	std	
70	30	-0.00	0.04	0.07 1.00	-0.00	0.00	-0.0	0.2	1289264
100	70	-0.01	0.05	0.04 0.98	0.00	0.00	0.0	0.2	716460
150	100	-0.03	0.07	-0.05 1.10	0.00	0.00	0.5	1.4	838908
200	150	0.02	0.10	-0.06 1.44	0.00	0.00	0.9	3.9	582709
250	200	-0.05	0.13	0.49 1.17	0.00	0.00	-0.2	4.5	445599
300	250	-0.13	0.11	0.24 0.64	0.00	0.00	-0.3	4.9	375715
400	300	-0.51	0.27	0.10 0.69	-0.00	0.03	-0.3	9.3	626762
500	400	-0.39	0.19	-0.06 0.49	-0.00	0.11	-0.3	10.8	517860
700	500	-1.02	0.50	-0.27 0.81	0.01	0.46	1.1	15.6	833777
850	700	-0.33	0.23	-0.21 0.99	0.10	0.94	2.0	15.9	506570
950	850	-0.08	0.10	0.10 0.71	-0.01	0.78	-0.9	9.8	299650
1000	950	-0.10	0.10	0.30 0.70	0.05	0.65	-1.2	6.9	133691

layers, then a positive on for the next five, and a null one for the remaining three. Looking at the right plot on Figure 4.16 there is a tendency to overestimate T on the thin pressure layers, with thickness below 1.5 km whereas the bias is almost null for thicker layers. The standard deviation of the error is more correlated to the height than the thickness of the layer considered.

From Figure 4.17 it can be seen that the partial pressure of water vapour e rapidly vanishes at height around 8 km. Below, no real bias can be observed although the standard deviation is rather high compared to the average value of e, revealing once more the difficulty to properly model the water vapour. Again, only the model performance is discussed. The mismatch between NWM and reality will add on the error induced by the model itself. From this point of view, it can be accepted that the model will, in the long term, perform acceptably but

Table 4.10: Average height in metres of equivalent NWM pressure levels. The heights were computed using 5 years of data from all five hiRes RS sites in the UK. Right hand column indicates the average thickness in metres of the pressure layers defined as the part of the atmosphere comprised between two consecutive pressure levels.

Pressure Level [hPa]	Height [m]	Pressure layer thickness [m]
0030	23695	
		5274
0070	18421	
		2259
0100	16162	
		2581
0150	13581	
		1835
0200	11746	
		1422
0250	10324	
		1186
0300	09138	
		1962
0400	07176	
		1610
0500	05566	
		2566
0700	03000	
		1549
0850	01451	
		894
0950	00557	
		383
1000	00174	

individual solutions could suffer substantial errors. It is emphasized again that e is not measured so the results found here are also the results of the impact of the T and RH models.

From Figure 4.18 it can be seen that the relative humidity RH exhibits overall no real bias, except maybe at pressure layers below the 700-500 one included. The uncertainty of RH is height dependent more than layer thickness dependent, with the shape of a spinning top. The RH being a relative value, it cannot be used as is to get an idea of the absolute error that would, in the end, be induced on the refractivity. That's why, in the following section, to asses the impact of the total pressure, absolute temperature and humidity on the estimation of the refractivity, e was used, and was considered as independent from P and, admittedly wrongly, from T. Before that, the temporal variation of the modelling error is investigated.

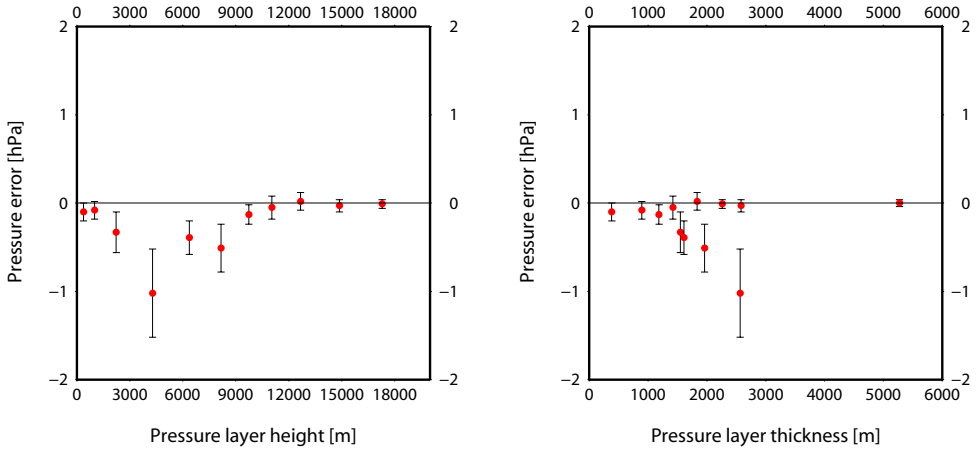

Figure 4.15: Total pressure P error (hPa) versus pressure layer (mean) height (left plot) and pressure layer thickness (right plot), as the difference between synthetic data generated using the models employed in the NWM ray-tracing and the hiRes RS data: <synthetic-measured> for all five hiRes RS sites in the UK over years 2004, 2005 and 2006 only.

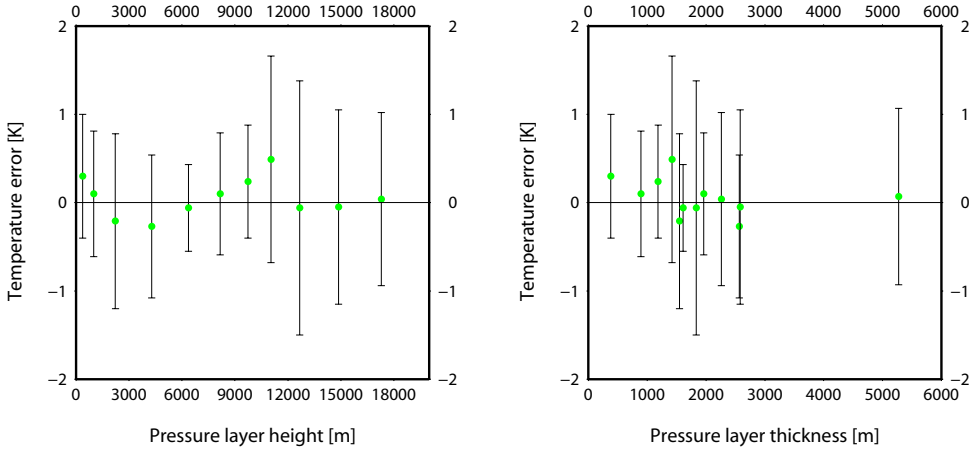

Figure 4.16: Absolute temperature T error (K) versus pressure layer (mean) height (left plot) and pressure layer thickness (right plot), as the difference between synthetic data generated using the models employed in the NWM ray-tracing and the hiRes RS data: <synthetic-measured> for all five hiRes RS sites in the UK over years 2004, 2005 and 2006 only.

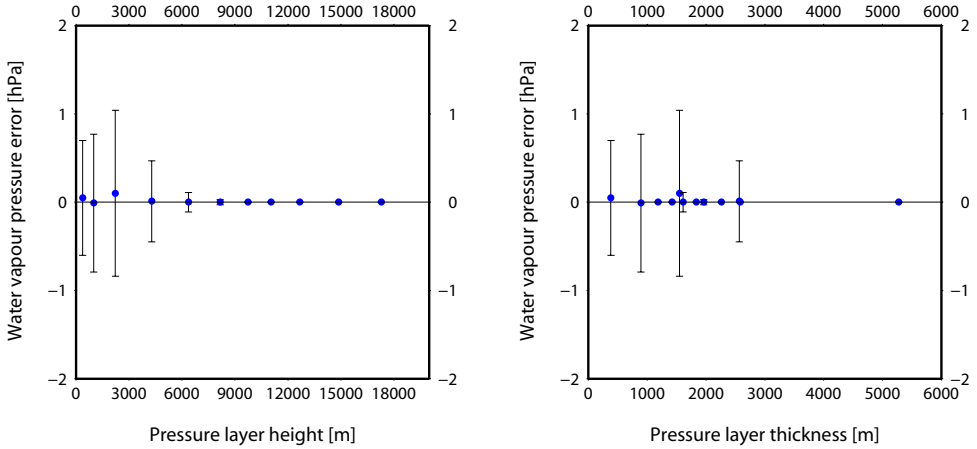

Figure 4.17: Water vapour partial pressure e error (mb) versus pressure layer (mean) height (left plot) and pressure layer thickness (right plot), as the difference between synthetic data generated using the models employed in the NWM ray-tracing and the hiRes RS data: <synthetic-measured> for all five hiRes RS sites in the UK over years 2004, 2005 and 2006 only.

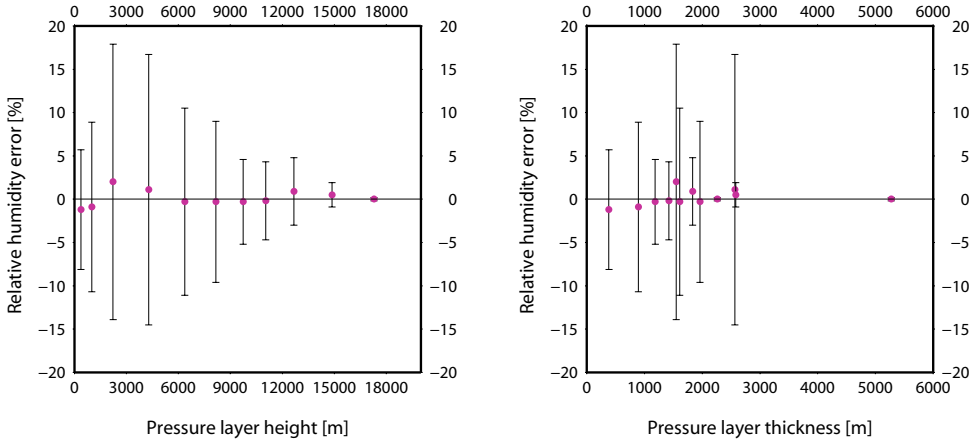

Figure 4.18: Relative humidity RH error (%) versus pressure layer (mean) height (left plot) and pressure layer thickness (right plot), as the difference between synthetic data generated using the models employed in the NWM ray-tracing and the hiRes RS data: <synthetic-measured> for all five hiRes RS sites in the UK over years 2004, 2005 and 2006 only.

4.4.4 Temporal variation of the models' performance

It was shown already that the model has a similar performance during daytime and nighttime. Here is examined the temporal variation of the error due to the model. To do so, on a daily basis, errors at heights comprised between two consecutive pressure levels (i.e. within a pressure layer) were averaged and plotted for a period of one year.

In this subsection, are presented the results for RS sites Albemarle (Figures 4.19 to 4.22)and Camborne (Figures 4.23 to 4.26 for completeness) over year 2005 for state variable P, T, e and RH. However, the discussion presented here applies to all sites (and all years):

- P: The systematic negative bias detected on P is, when existing, very stable over time from one day to the next. This is a real limitation in this work. No model development was attempted in this work but maybe a model tied to a more hydrostatic behavior would lead to better, less biased results.

- T: Apart from a bias which varies in sign with the pressure layer, T presents greater temporal fluctuation for pressure layers above 250 mb.

- e: For layers it is found in, e presents a typical model performance degradation for the summer period. This may be specific to 2005, but the model performed better before the summer than after.

- RH: The remark made for e partly applies to RH above 400 mb where the model performed better during the first quarter of the year. After that a degradation can be observed. For the lowest four pressure layers, however, the model performed equally over time.

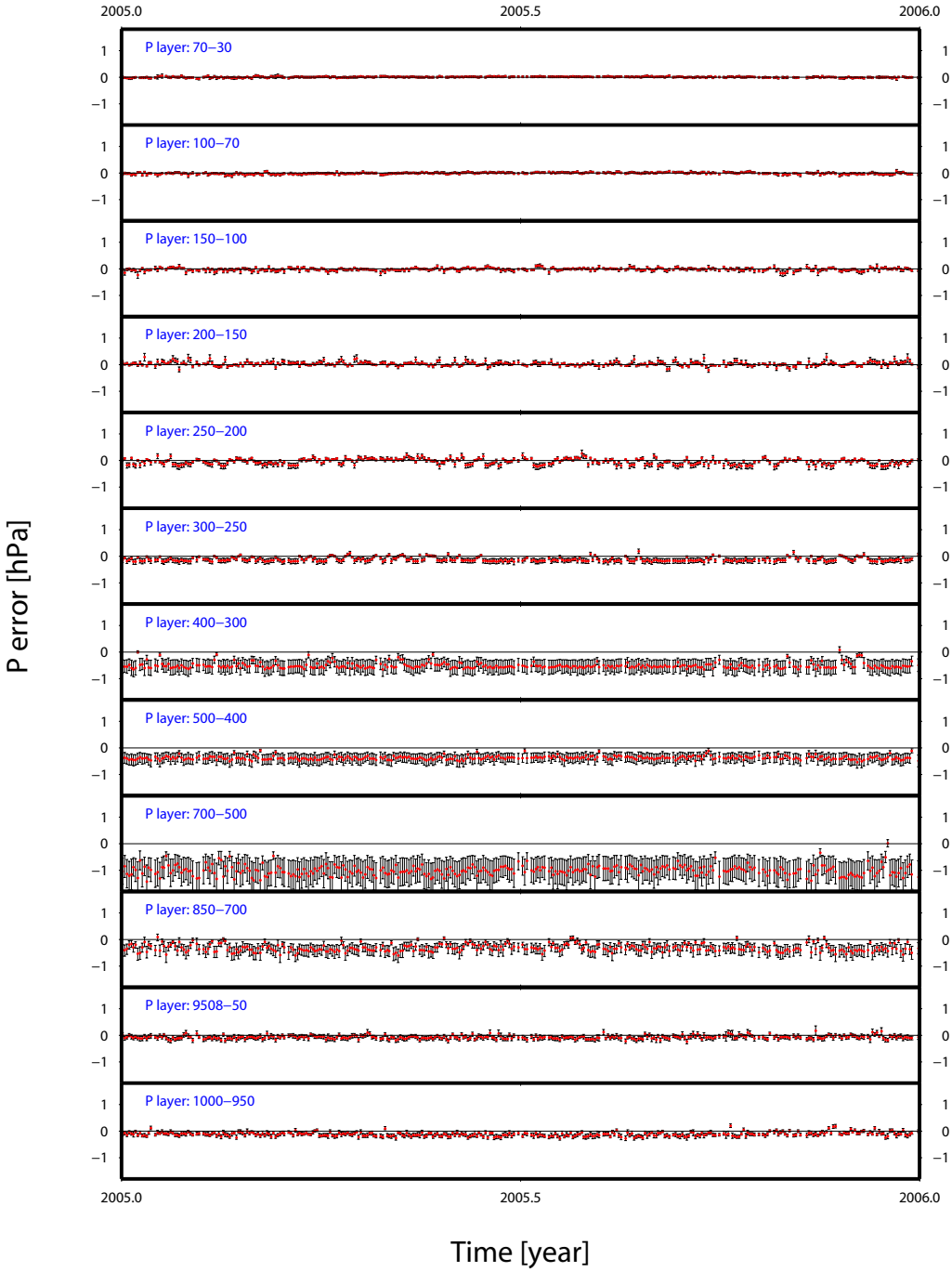

Figure 4.19: Time series of the daily total pressure P (hPa) average error (and 1 sigma error bars) with respect to pressure layers for hiRes RS site Albemarle over year 2005. By error is meant the difference between synthetic data generated using the models employed in the NWM ray-tracing and the hiRes RS data.

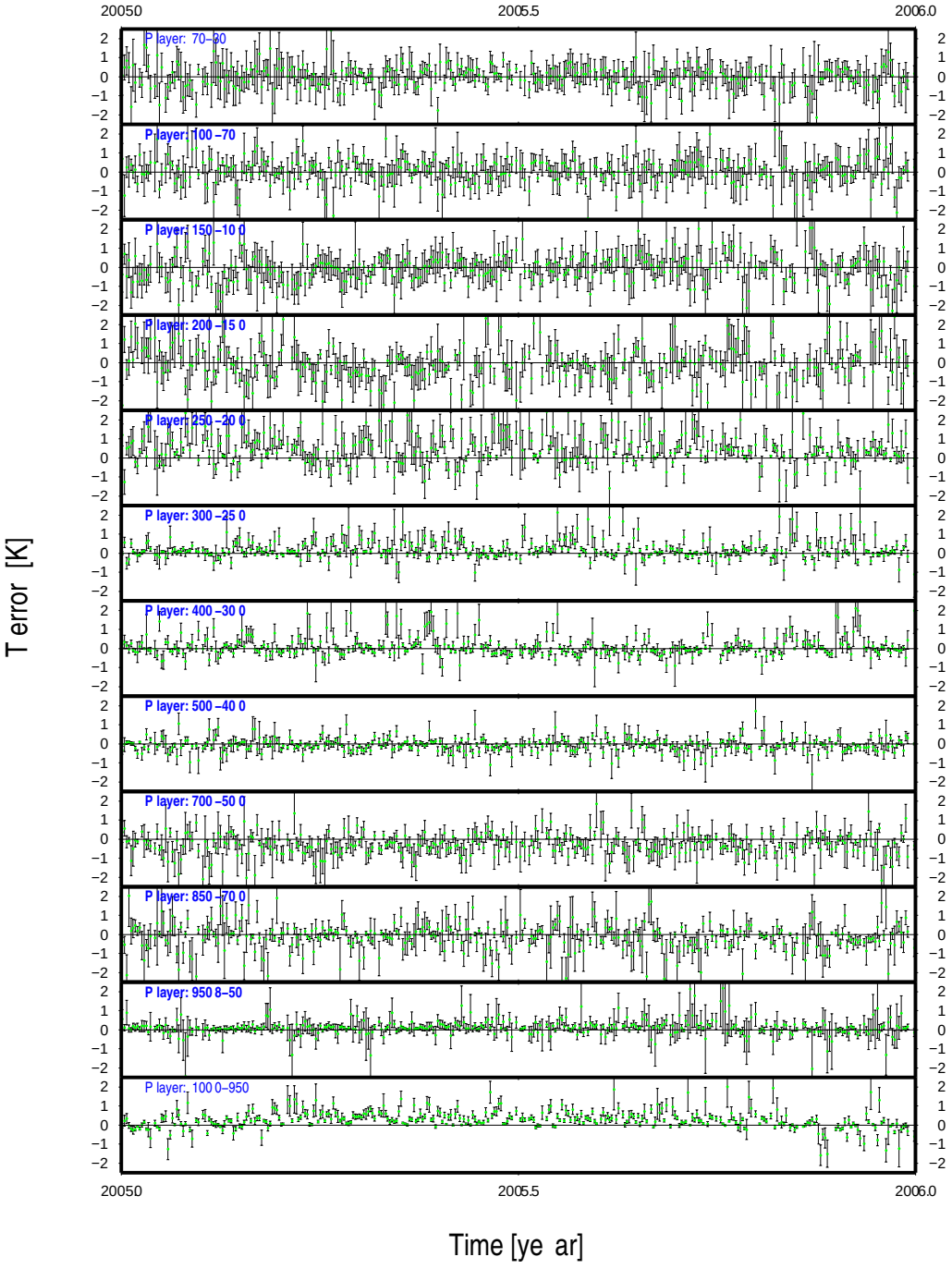

Figure 4.20: Time series of the daily absolute temperature T (K) average error (and 1 sigma error bars) with respect to pressure layers for hiRes RS site Albemarle over year 2005. By error is meant the difference between synthetic data generated using the models employed in the NWM ray-tracing and the hiRes RS data.

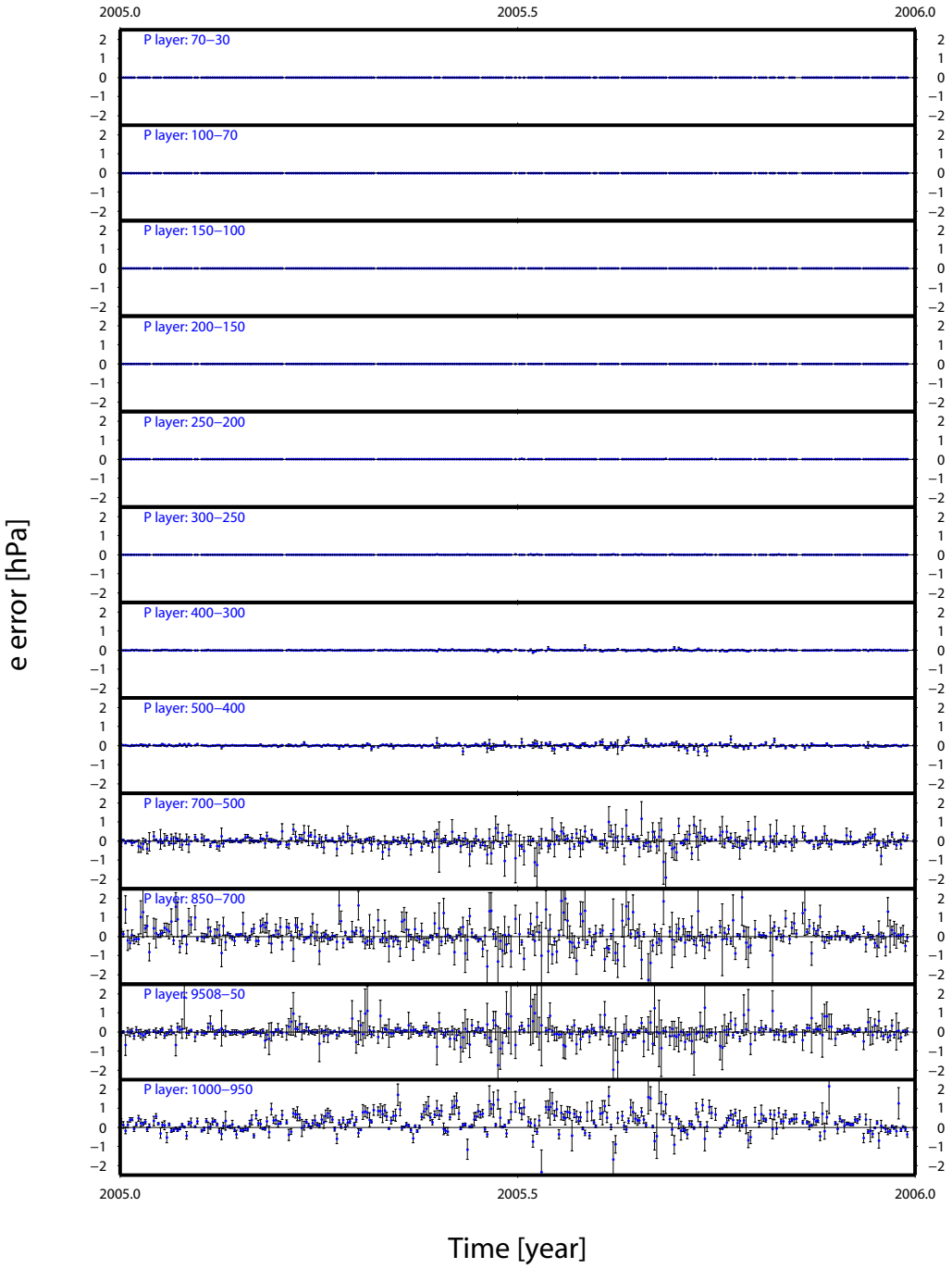

Figure 4.21: Time series of the daily water vapour partial pressure e (hPa) average error (and 1 sigma error bars) with respect to pressure layers for hiRes RS site Albemarle over year 2005. By error is meant the difference between synthetic data generated using the models employed in the NWM ray-tracing and the hiRes RS data. Actually, e is not observed but derived from other quantities.

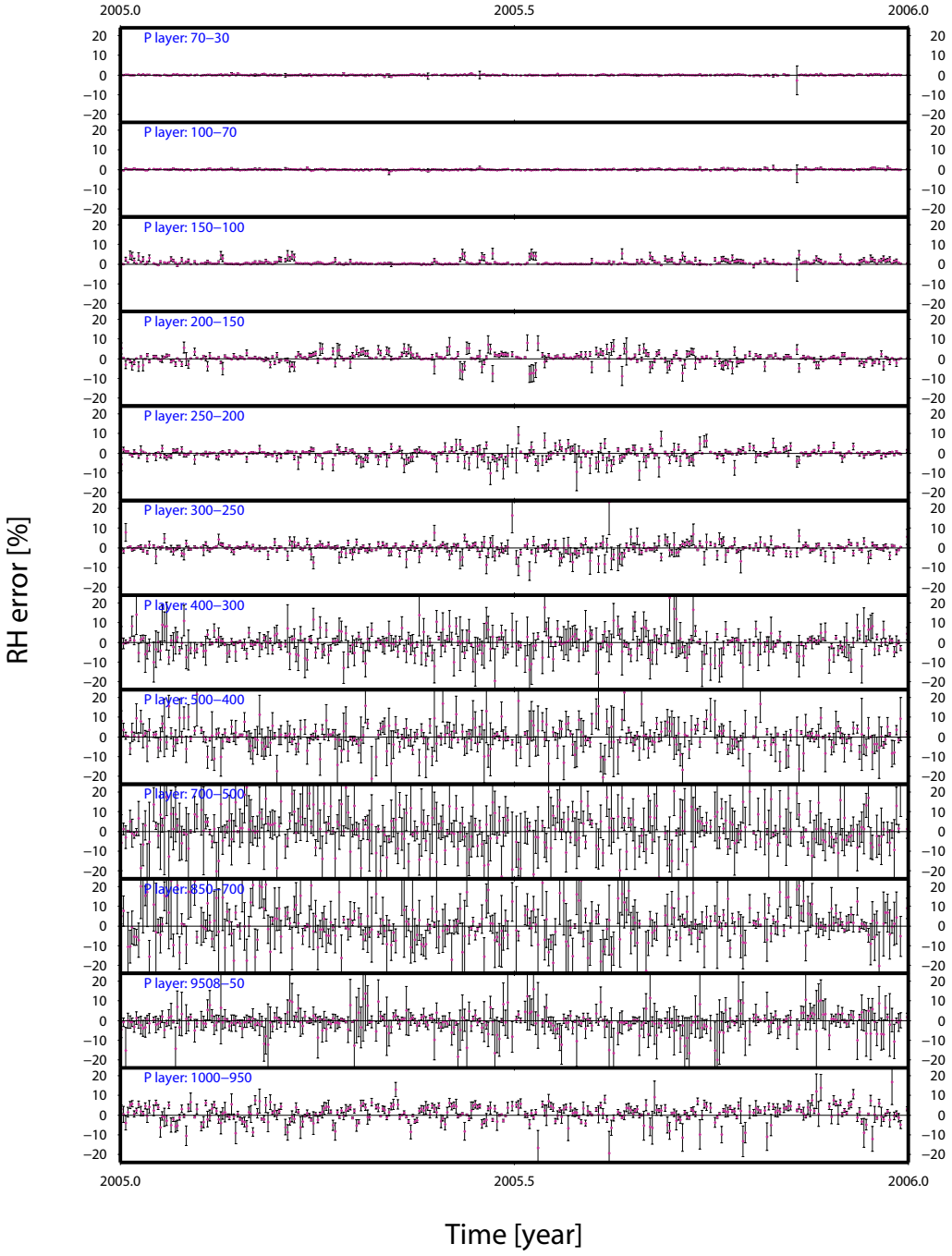

Figure 4.22: Time series of the daily relative humidity RH (%) average error (and 1 sigma error bars) with respect to pressure layers for hiRes RS site Albemarle over year 2005. By error is meant the difference between synthetic data generated using the models employed in the NWM ray-tracing and the hiRes RS data. Actually, RH is observed but the one used here was derived from other quantities (T and T_{dew}).

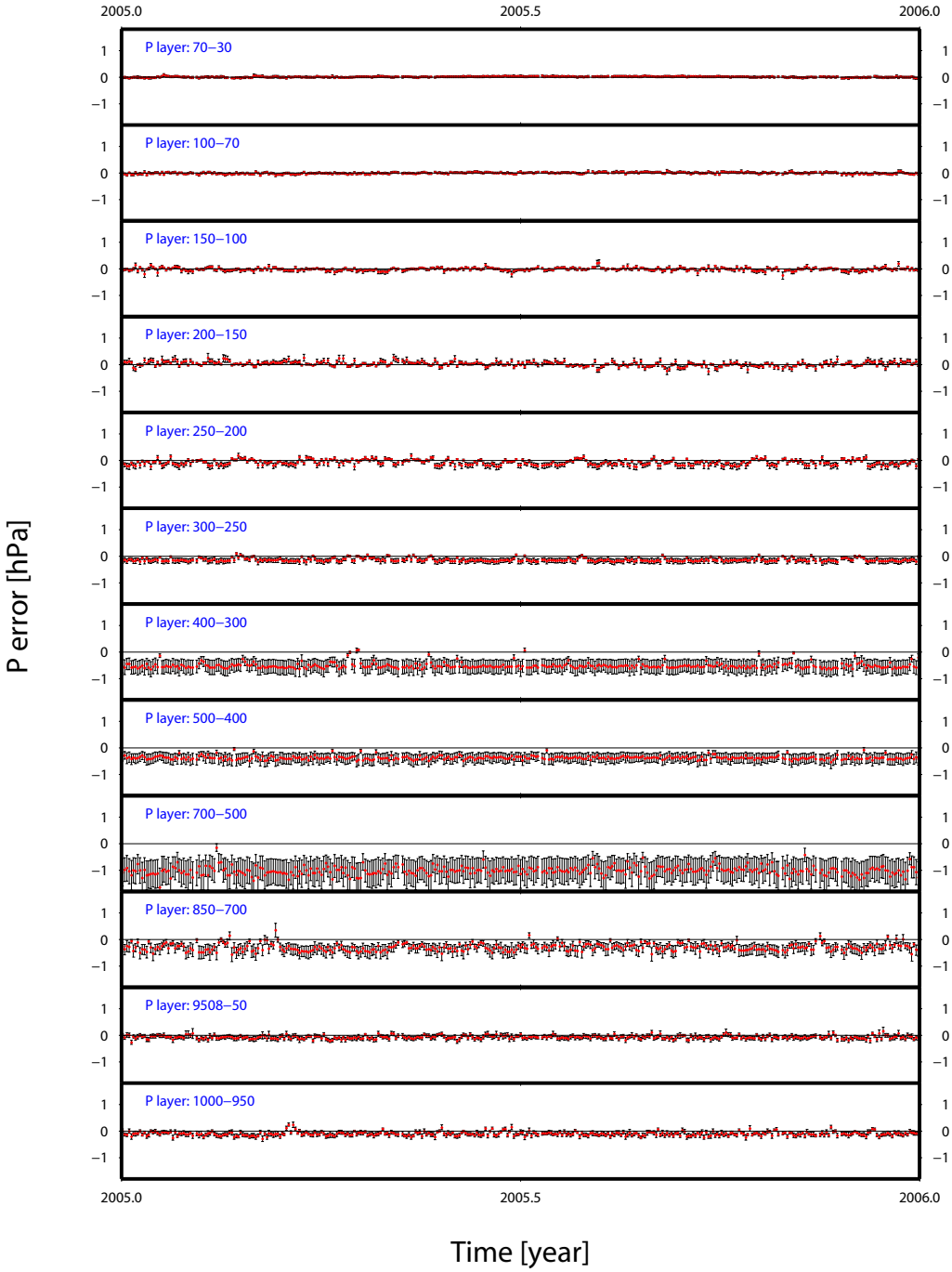

Figure 4.23: Time series of the daily total pressure P (hPa) average error (and 1 sigma error bars) with respect to pressure layers for hiRes RS site Camborne over year 2005. By error is meant the difference between synthetic data generated using the models employed in the NWM ray-tracing and the hiRes RS data.

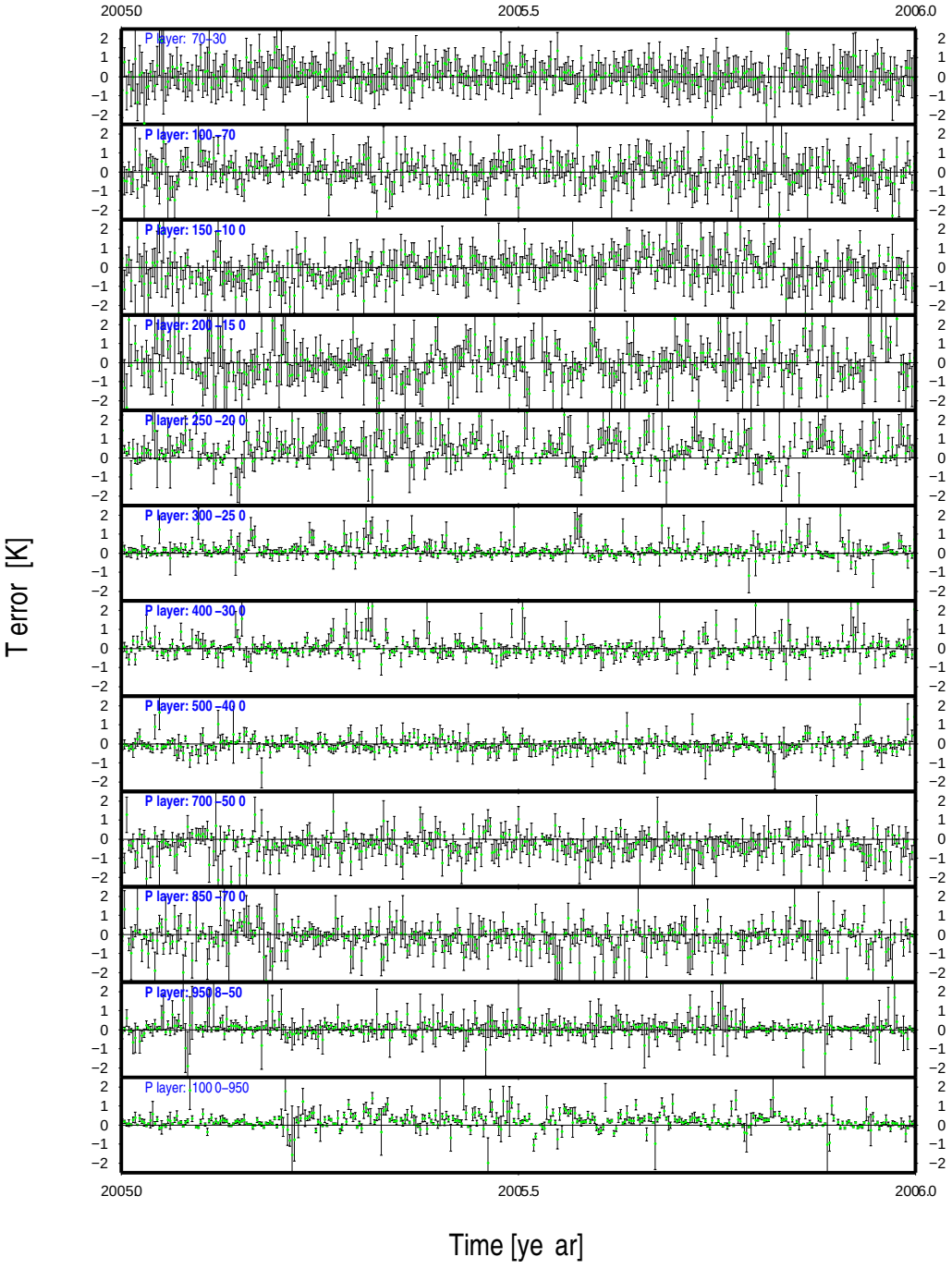

Figure 4.24: Time series of the daily absolute temperature T (K) average error (and 1 sigma error bars) with respect to pressure layers for hiRes RS site Camborne over year 2005. By error is meant the difference between synthetic data generated using the models employed in the NWM ray-tracing and the hiRes RS data.

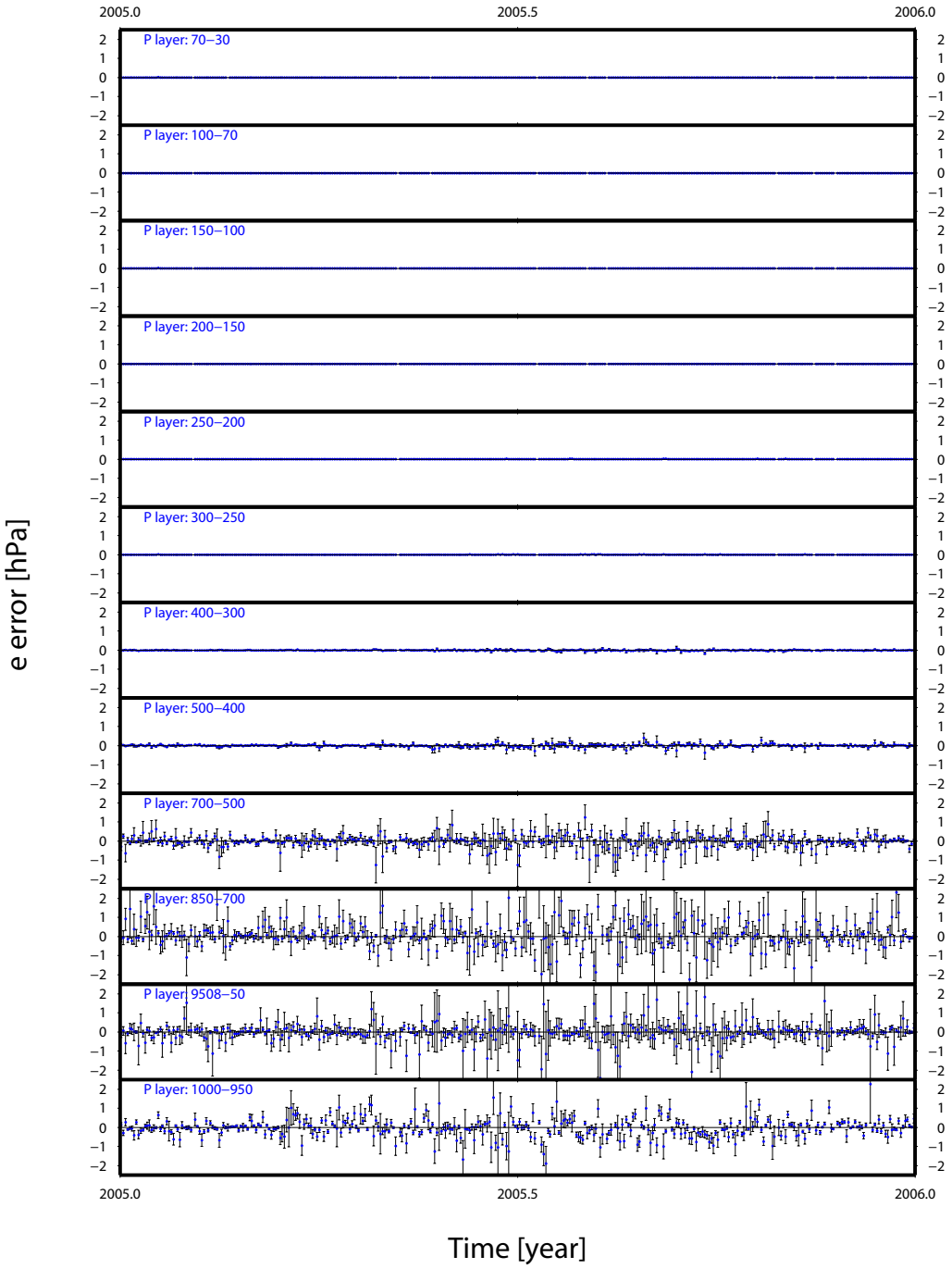

Figure 4.25: Time series of the daily water vapour partial pressure e (hPa) average error (and 1 sigma error bars) with respect to pressure layers for hiRes RS site Camborne over year 2005. By error is meant the difference between synthetic data generated using the models employed in the NWM ray-tracing and the hiRes RS data. Actually, e is not observed but derived from other quantities.

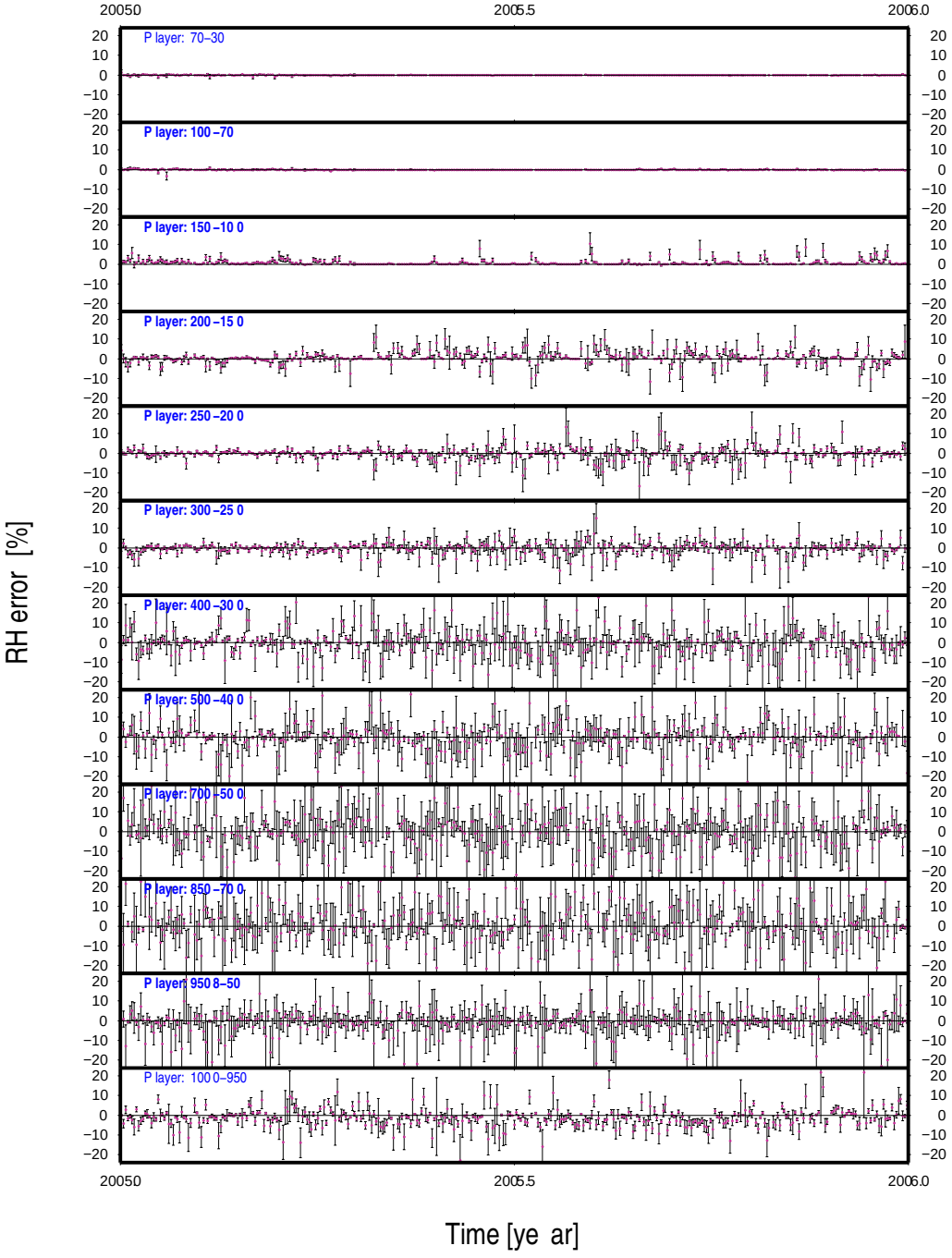

Figure 4.26: Time series of the daily relative humidity RH (%) average error (and 1 sigma error bars) with respect to pressure layers for hiRes RS site Camborne over year 2005. By error is meant the difference between synthetic data generated using the models employed in the NWM ray-tracing and the hiRes RS data. Actually, RH is observed but the one used here was derived from other quantities (T and T_{dew}).

4.5 Model Accuracy

This section offers an assessment of the accuracy of the models used to interpolated on height, P, T and U, from standard pressure level. To do so, integrated quantities ZHD, ZWD and ZTD were ray traced from both hiRes and standard RS data and compared. Several models for U were tested to identify possible better ways to model the variation of humidity on height, other than the one used in this work. Also, two methods of deriving the ZD were compared.

4.5.1 Methodology

From the hiRes RS data, the standard levels were extracted. The numbers of levels is roughly the same as the number of pressure levels of the NWM. Using as much data as possible between 2001 and 2007 for the five UK hiRes RS sites, there is a unique opportunity to test the interpolation models used to compute the refractivity along the ray's path. Note however that the standard data was extracted from the hiRes data as the distributed standard data have pressure with a resolution of 1 hPa instead of 0.1. Having in mind that a varation of 1 hPa corresponds roughly to a ΔZHD of 2.3 mm, it is below the precision of the possible achievements and could bias the results up to half that. Finally, only the zenith direction is considered in this section (as no three dimensional measured data are available).

4.5.2 Two methods for computing the zenith delays

Two methods for computing the zenith delays when ray-tracing a vertical atmospheric profile were compared. The discussion here is limited to the zenith direction. Starting with Thayer [1974] and dropping the compressibility factors,

the total refractivity can be written as:

$$N = k_1 P_d/T + k_2 P_w/T + k_3 P_w/T^2 \tag{4.15}$$

where P_d and P_w are the partial pressure of dry and wet air respectively and T the absolute temperature. Davis et al. [1985] rewrote this dry/wet distinction as a hydrostatic/non-hydrostatic one:

$$N = k_1 R_d \rho + k_2^{'} P_w/T + k_3 P_w/T^2 \tag{4.16}$$

where the first term now depends only on the total density ρ and not the mixing ratio [Davis et al., 1985].

The ZHD can either be obtained by integrating $N_{hyd} = k_1 R_d \rho$ with height or, using the differential formulation of the hydrostatic equilibrium $dP/dz = -\rho(z)g(z)$, by integrating $k_1 R_d/g$ with pressure [Vedel et al., 2001], i.e.:

- Method 1 ([Davis et al., 1985])

$$ZHD = 10^{-6} \int_{z_{site}}^{z_{top}} k_1 R_d \rho \delta z \tag{4.17}$$

- Method 2 ([Vedel et al., 2001])

$$ZHD = 10^{-6} \int_{0}^{p_{site}} \{k_1 \frac{R_d}{g}\} \delta p \tag{4.18}$$

For the wet, the following formulations were compared:

- Method 1 (Davis et al. [1985])

$$ZWD = 10^{-6} \int_{z_{site}}^{z_{top}} [k_2^{'} \frac{e}{T} + k_3 \frac{e}{T^2}] \delta z \tag{4.19}$$

- Method 2 (Vedel et al. [2001])

$$ZWD = 10^{-6} \int_0^{p_{site}} [\frac{R_d}{g\epsilon} q(k_2 - k_1\epsilon) + k_3/T]\delta p \tag{4.20}$$

The results of the comparison of the ray-tracing of vertical profiles using the two methods presented in this section are presented in Table 4.11. Preliminary results (see Table 4.12 for the hydrostatic) showed clearly the equivalence of the two methods on the hiRes data, although a noise level three times higher in the hydrostatic than in the wet, with a magnitude of 0.15 mm (1-sigma). This is still far better than the expected precision of the results, therefore the two methods can indeed be taken as equivalent. The statistics were computed using the maximum data available over the period 2001–2007 for the three zenith delays: hydrostatic, wet and total. It is important to stress the fact that the comparison is based on the hiRes RS data and no interpolation was used below the first measurement (what differs from NWM ray tracing in most cases). Above, the profile was augmented assuming a dry atmosphere in hydrostatic equilibrium.

4.5.3 Ray tracing of hiRes RS data, results: two ray tracing methods and seven different models to represent humidity

To assess models used to represent the vertical variation of the total pressure P, the absolute temperature T and humidity (e, RH, q or w) on height (or pressure), seven models were used, partly based on [Boehm and Schuh, 2003] and [Vedel et al., 2001]. With the hiRes RS data set, it is possible to directly assess the quality of those models, by processing the extracted standard pressure level data set as per the NWM. For the total pressure and temperature, only one model

was tested as found satisfactory, whereas several ones were tested for the humidity.

Here it is important to note that:

- Unless specified otherwise, the profiles were all augmented the same way up to a geometric height of 80 km assuming a dry atmosphere in hydrostatic equilibrium (based on a standard atmosphere). Only profiles with measurements up to 15 km were kept so that it can be safely assumed a dry atmosphere above the last measurement.

- Models are employed between two consecutive pressure levels only. This a limitation of the implemented ray-tracing. So interpolation schemes are limited. No cubic interpolation could be performed for example that would lead to smoother profiles.

A comparison is presented in Table 4.11 with the seven different models tested for the height dependence of humidity. In each case the height dependence of total pressure and absolute temperature were unchanged. From top to bottom, the following models were tested (some with no real physical a-priori data): **Case 1** Exponential variation of e with height; **Case 2** Linear variation of e with height; **Case 3** Exponential variation of q with height; **Case 4** Linear variation of q with height; **Case 5** Exponential variation of w with height; **Case 6** Linear variation of w with height, **Case 7** Linear variation of RH with height.

Table 4.11: Statistics on the difference on the zenith delays ray-traced from hiRes RS data and extracted standard data. The difference was taken as <Standard-Hires>. All numbers are given in mm.

(Hires) radiosonde site	**ZHD Difference (mm)** *Method 1* Av.	std.	*Method 2* Av.	std.	**ZWD Difference (mm)** *Method 1* Av.	std.	*Method 2* Av.	std.	**ZTD Difference (mm)** *Method 1* Av.	std.	*Method 2* Av.	std.	Nb. of profiles
	case 1: $\delta \ln p \propto \delta z, \delta T \propto \delta z, \delta \ln e \propto \delta z$												
ALBE	-1.33	1.76	-0.06	0.30	-2.02	6.72	-1.87	6.72	-3.35	7.21	-1.92	6.73	3601
CAMB	-1.21	1.63	-0.01	0.04	-2.34	7.56	-2.20	7.57	-3.54	7.99	-2.20	7.57	4042
HERS	-1.22	1.64	-0.01	0.11	-2.12	7.38	-1.95	7.37	-3.34	7.84	-1.96	7.37	3748
LERW	-1.48	1.67	-0.03	0.20	-1.88	6.02	-1.72	6.02	-3.36	6.47	-1.75	6.03	5529
WATN	-1.29	1.71	-0.01	0.06	-2.07	7.18	-1.92	7.21	-3.35	7.72	-1.93	7.21	5039
	case 2: $\delta \ln p \propto \delta z, \delta T \propto \delta z, \delta e \propto \delta z$												
ALBE	-1.48	1.76	-0.06	0.30	5.03	6.77	5.21	6.79	3.53	7.21	5.16	6.79	3584
CAMB	-1.38	1.63	-0.01	0.04	5.22	7.78	5.39	7.78	3.82	8.17	5.38	7.78	4049
HERS	-1.39	1.64	-0.01	0.11	5.24	7.35	5.41	7.35	3.84	7.77	5.40	7.35	3717
LERW	-1.62	1.67	-0.03	0.20	4.77	6.12	4.93	6.13	3.14	6.59	4.90	6.13	5527
WATN	-1.45	1.71	-0.01	0.06	5.13	7.35	5.28	7.35	3.67	7.82	5.27	7.35	5025
	case 3: $\delta \ln p \propto \delta z, \delta T \propto \delta z, \delta \ln q \propto \delta z$												
ALBE	-1.33	1.76	-0.06	0.30	-2.02	6.72	-1.87	6.73	-3.34	7.21	-1.92	6.74	3601
CAMB	-1.21	1.63	-0.01	0.04	-2.33	7.56	-2.20	7.58	-3.53	7.99	-2.20	7.58	4042
HERS	-1.22	1.64	-0.01	0.11	-2.11	7.38	-1.94	7.37	-3.34	7.84	-1.96	7.37	3748
LERW	-1.48	1.67	-0.03	0.20	-1.87	6.02	-1.72	6.02	-3.35	6.47	-1.75	6.03	5529
WATN	-1.29	1.71	-0.01	0.06	-2.06	7.18	-1.92	7.21	-3.35	7.72	-1.93	7.21	5039
	case 4: $\delta \ln p \propto \delta z, \delta T \propto \delta z, \delta q \propto \delta z$												
ALBE	-1.44	1.76	-0.06	0.30	3.01	6.61	3.18	6.60	1.55	7.09	3.12	6.61	3612
CAMB	-1.33	1.63	-0.01	0.04	3.10	7.48	3.27	7.50	1.75	7.92	3.27	7.50	4070
HERS	-1.35	1.64	-0.01	0.11	3.17	7.17	3.34	7.15	1.82	7.64	3.32	7.15	3751
LERW	-1.58	1.67	-0.03	0.20	2.80	5.89	2.96	5.87	1.22	6.38	2.93	5.88	5545
WATN	-1.40	1.71	-0.01	0.06	3.09	7.11	3.26	7.10	1.68	7.61	3.25	7.10	5067
	case 5: $\delta \ln p \propto \delta z, \delta T \propto \delta z, \delta \ln w \propto \delta z$												
ALBE	-1.33	1.76	-0.06	0.30	-2.01	6.72	-1.86	6.73	-3.33	7.21	-1.91	6.74	3601
CAMB	-1.21	1.63	-0.01	0.04	-2.32	7.57	-2.18	7.58	-3.53	7.99	-2.19	7.58	4043
HERS	-1.22	1.64	-0.01	0.11	-2.10	7.37	-1.93	7.37	-3.32	7.84	-1.94	7.37	3748
LERW	-1.48	1.67	-0.03	0.20	-1.86	6.02	-1.71	6.02	-3.34	6.47	-1.74	6.02	5529
WATN	-1.29	1.71	-0.01	0.06	-2.06	7.19	-1.91	7.21	-3.34	7.72	-1.92	7.22	5040
	case 6: $\delta \ln p \propto \delta z, \delta T \propto \delta z, \delta w \propto \delta z$												
ALBE	-1.44	1.76	-0.06	0.30	3.03	6.61	3.20	6.60	1.57	7.09	3.14	6.61	3612
CAMB	-1.34	1.63	-0.01	0.04	3.13	7.48	3.30	7.50	1.78	7.92	3.29	7.50	4070
HERS	-1.35	1.64	-0.01	0.11	3.19	7.16	3.36	7.15	1.83	7.62	3.35	7.15	3749
LERW	-1.58	1.67	-0.03	0.20	2.82	5.89	2.98	5.88	1.24	6.37	2.95	5.88	5544
WATN	-1.40	1.71	-0.01	0.06	3.11	7.10	3.29	7.10	1.70	7.60	3.28	7.10	5065
	case 7: $\delta \ln p \propto \delta z, \delta T \propto \delta z, \delta RH \propto \delta z$												
ALBE	-1.39	1.75	-0.06	0.30	0.97	6.58	1.11	6.53	-0.43	7.14	1.06	6.53	3625
CAMB	-1.29	1.63	-0.01	0.04	1.21	7.34	1.36	7.34	-0.09	7.83	1.35	7.34	4086
HERS	-1.30	1.63	-0.01	0.11	1.12	7.07	1.28	7.05	-0.19	7.60	1.27	7.06	3769
LERW	-1.53	1.66	-0.03	0.20	0.65	5.71	0.81	5.70	-0.89	6.27	0.78	5.70	5547
WATN	-1.36	1.71	-0.01	0.06	1.00	7.00	1.17	6.98	-0.36	7.58	1.16	6.98	5092

There are several important points to make out of Table 4.11:

1. Method 1 underestimates the ZHD by 1.2 to 1.6 mm depending on the station and the model used for the humidity.

2. Method 2 estimates of ZHD are in almost perfect agreement with the hiRes ones (the two hiRes methods were found to be equivalent) and the performance of this method is independent on the model used to represent the humidity. This comes from the fact that the integration on height (following [Davis et al., 1985] in the present case) requires the computation of ρ which requires the computation of e. So an error in e will affect ρ and therefore the ray-traced values. The impact of the model for the humidity is limited on the determination of the hydrostatic due to the fact that the total pressure is much larger than the partial pressure of water vapour. On the contrary, method 2 is driven solely by the model for the total pressure, hence is independent on the choice for e as part of the model chosen for the total pressure.

3. For ZWD, there is a clear winner for the modelling of the humidity, i.e. case 7: the linear variation of RH with height. Whereas the level of noise is overall the same at around 6–7.5 mm, it produces a bias of between 0.6 and 1.2 mm only, which is quite remarkable. It is twice better than the model that came second, i.e. in cases 3 and 5: the assumption of an exponential variation of e, q or w with height. The worst model is case 2 (the assumption of a linear variation of e with height) which clearly overestimates the real distribution, followed by cases 4 and 6: the assumption of a linear variation of the specific humidity (q) or mixing ratio (r) with height. In the ZWD case, method 1 is lightly better than method 2.

4. Looking at the ZTD, the statistics are improved whether or not the ZHD

and ZWD are both either under- or overestimated, or if one compensates the other. In the determination of ZTD, the best approach is method 1 and case 7, assuming a linear variation of the relative humidity RH with height. This gives biases of only -0.1 to -0.9 mm with the hiRes data, with a level of noise of 7.3 mm in average. It converges well towards a remark from H. Vedel ([Vedel, 2007], pers. communication) that "the model for the humidity should somehow include the one of the temperature, as this one plays a major role in the capacity of the air to retain humidity and is well predicted by NWM, much better than humidity itself".

4.5.4 Ray-traced ZHD versus Saastamoinen

From the results exposed in Table 4.11 a discrepancy exists between method 1 when using standard data and Method 1 with hiRes data, whereas method 2 performs the same on either the hiRes and standard data and Methods 1 and 2 are equivalent when using hiRes data. The ZHD were compared to the ones computed from the ground pressure using Saastamoinen [1972]. Davis et al. [1985] reformulated the equation of refractivity proposed by Thayer [1974] from a dry and wet formulation to a hydrostatic and non-hydrostatic one, the hydrostatic zenith delay being accurately computable from the ground pressure only if this last one is accurately known, following Davis et al. [1985]:

$$ZHD = [10^{-6} k_1 R_d g_m^{-1}] P_0 \tag{4.21}$$

where g_m "*very nearly represents the acceleration due to gravity at the center of mass of the vertical column*" and can be computed using the developments [Saastamoinen, 1972], and P_0 the ground (or antenna phase center) pressure.

In this study are compared only consistent zenith hydrostatic delays (from the ray-tracing and from Eq. 4.21) in the sense that the same value for k_1 was used in the two. The evaluation of the ZHD by Davis et al. [1985] varies with the ratio of the k_1 values when different. For example, the ratio between the k_1 value of Essen and Froome [1951] and the one proposed as best average by Rüeger [2002] is $77.624/77.689 \approx 0.999163$. For a ZHD of 2300 mm determined using Essen and Froome [1951] k_1, a ZHD of 2301.9 mm would be found using Rüeger [2002] k_1 value. That is, a bias of almost 2 mm only due to the k_1 constant used. Therefore, this order of magnitude should be kept in mind when comparing different values of ZHD (and ZTD) which are not fully consistent.

From Table 4.12, based on the hiRes RS data, it can be confidently said that method 1 and 2 produce similar results that both agree very well with the predicted hydrostatic, although method 1 exhibits a noise level twice as big as method 2 (0.18 mm versus 0.10 mm), both are very acceptable. It indicates that in general, the assumption of an hydrostatic equilibrium is justified and acceptable and that the chosen model for P respects that condition. It seems that the computation of the total density ρ is the limitation here, and that it introduces a negative bias of more than a millimetre in the ray-tracing of the ZHD. It is recalled here that the implementation of method 1 and 2 are equivalent, both driven by integration steps in geometric height, and that in both cases, values for state variables are exactly the same. As stated before, the ZHD determined with method 2 is independent of the handling of the wet. Looking at Table 4.11, it is clear that whatever model is used to represent the vertical variation of the humidity, the level of noise in ZHD doesn't change, whereas an overestimation of the wet leads, logically, to smaller hydrostatic delays.

It was suspected that the discrete integration could be a problem so the data was reprocessed this time with a regular 10 m instead of the ones adopted from Rocken et al. [2001]. In the case of 10 metres, this roughly corresponds to the vertical ascent of the balloon in 2 s, i.e. the sampling rate of the hiRes data used in this work. Results are presented in the bottom part of Table 4.12 and clearly show that no real degradation is introduced when preferring the optimized integration steps from Rocken et al. [2001] over a regular and much finer one of 10 m.

However different the model used for the humidity, Table 4.11 indicates rather clearly that the impact is rather limited on the hydrostatic zenith delay, as

$P >> e$; Could the determination of the absolute temperature T be of greater importance (keeping in mind that it plays a key role in the physics of the humidity)? To decide, the differences between measurements and models are investigated further in the next section.

Table 4.12: Mean offsets and associated standard deviations of the difference between the integrated ZHD and one computed using Saastamoinen [1972], using hiRes RS data and corresponding standard data. All values are given in mm. Radiosonde profiles were extended assuming a dry atmosphere in hydrostatic equilibrium, hence the null correction term.

Radiosonde site	Radiosonde data type	Method 1 Av. (st.dev.)	Method 2 Av. (st.dev.)	Correction term Av. (st.dev.)	Number of profiles
Integration steps from Rocken et al. [2001]					
albe	hiRes	0.08 (0.19)	0.05 (0.10)	0.00 (0.00)	3662
	standard	-1.14 (1.67)	0.05 (0.10)	0.00 (0.00)	3598
camb	hiRes	0.04 (0.16)	0.07 (0.09)	0.00 (0.00)	4152
	standard	-1.13 (1.59)	0.06 (0.09)	0.00 (0.00)	4108
hers	hiRes	0.09 (0.19)	0.06 (0.10)	0.00 (0.00)	3844
	standard	-1.08 (1.58)	0.06 (0.10)	0.00 (0.00)	3775
lerw	hiRes	-0.01 (0.18)	0.01 (0.10)	0.00 (0.00)	5581
	standard	-1.40 (1.59)	0.01 (0.10)	0.00 (0.00)	5472
watn	hiRes	0.04 (0.19)	0.05 (0.10)	0.00 (0.00)	5165
	standard	-1.18 (1.64)	0.05 (0.10)	0.00 (0.00)	5070
10 m integration steps					
albe	standard	-1.19 (1.67)	0.04 (0.10)	0.00 (0.00)	3593
camb	standard	-1.17 (1.59)	0.06 (0.09)	0.00 (0.00)	4106
hers	standard	-1.13 (1.58)	0.06 (0.10)	0.00 (0.00)	3773
lerw	standard	-1.43 (1.59)	0.01 (0.10)	0.00 (0.00)	5466
watn	standard	-1.23 (1.63)	0.05 (0.10)	0.00 (0.00)	5065

4.6 Impact of the modelling error on the determination of the refractivity

In the previous section were computed the standard deviations (1 σ) of P, T and e on each pressure level (see Table 4.9). Those standard deviations are now input to an error propagation in order to assess the impact on the determination of the total refractivity N. The parameter e was assumed to be independent from T so that the variance covariance matrix of the parameters X (C_{XX}) has null non-diagonal elements and (assuming perfect refractivity constants as well) can be written as:

$$C_{XX} = \begin{pmatrix} C_{PP}^2 & 0 & 0 \\ 0 & C_{TT}^2 & 0 \\ 0 & 0 & C_{ee}^2 \end{pmatrix} \tag{4.22}$$

with N being:

$$N = k_1 \frac{P-e}{T} + k_2 \frac{e}{T} + k_3 \frac{e}{T^2} \tag{4.23}$$

$$= k_1 \frac{P}{T} + (k_2 - k_1)\frac{e}{T} + k_3 \frac{e}{T^2} \tag{4.24}$$

and the transition matrix F written as:

$$F^T = \left[\frac{\partial N}{\partial P}, \ \frac{\partial N}{\partial T}, \ \frac{\partial N}{\partial e} \right] \tag{4.25}$$

$$= \left[\frac{k_1}{T}, \ \frac{k_1\,(e-P) - k_2\,e}{T^2} - \frac{2\,k_3\,e}{T^3}, \ \frac{k_2 - k_1}{T} + \frac{k_3}{T^2} \right] \tag{4.26}$$

To compute the results, average pressure in each pressure layer was used. Results for the total refractivity are presented in Figure 4.27. The value used for P is the average measured pressure on the pressure level over years 2005 and 2006 for

all sites. The range of the plots were limited to possible situations only, but it is emphasized the pressure used for various combination of T and e was fixed to the average one computed as mentioned above. Those plots indicate that the error on the total refractivity can easily reach several ppm. The worst case scenario is found for pressure layer 850–700 hPa with a propagated error of 7 ppm. No major difference could be observed when using the pressure of the bottom pressure level instead. It is also important to note that the thickness of the pressure layer might play a significant role in the error found in the refractivity (see Table 4.10).

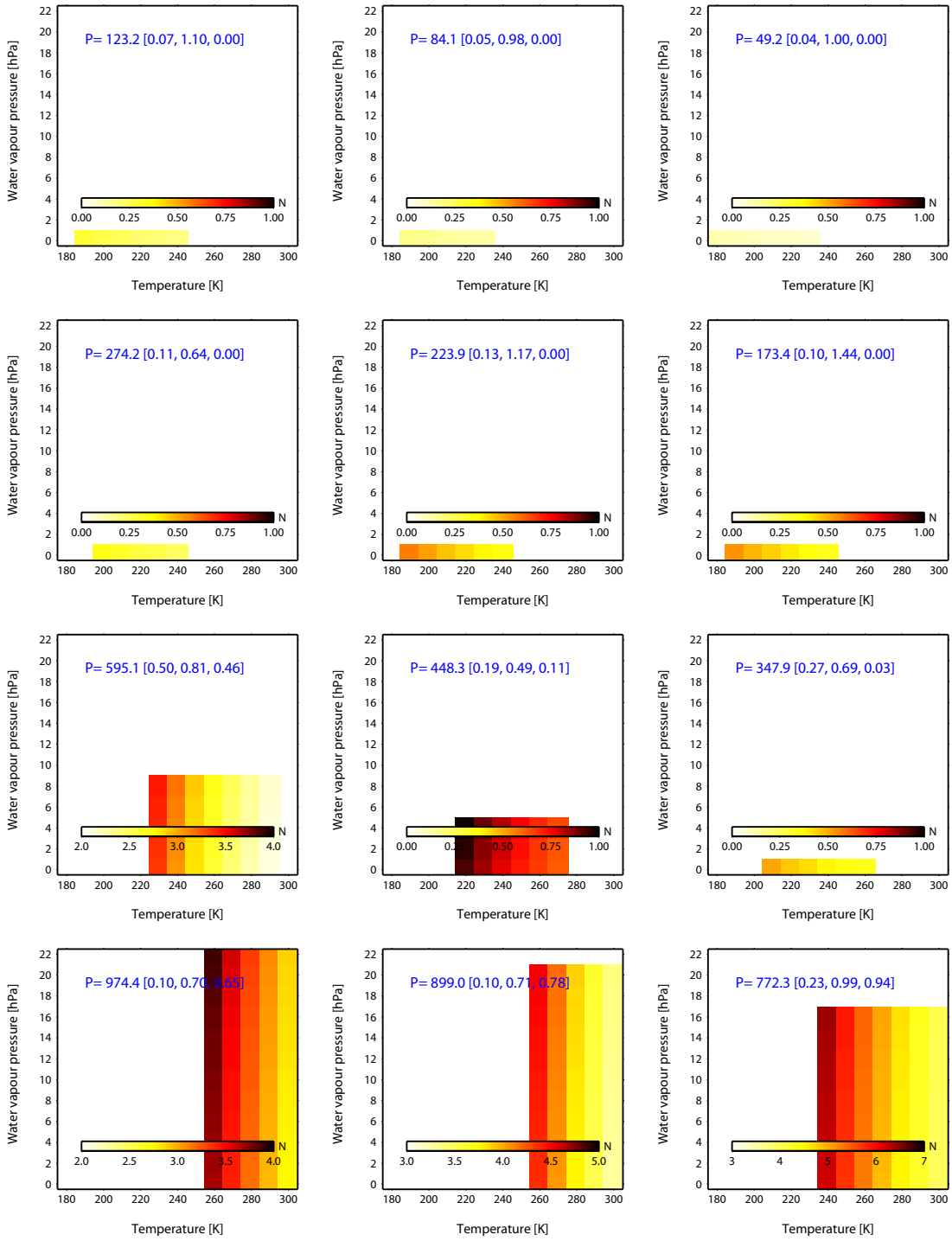

Figure 4.27: Error propagated on the total refractivity N (ppm) for the different pressure levels. A priori sigma for P, T, and e (assumed independent) were previously determined (Table 4.9) and are reproduced in brackets on each plot.

4.7 Zenith Delay Determination: High Resolution Radiosonde versus NWM, a comparison

The UK Met Office high resolution mesoscale NWM (MESO) was ray-traced at the location of the five hiRes RS sites (using exactly the same implementation as for the OMF derivation) and the zenith delays obtained compared. This comparison, after the assessment of the models themselves based solely on radiosonde data, includes not only the models' inherent limitations, but also the errors in the NWM itself. Radiosondes launched at around 11 (23) UTC, were compared to ZD ray-traced using the 12 (00 of the following day) UTC NWM output. The ascent takes about 30-45 minutes, so the approximation made here on the timing will be considered acceptable. Above it was already shown that Methods 1 and 2, based on standard data, were producing results in a relative disagreement, although found to be in a very close agreement when used on the hiRes RS data. Therefore, results are exposed for the two methods for completeness.

Table 4.13 shows that a much better agreement on the ZTD derivation is found for Method 1 between the NWM and the reference solution (either Method 1 or 2 on hiRes RS data) than found for Method 2. However, the ZHD is in a closer agreement for Method 2 than 1, that is, the difference is really made on the ZWD where biases are between 0.3 and 4.2 mm for Method 1 and between 5.2 and 10.0 mm for Method 2. Overall, the level of noise is of comparable magnitude.

Table 4.13: Statistics (mean and associated standard deviation) of the difference between zenith delays derived from the NWM and the hiRes RS data.

RS Site	ZTD Difference (mm)	ZHD Difference (mm)	ZWD Difference (mm)	Sample size
		Method 1		
ALBE	-0.2 ± 10.9	−1.5 ± 1.9	1.2 ± 10.6	2244
CAMB	2.5 ± 12.8	−1.7 ± 1.9	4.2 ± 12.6	2318
HERS	-2.3 ± 11.4	−3.2 ± 1.8	0.9 ± 11.1	2093
LERW	-0.6 ± 9.9	−0.9 ± 2.2	0.3 ± 9.4	2310
WATN	-0.5 ± 10.9	−2.8 ± 1.8	2.3 ± 10.8	2213
		Method 2		
ALBE	6.2 ± 10.7	−0.2 ± 1.5	6.4 ± 10.5	2243
CAMB	9.6 ± 12.7	−0.4 ± 1.6	10.0 ± 12.6	2317
HERS	4.6 ± 11.4	−1.8 ± 1.4	6.4 ± 11.3	2093
LERW	5.7 ± 9.8	0.6 ± 1.9	5.2 ± 9.4	2310
WATN	6.3 ± 11.1	−1.5 ± 1.5	7.8 ± 11.1	2213

4.8 Summary

The quality of the models used for interpolating meteorological states with height, based on pressure levels data, were studied using several years of high resolution radiosonde data. Running the models on extracted standard pressure levels allowed for a direct comparison between interpolated values for pressure, temperature and humidity to be quantified. It was found that the expected total refractivity error (assuming true data on pressure levels being used in the interpolation) to be about 0.5%, with annual variations, mostly induced by error in the humidity. Error in interpolating the pressure was found to be small in comparison, negative, but systematic. The error made on the absolute temperature averages to zero and appeared to be random. The models' performances was detailed on a pressure basis. The accuracy of the models was quantified in terms of total zenith delays (using two integration approaches), taking the high resolution RS results as the truth. Various models were tested for interpolating the humidity information, out of which, assuming a linear variation of the relative humidity with height as

a model for humidity, appeared to be the best.

Chapter 5

Results: Azimuthally Symmetric Mapping Functions

This chapter presents the results of a comparison of seven different modelling techniques of the troposphere delay in the processing of GPS data, all of which assume a symmetrical atmosphere. 3.8 years long time series for thirty stations in the UK are examined. All the processing was carried out using the Bernese GPS Software [Dach et al., 2007], and all the solutions were obtained using the precise point positioning technique. The seven solutions are the results of the combination of different a priori information on the zenith delay (Saastamoinen based or numerical weather model ray traced) and different mapping functions. The main objective is to compare and validate the azimuthally symmetric OMF against the best mapping functions currently available before examining in the next chapter the performance of the azimuth dependent OMF.

5.1 Introduction

The principal objective of this chapter is to validate/invalidate the concept of the OMF via the processing of GPS data. It was a necessary step to investigate the azimuthally symmetric version of the OMF before introducing the azimuthal dependency (Chapter 6). The performances of the azimuthally symmetric OMF are compared against those of the global mapping functions currently available, in particular the (gridded) VMF1, considered the best mapping function available, and that is recommended by the IGS.

The data processing described in the first section (5.2) covers the essential parts of how all results presented in this thesis (this chapter, and Chapters 6 and 7, and the appendices) were generated, although the scope of the present is limited to symmetric mapping functions. In particular, the atmospheric pressure loading models tested are examined and compared here for consistency but their impact on positioning is presented in Subsection 5.3.2 and Section 5.4.

5.2 Data Processing

5.2.1 NWM and GPS Data availability

To study the impact of mapping functions in the processing of GPS data, Niell [1996] recommended that at least one year of data should be processed (one full natural cycle). Blewitt and Lavallee [2002] recommended that a minimum of 2.5 years worth of data should be processed to properly estimate site velocities. Also, data gaps can influence low frequency estimates of an inferred signal [Ray et al., 2008]. Because - as shown below, the NWM and GPS data sets available are far from complete, it was decided to process the full period of data available at that time, although this would increase the volume of processing, the results

in turn would be statistically more robust.

The processed period was limited by the NWM data availability from the British Atmospheric Data Center (BADC). The UK Mesoscale Unified Model (MESO) from the UK Met Office used in this work was available from 2003 and was decommissioned at the end of October 2006, hence limiting the processing period to these dates. That is, the processing was carried out over a 3.8 year period, from January 2003 to October 2006 inclusive. To process day DD/MM/YY (DD+0MMYY), five NWM output files are needed: DD+0MMYY00, DD+0MMYY06, DD+0MMYY12, DD+0MMYY18, and DD+1MMYY00. Unfortunately, NWM files for every day of the processed period were not available at the time of download of the products, and days with some data available were not all complete.

Overall the period considered is 1401 days; however, only 1105 could be fully ray traced (see Figure 5.1), that is 78.9% of the potential sample. For days with missing NWM files, a linear interpolation could have been performed to "replace" the missing data, but this idea was left out because the significant number of missing days (296 out of 1401 or 21.1%) would have certainly affected the results and conclusions of the research presented.

As the MESO only covers the UK, thirty continuous GPS (CGPS) stations in the UK were selected based on their good data availability over the period from January 2003 to October 2006 and their geographical spread over the UK. A map of the selected sites is presented as Figure 5.2. The UK IGS stations HERS, MORP and NPLD were included, although MORP is known to be rather noisy. The combined, definitive data availability (NWM data availability $\times$ GPS data

availability) is presented in Figure 5.3 for each station. The number of days that can be processed for each station is given on the right hand side of the figure. If no further events prevent the station being processed, this number is the maximum number of days that will constitute the time series analyzed later in this work, and on which residuals and statistics like weighted RMS will be computed. The maximum station wise NWM $\times$ GPS data availability varies between 806 days for THUR to 1101 days for HERS, that is, over the 1401 days period considered, from 57.5% to 78.6 %. The missing NWM data can be expected to cause a systematic effect. Patterns in the data availability can influence the sampling of the frequencies of the position time series according to Ray et al. [2008], especially in the low frequency bin, hence the importance to know the NWM $\times$ GPS data availability over time. As can be seen on Figure 5.3, major gaps exist but no immediate pattern can be detected. Simulations would be needed to properly assess the impacts of those gaps but this was judged to be beyond the scope of this work, which is not mainly concerned with signal periods retrieval.

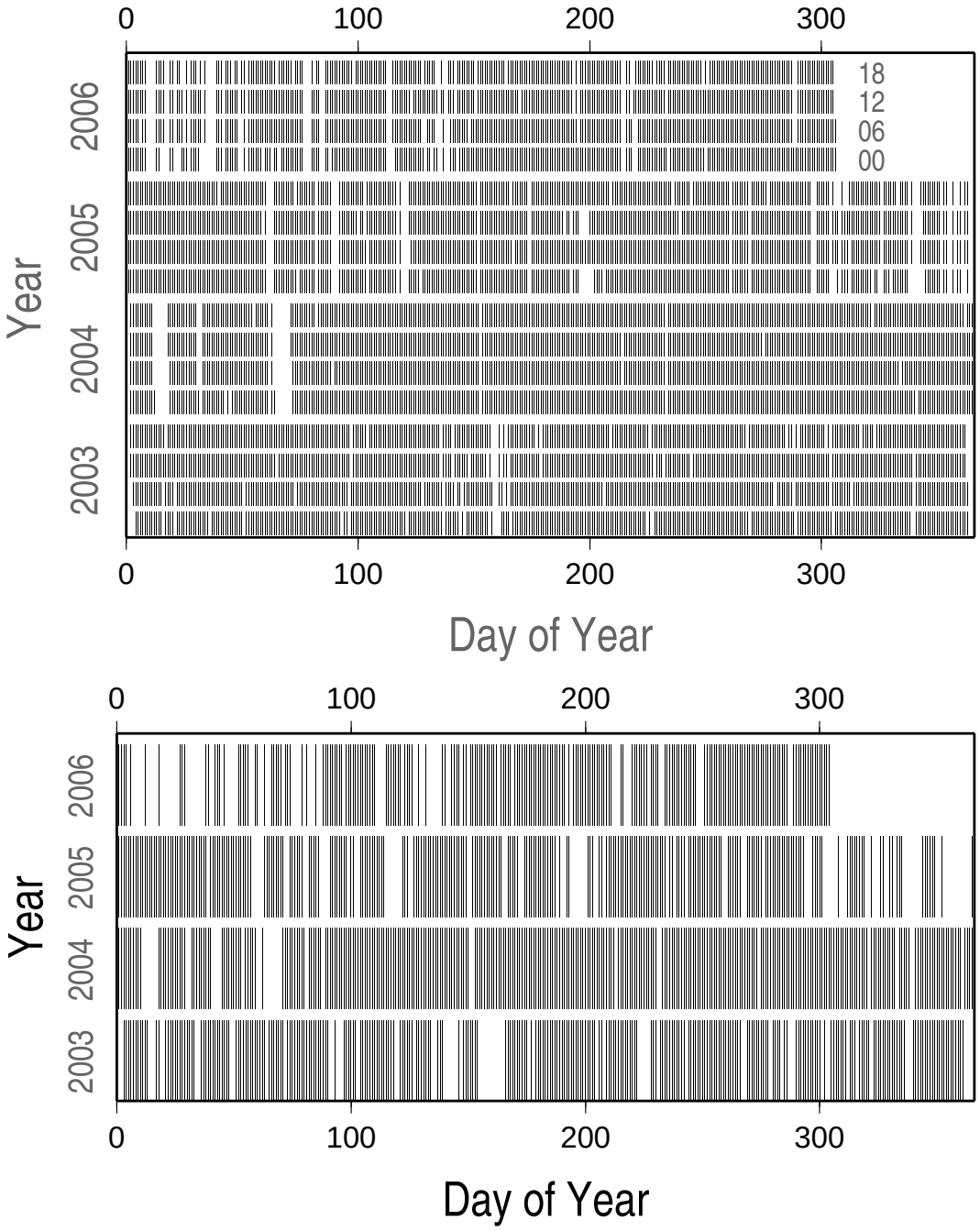

Figure 5.1: Six hourly (top) and daily (bottom) NWM data availability for the period January 2003 to October 2006.

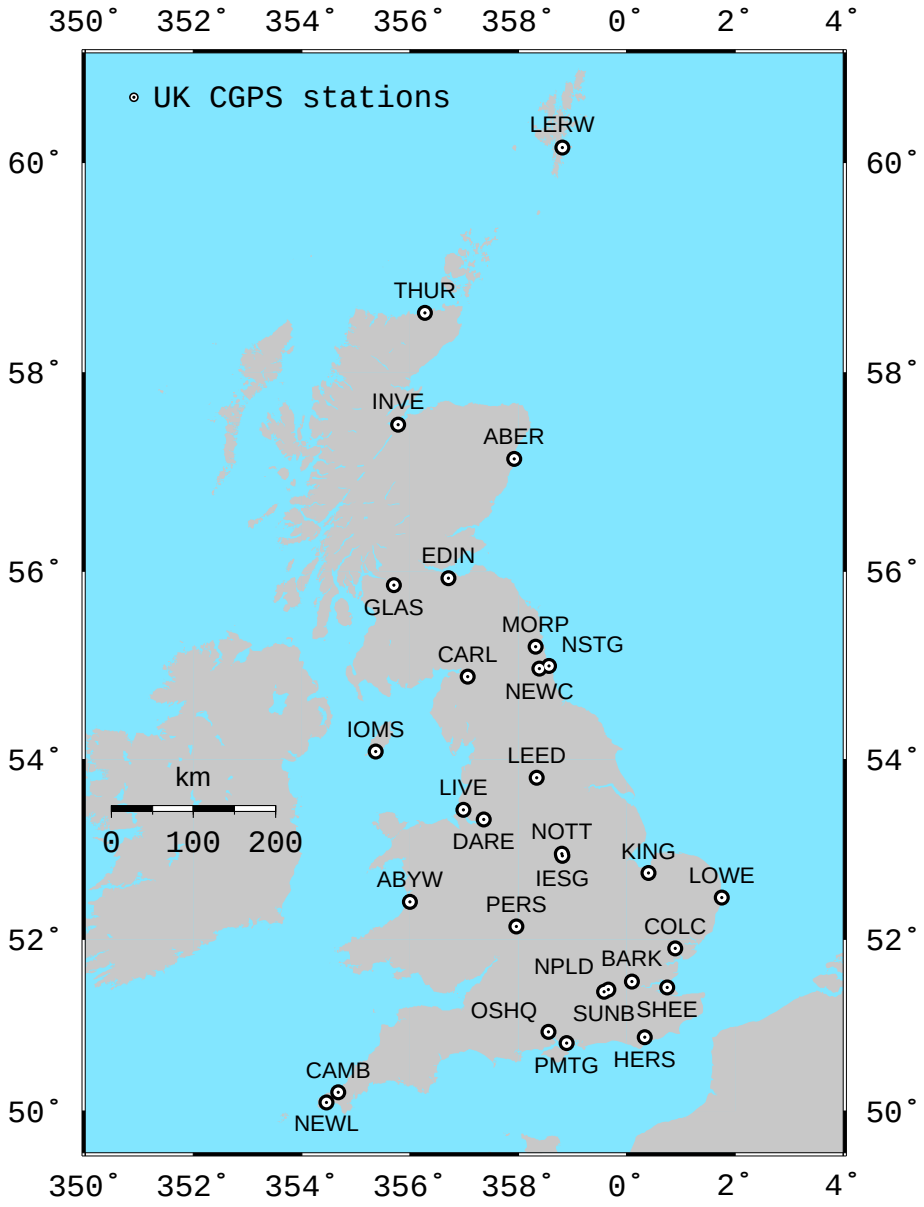

Figure 5.2: Station selection for testing the new OMF mapping functions, as a tradeoff between GPS and NWM data availability and geographic distribution.

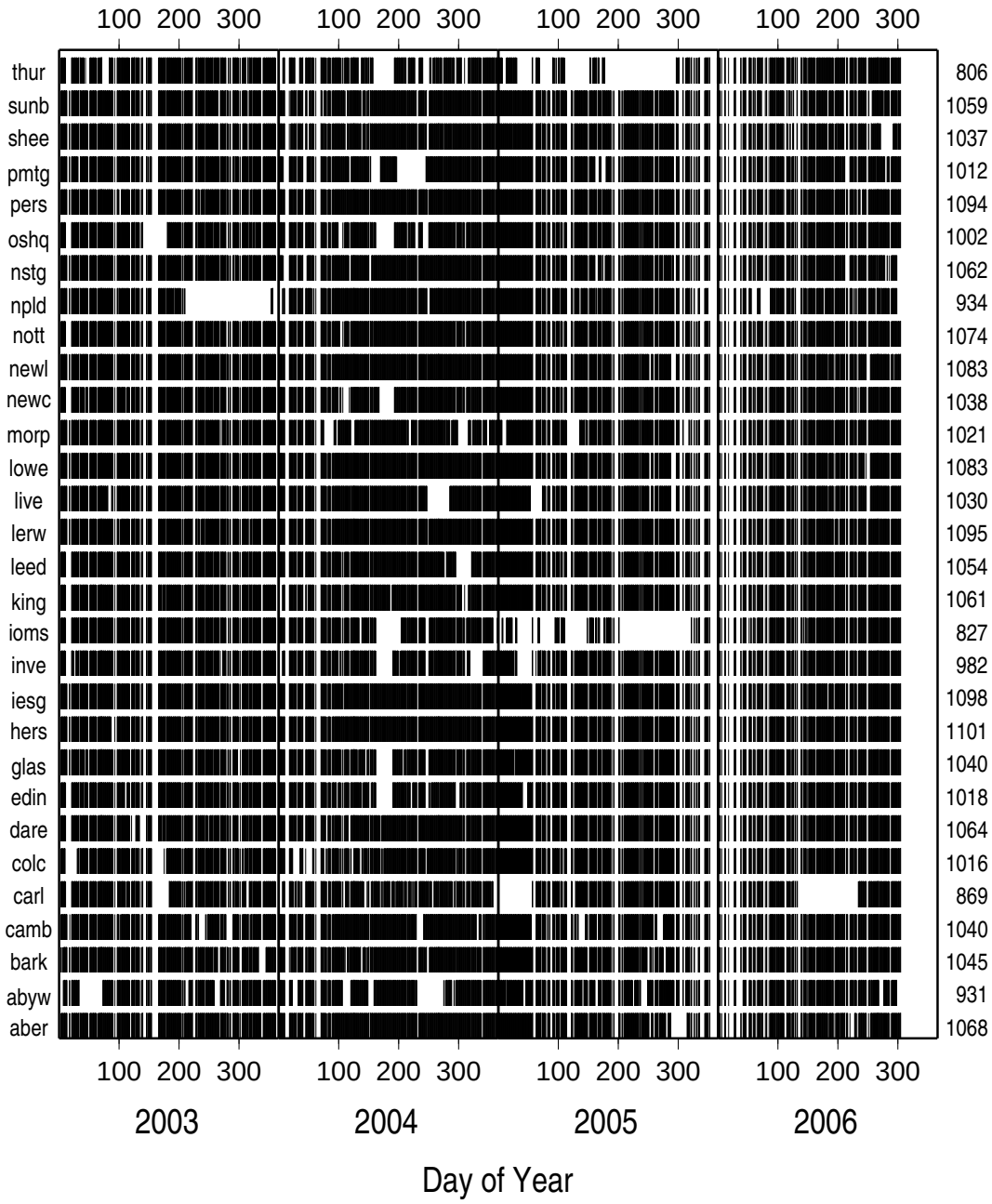

Figure 5.3: Combined daily data availability (based on NWM and GPS data availability). Numbers on the right hand side are the number of full days per station.

5.2.2 Strategy and Solution Description

Each neutral atmosphere modelling strategy used in this study, as listed and described in Table 5.1, was used to process the full data set (30 stations over 3.8 years) at least once, with no atmospheric pressure loading corrections applied. All the processing was carried out using the Bernese GPS software V5.0 ([Dach et al., 2007], BSW50 hereafter) in the precise point positioning (PPP) mode. In Table 5.1, 'Standard ZHD' refers to an a priori information computed using the Saastamoinen model with meteorological input adjusted for height using Berg [1948] from reference values (reference pressure of 1023.25 hPa at the reference altitude h_r of 0 metre). In the OMF solutions an 'S' means Symmetric (not explicitly mentioned in NMF, GMF of VMF1 solutions, as the corresponding mapping functions are only available in a symmetric fashion). The 'G' in the VMF1G means 'Gridded', to stress the fact the gridded version of the VMF1 is used, as opposed to the site specific one. The 'RT' and 'HRT' mean that consistent ray traced a priori hydrostatic ZHD is used in the solution. The 'T' in OMTS means that the 'Total' version of the OMFS is used.

Table 5.1: Description of the different tropospheric modelling strategies used in the study.

Strategy	A priori information	Mapping function
NMF	Standard ZHD	NMF (hyd + wet)
GMF	Standard ZHD	GMF (hyd + wet)
VMF1G	Standard ZHD	Gridded VMF1 (hyd + wet)
VMF1GRT	Interpolated gridded ray traced ZHD	Gridded VMF1 (hyd + wet)
OMFS	Standard ZHD	OMF (hyd + wet)
OMFSHRT	Site ray traced ZHD	OMF (hyd + wet)
OMTS	*Anything*	OMF total

All the mapping functions are covered in the background chapters of this thesis. Note that using a total mapping function in place of the usual pair of hydrostatic

and wet mapping functions means using it twice in BSW50 and makes the modelling of the ZTD purely linear, therefore independent from the a priori value. The gridded VMF1 was implemented in BSW50 by the author following Kouba [2008] except that no height corrections were applied to the wet mapping function. As a check of the implementation, time series of mapping functions coefficients and zenith delays presented in Kouba [2008] were reproduced but no GPS processing was carried out to this end because of the different GPS software used in [Kouba, 2008].

A better, more realistic, modelling of the troposphere delay should lead to a better retrieval of the effect of atmospheric pressure loading (APL), one of remaining signals not modelled by default. Hence, by compensating the induced effect of APL, an improvement in the positioning performance is expected.

For all seven strategies in Table 5.1, two further solutions can be readily obtained by applying daily average coordinate corrections for atmospheric pressure loading, from two models: (*i*)the first one, labelled as LP ([Petrov and Boy, 2004]) is a non-tidal model; (*ii*) the second one, labelled as TVD, is a partially tidal model (T. van Dam, pers. communication, 2008). These two different APL models were tested as significant differences exist between the two (see below), and in the light of the findings of Tregoning and van Dam [2005], where different combinations of tidal and non-tidal models were investigated. A fourth solution was also obtained by applying APL corrections at the observation level, but this was not done for all strategies, as it required reprocessing of all of the GPS data. Still, according to Tregoning and van Dam [2005], this should be worth the effort, as they found that observation level corrections yielded better accuracy for 77% of the globally distributed sites they processed (double difference mode using GAMIT `http://www-gpsg.mit.edu/~simon/gtgk/index.htm`). In summary, therefore,

up to four solutions were obtained for each tropospheric modelling strategy:

Solution 1 ... No atmospheric pressure loading correction (OFF).
Solution 2 ... Daily coordinate estimates corrected with daily time averaged APL corrections, with six hourly corrections from the LP model (aplo package).
Solution 3 ... Daily coordinate estimates corrected with daily time averaged APL corrections, with six hourly corrections from the TVD model.
Solution 4 ... APL corrections applied at the observation level, with six hourly corrections from the TVD model.

5.2.3 Modification of the Bernese GPS Software V5.0

Some further modifications (apart from the implementation of the GMF, gridded VMF1 and OMF mapping functions themselves and modifications of related printing subroutines) were made to BSW50 by the author in order to carry out the desired processing.

1. New observation weighting scheme

Because low elevation GNSS observations (let's say below 15 degrees) are more likely to be noisier than higher elevation ones, due in particular to their longer travel path in the atmosphere and their higher probability to be affected by multipath, they are usually down weighted in the parameter estimation. In the BSW50 package, the standard weighting scheme is defined as follows:

$$w(z) = \cos^2(z) \tag{5.1}$$

where w is the weight and z the zenith angle. Rewritten in terms of observation covariance and elevation angle instead of zenith angle is obtained:

$$\sigma^2(\epsilon) = 1/\sin^2(\epsilon) \tag{5.2}$$

where σ^2 is the variance of the observation taken at ϵ degrees elevation. As the focus of this work is to improve the mapping of the zenith delay(s), and part of the weighting justification is due to uncertainties in existing mapping functions, the weighting scheme as used in Tregoning and Herring [2006] was preferred:

$$\sigma^2(\epsilon) = a^2 + \left(\frac{b}{\sin(\epsilon)}\right)^2 \tag{5.3}$$

where ϵ is the elevation angle and σ the covariance factor that equals the inverse square root of the equivalent weight, and a and b two constants. A constraint in BSW50 is that the weight at zenith should always be equal to 1.0. Therefore Equation 5.3 had to be normalized by $a^2 + b^2$. Figure 5.4 represents the difference in term of observation weight between the default BSW50 scheme and the one used in Tregoning and Herring [2006] (TH9,5 hereafter) for elevation angles ranging from 3 degrees to zenith. The relative weight given to any observation is always higher with the TH9,5 approach than for the default BSW one.

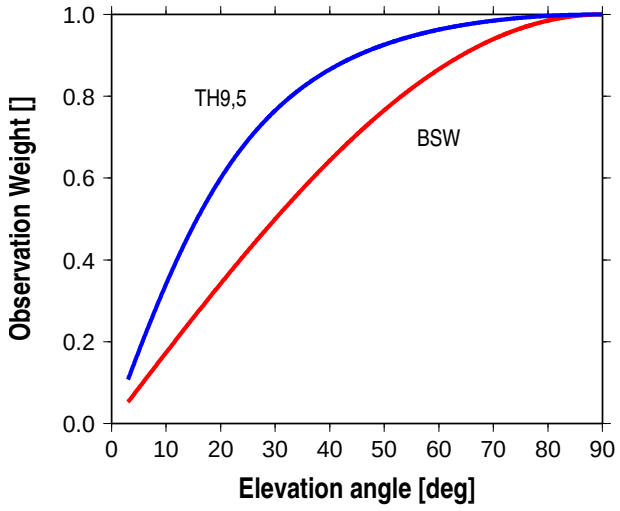

Figure 5.4: Default BSW50 GNSS observation elevation weighting function (red curve) versus the (normalized) weighting function used in Tregoning and Herring [2006] (blue curve).

2. Correcting for atmospheric pressure loading (APL) at the observation level

Time series are given as horizontal and radial displacements. Background information on APL is given in Sections 2.5.3 and 5.3. The BSW50 package was modified to correct coordinates at the observation level. From the APL North, East and Up displacement time series, a series of files containing the equivalent geocentric APL displacements were generated using the following relationship between the local displacements d_{ENU} and geocentric displacements d_{XYZ}:

$$\begin{pmatrix} d_X \\ d_Y \\ d_Z \end{pmatrix} = \begin{pmatrix} -\sin\lambda_0 & \cos\lambda_0 & 0 \\ -\sin\phi_0\cos\lambda_0 & -\sin\phi_0\sin\lambda_0 & \cos\phi_0 \\ \cos\phi_0\cos\lambda_0 & \cos\phi_0\sin\lambda_0 & \sin\phi_0 \end{pmatrix}^{-1} \begin{pmatrix} d_E \\ d_N \\ d_U \end{pmatrix} \tag{5.4}$$

where λ_0 and ϕ_0 are the longitude and latitude of the GPS site supplied to generate the APL time series. The information is stored in files for each station and each epoch (00, 06, 12 and 18 UTC every day). The nomenclature of the expected file is the following: SSSSMMMMMX.TVD where SSSS is the 4 char ID of the station, MMMMM is the modified Julian day (MJD) and X is A for 00 UTC, B for 06 UTC and so on. A subroutine called GETAPL.f was created by the author to compute the APL displacement from the available information. According to the observation time T_{obs}, it will load the two files surrounding T_{obs} and simply linearly interpolate in between. GETAPL.f is called from XYZTIM.f (subroutine part of the BSW50 package for "correcting geocentric coordinates for time-dependent effects", Dach et al. [2007]) after the computed geocentric coordinates have been corrected for Earth tides and ocean tide loading.

5.2.4 Modelling of offsets in the time series

It is common in position estimate time series analysis to assume that the true change of position of a station over time is strictly linear except at epochs of discrete discontinuities (Ray et al. [2008]), otherwise known as offsets. Properly modelling them is crucial for position estimation and its time derivatives (e.g. [Williams et al., 2004]). An offset can have different origins, among them, two major causes were considered in this work: (i) a change of hardware at the site (receiver and/or antenna), and (ii), a change in the processing strategy of the IGS analysis center, such as CODE, that created the products (orbits, ERP and clocks) used to process the data.

Global offsets

Global offsets are discontinuities with known origin that affect all time series. Generally, this will reflect a change in the processing strategy, usually a change in the modelling of a physical effect or phenomenon. Five potential offsets were identified from Hugentobler et al. [2005] available from `http://www.aiub.unibe.ch/download/papers/codar\_0304.pdf`. Identified offsets from this list were introduced, on a direction basis only (North, East or Up), for all stations. No similar reference seems available for years 2005 and 2006 but from a visual inspection of the time series, it is likely that any change in the CODE processing strategy did not significantly affect the solutions obtained here. Table 5.2 summarizes the changes that were identified as potential offset causes, as extracted from Table 2 in Hugentobler et al. [2005]. Some changes were related to a move to IERS 2003 conventions. Probably the most significant change was related to a bug discovered in the IERS 2000 conventions, (present already in IERS 1996) in the computation of site displacements due to solid Earth tides [Hugentobler et al., 2005]. Here is the assessment of the magnitude of the impact provided by CODE (available

Table 5.2: Selection of changes in the CODE processing strategy that were considered to potentially impact time series of estimated coordinates and/or ZTDs (extracted from Table 2 in Hugentobler et al. [2005]).

Change date		Description of the change
16-Sep-03	...	Geometric part of phase windup considered in zero-difference processing
29-Oct-03	...	IERS 2000 subdaily pole model implemented
07-Jul-04	...	Tidal step 2 corrections updated to IERS standards
14-Jul-04	...	Computation of solid Earth tides step 2 corrected
15-Dec-04	...	Update from JPL DE200 to DE405 ephemeris and ocean tide model changed to CSR30 (previously FES95.2).

from `http://www.bernese.unibe.ch/Bugs07-JUL-04.html`, bug 9): "*Error in step 2 correction of solid Earth tides [...] causes sub-daily station height variations with an amplitude of 1 cm at mid-latitudes. Station heights in small networks are not affected (0.1 mm), in large regional networks the scale may show an annual variation, and in global networks the height component of mid-latitude stations is affected by up to 1 cm. Troposphere zenith path delays show a periodic daily variation with an amplitude of 4 mm at midlatitudes*".

Local offsets

Local offsets were selected on the basis of known hardware changes at the station or when visually identified in time series. They are site and direction dependent, contrary to the global offsets which are only direction dependent.

Offset selection

The selection of offsets to be modelled in time series is somewhat subjective as not all hardware changes will create an offset in the coordinate time series. Some analysis centers opt for systematic modelling, where all antenna changes

are marked as offsets in time series. However, it was decided in this work to select only significant offsets. Based on their estimated magnitude and attached uncertainty when the time series was processed using CATS [Williams, 2008], with annual and semi annual signals for functional model and white noise for the stochastic one. This is an iterative process. In Figures 5.5 and 5.6 are presented examples of time series that illustrate the procedure. Plots on the left hand side contain all potential offsets, whereas plots on the right hand side only contain the significant offsets selected. These two time series are presented here because they were rejected from the study due to their rather abnormal behaviors. Similar time series for all 30 CGPS stations are presented in Appendix 9.

Cleaning of time series

Time series were also screened for outliers using an iterative moving average procedure with fixed a priori sigma (roughly the average weighted RMS of the GMF solution over the 30 stations, respectively 2.5, 3.0 and 5.5 mm for the North, East and Up components) and a threshold of 3.0 (interval of confidence of 99.73%). The window length was set to 40 days and was moved forward by steps of 10 days. Gaps in the time series didn't allow for the computation of the sigma zero 'on the fly'. Too wide windows were required to process all time series and some outliers were left unidentified, hence the fixed a priori sigma. Bad periods were simply rejected from all three directions when identified in at least one of them. This was a decision of the author, although one could argue that the deletion should be based on a direction basis only.

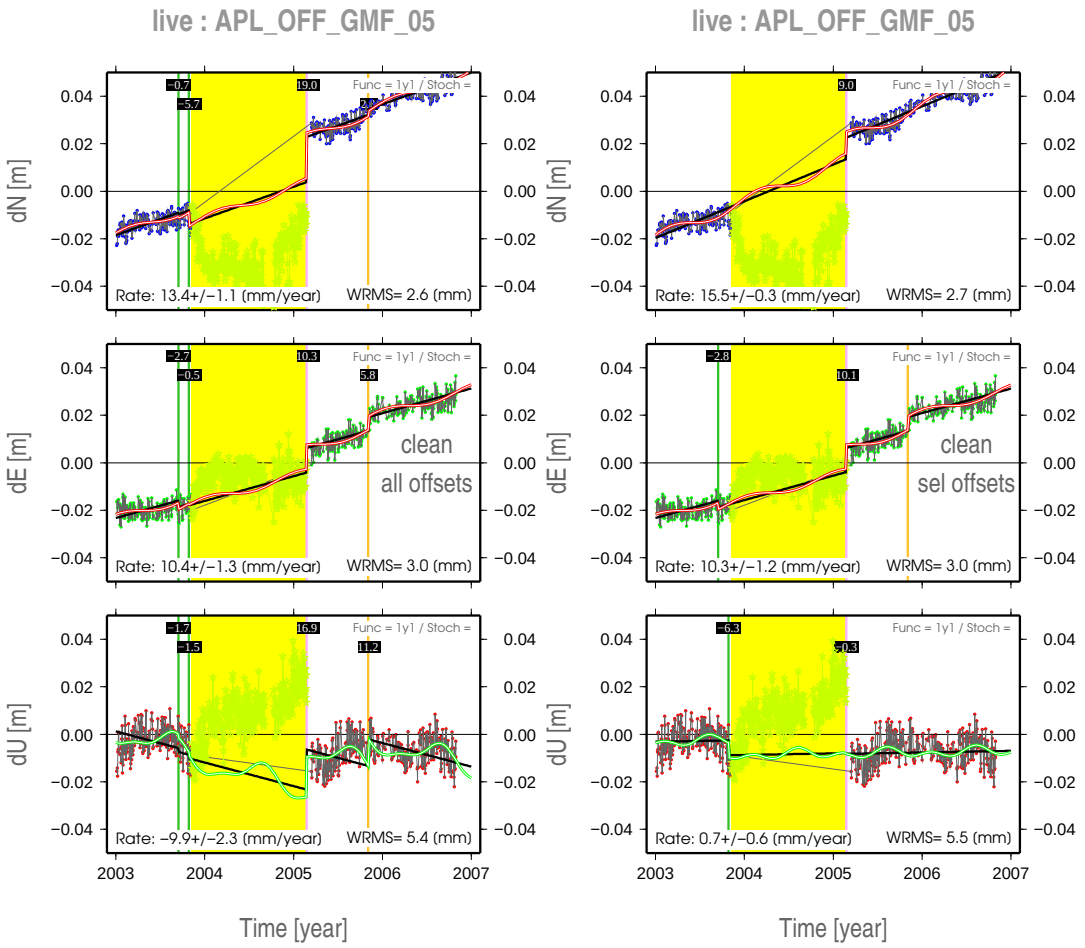

(a) All Offsets

(b) Selected Offsets

Figure 5.5: Example offset selection for CGPS station LIVE. **Left plot**: all potential global offsets induced by changes in product generation, local offsets due to hardware changes (receiver/antenna) and visually identified offsets included. **Right plot**: only offsets identified as significant included. Green bars represent "global" offsets (from product generation). Light grey bars represent receiver changes. Pink bars represent antenna changes. Black bars are simultaneous receiver plus antenna changes. Orange bars indicate where an offset was not attributed to a hardware change nor a change in the processing strategy of the analysis center who generated the products but was manually added. Yellow areas are bad periods which were taken away from the analysis. Black lines represent (broken) linear variations whereas white on red lines (East and North) and white on green (Up) represent (broken) linear plus annual plus semi-annual signals as estimated using MLE using respectively all offsets (left) and selected only (right) offsets.

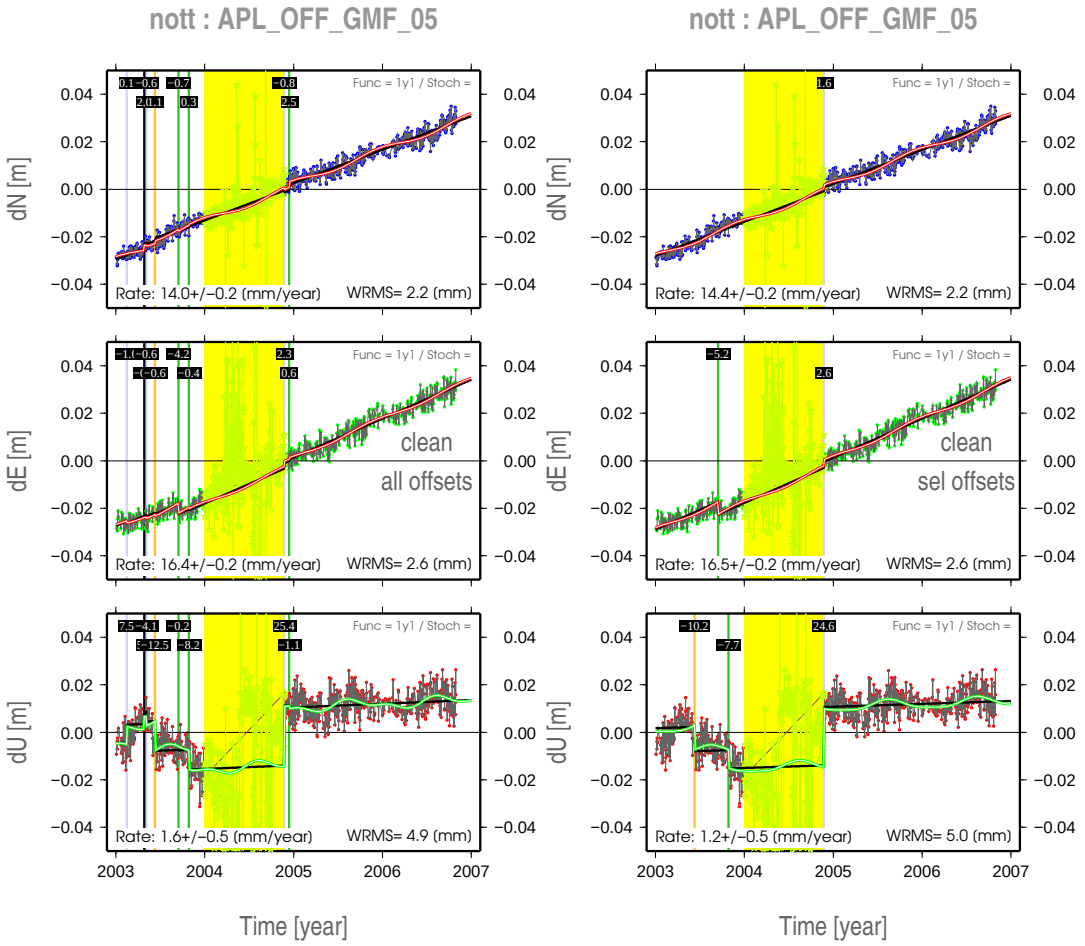

(a) All Offsets

(b) Selected Offsets

Figure 5.6: Example offset selection for CGPS station NOTT. **Left plot**: all potential global offsets induced by changes in product generation, local offsets due to hardware changes (receiver/antenna) and visually identified offsets included. **Right plot**: only offsets identified as significant included. Green bars represent "global" offsets (from product generation). Light grey bars represent receiver changes. Pink bars represent antenna changes. Black bars are simultaneous receiver plus antenna changes. Orange bars indicate where an offset was not attributed to a hardware change nor a change in the processing strategy of the analysis center who generated the products but was manually added. Yellow areas are bad periods which were taken away from the analysis. Black lines represent (broken) linear variations whereas white on red lines (East and North) and white on green (Up) represent (broken) linear plus annual plus semi-annual signals as estimated using MLE using respectively all offsets (left) and selected only (right) offsets.

5.3 Atmospheric Pressure Loading

Variations in the loading of the Earth's crust by atmospheric masses yield deformations in the up component of up to 20 mm ([Petrov and Boy, 2004], [Tregoning and van Dam, 2005]) and 3 mm in the horizontal ([Petrov and Boy, 2004]). Several publications have been dedicated to the detection and mitigation of the atmospheric pressure loading in coordinate time series inferred either from GPS or VLBI data. A literature review is given in the introduction of Petrov and Boy [2004]. The computation of APL induced displacements at a location and epoch require the convolution of the global pressure variation field with Green's function [Farell, 1972]. Details on the computation are available in Petrov and Boy [2004] where four major sources of error in the computation of the APL induced displacement were identified: "*(1) errors in the Green's functions; (2) errors in the land-sea mask; (3) errors in the pressure field; and (4) mismodeling the ocean response to atmospheric pressure forcing*". They estimated a global error budget of 15% in their computation.

An unfortunate aspect of the main reanalysis pressure data sets available (like NCEP Reanalysis [Kalnay et al., 1996]) is their time resolution of 6 hours, as the S2 tide has exactly the Nyquist frequency of their sampling resolution. Consequently S2 cannot be modelled properly. van den Dool et al. [1997] report that "*while the semidiurnal cycle can be easily seen in data every 6 hours, certain formal calculations (for example, as to the temporal phase of the tide) are difficult with sampling at the Nyquist frequency*". From the climatological daily cycle in pressure (as pictured at 00, 06, 12 and 18) "*S2 appears as a standing wave rather than a known westward propagating wave, with much reduced amplitudes at certain longitudes where S2 happens to be sampled near its node*" [Ponte and Ray, 2002]. Building on the work of van den Dool et al. [1997], Ponte and Ray [2002] showed that no simple models with amplitude and phase grids at fixed

frequencies could fully represent ECMWF tides temporal variability. To handle this temporal variability, they used monthly mean amplitude and phase grids. If the climatological daily cycle (in [Ponte and Ray, 2002] estimated using 13 years of data) is removed from the original 6 hours time series, a new time series with weak residual daily cycle is obtained. This new time series can be used to produce a "non-tidal" APL model although it will inevitably contain residual tides. To produce a "tidal" APL model, a monthly model pressure for S1 and S2 can be added to the non-tidal APL model [Ponte and Ray, 2002]. This procedure was followed by Petrov and Boy [2004] to produce their non-tidal model. However, it is clear from their power spectra plots that their model is not purely non-tidal as there are significant peaks at S1 and S2 (see Figures 5.7, 5.11 and 5.12, later).

However, Tregoning and van Dam [2005] found that only applying tidal models for S1 and S2 (at observation level) yields a decrease in positioning accuracy except at stations around the equator, and that application of only daily-average corrections was better than daily-average correction plus tidal models, both relative to an uncorrected solution. In other words, applying just daily-average correction is the best solution of the three mentioned. Whereas, applying the non-tidal model at the observation level improved the solution (height WRMS) for 77% of the sites processed, compared to (non-tidal) daily-average correction. Furthermore, the tidal performed worse than the "partially-tidal" (raw NCEP correction) when both are applied at the observation level, likely because of the tidal components being applied more than once [Tregoning and van Dam, 2005].

5.3.1 Comparison of the two Atmospheric Pressure Loading Models

Two atmospheric pressure loading models were compared. The first one, labelled as TVD, is run by T. van Dam. The second one, labelled as LP (for Leonid Petrov), is described in details in Petrov and Boy [2004]. The *aplo*@L.Petrov (version dated of 2007/06/20) was run to produce the LP corrections whereas the TVD ones were produced by Tonie van Dam [pers. communication, 2007] herself.

LP (*aplo*, Leonid Petrov at NASA)

Petrov and Boy [2004] presented a procedure to compute north, east and up APL induced displacements. It makes use of the NCEP reanalysis product [Kalnay et al., 1996] which has a 6 hourly temporal resolution on a 2.5 x 2.5 degree grid. They claim a maximum error of 15%. Displacements are computed following Farrell [1972]. The *aplo* package, written by Leonid Petrov, is publicly available. The release used in this study is from June 2007. According to L. Petrov [pers. communication, 2007] several errors were corrected from the previous release. For seven stations in the UK, APL displacements routinely produced by Petrov are available as atmospheric pressure loading time series provided by the Goddard VLBI group, which are available on the web at http://gemini.gsfc.nasa.gov/aplo. Before producing APL corrections for the 30 stations used throughout this work, 7 year long time series were produced for those seven stations in the UK in order to validate the implementation and assess the magnitude of the bug corrections brought between the version of *aplo* used in this work and the one used to produce the published time series.

Results are presented in Table 5.3 where no significant bias can be observed. The standard deviations of the 6 hourly differences are almost null for the horizontal but can reach 0.3 mm (NSTG) for the up component. Based on these

Table 5.3: Statistics on the difference between published APL predicted displacements for available UK sites from the NASA APL loading service and the ones produced locally running aplo@Petrov, L. Values given in mm.

	North		East		Up	
GPS site	mean	st. dev.	mean	st. dev.	mean	st. dev.
aber	-0.00	0.01	0.00	0.03	0.00	0.11
hers	-0.00	0.01	0.00	0.02	-0.00	0.10
morp	-0.00	0.04	0.00	0.05	-0.00	0.20
newl	-0.00	0.01	0.00	0.01	0.00	0.03
npld	-0.00	0.01	0.00	0.01	-0.00	0.07
nstg	-0.00	0.06	0.00	0.08	-0.00	0.32
shee	-0.00	0.01	0.00	0.01	-0.00	0.07

results it is safe to assume hereafter that the implementation of the *aplo* package was successful and that results generated for the 30 CGPS stations in the UK are of a similar quality to the ones officially published.

TVD (Tonie van Dam, U. of Luxembourg)

T. Van Dam kindly produced some APL corrections using the NCEP pressure fields. Following Tregoning and van Dam [2005] the model can be understood as a "partially tidal" model as nothing was removed from the original NCEP time series (see above).

Comparison of the LP and TVD APL corrections

Figure 5.7 presents the six hourly time series for two CGPS stations: IESG and CAMB, as predicted by the two models, and the time series of the difference between them (taken as LP minus TVD), for the North, East and Up components. IESG is the most 'inland' of the sites processed whereas CAMB is on the coast, on the Cornish peninsula which is surrounded by the sea. The shape of the UK doesn't allow a site to be approximatively more than 150 km from the coastline.

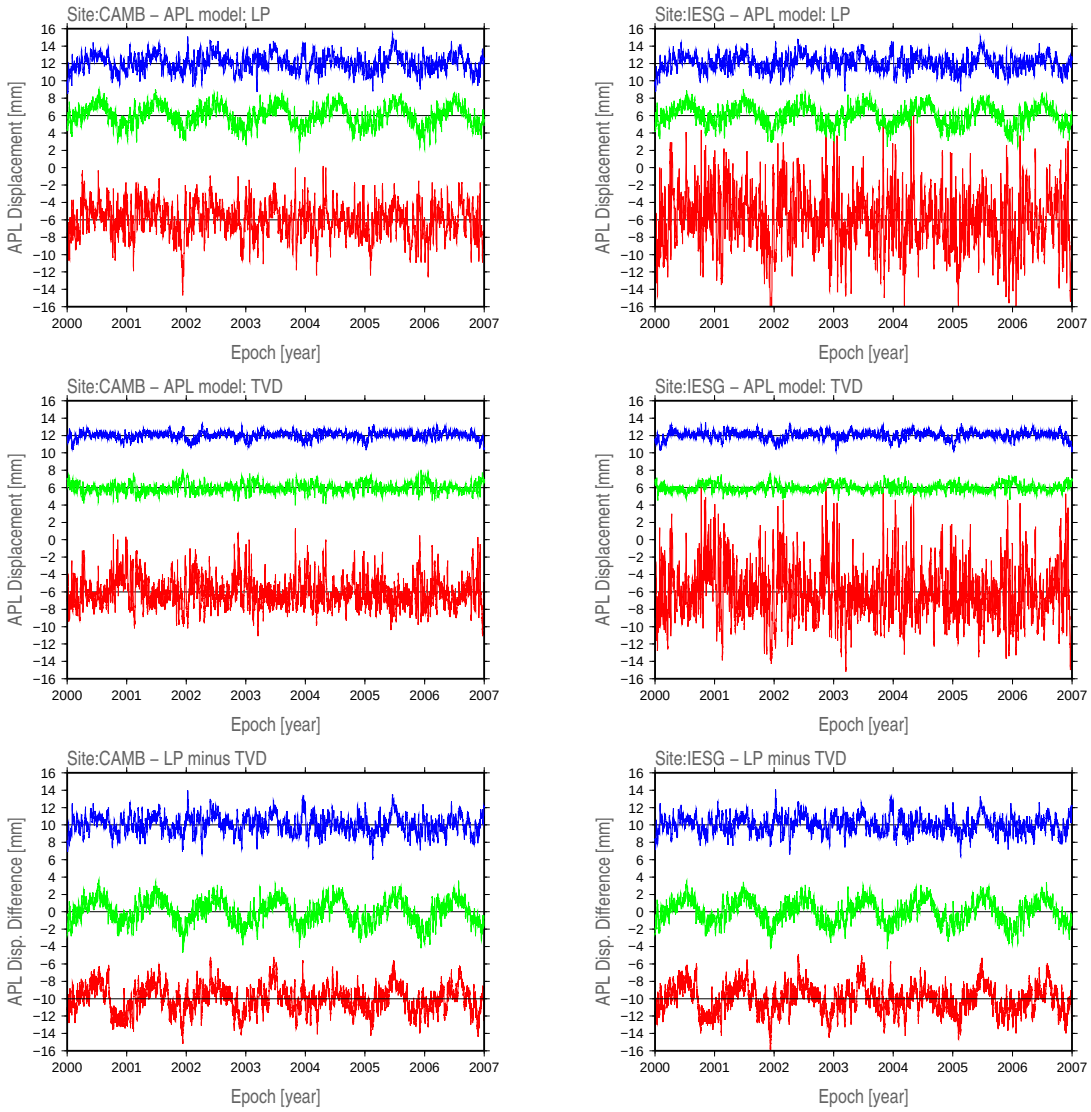

(e) GPS site: CAMB (coastal)

(f) GPS Site: IESG (inland)

Figure 5.7: APL induced displacement time series predicted by the two models LP (top row) and TVD (middle row), for the North, East and Up components at two CGPS stations: CAMB and IESG, and the difference between them, taken as LP minus TVD (bottom row).

From Table 5.4 and Figures 5.8 to 5.10 it can be seen that the TVD model predictions for the horizontal are rather flat, although some seasonal variations are detected. The LP model produces East corrections with a much higher amplitude (1.24 mm) but which is rather constant over the UK, as indicated by a small associated standard deviation (0.03 mm) versus 0.30±0.02 mm for the TVD model. The semi-annual component of LP is about 3.5 times bigger in amplitude than the one obtained by TVD. For the North component, LP produces an annual signal amplitude twice as big as the one of TVD (0.54±0.07 mm versus 0.27±0.02 mm). LP predicts a much noisier vertical APL induced displacement (see Figures 5.8 to 5.10) with much greater peak to peak amplitudes. For the LP model, the seasonal variations in the up component are weaker than the ones found for the East component, with respectively 0.88±0.20 mm and 0.17±0.07 mm for the annual and semi-annual signals whereas this is the contrary for TVD with respectively 0.57±0.20 mm and 0.40±0.12 mm. Although the phase of the annual signals predicted for the North component agree pretty well, there is a significant phase shift of almost 180 degrees for the East and radial component.

The differences between the two models are constant over the processed area (see the bottom plots of Figures 5.8 to 5.10) where the RMS of the 6 hourly differences computed over 7 years are plotted) and found to be, in terms of RMS, 1.0 mm for the north, 1.4 mm for the east component, and 1.6 mm for the up component.

The power spectra of sites CAMB and IESG (Figures 5.11 and 5.12) confirm some findings of previous studies mentioned above, more specifically that the non-tidal model of Petrov and Boy [2004] is clearly not non-tidal, as strong power remains at the daily and semi-daily periods, although the power is reduced against background noise when compared to the TVD model which is based on the convolution of the raw NCEP pressure data field and is known to contain

partially aliased tidal signal.

All of these results highlight that significant differences exist between the predictions of the two models. The amplitudes and phase of the differential time series should be kept in mind when applied as corrections to GPS data as, for example, the seasonal signal observed could explain part of the residual signal seen in GPS time series. Below is compared two approaches of correcting for APL effects in the processing of GPS data: observation level versus average daily corrections.

Table 5.4: Amplitude A (mm) and phase ϕ (deg) of the annual and semi-annual components of the atmospheric pressure loading induced displacement computed from the TVD and LP APL models over a 7 year period. Details are given on a station by station basis for the radial component only and averages plus associated standard deviation for horizontal and radial components.

Details on the up component

	TVD				LP			
	Annual		*Semi-annual*		*Annual*		*Semi-annual*	
site	A	ϕ	A	ϕ	A	ϕ	A	ϕ
ABER	0.83	345.7	0.21	66.6	0.67	166.7	0.24	179.6
ABYW	0.58	340.6	0.45	47.6	0.82	169.0	0.12	102.0
BARK	0.35	337.3	0.46	37.6	1.12	171.8	0.19	46.4
CAMB	0.48	350.2	0.33	40.9	0.85	163.5	0.07	165.0
CARL	0.75	339.8	0.42	55.9	0.71	172.2	0.17	124.1
COLC	0.35	335.0	0.47	37.5	1.15	170.8	0.12	46.4
DARE	0.59	337.1	0.49	48.5	0.83	173.5	0.18	85.5
EDIN	0.80	343.1	0.32	60.3	0.61	173.0	0.20	134.2
GLAS	0.85	341.6	0.39	60.7	0.58	171.6	0.20	138.4
HERS	0.27	336.0	0.50	34.3	1.16	168.7	0.10	37.0
IESG	0.52	334.2	0.51	44.9	0.94	173.9	0.19	71.0
INVE	1.00	343.8	0.30	69.2	0.46	171.2	0.24	155.7
IOMS	0.69	345.0	0.32	54.1	0.72	167.2	0.14	150.2
KING	0.43	339.5	0.40	40.3	1.05	171.8	0.11	67.5
LEED	0.62	337.5	0.46	50.3	0.86	173.1	0.15	94.9
LERW	0.86	349.9	0.06	128.6	0.73	160.6	0.41	22.3
LIVE	0.60	340.4	0.42	49.1	0.81	172.1	0.16	95.8
LOWE	0.34	341.4	0.37	34.7	1.17	168.1	0.04	32.7
MORP	0.71	341.5	0.36	56.1	0.76	171.4	0.15	139.7
NEWC	0.68	341.4	0.36	54.7	0.78	171.4	0.15	136.3
NEWL	0.49	351.4	0.30	41.0	0.84	163.1	0.07	168.9
NOTT	0.52	334.3	0.51	44.9	0.94	173.9	0.19	71.4
NPLD	0.37	333.1	0.53	38.8	1.10	171.9	0.20	47.9
NSTG	0.66	342.9	0.32	54.0	0.81	170.5	0.14	147.2
OSHQ	0.38	335.7	0.55	38.6	1.04	169.4	0.13	53.9
PERS	0.51	334.0	0.55	45.0	0.94	173.6	0.23	63.5
PMTG	0.34	336.5	0.53	36.9	1.07	169.1	0.12	49.9
SHEE	0.31	339.2	0.44	35.3	1.17	170.8	0.15	41.0
SUNB	0.37	333.0	0.53	38.9	1.09	171.9	0.20	48.2
THUR	0.85	348.9	0.12	79.1	0.52	165.2	0.30	1.1

North, East and Up Averages

	TVD				LP			
	Annual		*Semi-annual*		*Annual*		*Semi-annual*	
	A	ϕ	A	ϕ	A	ϕ	A	ϕ
NORTH	0.27(0.02)	177.1(3.9)	0.19(0.02)	16.5(6.9)	0.54(0.07)	167.2(1.6)	0.31(0.02)	128.3(77.4)
EAST	0.30(0.02)	349.5(3.4)	0.08(0.02)	105.7(32.6)	1.24(0.03)	173.2(0.7)	0.30(0.03)	70.6(2.4)
UP	0.57(0.20)	340.3(5.3)	0.40(0.12)	50.8(18.5)	0.88(0.20)	170.0(3.4)	0.17(0.07)	90.6(50.7)

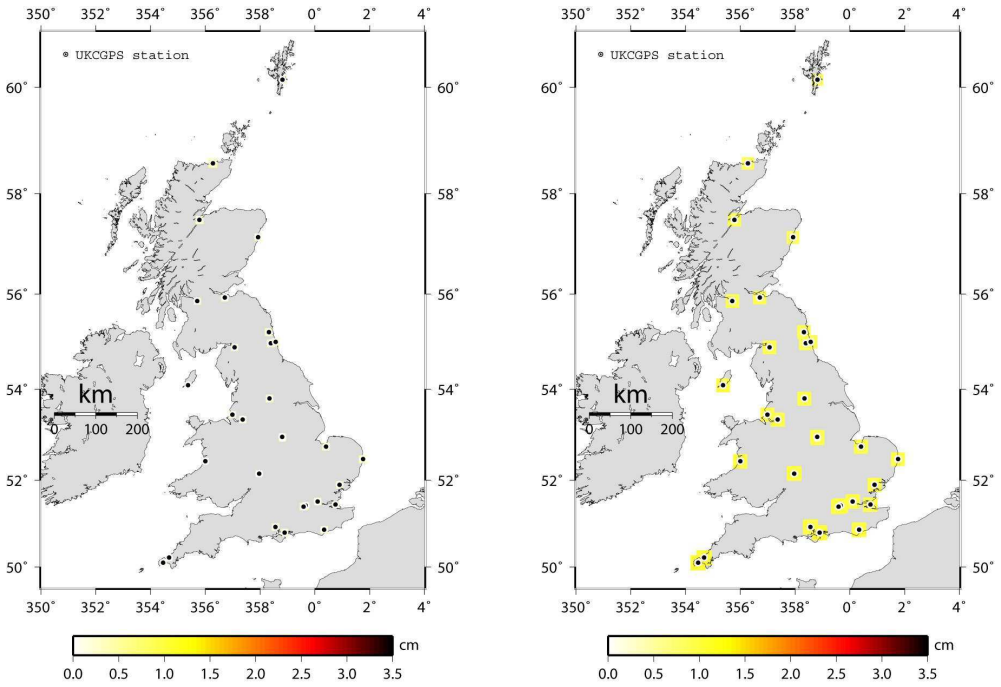

(a) North/TVD

(b) North/LP

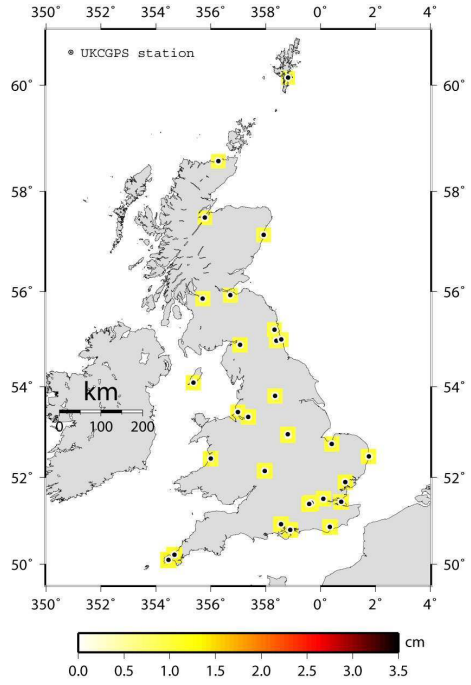

(c) North diff.

Figure 5.8: RMS in mm of the predicted APL induced displacement by the TVD model (top left), the LP model (top right) and the difference <LP minus TVD> (bottom), for the north component. RMS were computed over a 7 years period. Colour and size of the squares are according the magnitude of the RMS.

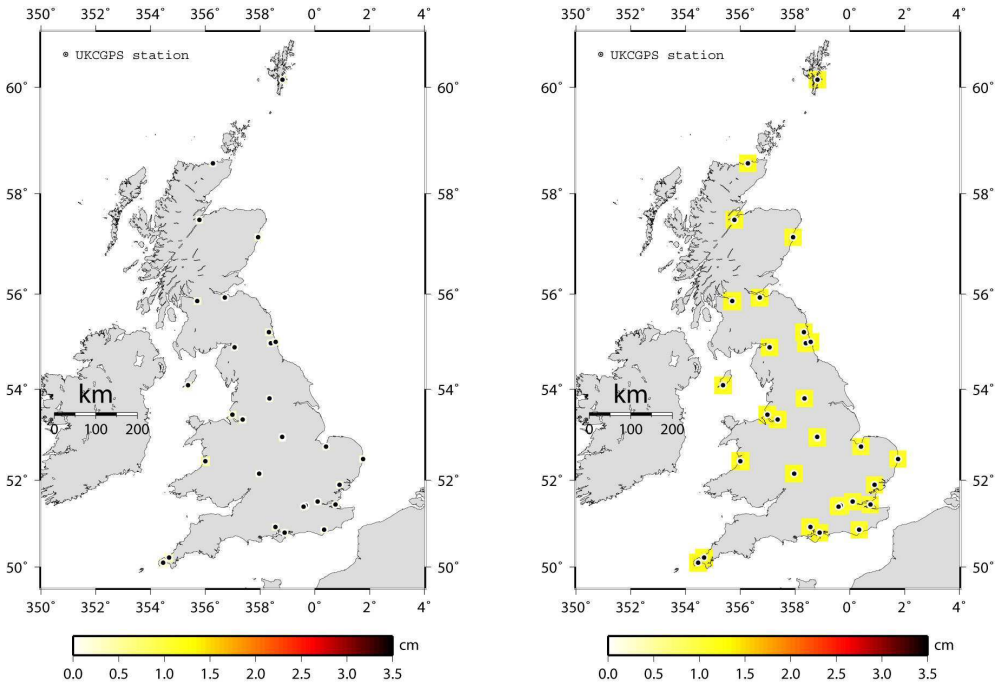

(a) East/TVD

(b) East/LP

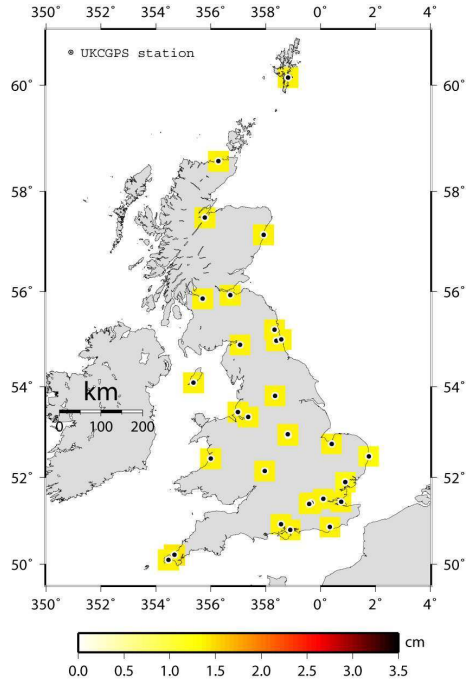

(c) East diff.

Figure 5.9: RMS in mm of the predicted APL induced displacement by the TVD model (top left), the LP model (top right) and the difference <LP minus TVD> (bottom), for the east component. RMS were computed over a 7 years period. Colour and size of the squares are according the magnitude of the RMS.

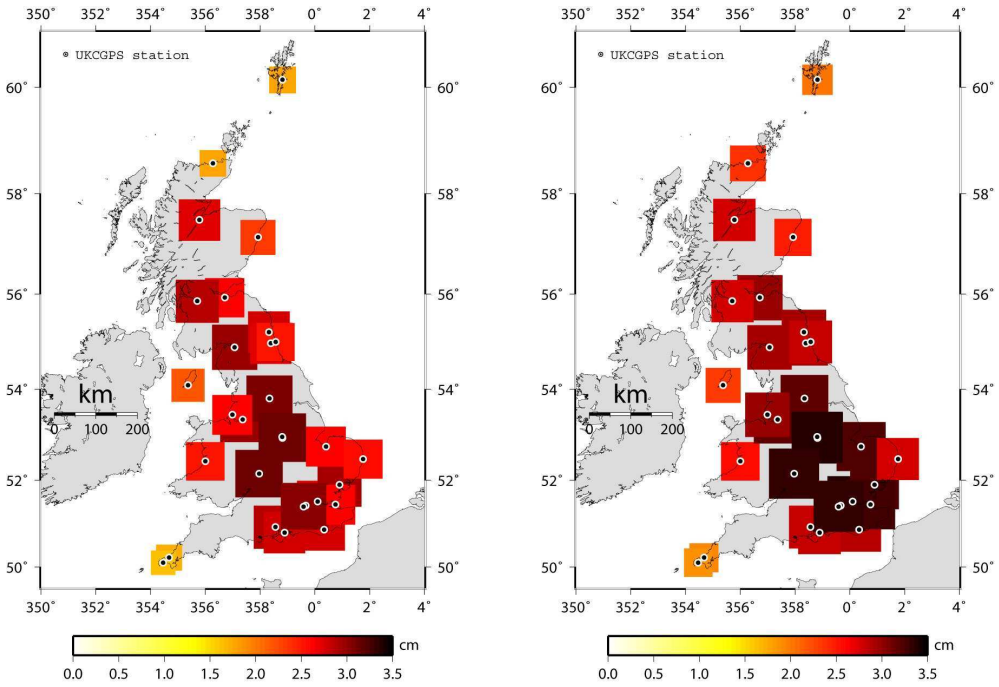

(a) Up/TVD

(b) Up/LP

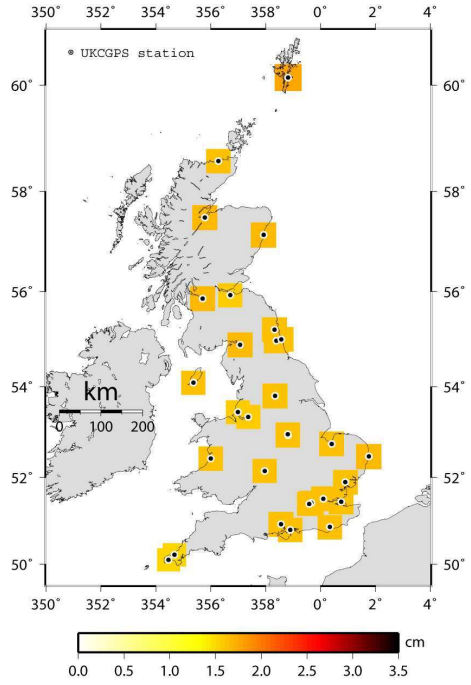

(c) Up diff.

Figure 5.10: RMS in mm of the predicted APL induced displacement by the TVD model (top left), the LP model (top right) and the difference <LP minus TVD> (bottom), for the up component. RMS were computed over a 7 years period. Colour and size of the squares are according the magnitude of the RMS.

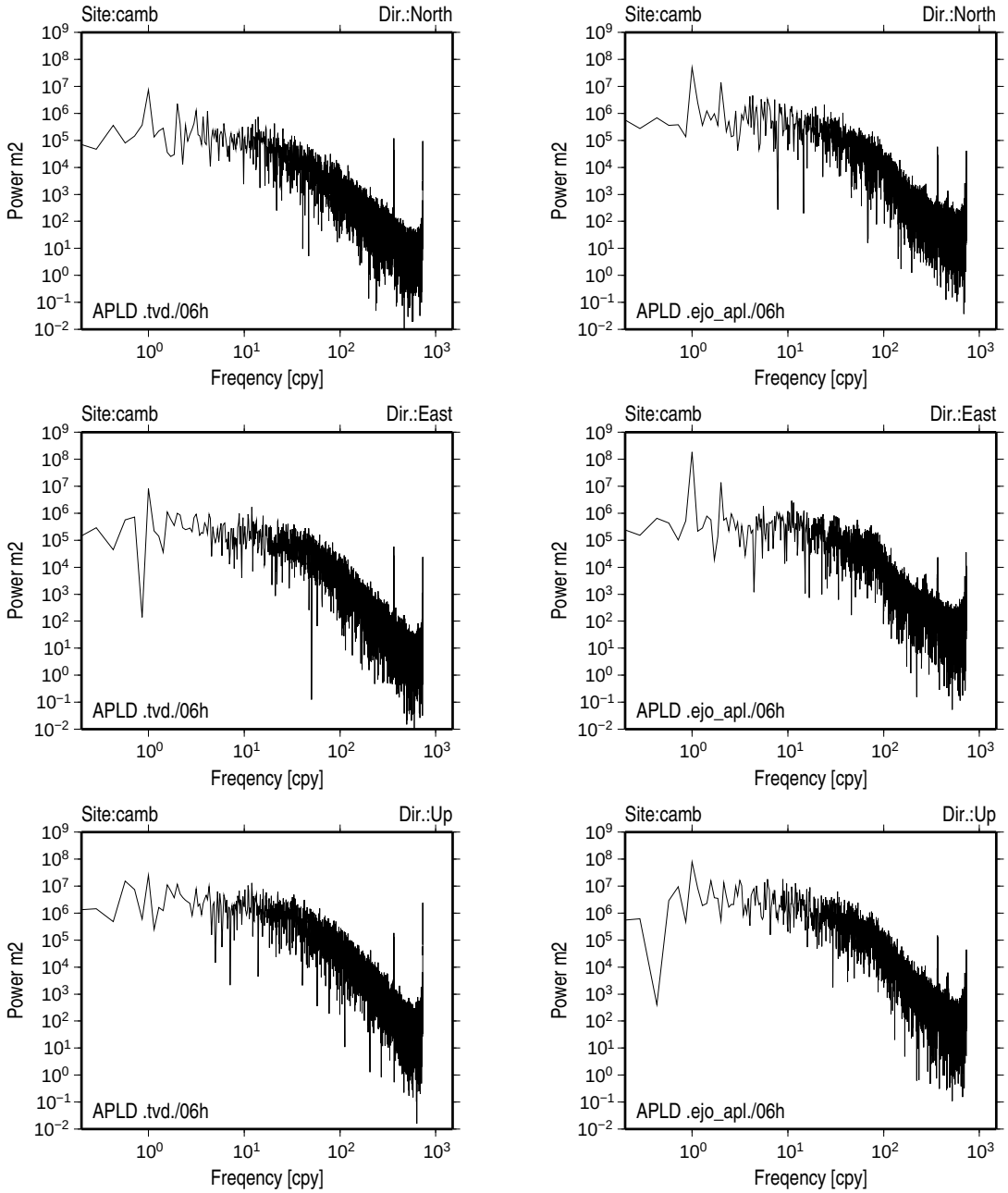

Figure 5.11: Power spectrum densities of the APL induced displacement for the North, East and Up component as computed for CGPS station CAMB for the TVD model (left) and LP model (right).

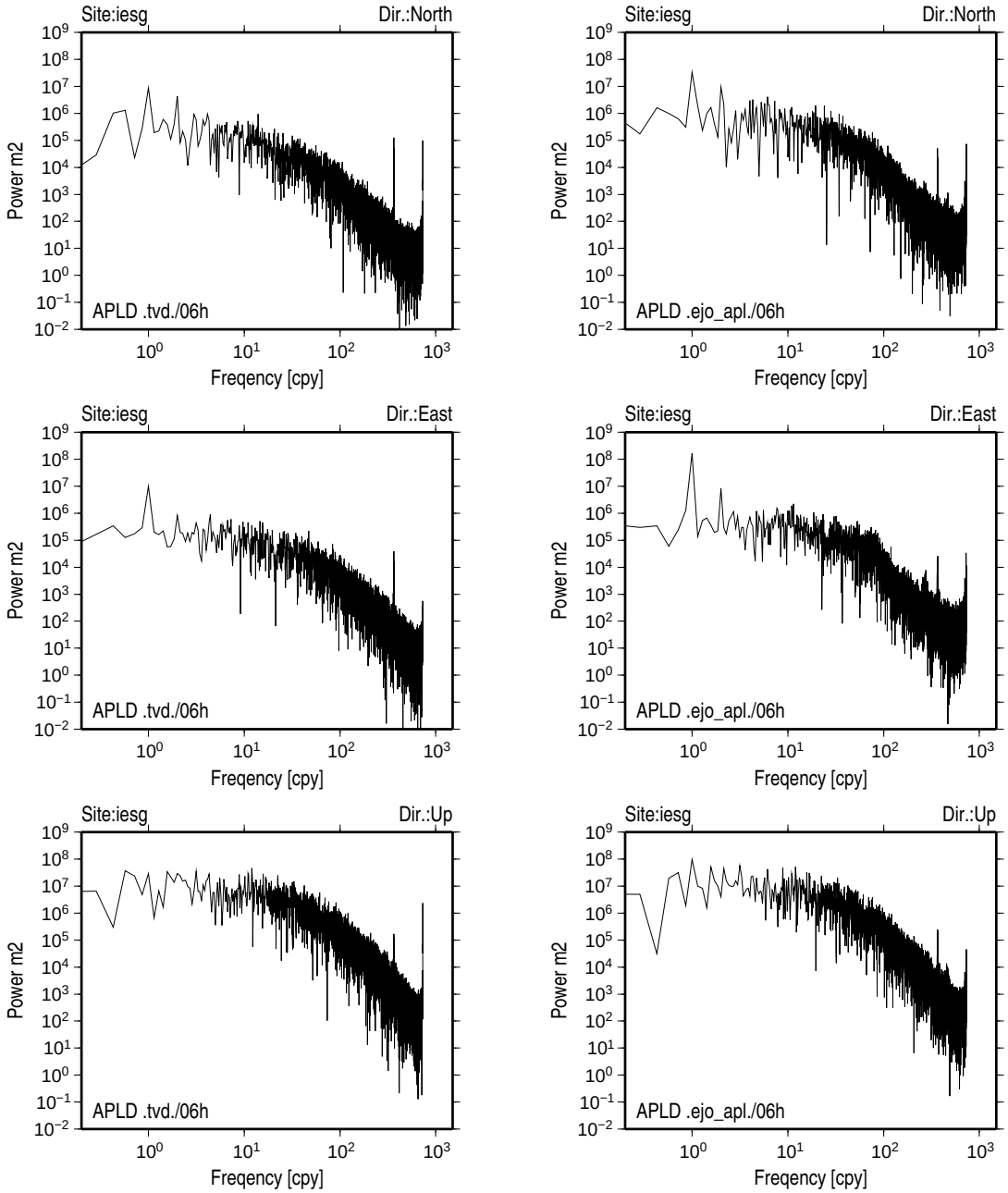

Figure 5.12: Power spectrum densities of the APL induced displacement for the North, East and Up component as computed for CGPS station IESG for the TVD model (left) and LP model (right).

5.3.2 Atmospheric Pressure Loading: Correcting at Observation Level versus Applying Daily Average Corrections to Daily Coordinate Estimates

Position time series obtained by correcting for APL at the observation level and by applying daily average corrections (average computed over five 6 hourly APL estimates available in a day, from midnight to midnight) onto daily position estimates are compared. Background information can be found in Tregoning and van Dam [2005]. Logically, all time varying corrections (like Earth tide or ocean tide loading) should be applied at the observation level. Furthermore, in the case of the APL, both tidal and non-tidal should be applied. However, as mentioned already, Tregoning and van Dam [2005] found a general degradation in positioning accuracy when the tidal component was applied at the observation level. They obtained better accuracy when the non-tidal was applied at the observation level compared to daily average corrections made on estimated coordinates. The corrections applied in the case of the research presented here are somewhere in between, as the model used is partially-tidal. It is not possible however to estimate how partial the model is. Position performances will be examined later on in this chapter (see Section 5.5). For now, the focus is put on differential time series obtained by subtracting the vertical position obtained after daily average correction on the coordinates from the one obtained when the data was processed with corrections for the APL at the observation level.

It was found that, when processing the data using the Niell mapping functions ([Niell, 1996]), for all stations but NOTT and PMTG, the daily difference for the Up component was, on average, 0.00±0.00 mm with an average standard deviation of 0.22±0.04 mm (computed as the mean of the means and the mean

of the standard deviations). All stations exhibit negligible (below one hundredth of a mm) bias between the two solutions except NOTT and PMTG, which, with biases of respectively 0.36±0.31 mm and 3.39±0.24 mm behave not as well. Note that this not true for all mapping functions. Whereas the same behavior with the OMFS is observed, with the OMTS, only NOTT looks abnormal; whereas for time series obtained using the GMF no abnormal behavior is seen at all. Results were checked to make sure this was not due to isolated outliers. When looking at the impact of the mapping function on the ZTD estimates, PMTG was found to exhibit a clear abnormal behavior for some tropospheric modelling and was therefore discarded all together.

With the exceptions of NOTT and PMTG, the standard deviation of the differences are below 0.25 mm although daily differences above 1 mm can occur. See for example Figure 5.13.

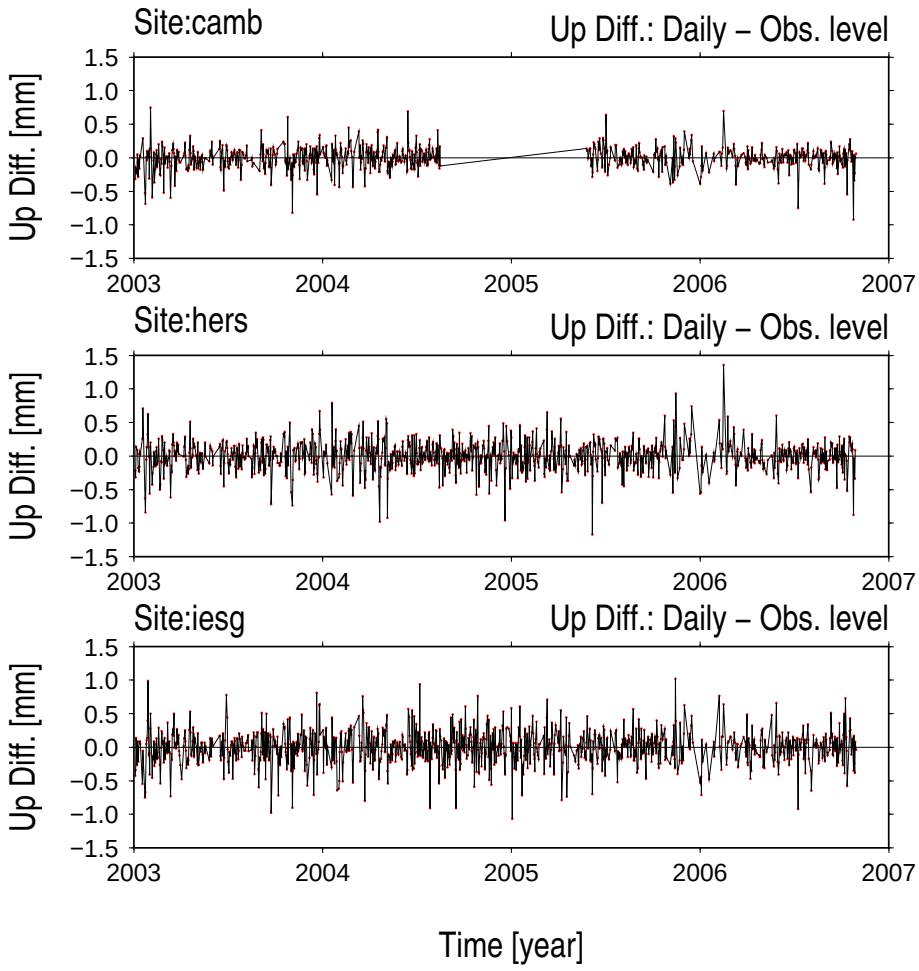

Figure 5.13: Example of time series of the difference in mm in the vertical positions obtained after daily correction for the APL minus positions obtained when processing data corrected at the observation level for APL. All time series shown were obtained using the NMF mapping functions and standard a priori ZHD.

5.4 Impact of Applying Atmospheric Pressure Loading Corrections on Positioning Performances

First summarized in Table 5.5 are the results of a series of tests conducted on the solutions mentioned above over 27 sites. Sixteen solutions were obtained by applying APL corrections estimated from two models, TVD and LP. TVD corrections were applied in two different ways: at the observation level and as daily average coordinate corrections. LP corrections were only applied as daily average coordinate corrections. The weighted RMS (WRMS) of the residuals of detrended time series is taken as the measure of the positioning performance of the solutions.

Table 5.5: Weighted RMS (mm) for the vertical component of site time series obtained using 16 combinations of tropospheric modelling strategies and atmospheric pressure loading correction schemes. (Functional model: linear regression plus annual and semi-annual signals. Stochastic model is white noise plus Flicker noise.)

Atmospheric pressure loading (APL) correction scheme	Mapping function			
	GMF	NMF	OMFS	OMTS
No APL correction applied	6.0±0.6	6.1±0.6	5.5±0.6	5.4±0.5
TVD APL corrections applied at observation level	7.1±0.7	7.2±0.8	6.3±0.7	5.6±0.6
TVD APL corrections applied as daily coordinate patch	7.2±0.7	7.3±0.8	6.3±0.7	5.6±0.6
LP APL corrections applied as daily coordinate patch	7.3±0.7	7.4±0.7	6.5±0.6	5.8±0.6

Overall, best performances are obtained when using the OMTS, closely followed by the OMFS, both when not correcting for atmospheric pressure loading effect. When applying APL corrections, OMTS performs much better than all other solutions with a WRMS of 5.6 mm, smaller than the one of the OMFS by 0.7

mm, and smaller than the ones of the GMF and NMF solutions by 1.5 and 1.6 mm respectively (for TVD corrections applied at the observation level).

The results show in particular the negative impact on the positioning quality for all solutions when APL corrections are applied, regardless of the APL model (TVD or LP) and the way of accounting for APL, at the observation level or as daily average corrections. The most affected solutions are the NMF and the GMF. The OMFS and the OMTS, which perform best among the four, are affected but quite differently: the OMFS exhibits a WRMS increase of 0.8-1.0 mm when APL is applied, whereas the effect is less perceptible on the OMTS solution with an increase of only 0.2-0.4 mm WRMS. The general negative impact highlights the fact that correcting for APL only adds noise. In other words, either the APL signal is not properly sensed by the technique employed to process the data, or the models are wrong.

Given their negative impact, APL corrections were discarded and not further considered in this chapter or in Chapter 6, but are re-considered in Chapter 7.

5.5 Mapping functions' Performances Analysis

Time series analysis was carried out in order to decide which tropospheric modelling performs best among the different combinations tested. The reader is referred to the previous sections of this chapter for details on the different strategies (Table 5.1) and solutions, data editing and offset modelling.

5.5.1 Positioning Precision

As a measure of the positioning quality, the weighted root mean squares (WRMS) of local coordinate residuals in the north, east and up components were used. Residuals were computed over a functional model composed of a linear trend plus

annual and semi-annual signals, whereas the stochastic model assumed for the data was a combination of white noise and Flicker noise [Williams et al., 2004]. To assess the performances of the different tropospheric modelling strategies, statistics were computed over all the remaining stations. Of the thirty stations selected for this study, three of them (LIVE, NOTT, and PMTG) were left out because of the poor data quality. The case of LIVE and NOTT because of abnormal time series (see Subsection 5.2.4); and PMTG for the reasons exposed under Subsection 5.3.2. The WRMS averaged over the 27 remaining stations are presented in Table 5.6. For clarity the label '_OFF' is used to make clear that no APL corrections of any sort were applied in these tests.

Table 5.6: Weighted RMS (mm) for the north, east and up components obtained for 7 different tropospheric modelling strategies and vertical offset to the NMF_OFF solution. (Functional model: linear regression plus annual and semi-annual signals; Stochastic model: combination of white noise plus Flicker noise; Offsets in time series: selected only)

Strategy/Solution	North (std)	East (std)	Vert. (std)	Vertical mean offset (std) to NMF_OFF
NMF_OFF	2.47 (0.20)	3.03 (0.26)	5.96 (0.57)	0.00 (0.00)
GMF_OFF	2.47 (0.20)	3.03 (0.25)	5.89 (0.56)	-0.70 (0.41)
OMFS_OFF	2.48 (0.20)	3.02 (0.25)	5.39 (0.60)	-1.02 (0.52)
VMF1G_OFF	2.47 (0.20)	3.03 (0.26)	5.38 (0.60)	-0.47 (0.39)
OMFSHRT_OFF	2.48 (0.20)	3.03 (0.25)	5.36 (0.45)	-2.20 (0.74)
VMF1GRT_OFF	2.48 (0.20)	3.03 (0.25)	5.37 (0.45)	-1.58 (0.46)
OMTS_OFF	2.47 (0.20)	3.03 (0.26)	5.35 (0.45)	-2.37 (0.82)

Four categories of tropospheric modelling strategy can be identified in Table 5.6:

Category 1 : Parametric mapping functions with standard a priori ZHD (NMF_OFF & GMF_OFF)

Category 2 : Non- and Semi-parametric mapping functions with standard a priori ZHD (OMFS_OFF & VMF1G_OFF).

Category 3 : Non- and Semi-parametric mapping functions with consistent ray traced a priori ZHD (hydrostatic) (OMFSHRT_OFF & VMF1GRT_OFF)

Category 4 : Non-parametric mapping functions independent of a priori ZHD (OMTS_OFF).

All categories exhibit similar performances in the horizontal components which is, as expected, not significantly affected by a change in the mapping functions. Therefore, only the up component is discussed hereafter. Two classes of performers can be formed: the first class is composed of uniquely Category 1, with up component WRMS in the region of 6 mm. The second class contains Categories 2, 3 and 4, with up component WRMS of about 5.4 mm, which is a 10% improvement over category 1. In the last column of Table 5.6 are given the mean height differences with respect to the NMF_OFF solution and the associated standard deviation. There are clear biases between solutions, which can be partly explained by the mapping functions and partly by the a priori information input in the system, as discussed below.

Plotted on Figures 5.14 to 5.17 are all possible comparisons between pairs of mapping functions, on the basis of their induced height effect. The common reference was taken as the mean height of the reference solution (abscissa), therefore the intercept reflects the bias between the solutions. The slope is an indication

of the relative scale effect. Perfect agreement would lead to zero intercept, unity slope and no scatter. On the following two pages, the plots were arranged by decreasing level of agreement between mapping functions. Station PMTG was kept in blue as per previous plots and was excluded from the computation of given intercepts and slopes.

The scatter is most important when comparing pure parametric mapping functions (Category 1) to non or semi parametric mapping functions; the effect is enhanced when a priori ray traced ZHD is preferred to a standard a priori ZHD. Bias is caused by the lack of proper calibration onto real atmospheric conditions when solely relying on climatological models, on both the mapping functions and a priori ZHD sides, although the real bias introduced is reduced when estimating ZTD, it cannot generally be always compensated (see [Tregoning and Herring, 2006] and discussion above). NMF and GMF agree pretty well; one couldn't be preferred to the other only based on their WRMS. For the stations in the UK, an average bias of 0.7 mm is found and the scatter is rather limited. The main difference observed is an annual signal in the up component (see for illustration the top plot in Figure 7.5 later).

Two points shall be emphasized here: (i) the very good agreement between the OMF and the VMF1G, with and without ray traced a priori ZHD and (ii) the very good agreement between the OMTS and the OMFSHRT. The latter is discussed below. The former validates the OMF which, although built differently, may have an impact on the discussion offered below on the total mapping function OMTS.

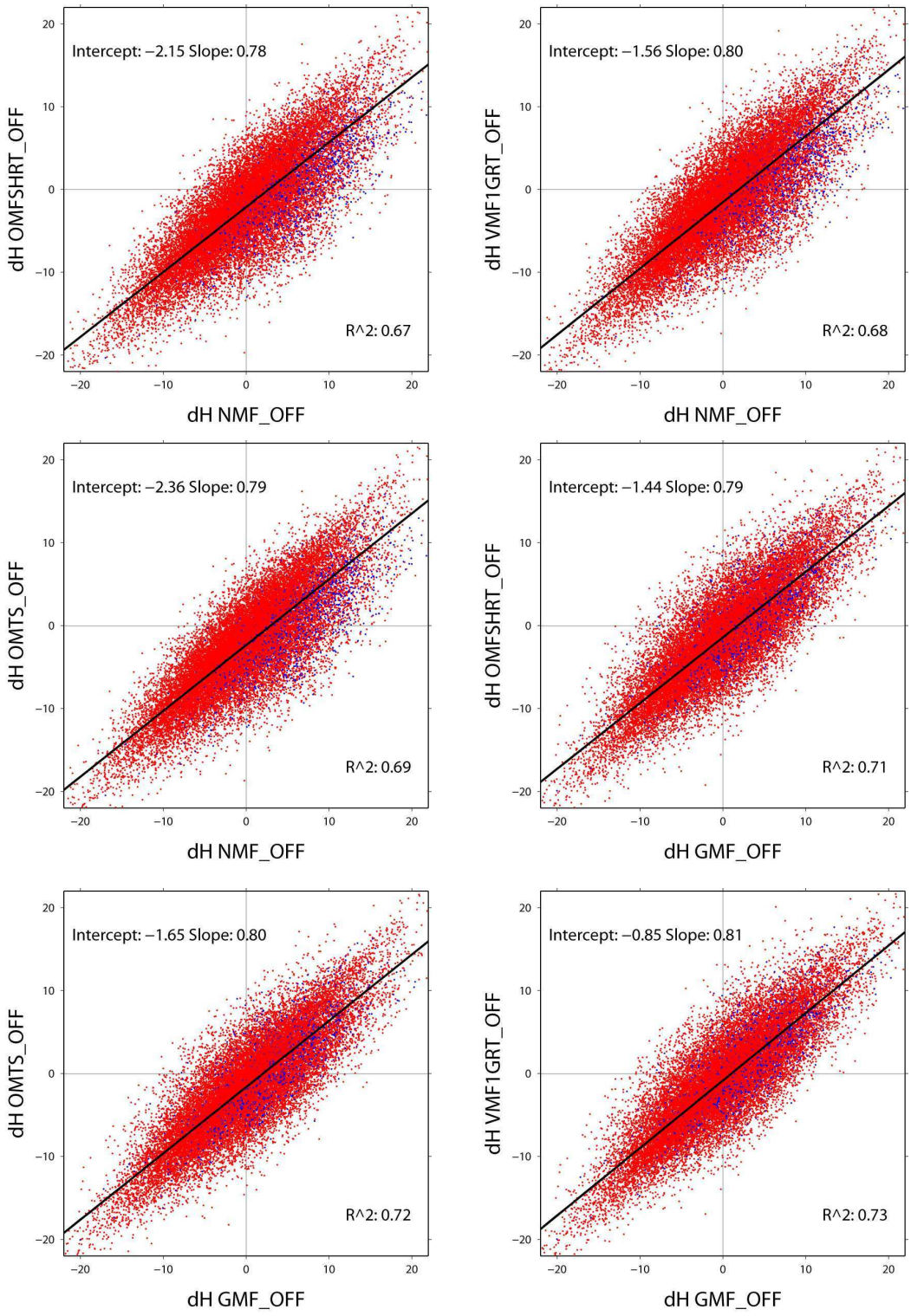

Figure 5.14: (Part 1 out of 4) Daily height comparisons between 7 different tropospheric modelling strategies over a 3.8 year period. Common level is the average height of the solution in abscissa.

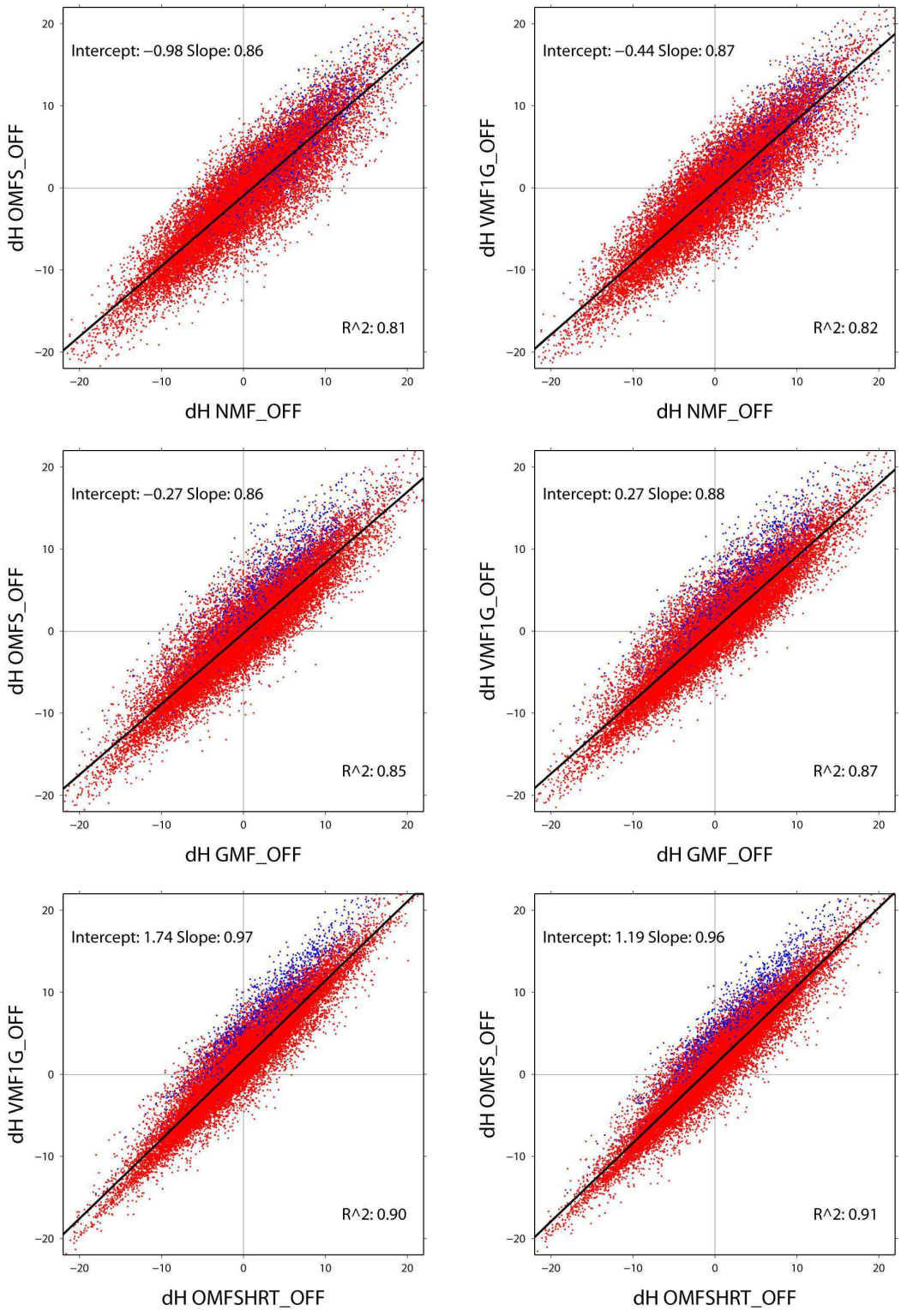

Figure 5.15: (Part 2 out of 4) Daily height comparisons between 7 different tropospheric modelling strategies over a 3.8 year period. Common level is the average height of the solution in abscissa.

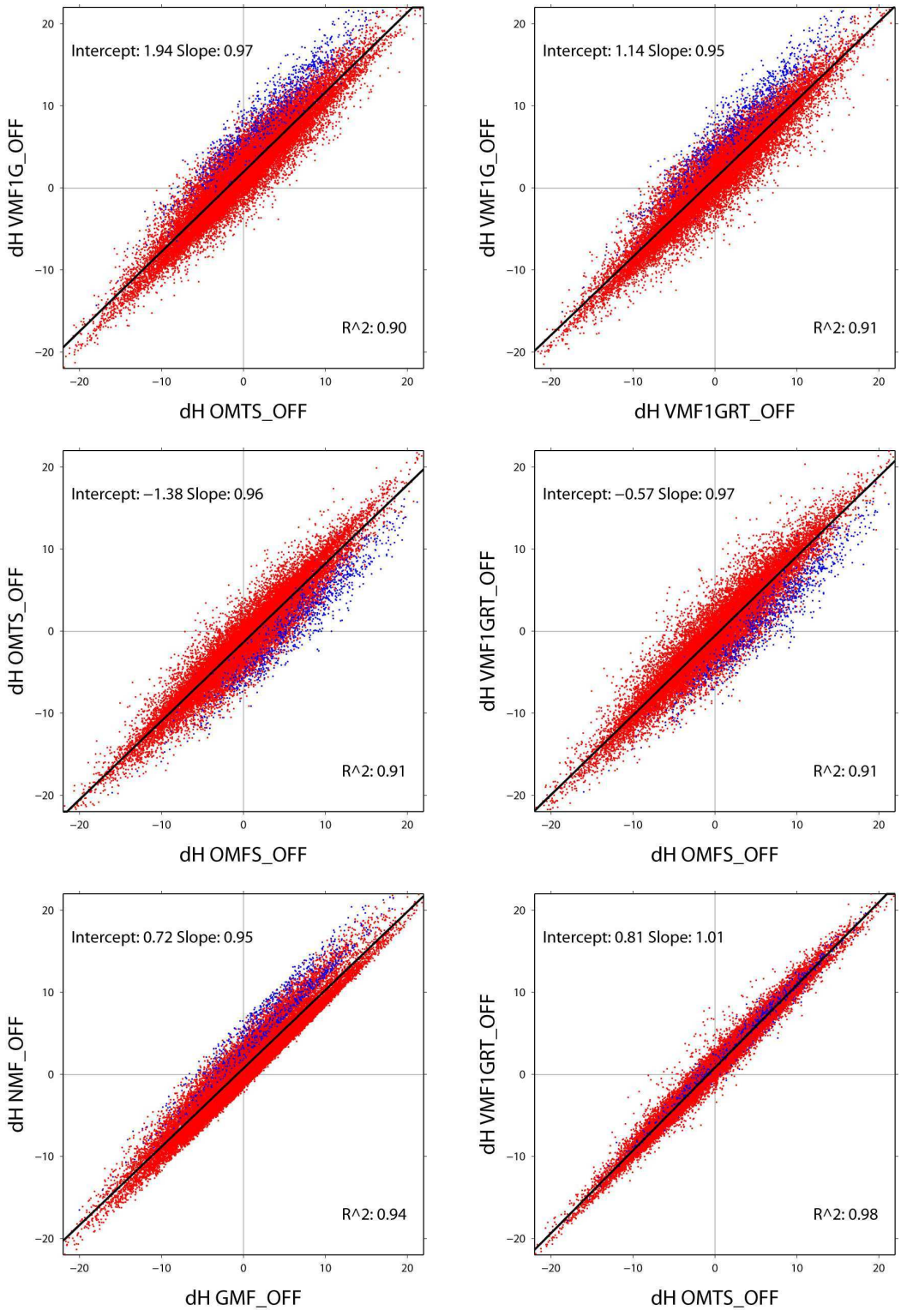

Figure 5.16: (Part 3 out of 4) Daily height comparisons between 7 different tropospheric modelling strategies over a 3.8 year period. Common level is the average height of the solution in abscissa.

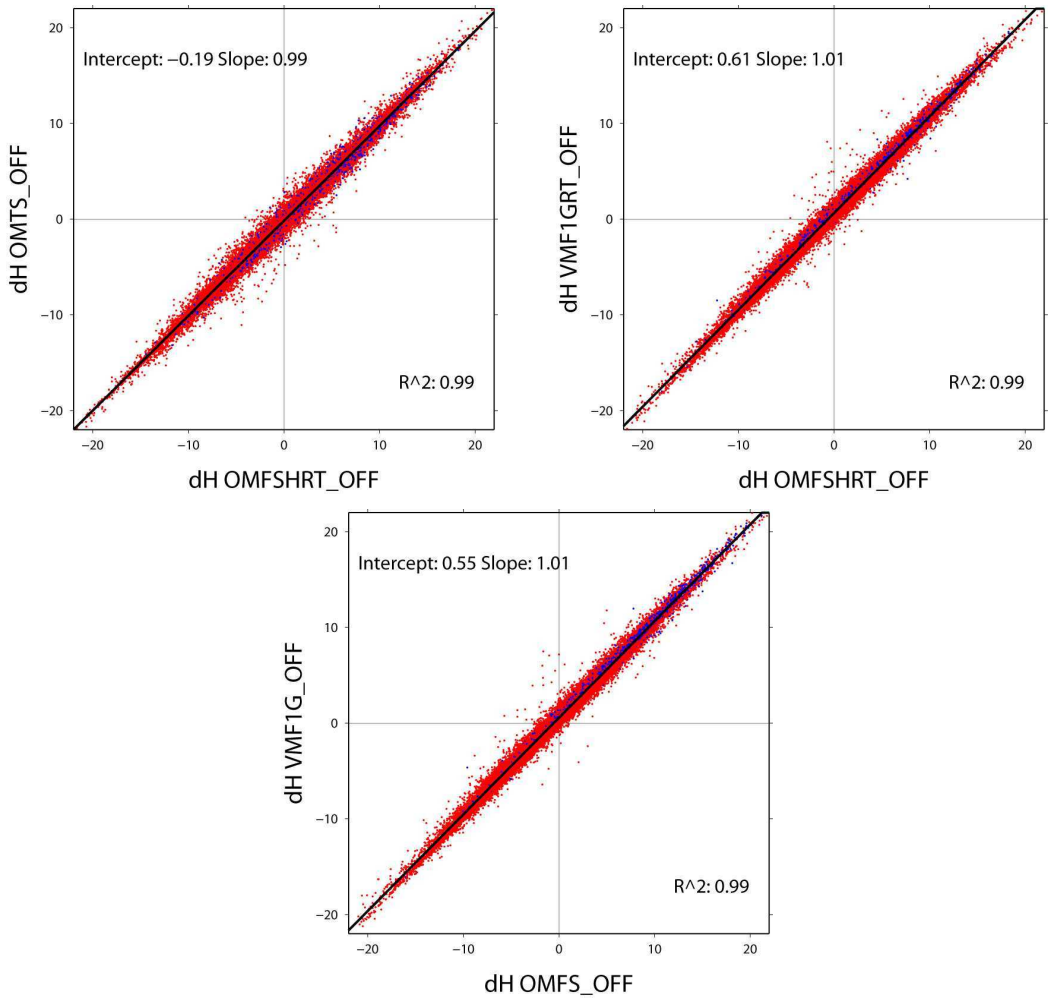

Figure 5.17: (Part 4 out of 4) Daily height comparisons between 7 different tropospheric modelling strategies over a 3.8 year period. Common level is the average height of the solution in abscissa.

5.5.2 On a priori zenith hydrostatic delay

Tregoning and Herring [2006] discussed the need for accurate a priori ZHD in the tropospheric modelling for space geodetic data. The need stems from the fact that one commonly relies on the wet mapping function (as the partial derivative of the ZTD with respect to the observed phase) to estimate a correction to the a priori ZHD, usually the predicted hydrostatic delay using Saastamoinen [1972] model. The pressure can be the standard sea level (SSL) adjusted for height difference, from a model (NWM in general or e.g. the Global Pressure and Temperature (GPT) [Boehm et al., 2007]) or locally measured or interpolated. Accurate measured pressure at each processed epoch would be ideal, although permanent sites with such available pressure data are not yet very common. For example, at the time of writing, only a few of the 120 plus stations that compose the CGPS network in the UK have collocated met sensors. Some of the scientific stations were set up by the Met Office to be collocated with other instruments like radiosonde and water vapour radiometers, but there are only a couple of these over the UK (CAMB and LERW). Tregoning and Herring [2006] found that error in the a priori ZHD end up in height error with "*typical sensitivities up to -0.2mm/hPa*". They pointed to the difference between the hydydrostatic and wet mapping functions (especially at low elevation angles) as solely the wet is used to estimate the ZTD correction and that might not be able to 'catch up' all of the hydrostatic error. Related considerations are given below with respect to the use of a total mapping function instead of the usual pair of the hydrostatic and wet.

In the processing carried out by the author, the effect of the a priori ZHD can be directly assessed by comparing solutions (dropping the _OFF suffix for simplicity) OMFS and OMFSHRT, and VMF1G and VMF1GRT. OMFS and VMF1G use standard sea level pressure (1013.25 in BSW50) corrected for height using

Berg [1948] ([Dach et al., 2007]) whereas OMFS and VMF1GRT use ray traced ZHD, consistent with the mapping functions. Recalling that in the case of the OMF, the ray-tracing is performed at each site whereas for VMF1G, ZHD (together with the a_h and a_w coefficients) are interpolated from a grid (and adjusted for height).

Figures 5.18 and 5.19 present differential height and ZTD time series for sites HERS and CAMB together with pressure variation and predicted atmospheric pressure loading induced radial displacement. In each figure, the top plot features the difference OMFS minus OMFSHRT, the middle plot the difference VMF1G minus VMF1GRT, and the bottom plot the difference OMFS minus VMF1G. The pressure time fluctuation (dPress) is given as the the corrected SSL ([Berg, 1948]). Following the findings of Tregoning and Herring [2006], dPress is plotted in hPa with a Y scale that matches their typical sensitivity (i.e. 5 hPa dPress for 1 mm dHeight). For visual impact, the differences were taken so that they are in phase with the dPress (instead of being 180 degrees phase shifted as per the ZTD). The match is almost perfect, confirming the finding of Tregoning and Herring [2006].

From Table 5.6, one could only say that the two approaches yield positioning with similar precision, however, it cannot be claimed that one is more accurate than the other. External evidence is needed to make that point. One way would be to compare the GPS ZTD to the ones ray traced from the NWM (a comparison with ZTD ray traced from hiRes RS profiles was given in the previous chapter, limited to 5 collocated sites). This is investigated in Section 5.5.4.

To directly assess the impact on the height of the a priori ZHD, the daily height difference was plotted versus the daily average a priori ZHD. The results are pre-

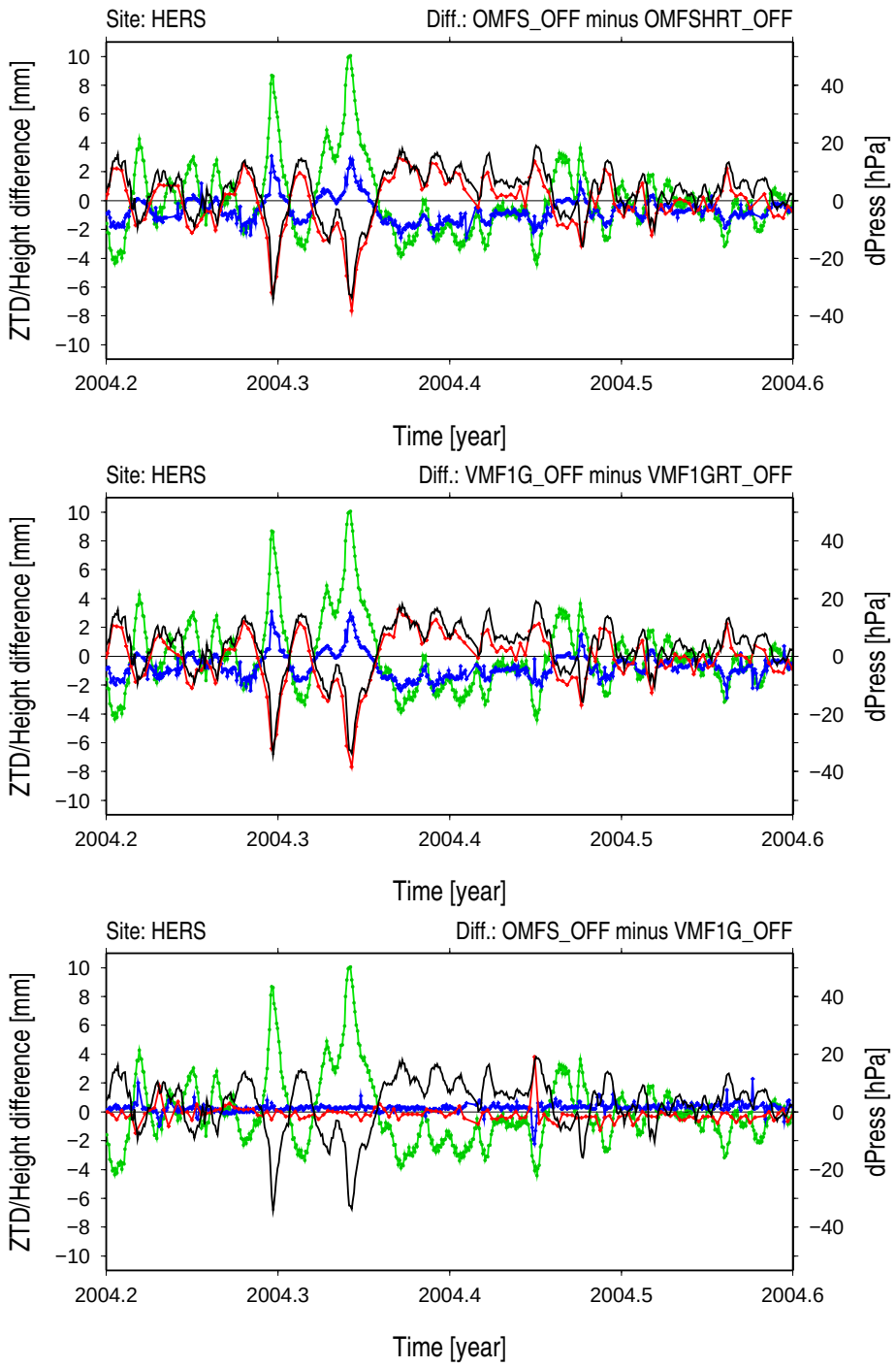

Figure 5.18: Example of time series of the difference in the vertical position of CGPS station HERS obtained with different mapping functions, as indicated on the top right of each plot. No APL corrections were applied. In red: differential vertical position in mm; In blue: differential 6 hourly ZTD in mm; In black: pressure variation in hPa; and in green: predicted radial induced APL displacement in mm.

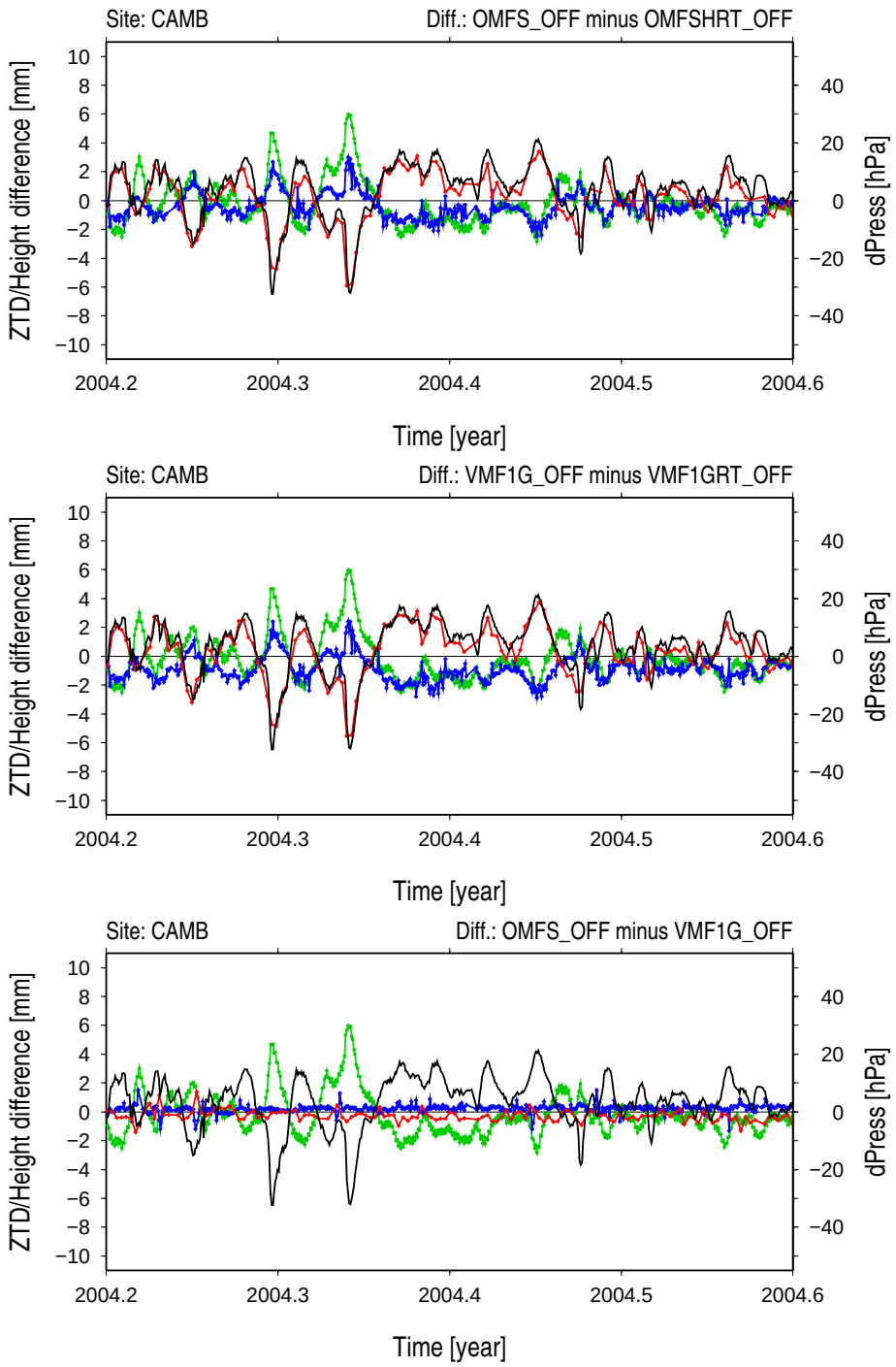

Figure 5.19: Example of time series of the difference in the vertical position of CGPS station CAMB obtained with different mapping functions, as indicated on the top right of each plot. No APL corrections were applied. In red: differential vertical position in mm; In blue: differential 6 hourly ZTD in mm; In black: pressure variation in hPa; and in green: predicted radial induced APL displacement in mm.

sented in Figure 5.20. A sensitivity of -0.75 mm/cm was found. The abscissa in Figure 5.20 represent the effective error in the a priori ZHD when computed using Berg [1948] and Saastamoinen [1972] as per in BSW50, assuming the ray traced ZHD is the truth. The error in the surface pressure approximation can induce a height error of $\pm$ 10 mm. The small intercept is probably due to errors stemming from the averaging process to compute the daily pressure. It corresponds, on average, to a sensitivity of -0.17 mm/hPa, as shown in Figure 5.21, where it seems that the sensitivity can be quite different from one station to the other (visible presence of lines).

Figure 5.22 gives the error made in the computation of the a priori ZHD using the Saastamoinen [1972] model when the pressure is assumed constant (as derived from constant height). The delta pressure on the abscissa of Figure 5.22 represents the error between 'true' pressure, in this case given by the NWM, and the constant pressure derived for the site from its height.

Figure 5.24 presents a map of the sensitivity of the height change with respect to a change/error in the surface pressure used to compute the a priori ZHD input to the data reduction. There are clear geographical variations. However, as evident from the scatter of Figure 5.23, there appears to be no link between the station height and the sensitivity to a pressure error, nor is there a clear dependence on the station's latitude. However, inland sites may have a higher sensitivity to a pressure error than coastal sites and the Thames region in the South East of England seems the least sensitive.

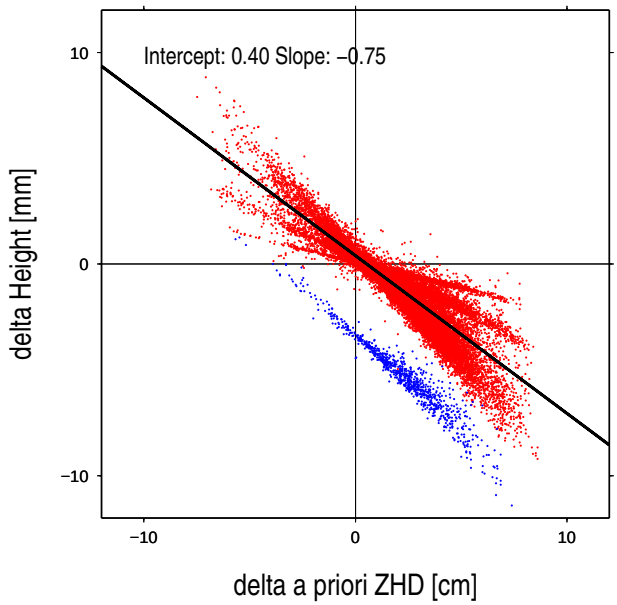

Figure 5.20: Impact on height estimate (mm) of the error in the a priori ZHD introduced (cm) in the GPS data processing. In blue: CGPS station PMTG. Slope and intercept were computed excluding PMTG.

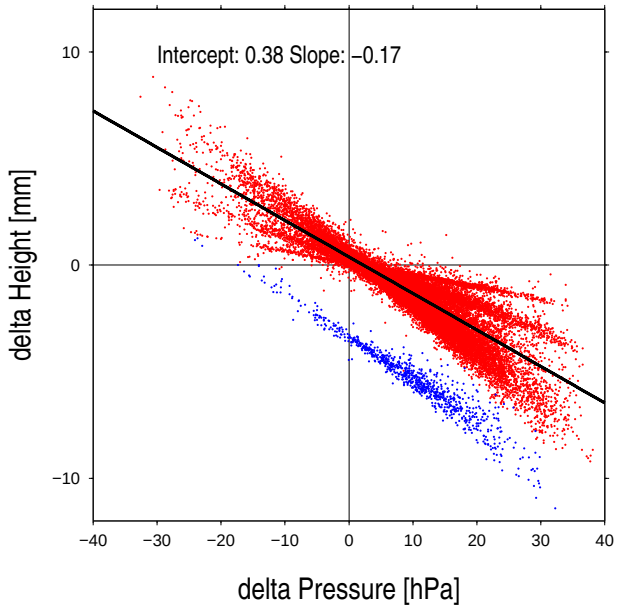

Figure 5.21: Impact on height estimate (mm) of the error in the estimated surface pressure introduced (hPa) in the GPS data processing when computing the a priori ZHD. In blue: CGPS station PMTG. Slope and intercept were computed excluding PMTG.

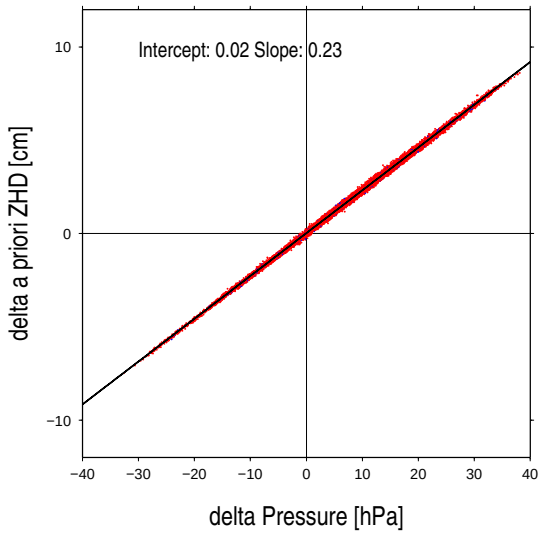

Figure 5.22: Error in the a priori ZHD (cm) computed using the Saastamoinen [1972] model with respect to the error in the surface pressure (hPa).

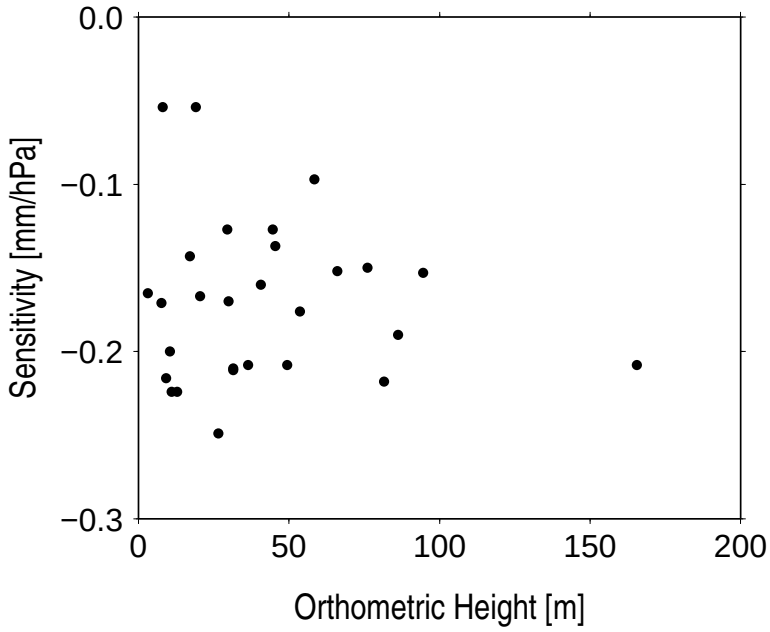

Figure 5.23: Sensitivity in mm/hPa of the inferred height to the error in the surface pressure used to compute the a priori ZHD plotted against the orthometric height of station (m).

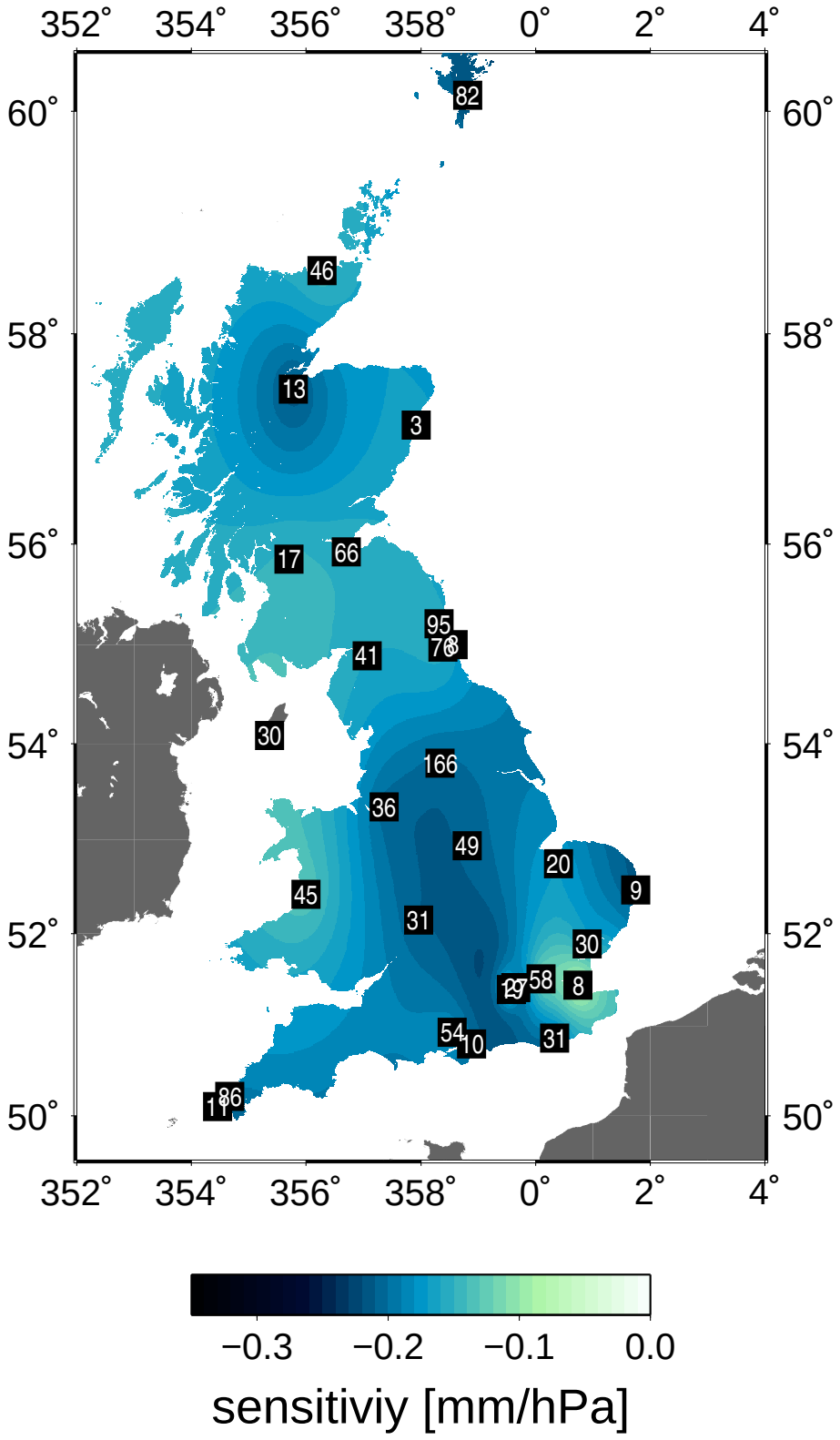

Figure 5.24: Sensitivity in mm/hPa of the inferred height to the error in the surface pressure used to compute the a priori ZHD. Black squares: orthometric height of the station.

5.5.3 Total mapping function

[Boehm et al., 2006a] reported a deficiency of the total mapping function as being affected by the not accurate representation of the wet part in the NWM. They argue that even if the 6 hourly information used was perfect, the variation in between may differ greatly from the linear interpolation and could not be handled properly, and hence introduces noise in the up component. From the validation of the NWM ray tracing algorithm (see previous Chapter 4), the ray traced ZHD is in a very close agreement with the one computed using Saastamoinen [1972] and pressure as interpolated from the NWM. Consequently the numbers presented in the following section (5.5.4) can be associated to the wet part of the difference as well, as the ZHD from the two sources do match almost perfectly. (What is measured here is really the ray-tracing algorithm error, not the real but unknown error in the interpolated surface pressure). The comparison of the 6 hourly ZTD for the full period (in average 107,000 samples) gave a negligible bias for all solutions (only up to 1.0 mm) and a scatter of 1.4 cm. There is no doubt that the scatter is explained by errors on both sides. A comparison of ZWD inferred from RS and NWM vertical profiles gave an agreement of -0.2 $\pm$ 11.2 mm for the best method (see Table 4.13 earlier).

The derivative of the phase with respect to the zenith path delay correction (usually the wet, or potentially the total mapping function) is determinant. A mapping function overestimating the truth will lead to an underestimated correction and ZTD, and vice-versa. In that respect, it would make sense to minimize the correction to be estimated. Although the total will inevitably be affected by a representation not as good as the hydrostatic, one may ask what is best between: (i) using the usual hydrostatic + wet mapping functions or (ii), using the total + total mapping function, or (iii) using the total + wet mapping functions, if as

according to Niell's comments, the wet mapping function is better than the total mapping function for estimating the correction. The point here is that for cases (ii) and (iii), the remaining part is in the order of the scatter of the observed discrepancy between GPS and NWM, i.e about 1.5 cm, which is about one order of magnitude less than the estimated (truly wet or not) part. (iii) was not tested but could be considered in further investigations.

In Table 5.6, a bias of 0.17 mm and a scatter of 0.19 mm were found for the difference OMFSHRT minus OMTS, and a bias 1.35 mm with and a scatter of 0.55 mm for the difference OMFS minus OMTS. The difference OMFSHRT minus OMFS exhibits a bias of -1.17 mm and a scatter of 0.50 mm. So the results do not show a significant difference between using the total mapping function and using the usual hydrostatic plus wet mapping function approach, when used with a consistent ray traced a priori ZHD (see Figure 5.25 for illustration). On the contrary, this would validate the fact that the total mapping function approach presents the advantage of being independent of the a priori ZHD, at least in BSW50.

There is also maybe some indication that the cubic spline interpolation (CSI) makes a better use of the information derived from the NWM compared to using the least-squares approach to fit the Marini model; which is not pure speculation in view of Figure 3.14 in Chapter 3.

5.5.4 ZTD: GPS versus NWM

The literature on the comparison of GPS ZTD versus NWM ZTD has been growing steady over the last few years with the increasing availability of numerical weather models. See for example Vedel et al. [2001] as referred to it in the ray

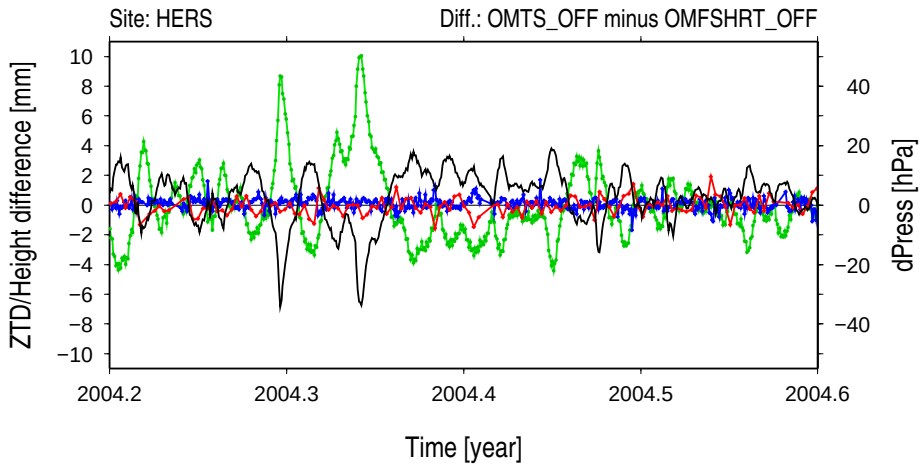

Figure 5.25: Comparison of the total mapping function versus the usual pair of hydrostatic and wet mapping function (with ray traced a priori ZHD). Differential coordinates in red and differential ZTD in blue.

tracing algorithm implementation (for both NWM and RS profiles). Here, a comparison is performed over 6 hourly ZTD estimates and the results presented in Table 5.7.

Table 5.7: Statistics for the difference <GPS - NWM> for 6 hourly ZTD estimated from GPS and the ones ray traced from NWM. Data from site PMTG excluded.

Solution	Diff: Mean (Std. dev.) [mm]	Sample Size
NMF_OFF	0.0 (14.2)	108138
GMF_OFF	0.4 (14.2)	108144
OMFS_OFF	0.4 (14.0)	107900
VMF1G_OFF	0.3 (14.0)	108059
OMFSHRT_OFF	0.8 (13.8)	105970
VMF1GRT_OFF	0.8 (13.8)	108114
OMTS_OFF	1.0 (14.1)	107890

In the case of GPS, estimates at midnight were taken as the average of the last estimate of the day and the first estimate of the following day. The same was done for the uncertainty. Overall all solutions compare well between GPS and NWM although there is a systematic positive bias, indicating that GPS tends to overestimate the ZTD when compared to NWM ray tracing. This was also found by Vedel et al. [2001] who obtained a mean offset of 3.2 mm $\pm$ 17.1 mm when comparing GPS ZTD to ZTD ray traced from the HIRLAM model for GPS stations of the MAGIC project. Statistics were computed over the data from all stations, resulting in a sample size of about 106,000 to 108,000. The data were cleaned for outliers at a 3.5 zero sigma level.

The noise in the difference was about 14 mm. The lowest scatter values were found for solutions that had their a priori ZHD based on NMW ray-tracing. The highest were found for the two parametric mapping functions, the NMF and GMF. This probably reflects the incapacity of such mapping functions to handle short term variations of the atmosphere, although the climatology seems to be properly handled given the small biases found (0.0 and 0.4 mm respectively). Comparing our OMFS to OMFSHRT and VMF1G and VMF1GRT, it is interesting to note the very similar change in the statistics. It was already shown that the two solutions, although completely independent, perform very similarly (see above). The OMFS sees its bias increasing by 0.4 mm (from 0.4 to 0.8 mm), and the VMF1G by 0.5 mm (from 0.3 to 0.8 mm), when replacing the SSL a priori ZHD by NWM based one, although a slight noise reduction is observed meanwhile. The bias increase is somewhat surprising as it could be argued that bringing more of the NWM information into the GPS processing would make the two closer. The OMTS exhibits the highest bias with 1.0 mm (which is still admittedly a very decent agreement). Here the a priori ZHD plays no role. Again, these numbers do not allow to say which solution is best however, they might highlight a deficit in the

overall modelling based on NWM information: the more is injected, the bigger the bias with GPS. The very similar behavior of OMFS and VMF1G allow us here to speak indifferently of the NWM used (MESO for the OMFS and ECMWF for the VMF1G).

In Figure 5.26, Table 5.7 is decomposed on a station by station basis, again for the 6 hourly ZTD difference: <GPS - NWM>. Overall, biases vary between -3.31 mm (NEWL@NMF) and 6.00 mm (MORP@OMTS). Patterns are similar among differences showing the rather 'controlled' effect of the tropospheric modelling in the GPS data processing.

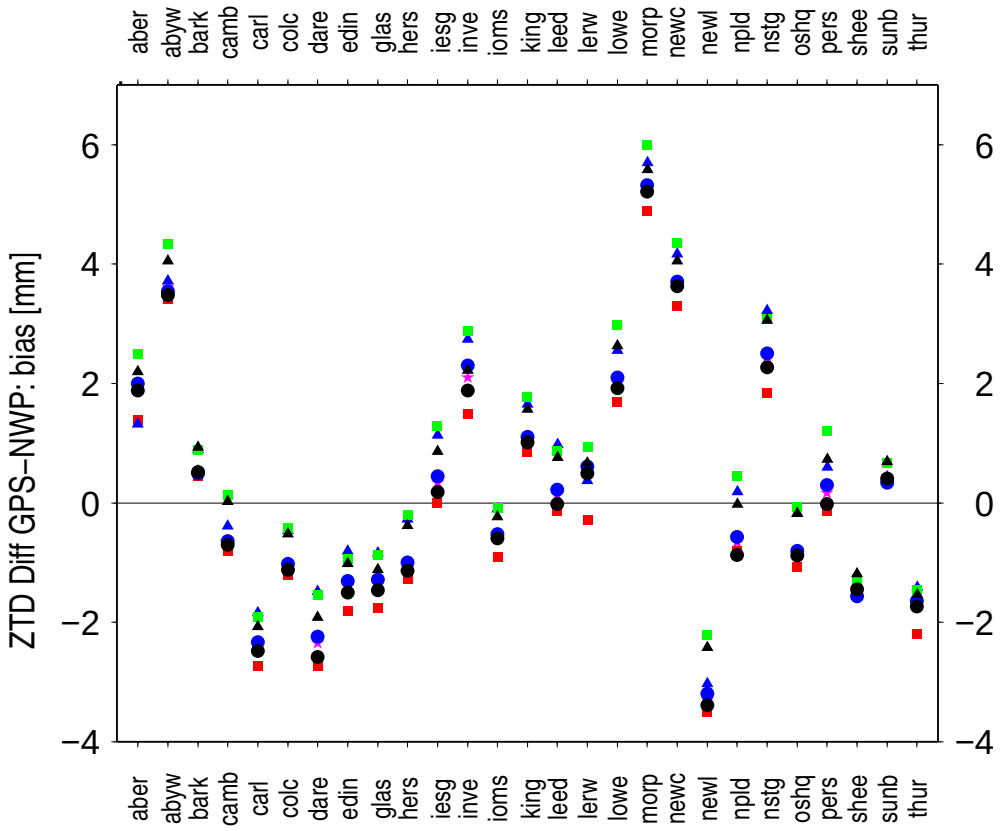

Figure 5.26: Mean offsets of the 6 hourly ZTD difference <GPS-NWM> computed over samples of size 106,000 to 108,000. NMF: red square; GMF: purple stars; OMFS: blue circles; OMFSHRT: blue triangle; VMF1G: black circle; and VMF1GRT: black triangles. Error bars were left out for clarity but are about 14 mm.

5.6 Summary

In this chapter was compared the performances of various tropospheric modelling strategies, based on different combinations of symmetric mapping functions and a priori ZHD modelling. Best combinations were found to be mapping functions based on NWM used with their consistent ray traced ZHD. The results for the symmetric version of the OMF were found to be similar to those of the VMF1G, which indeed validates the concept of the OMF, although some differences between the two were observed, e.g. in the absolute height determination.

It was found that applying APL corrections, regardless of which model and

the way of applying the correction (at the observation level or as daily position corrections), degraded the solutions tested in this chapter. This point is further examined in Chapter 7.

Chapter 6

Results: Azimuth Dependent Mapping Functions

Here are presented the results of the analysis of GPS data processed with accounting for the atmosphere's asymmetry, in two ways. The procedure is essentially the same as in the previous chapter but three new solutions are introduced and compared here: the first solution was obtained with the azimuth dependent OMF (OMFA) hydrostatic and wet mapping functions (with ray-traced a priori zenith hydrostatic); whereas the second and third solutions were obtained using the azimuthally symmetric OMF hydrostatic and wet mapping functions (with ray-traced a priori zenith hydrostatic), but with either, six hourly or daily, step-wise atmospheric gradients estimated.

6.1 Introduction

Numerous publications have shown that estimating gradients to account for the atmosphere azimuthal variation leads to better space geodetic solutions. However, the validity of these gradients has not always been discussed. Several differences in the way that tropospheric asymmetry is handled in GNSS data processing when either estimating gradients or using an azimuth dependent mapping function (AMF) can be identified:

- Gradients are estimated, whereas an AMF is a priori information (a three dimensional relative representation of the atmosphere around the station, scalable by the estimated ZTD).
- Estimating gradients increases the number of unknowns whereas the use of an AMF leaves the number of unknowns unchanged.
- Adding parameters, e.g. when estimating gradients, enhances the flexibility of the processing and can lead to smaller residuals, without real physical justification, e.g. by absorbing another un-mitigated effect (like multipath or loading).
- In estimating gradients, the GPS data contribute to this estimation, whereas this data have no effect on the derivation of the AMF, which is independent of the GPS data.

Publications which have shown the positive impact of atmospheric gradient estimation on position repeatability when using VLBI and/or GPS include, for example [MacMillan, 1995], [Chen and Herring, 1997], [Bar-Sever et al., 1998] and [Meindl et al., 2004]. However, in some cases, e.g. Bar-Sever et al. [1998], it is not clear wether the improvement found was due to gradient estimation or lowering the elevation cut-off angle ([Niell et al., 2001]). Meindl et al. [2004] found

a factor of reduction of about three (in terms of RMS) when estimating gradients with an elevation cut-off angle of 3 degrees instead of 10 degrees. Using the Niell wet mapping function as the gradient mapping function, the effect of gradients at 3 degrees elevation can be shown to be 2.90 times bigger than the effect observed at 10 degrees, as predicted by the ratio of the elevation angle derivative of the wet Niell mapping function.

The research work presented here is a unique opportunity to assess the gradients estimates by comparing results from the combination of the use of a symmetric mapping function plus gradient modelling, with results from using azimuth dependent mapping functions. Differences in the two approaches are identified along with their advantages and limitations. Then a comparison of the positioning performances is offered, before finally considering the slant delay differences with respect to the azimuth.

6.2 Asymmetry in Mapping Functions Derived from a Numerical Weather Model

Short time series are first presented here to illustrate the difference between azimuth dependent mapping functions and symmetric ones. Examples of the differences are shown in Figures 6.1 to 6.4 as the differences between the azimuth dependent OMF (OMF_AZI) and the NMF for CGPS stations ABER and IESG on two days. Mapping function differences were mapped to the elevation cut-off angle of the GPS processing, that is 5 degrees, for an hypothetical zenith hydrostatic delay of 2300 mm and wet delay of 100 mm. Similar time series for five more CGPS stations can be found in Appendix 10.

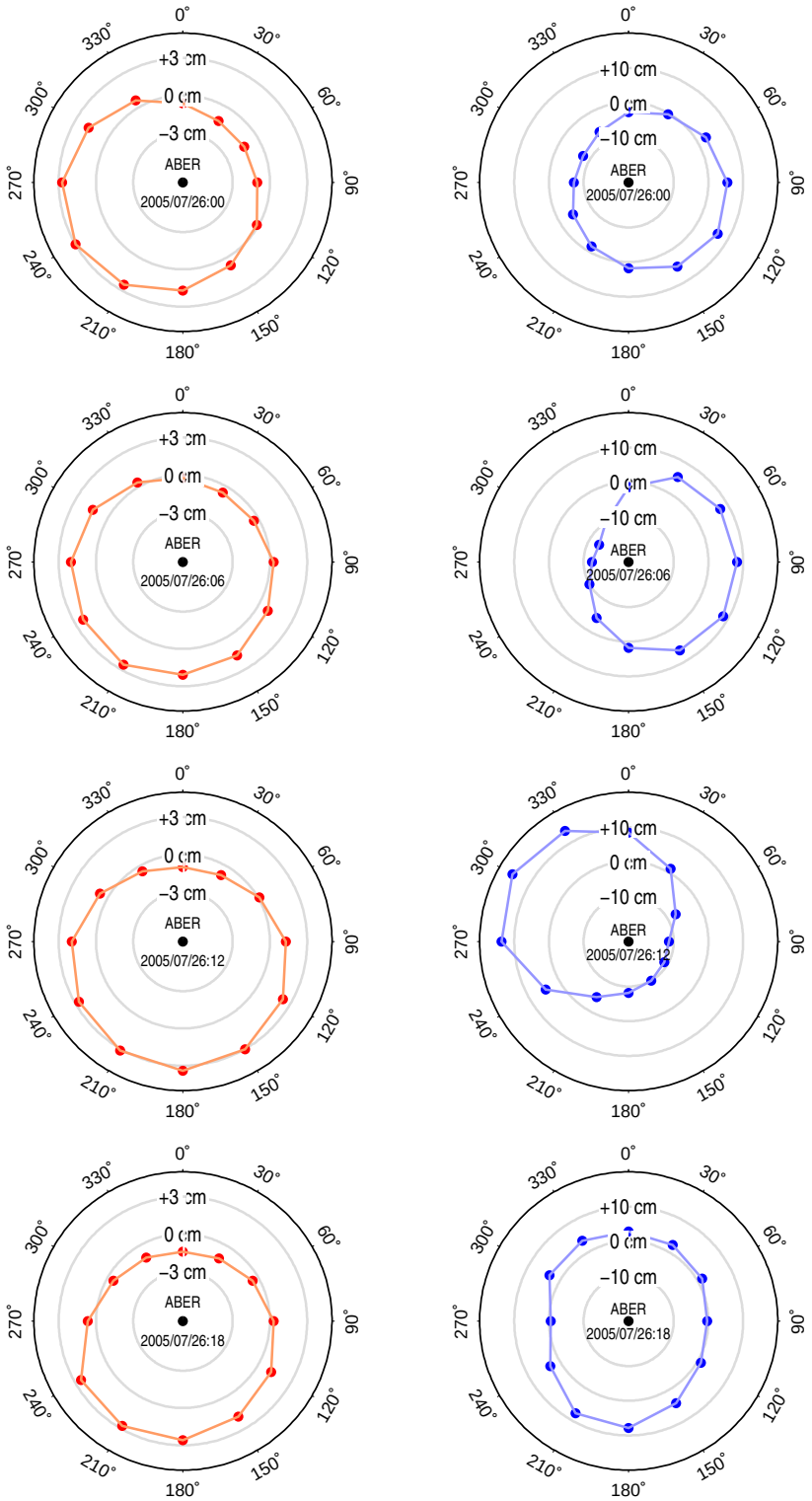

Figure 6.1: Slant atmospheric delay difference for CGPS station ABER between the azimuth dependent mapping function OMFA and the NMF at 5 degrees elevation for a standard ZHD of 2300 mm (left column) and ZWD 100 mm (right column) for 26 July, 2006.

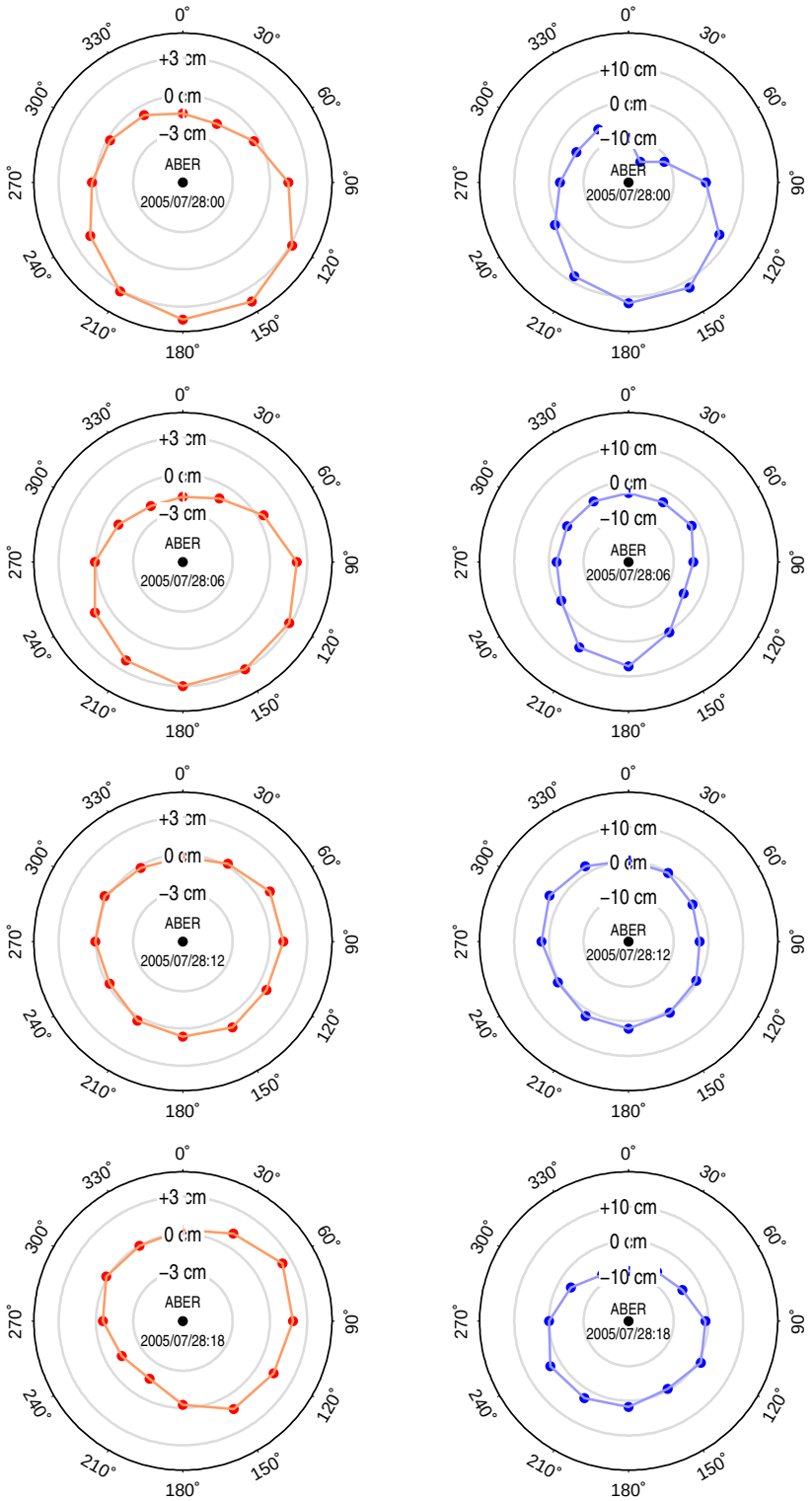

Figure 6.2: Slant atmospheric delay difference for CGPS station ABER between the azimuth dependent mapping function OMFA and the NMF at 5 degrees elevation for a standard ZHD of 2300 mm (left column) and ZWD 100 mm (right column) for 28 July, 2006.

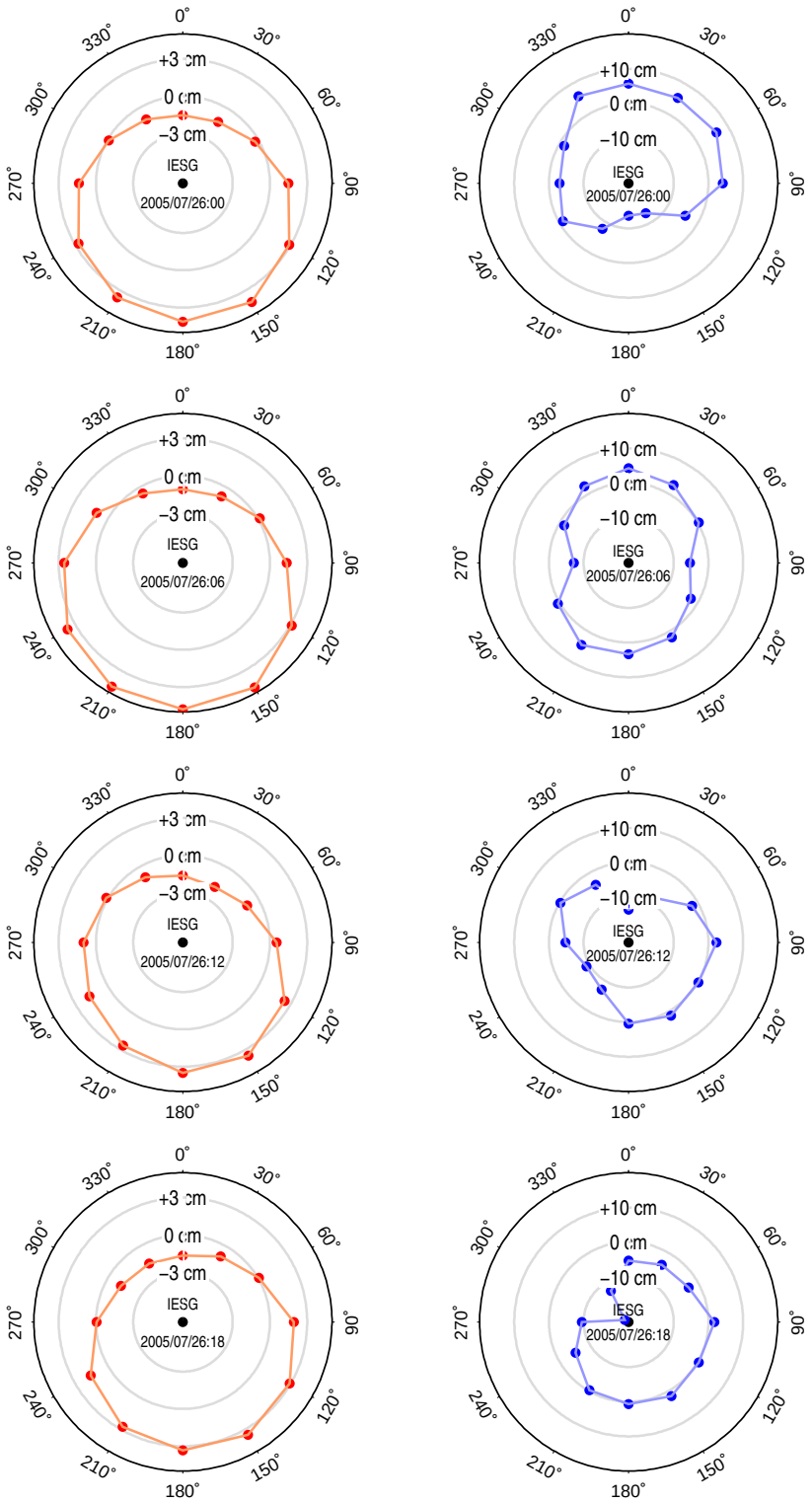

Figure 6.3: Slant atmospheric delay difference for CGPS station IESG between the azimuth dependent mapping function OMFA and the NMF at 5 degrees elevation for a standard ZHD of 2300 mm (left column) and ZWD 100 mm (right column) for 26 July, 2006.

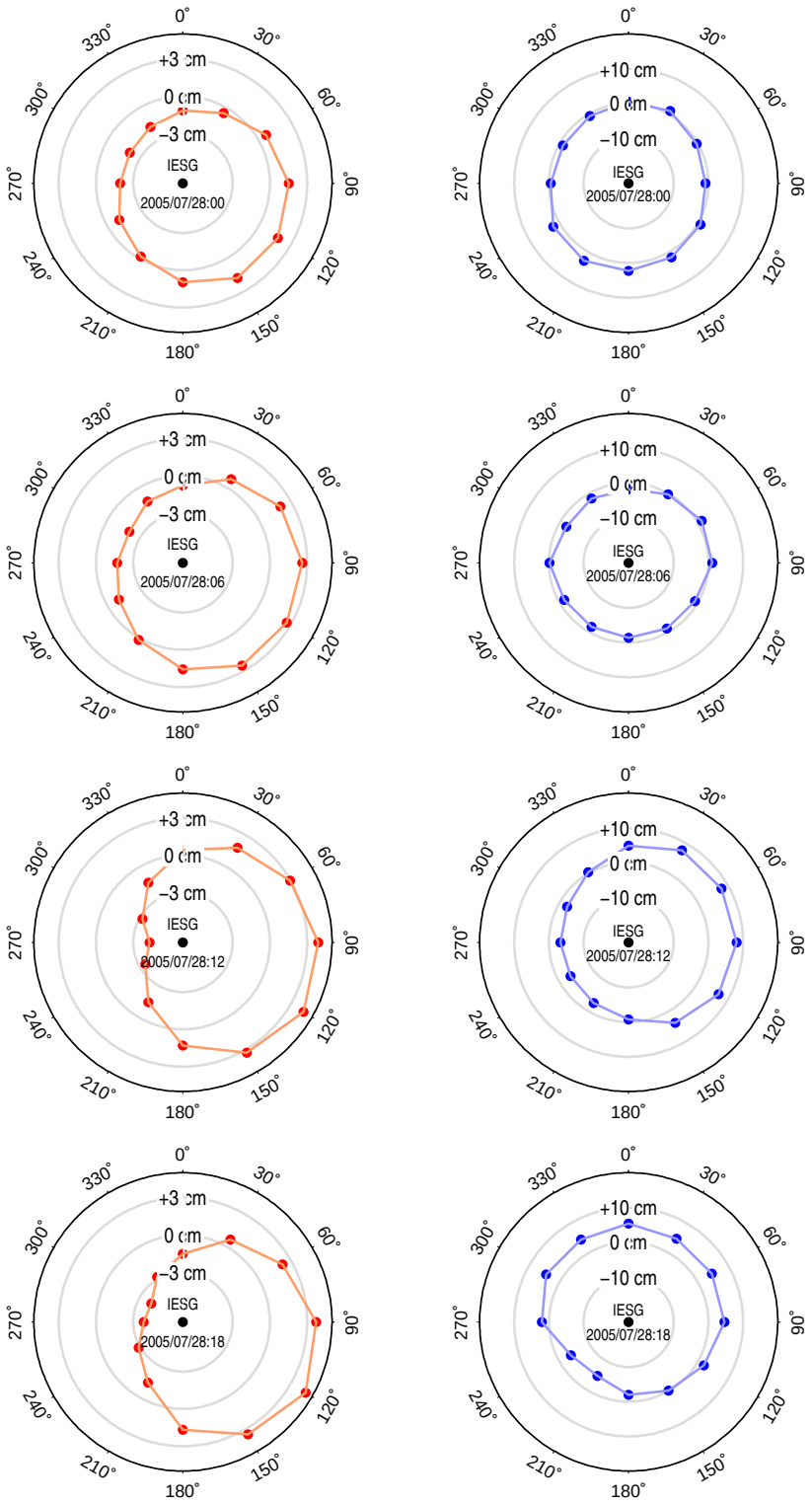

Figure 6.4: Slant atmospheric delay difference for CGPS station IESG between the azimuth dependent mapping function OMFA and the NMF at 5 degrees elevation for a standard ZHD of 2300 mm (left column) and ZWD 100 mm (right column) for 28 July, 2006.

Tables 6.1, 6.2 and 6.3 summarize, for the hydrostatic, wet and total mapping functions respectively, the characteristics of the signal (modelled as an offset + linear trend + seasonal variations) found in the asymmetric mapping functions on an azimuthal basis, every 30 degrees, as ray-traced from the NWM. The values are the averages and one sigma errors computed over 30 CGPS stations (none were excluded here), with the standard deviation provided to give an impression of the underlying noise and the significance of the signal. Time series used were 3.8 years long, but contain gaps (see Section 5.2), and the time series analysis was carried out using CATS [Williams, 2008] on a station and azimuth basis before averaging. Some time series are presented in Figures 6.5 to 6.10 with the modelled signal plotted over the raw time series, for two CGPS stations: IESG and HERS.

From Figures 6.1 to 6.4 and Table 6.1, it is clear that there is asymmetry in the hydrostatic mapping function as the offset is generally negative in the north direction (330, 000, 030 degrees), and positive in the south direction (150, 180, 210 degrees), with a similar magnitude of around 18-23 mm, and gradually changes from -22 mm directly north (0), to +1.5 mm directly east (090), to +21 mm directly south (180) then -1.7 mm directly west (270). The trends are less significant, with a magnitude usually less than 1.6 mm/year, but with a clear separation between negative value to the east (0-150) and positive values to the west (180-330) and maximum value around east (90) and west (230). The amplitude of the annual signal is generally between 4 and 8 mm and the phase is clear changing with azimuth, completing a full cycle, with a null phase around an azimuth of 210 degrees. Whereas the amplitude of the semi-annual is between 3 and 6 mm but with no regular pattern, with regard to azimuth.

From Figures 6.1 to 6.4 and Table 6.2, it can be concluded that the behavior of the

wet component is clearly not the same as the hydrostatic component. Although the level of noise is generally several times greater than that of the hydrostatic (see Figures 6.5 to 6.10), there are still discernible patterns in the offsets which tend to be negative to the north-east direction (030, 060, 090, 120) and positive to the west direction (180, 210, 240, 270, 300, 330), and in the trends, which have a clear separation between positive and negative values but rotated by about 120 degrees anti-clockwise from the hydrostatic component trends. Amplitudes of the annual and semi-annual signals are about half those for the hydrostatic and the phase of the annual and semi-annual signal are much more constant in nature at around 135 to 215 degrees (annual) and 70 to 110 degrees (semi-annual).

From Table 6.3, it is clear that the assymetry for the total mapping function is noisier than the hydrostatic (due to the contribution of the wet). However it's characteristics are similar to those of the hydrostatic mapping function but with some features inherited from the wet mapping function. For example, the trend values are reduced and rotated by about 60 degrees anti-clockwise from the hydrostatic component trends.

Table 6.1: Characteristic of the signal found in the azimuth dependent hydrostatic mapping function (modelled as white noise only and solving for an offset plus linear trend plus seasonal variations), averaged over all 30 sites. Values (and associated standard deviation) are given for an elevation angle of 5 degrees and a nominal hydrostatic zenith delay of 2300 mm.

Azimuth	Offset	Trend	Annual signal		Semi-annual signal	
(deg)	(mm)	(mm/year)	Amp.(mm)	Phase (deg)	Amp.(mm)	Phase (deg)
000	-22.2 (2.7)	-0.5 (0.2)	5.1 (2.4)	133.9 (15.5)	3.7 (0.8)	144.4 (10.8)
030	-18.1 (1.2)	-1.1 (0.3)	6.8 (2.2)	178.5 (3.7)	4.7 (0.5)	120.1 (81.2)
060	-9.4 (0.9)	-1.3 (0.4)	8.3 (1.0)	199.6 (3.5)	5.6 (0.3)	22.9 (6.1)
090	1.5 (1.5)	-1.3 (0.3)	8.6 (0.4)	214.9 (3.0)	5.8 (0.8)	41.7 (2.9)
120	11.8 (2.0)	-0.9 (0.2)	7.5 (0.6)	231.1 (13.5)	5.1 (0.9)	62.5 (7.9)
150	19.0 (2.2)	-0.2 (0.1)	5.5 (0.6)	254.0 (25.8)	3.9 (0.4)	92.2 (17.1)
180	21.0 (1.8)	0.6 (0.2)	4.0 (2.3)	301.2 (21.9)	3.3 (0.9)	142.8 (9.4)
210	17.6 (1.0)	1.2 (0.2)	5.9 (2.0)	169.8 (177.2)	4.5 (0.6)	41.2 (69.0)
240	9.2 (1.1)	1.6 (0.2)	7.9 (1.0)	20.6 (4.1)	5.5 (0.4)	26.1 (5.8)
270	-1.7 (2.0)	1.5 (0.2)	8.4 (0.8)	35.1 (4.8)	5.5 (1.1)	43.5 (2.9)
300	-12.4 (2.4)	0.9 (0.2)	7.2 (0.8)	55.7 (16.3)	4.6 (1.1)	67.8 (10.7)
330	-19.9 (2.4)	0.2 (0.1)	5.7 (0.9)	85.9 (26.8)	3.8 (0.4)	101.9 (20.4)

Table 6.2: Same as Table 6.1 but for the azimuth dependent wet mapping function and a nominal wet zenith delay of 100 mm.

Azimuth	Offset	Trend	Annual signal		Semi-annual signal	
(deg)	(mm)	(mm/year)	Amp.(mm)	Phase (deg)	Amp.(mm)	Phase (deg)
000	0.1 (4.3)	-0.6 (1.2)	2.8 (2.1)	134.2 (114.7)	1.8 (1.1)	94.6 (47.0)
030	-2.0 (3.8)	-0.1 (1.1)	3.1 (2.1)	164.6 (113.8)	1.8 (1.0)	88.0 (51.4)
060	-3.2 (3.3)	0.4 (1.1)	3.6 (1.7)	199.7 (104.5)	2.0 (1.0)	77.6 (47.7)
090	-3.3 (2.7)	0.8 (1.2)	3.7 (1.8)	211.8 (104.3)	2.2 (1.2)	69.4 (38.0)
120	-2.3 (2.9)	1.0 (1.3)	3.6 (2.1)	214.0 (98.1)	2.5 (1.1)	78.7 (51.4)
150	-0.1 (3.8)	0.8 (1.3)	3.8 (2.4)	205.7 (84.8)	2.4 (1.1)	77.0 (55.3)
180	2.0 (4.0)	0.5 (1.4)	4.0 (2.6)	210.2 (91.7)	2.1 (1.0)	104.1 (58.5)
210	3.7 (4.1)	0.1 (1.3)	3.9 (3.2)	210.7 (98.0)	1.9 (0.9)	109.2 (46.2)
240	5.5 (3.9)	-0.4 (1.2)	4.1 (2.9)	186.3 (125.1)	1.7 (1.0)	94.8 (51.3)
270	6.5 (2.8)	-0.9 (1.3)	3.8 (2.5)	172.5 (120.9)	1.7 (1.0)	88.1 (49.5)
300	5.1 (3.6)	-1.2 (1.4)	3.4 (2.2)	152.2 (124.0)	1.9 (0.7)	99.6 (51.1)
330	2.5 (4.5)	-1.0 (1.4)	3.2 (2.0)	118.5 (116.8)	2.1 (0.9)	99.4 (49.9)

Table 6.3: Same as Table 6.1 but for the azimuth dependent total mapping function and a nominal total zenith delay of 2400 mm.

Azimuth	Offset	Trend	Annual signal		Semi-annual signal	
(deg)	(mm)	(mm/year)	Amp.(mm)	Phase (deg)	Amp.(mm)	Phase (deg)
000	-25.0 (5.7)	-0.7 (1.3)	6.1 (2.3)	117.6 (31.6)	3.7 (1.7)	125.6 (44.7)
030	-22.5 (4.5)	-0.7 (1.4)	6.5 (3.1)	153.1 (38.9)	4.5 (1.9)	66.4 (68.0)
060	-14.6 (3.8)	-0.6 (1.3)	7.5 (3.8)	203.9 (40.4)	6.5 (1.8)	39.4 (27.2)
090	-3.5 (3.3)	-0.2 (1.3)	8.5 (3.4)	223.3 (23.6)	7.4 (2.1)	46.8 (11.0)
120	7.9 (4.3)	0.3 (1.3)	8.1 (2.4)	239.5 (29.2)	7.1 (1.8)	63.0 (17.7)
150	17.3 (5.4)	0.8 (1.4)	6.9 (2.2)	259.2 (35.3)	5.4 (1.2)	82.7 (27.4)
180	21.4 (5.3)	1.0 (1.6)	5.9 (2.9)	271.0 (81.2)	3.7 (1.5)	119.0 (42.4)
210	19.5 (4.4)	1.2 (1.5)	6.9 (3.9)	247.0 (140.6)	4.5 (1.8)	82.5 (74.7)
240	12.6 (3.6)	0.9 (1.3)	8.8 (4.2)	67.9 (105.9)	6.1 (1.4)	33.9 (14.0)
270	2.1 (3.5)	0.3 (1.3)	9.3 (3.7)	43.7 (33.5)	6.5 (1.7)	49.1 (11.1)
300	-10.3 (4.9)	-0.3 (1.4)	8.7 (2.8)	59.2 (27.9)	5.9 (2.0)	66.0 (19.0)
330	-20.5 (5.4)	-0.6 (1.4)	7.4 (2.0)	80.8 (30.2)	4.6 (1.9)	93.0 (32.4)

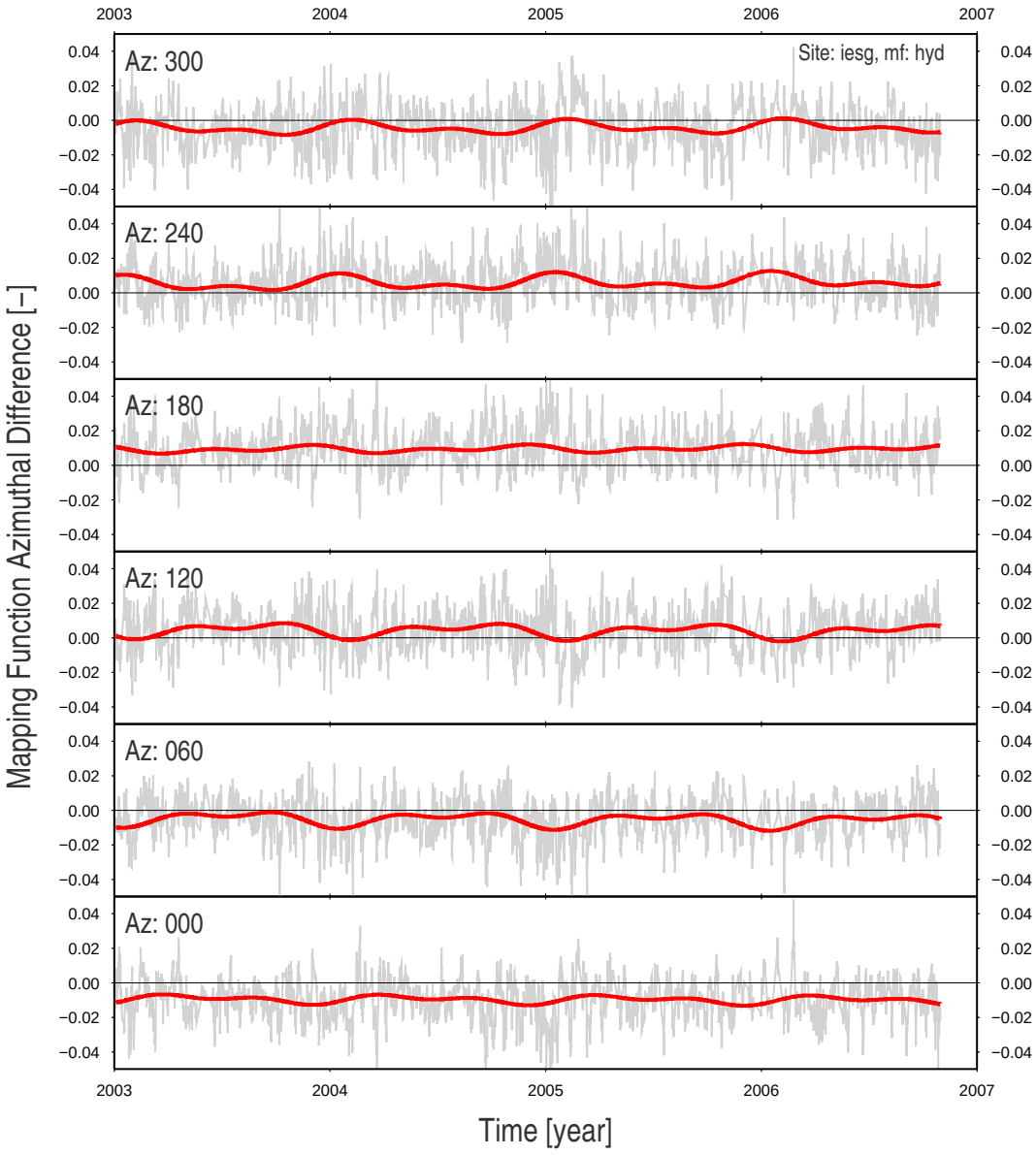

Figure 6.5: Time series of the hydrostatic mapping functions asymmetry at 5 degrees elevation for CGPS station IESG. Time series are plotted every 60 degrees (although ray-traced every 30 degrees) for clarity.

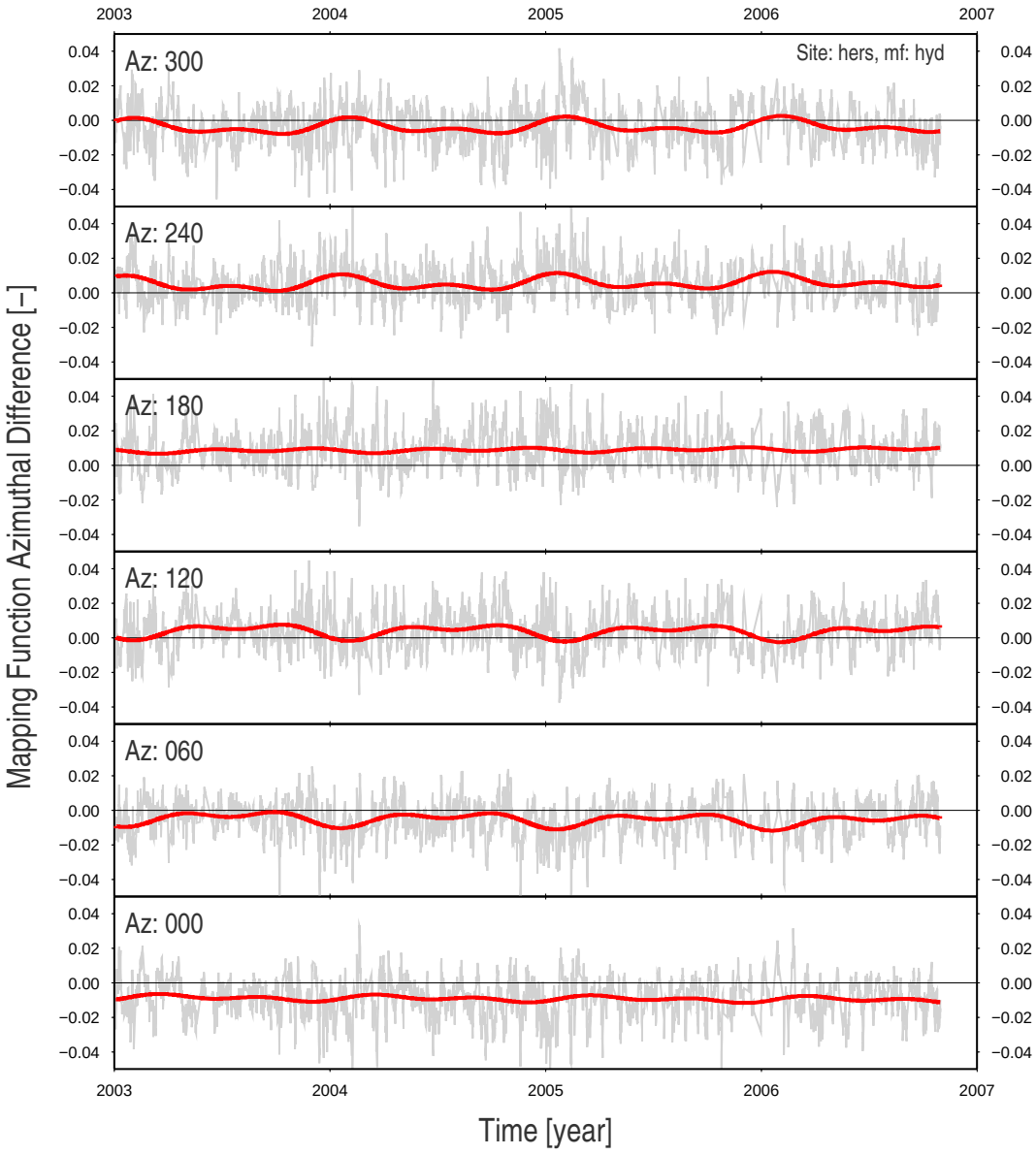

Figure 6.6: Time series of the hydrostatic mapping functions asymmetry at 5 degrees elevation for CGPS station HERS. Time series are plotted every 60 degrees (although ray-traced every 30 degrees) for clarity.

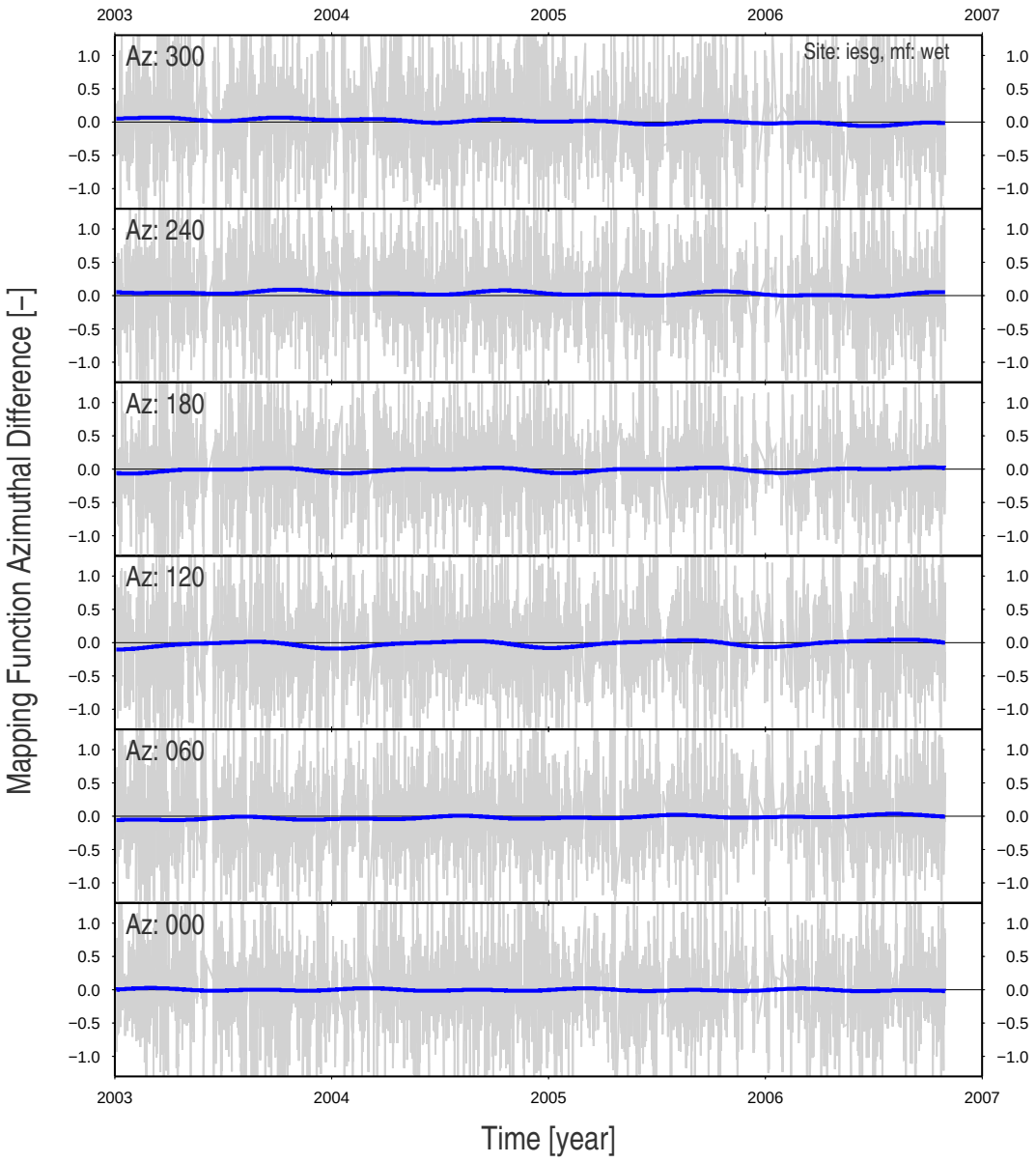

Figure 6.7: Time series of the wet mapping functions asymmetry at 5 degrees elevation for CGPS station IESG. Time series are plotted every 60 degrees (although ray-traced every 30 degrees) for clarity.

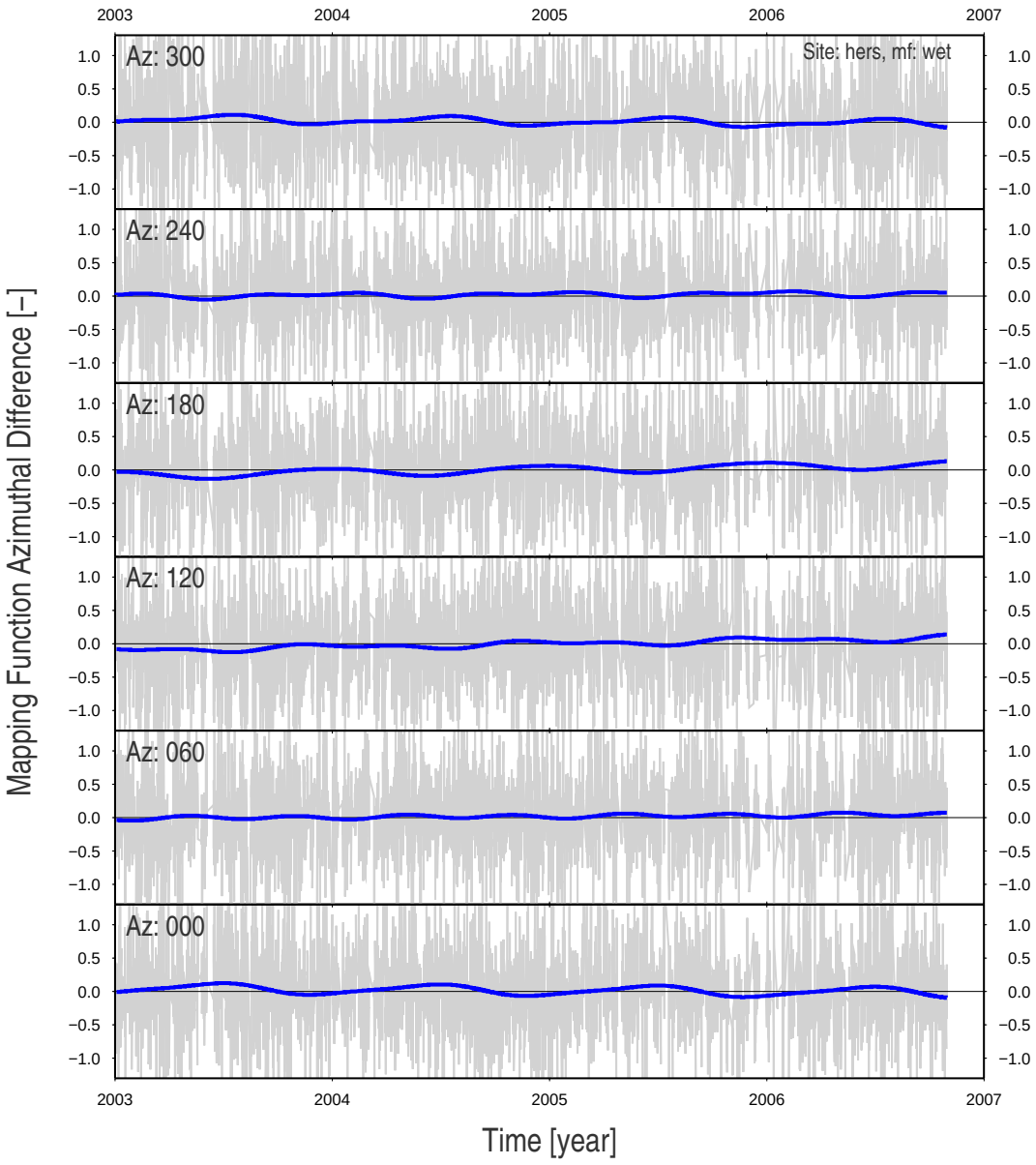

Figure 6.8: Time series of the wet mapping functions asymmetry at 5 degrees elevation for CGPS station HERS. Time series are plotted every 60 degrees (although ray-traced every 30 degrees) for clarity.

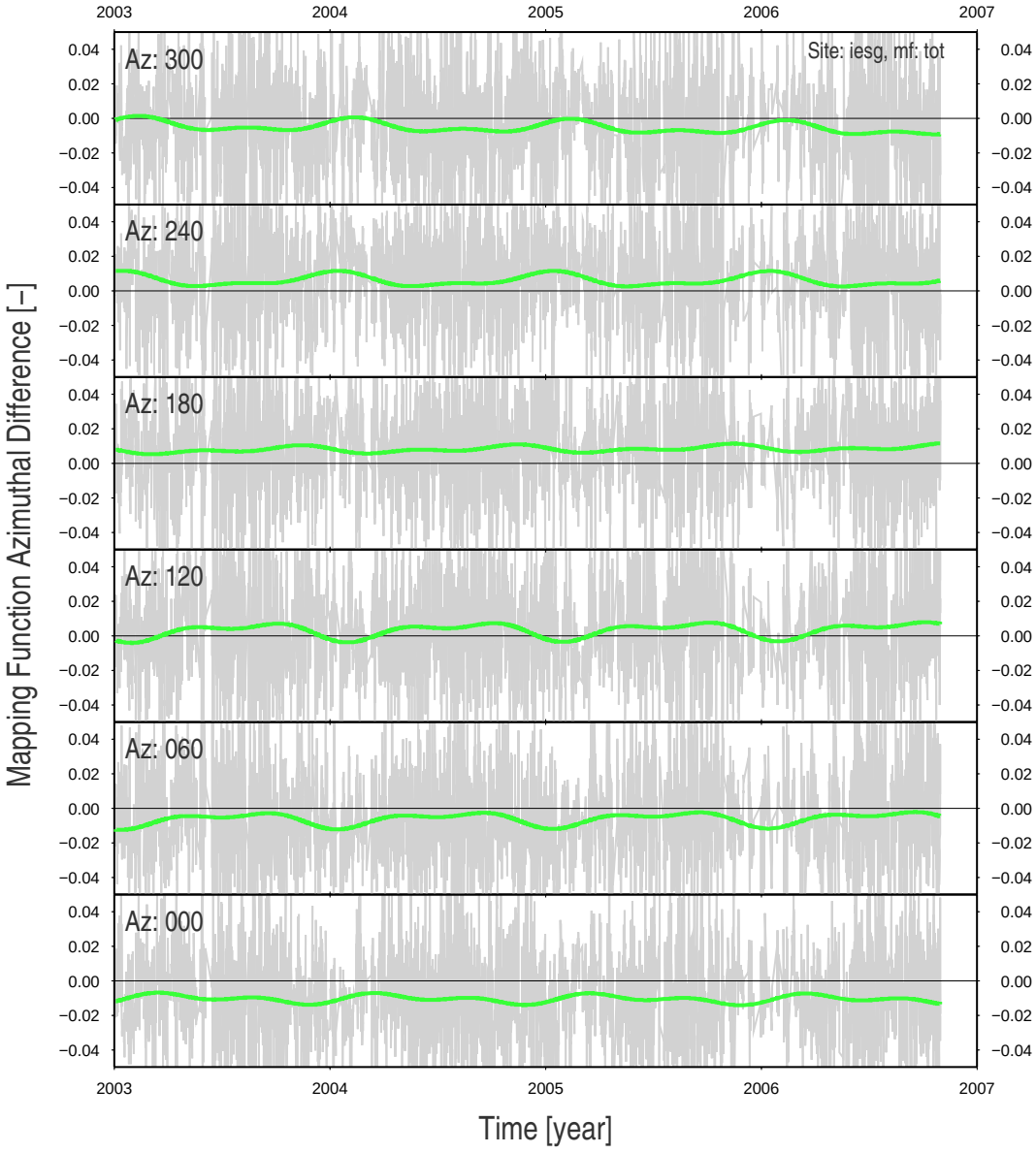

Figure 6.9: Time series of the total mapping functions asymmetry at 5 degrees elevation for CGPS station IESG. Time series are plotted every 60 degrees (although ray-traced every 30 degrees) for clarity.

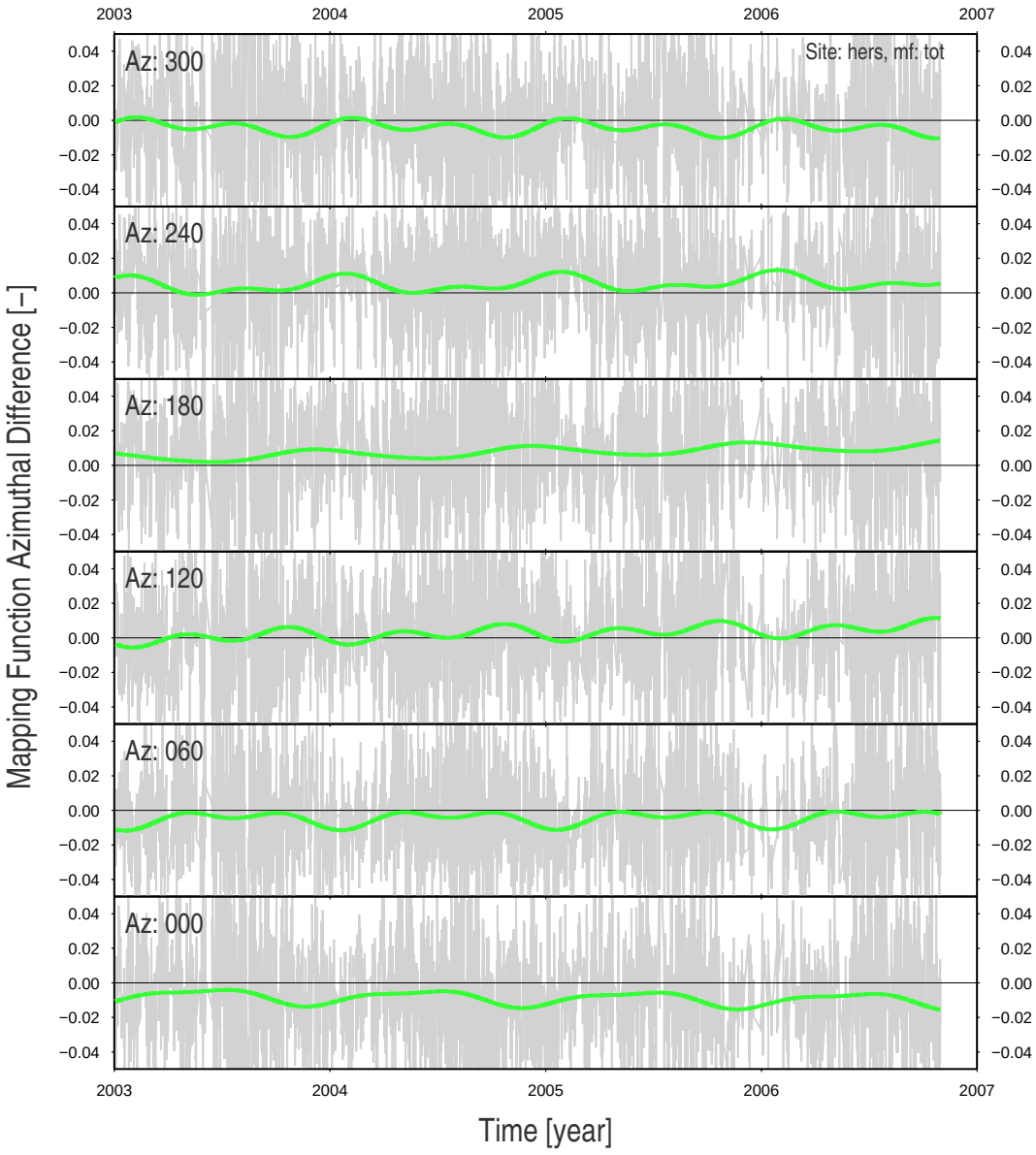

Figure 6.10: Time series of the total mapping functions asymmetry at 5 degrees elevation for CGPS station HERS. Time series are plotted every 60 degrees (although ray-traced every 30 degrees) for clarity.

6.3 Positioning performances

In the previous two sections of this chapter the major differences between estimating gradients in the GPS data processing or employing an azimuthal dependent mapping function were highlighted, and the characteristics of such a mapping function were identified. In this section, the positioning performances of the two approaches are examined. Table 6.4 presents an extended version of Table 5.6, with three new solutions added: **OMFAHRT_OFF**, **OMFSHRTGRD_OFF** and **OMFSHRTGRD06H_OFF**. As with Table 5.6, for clarity the label '_OFF' is still used to make clear that no APL corrections of any sort were applied in these tests. The OMFAHRT_OFF solution only differs from OMFSHRT_OFF by the use of the azimuth dependent OMF instead of the symmetric one. The two 'GRD' solutions are similar to OMFSHRT_OFF except that daily gradients were estimated in OMFSHRTGRD_OFF and 6 hourly gradients were estimated in OMFSHRTGRD06H_OFF. The goal was to have gradients estimated as consistently as possible with the OMFAHRT_OFF solution, therefore the OMFS was preferred to the NMF (wet), and ray-traced ZHD was introduced, as in OMFSHRT_OFF.

From Table 6.4, it can be seen that the two solutions which solved for gradients (OMFSHRTGRD_OFF and OMFSHRTGRD06H_OFF) clearly have the lowest WRMS values. When compared to OMFS_OFF, they show a big improvement in the horizontal precision with about 20% WRMS reduction on the north component, and 10% reduction on the east one. The lowest WRMS in the vertical is obtained for OMFSHRTGRD06H_OFF (5.17 mm) which is a 13.3% improvement over NMF_OFF, a 3.7% improvement on VMF1GRT_OFF (and OMTS_OFF, OMFSHRT_OFF), and a 9.1% improvement over OMFAHRT_OFF.

Table 6.4: Weighted RMS (mm) for the north, east and vertical components for 10 different tropospheric modelling strategies and mean vertical offset to OMFS_OFF solution. (Functional model: linear regression plus annual and semi-annual signals; Stochastic model: combination of white noise plus Flicker noise; Offsets in time series: selected only.)

Strategy/Solution **Note: all _OFF**	north WRMS (mm) (std)	east WRMS (mm) (std)	Vert. WRMS (mm) (std)	Mean vertical offset to OMFS_OFF (mm) (std)
NMF	2.48 (0.20)	3.04 (0.25)	5.96 (0.56)	1.01 (0.51)
GMF	2.48 (0.20)	3.04 (0.25)	5.89 (0.55)	0.33 (0.18)
OMFS	2.49 (0.21)	3.03 (0.25)	5.40 (0.59)	0.00 (0.00)
VMF1G	2.48 (0.21)	3.04 (0.26)	5.39 (0.59)	0.56 (0.29)
OMFSHRT	2.49 (0.20)	3.04 (0.24)	5.36 (0.45)	-1.19 (0.50)
VMF1GRT	2.49 (0.21)	3.04 (0.25)	5.37 (0.44)	-0.57 (0.43)
OMTS	2.48 (0.20)	3.04 (0.26)	5.36 (0.45)	-1.37 (0.56)
OMFAHRT	2.40 (0.25)	2.97 (0.29)	5.69 (0.33)	-0.53 (0.77)
OMFSHRTGRD06H	2.00 (0.27)	2.73 (0.35)	5.17 (0.41)	-1.29 (1.32)
OMFSHRTGRD	2.03 (0.27)	2.76 (0.33)	5.24 (0.43)	-1.52 (1.27)

For the solution which used an azimuthal dependent mapping function (OMFAHRT_OFF) there was also an improvement in horizontal precision but only about 3% in the north and east and in the vertical 4.5% when compared to NMF_OFF and 6% when compared to VMF1GRT_OFF.

In terms of precision, the solution which used an azimuthal dependent mapping function (OMFAHRT_OFF) performs worse than the two solutions which solved for gradients (OMFSHRTGRD_OFF and OMFSHRTGRD06H_OFF). The WRMS in the north is about 0.4 mm higher, the east about 0.2 mm higher, and the up about 0.5 mm higher. However, the inter station consistency is better, as indicated by the lower standard deviations obtained for OMFAHRT_OFF, which in the vertical are the lowest of all solutions and could indicate that the real tropospheric noise is being effectively reduced on a station basis, making the overall

solution more homogenous.

Table 6.4 also presents the Mean vertical offset to OMFS_OFF (as the reference). Here it can be seen that the two solutions which solved for gradients (OMFSHRTGRD_OFF and OMFSHRTGRD06H_OFF) have the largest offsets of -1.52 and -1.29 mm, and the largest standard deviations of about 1.3 mm. Whereas the solution which used azimuthal dependent mapping function (OMFAHRT_OFF) differs from these two solutions by about 1 and 0.8 mm and has an offset of only -0.53 mm. Unfortunately, from our processing, there is no way to say which solution is closest to the truth. However it is interesting to note that, in terms of the mean vertical offset, OMFSHRTGRD_OFF and OMFSHRTGRD06H_OFF are most closely aligned to the OMTS_OFF solution, by being the most negative, but are also least homogeneous. Whereas, the OMFAHRT_OFF is most closely aligned to the VMF1GRT_OFF which is now part of the IGS 2008 recommendations (if not available, GMF is recommended) (`http://www.ngs.noaa.gov/IGSWorkshop2008/docs/IGS08_recommendations.pdf`).

6.4 Estimated Troposphere Azimuthal Variability

Troposphere Azimuthal Variability (TAV) was estimated in two ways: (i) by fitting a model (linear gradients) in the GPS data processing and (ii) by ray-tracing a NWM at a set of azimuths, to derive azimuth dependent mapping functions. In the former case (i), it should be noted that the geometrical configuration is fixed by the model itself (and the derivative of the mapping function used to estimate the correction to the a priori zenith delay) with, in general, a north-south and an east-west component introduced. Whereas, no more parameters were estimated

in the latter case (ii).

It was demonstrated in the previous section that the number of gradients estimated does not impact on the position quality. The data was originally reprocessed accounting for 6 hourly gradient parameters for two reasons. The first, was to test the impact of estimating more parameters on the quality of the position estimate. The second, was to match the time resolution of the NWM products used to derive the azimuth dependent mapping functions.

To compare the two, gradients were converted to azimuthal effect at 5 degrees elevation following Meindl et al. [2004]:

$$AE_{grd} = \frac{\partial m}{\partial \epsilon}[G_N \cos\alpha + G_E \sin\alpha] \tag{6.1}$$

where m is the mapping function, normally the wet, (OMFS wet in this case, to be as consistent as possible with the azimuth dependent mapping function for comparison), ϵ is the elevation angle, α the azimuth of the satellite, and G_N and G_E the north and east gradients parameters, estimated every 6 hours and set to vary linearly in between. The azimuthal effect from the azimuth dependent mapping functions was estimated as follows:

$$AE_{azi} = (NMF - OMFS + OMFA)_{hyd}(\epsilon) * ZHD_{rt} \tag{6.2}$$

$$+ \quad (NMF - OMFS + OMFA)_{wet}(\epsilon) * ZTD\_COR \tag{6.3}$$

where $(NMF - OMFS + OMFA)$ is the absolute AMF (it is recalled here that OMFS and OMFA are built as a correction upon respective NMF hydrostatic and wet, where OMFS is the symmetric mapping function, and OMFA, the asymmet-

ric mapping function), ZHD_{rt} the ray-traced ZHD, and ZTD_COR the estimated correction to the ZTD.

Note: In the conversion of gradients to delays at a certain elevation angle, the role of the mapping function should not be undermined as its derivative with respect to the elevation angle is used. It means that whatever the signal, true or residual, it can be directly mapped into those equivalent delays.

In the following, are compared the azimuth effect in the north and east directions over 3.8 years, using all 30 CGPS stations. Gradient parameters are somewhat expected to lead to smoother time series as their estimation is based on data observed from any azimuth and elevation, with data at low elevations being down weighted in the least squares adjustment. On the contrary, the azimuth effect estimated from an azimuth dependent mapping function relies only on a single value of the ray-traced mapping function. The noise is driven by the NWM itself and the quality of the ray-tracing algorithm. Tables 6.5 and 6.6 present the results of the comparison at 5 degrees elevation and 0 and 90 degrees azimuth. But before examining those results, short time series of TAV are presented for CGPS stations IESG and HERS as Figures 6.11 and 6.12. Considering Figures 6.11 to 6.13, the time series reveal two essential points:

- The agreement is generally good between the two techniques. Variations at various time scales are handled the same for all directions.
- Overall, the background noise in the AMF time series is higher than the one found in the gradient derived time series although there are CGPS stations, like NSTG presented here, for which gradient estimation does not look successful.

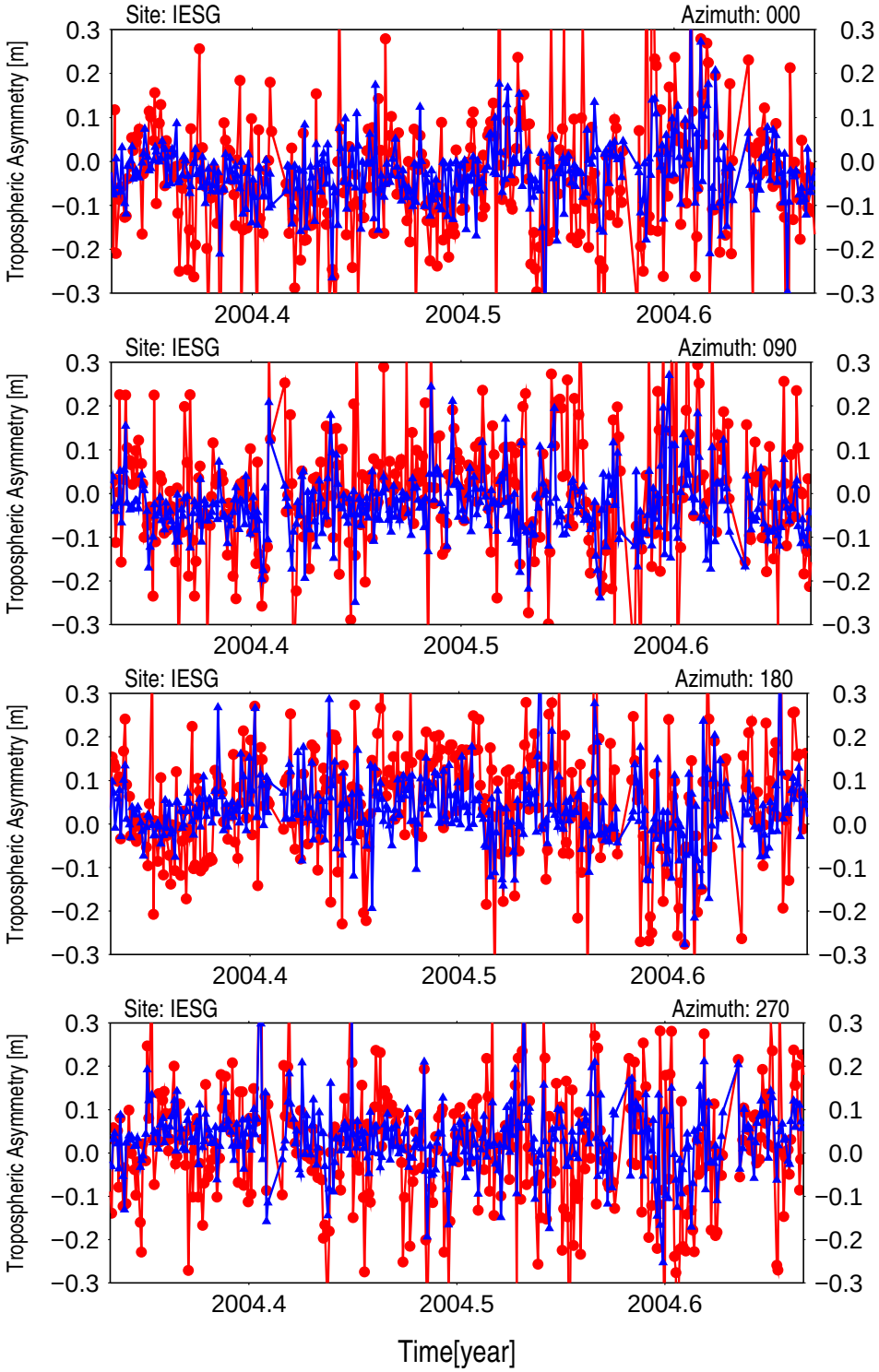

Figure 6.11: Four months time series of the tropospheric asymmetry at 5 degrees elevation and on different azimuths at CGPS station IESG. Red: estimated using azimuth dependent mapping functions; Blue: estimated using 6 hourly horizontal tropospheric gradients.

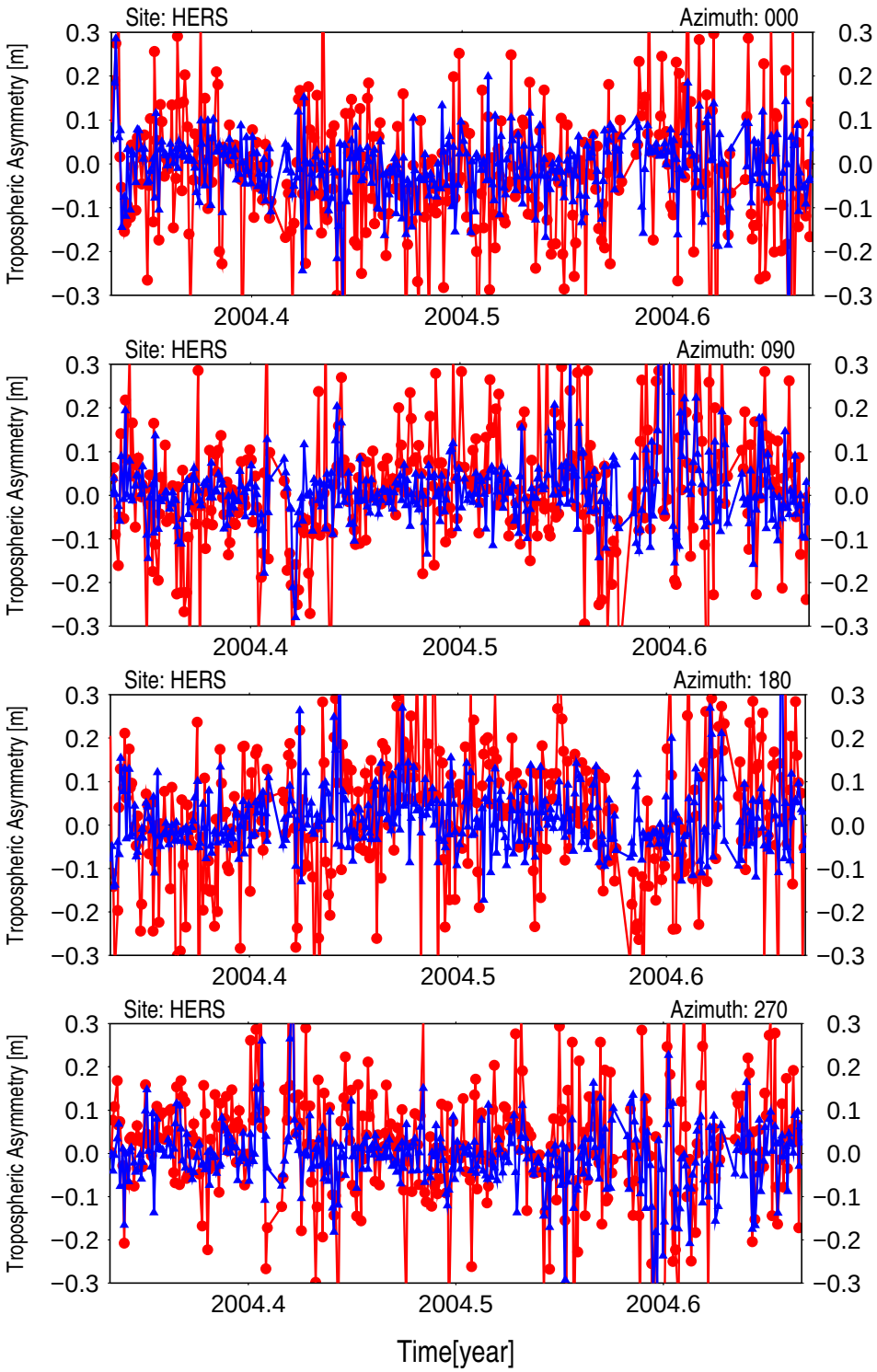

Figure 6.12: Four months time series of the tropospheric asymmetry at 5 degrees elevation and on different azimuths at CGPS station HERS. Red: estimated using azimuth dependent mapping functions; Blue: estimated using 6 hourly horizontal tropospheric gradients.

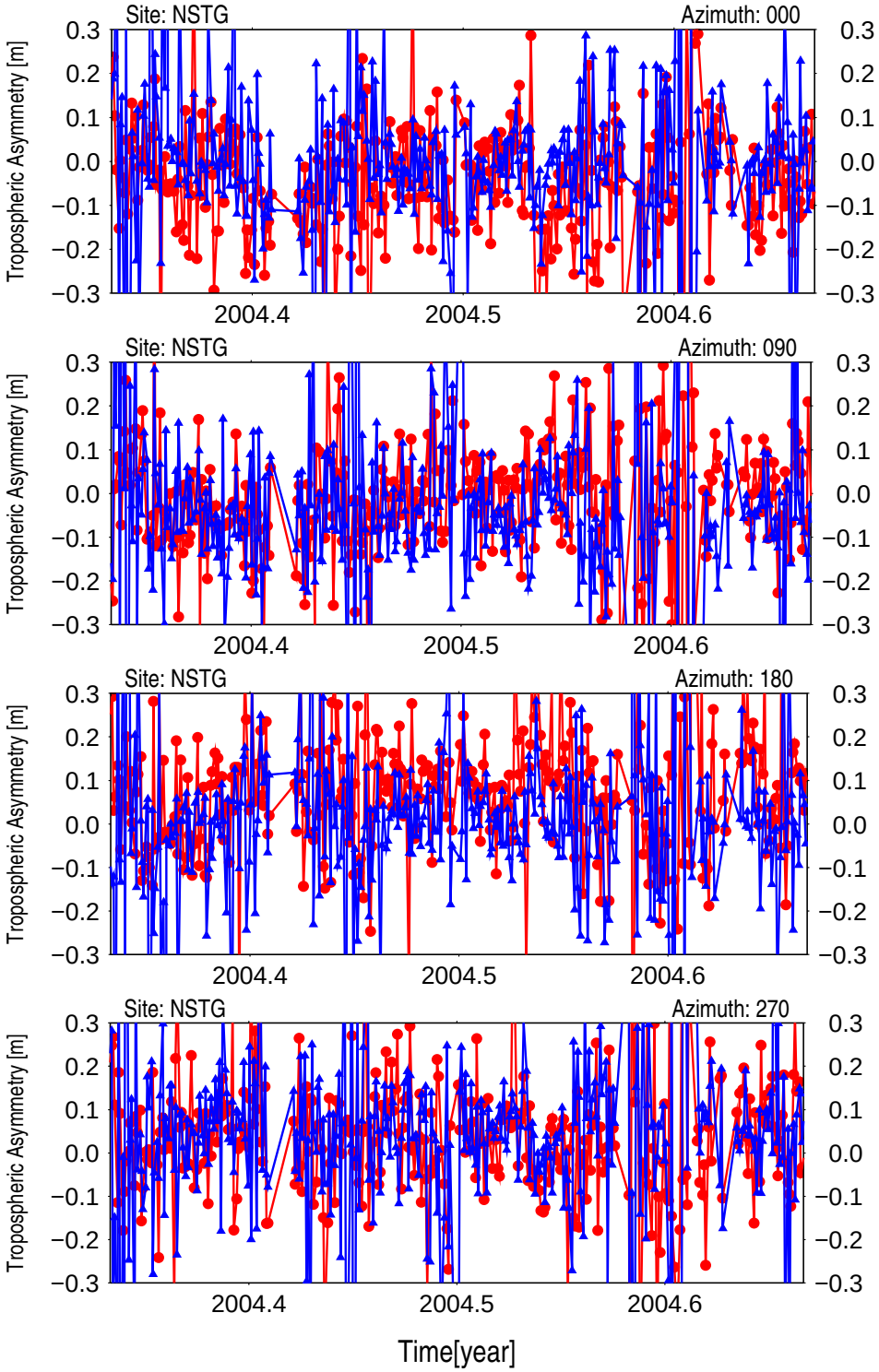

Figure 6.13: Four months time series of the tropospheric asymmetry at 5 degrees elevation and on different azimuths at CGPS station NSTG. Red: estimated using azimuth dependent mapping functions; Blue: estimated using 6 hourly horizontal tropospheric gradients.

Considering Table 6.5, it can be seen that the overall average effect in the north is -0.061 m estimated using AMF, and -0.025 m when inferred from gradients, indicating the azimuthal effect for the AMF (AE_{azi}) is about 2.5 times larger than the one given by the gradients (AE_{grd}). RMS are consistent in the two directions for both the AMF and gradients solutions, with respectively average RMS of about 0.13 m and 0.08 m. However, a further inspection of Table 6.5 shows that the average values for each station are much more homogeneous in the case of AE_{azi} when compared to AE_{grd}, with RMSs varying much less in the case of the AMF than for the gradients solution. This might reveal a limitation in the physics of the NWM, e.g. if it was too 'smooth' (consistent over the covered area) leading to homogeneity in the AMF, but is more likely to be the fact that the AE_{grd} is dependent on the overall quality of the GPS data itself, which is far from the same for all stations involved. From Table 6.6, it can be seen that the effect in the east and west are similar and much lower in amplitude than the effects on the north and south components.

A periodic (annual only) variation was fitted to the time series of azimuthal variability from both sources, in the four cardinal directions. Figures 6.14 and 6.15 present the amplitudes and phases of the annual signals evaluated at 5 degrees elevation from the two techniques. In general, the amplitude of the signal is very weak compared to the background noise of the time series (especially in the east-west direction).

Considering Figure 6.14, there is a clear disparity between the two techniques in that there is almost no signal in the gradient derived asymmetry at 5 degrees to be found in the time series in the north and south directions, except maybe at four of CGPS stations, namely ABYW, MORP, SUNB (the largest) and SHEE. The phase of the signal is rather erratic over the UK, very likely a consequence of the quasi absence of an annual signal.

Table 6.5: Average amplitude and RMS of the northern and southern tropospheric asymmetry, estimated using both AMF and gradients, and their difference for 30 CGPS stations in the UK. Values are given for an elevation of 5 degrees.

		AMF		Gradients		AMF minus gradients			
	site	Average	RMS	Average	RMS	Average	RMS	Sample	Outliers
	(m)	(m)	(m)	(m)	(m)	(m)			
	ABYW	-0.058	0.144	-0.098	0.095	0.040	0.155	2473	29
	BARK	-0.069	0.143	-0.038	0.095	-0.030	0.150	2826	38
	CAMB	-0.057	0.137	-0.021	0.081	-0.036	0.134	2785	36
	CARL	-0.068	0.125	-0.031	0.070	-0.037	0.119	2277	37
	COLC	-0.061	0.147	-0.016	0.067	-0.045	0.135	2701	47
	DARE	-0.066	0.125	-0.026	0.063	-0.040	0.111	2856	47
	EDIN	-0.062	0.124	-0.041	0.112	-0.022	0.148	2711	33
	GLAS	-0.076	0.123	-0.032	0.072	-0.044	0.119	2798	40
	HERS	-0.046	0.143	-0.012	0.067	-0.034	0.126	3137	47
	IESG	-0.060	0.135	-0.028	0.064	-0.033	0.122	2993	46
N	INVE	-0.067	0.116	-0.026	0.070	-0.041	0.109	2610	34
O	IOMS	-0.064	0.124	-0.015	0.074	-0.049	0.115	2126	31
R	KING	-0.062	0.136	-0.032	0.069	-0.030	0.128	2805	48
T	***LEED***	*-0.066*	*0.127*	*-0.047*	*0.878*	*-0.019*	*0.882*	*2825*	*22*
H	LERW	-0.093	0.117	-0.027	0.057	-0.066	0.106	2955	44
	LOWE	-0.055	0.138	-0.021	0.062	-0.035	0.125	2911	46
	MORP	-0.066	0.121	0.011	0.090	-0.077	0.124	2704	35
	NEWC	-0.064	0.121	-0.032	0.070	-0.032	0.116	2721	41
	NEWL	-0.053	0.130	-0.026	0.063	-0.027	0.120	2871	52
	NPLD	-0.044	0.140	-0.016	0.064	-0.028	0.127	2039	33
	NSTG	*-0.068*	*0.127*	*-0.007*	*0.595*	*-0.062*	*0.606*	*2839*	*27*
	OSHQ	-0.055	0.143	-0.011	0.070	-0.044	0.131	2587	35
	PERS	-0.053	0.132	-0.022	0.067	-0.030	0.122	2881	57
	SHEE	-0.062	0.143	-0.048	0.111	-0.014	0.157	2767	39
	SUNB	-0.041	0.145	0.034	0.143	-0.074	0.181	2774	34
	THUR	-0.068	0.110	-0.028	0.069	-0.040	0.107	2012	22
	AVERAGE	-0.061	0.132	-0.025	0.078	-0.036	0.022	2680	39
	ABYW	0.047	0.139	0.103	0.101	0.150	0.198	2474	28
	BARK	0.035	0.140	0.042	0.100	0.077	0.195	2831	33
	CAMB	0.026	0.135	0.025	0.085	0.051	0.184	2795	26
	CARL	0.035	0.133	0.033	0.072	0.068	0.174	2283	31
	COLC	0.029	0.145	0.018	0.069	0.047	0.183	2695	53
	DARE	0.035	0.134	0.028	0.066	0.064	0.174	2863	40
	EDIN	0.034	0.130	0.043	0.107	0.077	0.191	2704	40
	GLAS	0.033	0.129	0.036	0.076	0.069	0.172	2805	33
	HERS	0.025	0.146	0.015	0.069	0.041	0.184	3148	36
	IESG	0.028	0.131	0.030	0.067	0.058	0.171	2989	50
S	INVE	0.030	0.120	0.029	0.072	0.059	0.161	2606	38
O	IOMS	0.037	0.123	0.018	0.076	0.055	0.165	2125	32
U	KING	0.036	0.140	0.035	0.074	0.072	0.181	2812	41
T	***LEED***	*0.045*	*0.131*	*0.051*	*0.872*	*0.096*	*0.883*	*2818*	*29*
H	LERW	0.038	0.107	0.029	0.061	0.067	0.145	2954	45
	LOWE	0.037	0.140	0.024	0.065	0.061	0.177	2914	43
	MORP	0.040	0.124	-0.009	0.092	0.031	0.173	2703	36
	NEWC	0.039	0.121	0.035	0.073	0.074	0.163	2721	41
	NEWL	0.027	0.131	0.029	0.066	0.056	0.169	2889	34
	NPLD	0.033	0.148	0.019	0.068	0.052	0.189	2045	27
	NSTG	*0.044*	*0.127*	*0.016*	*0.559*	*0.060*	*0.582*	*2844*	*22*
	OSHQ	0.025	0.143	0.014	0.070	0.039	0.181	2590	32
	PERS	0.035	0.134	0.025	0.070	0.060	0.174	2889	49
	SHEE	0.055	0.149	0.054	0.116	0.109	0.215	2767	39
	SUNB	0.034	0.142	-0.030	0.142	0.004	0.218	2773	35
	THUR	0.032	0.109	0.030	0.070	0.061	0.149	2009	25
	AVERAGE	0.034	0.133	0.028	0.080	0.063	0.027	2682	36

Table 6.6: Average amplitude and RMS of the eastern and western tropospheric asymmetry, estimated using both AMF and gradients, and their difference for 30 CGPS stations in the UK. Values are given for an elevation of 5 degrees.

		AMF		Gradients		AMF minus gradients			
	site	Average	RMS	Average	RMS	Average	RMS	Sample	Outliers
	(m)	(m)	(m)	(m)	(m)	(m)			
	ABYW	-0.019	0.148	0.013	0.090	-0.033	0.148	2461	41
	BARK	-0.020	0.140	-0.009	0.096	-0.010	0.148	2817	47
	CAMB	-0.025	0.143	0.001	0.087	-0.027	0.142	2793	28
	CARL	-0.018	0.140	-0.019	0.073	0.001	0.132	2273	41
	COLC	-0.027	0.141	-0.013	0.070	-0.014	0.133	2701	47
	DARE	-0.024	0.132	-0.012	0.067	-0.012	0.123	2851	52
	EDIN	-0.016	0.136	-0.008	0.174	-0.008	0.206	2712	32
	GLAS	-0.024	0.138	-0.003	0.076	-0.020	0.131	2792	46
	HERS	-0.009	0.145	-0.003	0.067	-0.006	0.132	3115	69
	IESG	-0.017	0.135	-0.035	0.065	0.019	0.125	2984	55
E	INVE	-0.008	0.135	-0.016	0.075	0.007	0.128	2596	48
A	IOMS	-0.015	0.129	-0.025	0.080	0.010	0.125	2109	48
S	KING	-0.022	0.138	-0.010	0.068	-0.012	0.127	2788	65
T	***LEED***	*-0.022*	*0.132*	*0.019*	*1.557*	*-0.041*	*1.560*	*2817*	*30*
	LERW	-0.014	0.120	-0.012	0.065	-0.002	0.108	2944	55
	LOWE	-0.026	0.144	-0.026	0.067	0.001	0.135	2901	56
	MORP	-0.028	0.135	-0.031	0.091	0.003	0.138	2693	46
	NEWC	-0.025	0.136	-0.017	0.075	-0.008	0.130	2716	46
	NEWL	-0.013	0.138	-0.021	0.068	0.008	0.129	2870	53
	NPLD	-0.005	0.145	-0.011	0.065	0.006	0.134	2034	38
	NSTG	*-0.023*	*0.146*	*-0.031*	*0.606*	*0.008*	*0.617*	*2839*	*27*
	OSHQ	-0.030	0.141	-0.012	0.069	-0.017	0.131	2576	46
	PERS	-0.032	0.143	-0.017	0.069	-0.015	0.135	2886	52
	SHEE	-0.028	0.147	0.029	0.116	-0.057	0.158	2745	61
	SUNB	-0.007	0.143	-0.017	0.124	0.010	0.169	2773	35
	THUR	-0.022	0.127	-0.022	0.073	-0.001	0.114	1999	35
	AVERAGE	-0.020	0.138	-0.012	0.082	-0.007	0.016	2672	47
	ABYW	0.006	0.148	-0.011	0.089	-0.004	0.195	2460	42
	BARK	0.003	0.149	0.013	0.098	0.016	0.204	2832	32
	CAMB	-0.010	0.143	0.003	0.086	-0.007	0.192	2788	33
	CARL	-0.009	0.131	0.022	0.073	0.013	0.175	2276	38
	COLC	-0.013	0.151	0.017	0.072	0.004	0.194	2697	51
	DARE	-0.009	0.132	0.014	0.068	0.005	0.173	2862	41
	EDIN	-0.010	0.131	0.013	0.188	0.003	0.249	2713	31
	GLAS	-0.013	0.127	0.006	0.075	-0.007	0.175	2797	41
	HERS	-0.001	0.142	0.005	0.066	0.003	0.182	3132	52
	IESG	-0.003	0.138	0.038	0.068	0.035	0.181	2994	45
W	INVE	-0.019	0.132	0.018	0.076	-0.001	0.179	2607	37
E	IOMS	-0.010	0.135	0.028	0.083	0.017	0.186	2125	32
S	KING	0.007	0.145	0.012	0.070	0.019	0.186	2806	47
T	***LEED***	*-0.005*	*0.145*	*0.009*	*2.076*	*0.004*	*2.079*	*2824*	*23*
	LERW	-0.019	0.127	0.015	0.066	-0.005	0.173	2959	40
	LOWE	0.011	0.145	0.030	0.071	0.040	0.191	2901	56
	MORP	-0.004	0.145	0.035	0.093	0.032	0.203	2707	32
	NEWC	-0.002	0.145	0.019	0.077	0.017	0.193	2720	42
	NEWL	-0.014	0.139	0.024	0.068	0.010	0.181	2878	45
	NPLD	0.012	0.141	0.014	0.067	0.025	0.182	2041	31
	NSTG	*-0.000*	*0.149*	*0.034*	*0.688*	*0.034*	*0.721*	*2837*	*29*
	OSHQ	-0.000	0.138	0.015	0.071	0.015	0.180	2583	39
	PERS	0.009	0.142	0.021	0.071	0.030	0.186	2889	49
	SHEE	0.010	0.155	-0.026	0.118	-0.016	0.217	2757	49
	SUNB	0.011	0.136	0.019	0.125	0.030	0.208	2774	34
	THUR	-0.025	0.125	0.024	0.075	-0.001	0.176	2003	31
	AVERAGE	-0.004	0.139	0.015	0.084	0.011	0.015	2679	40

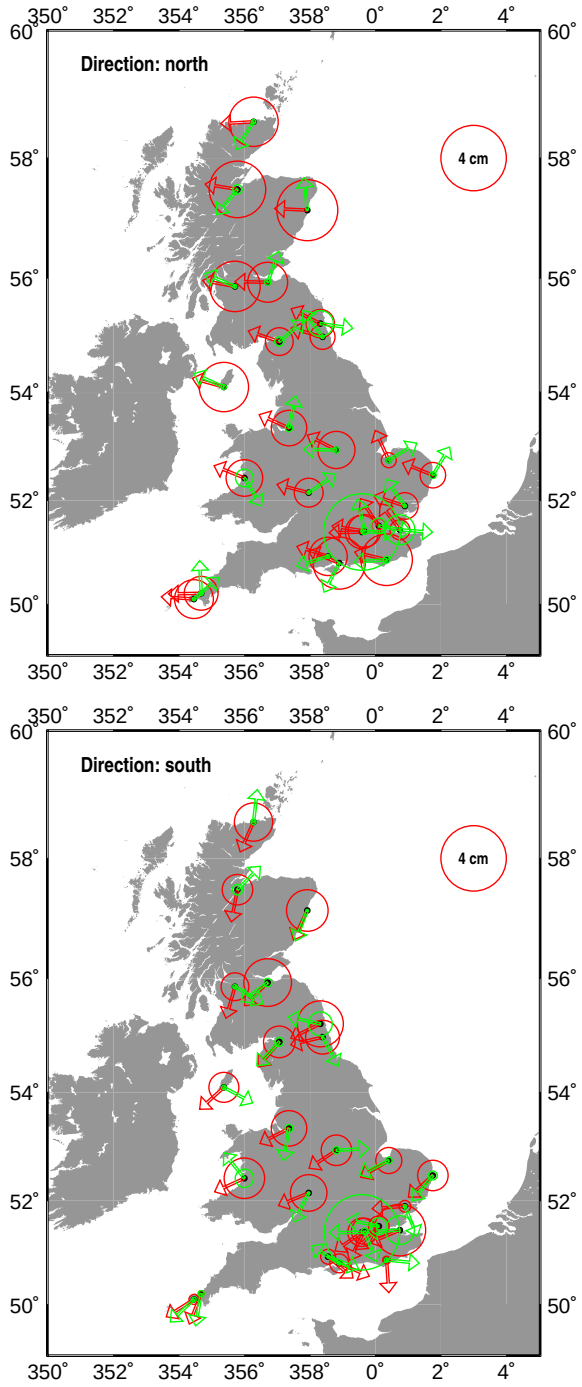

Figure 6.14: Amplitude and phase of the annual signal found in the azimuthal tropospheric asymmetry evaluated at 5 degrees elevation for the north (top) and south (bottom) directions. Red: using the azimuth dependent OMF; Green: estimating horizontal gradients.

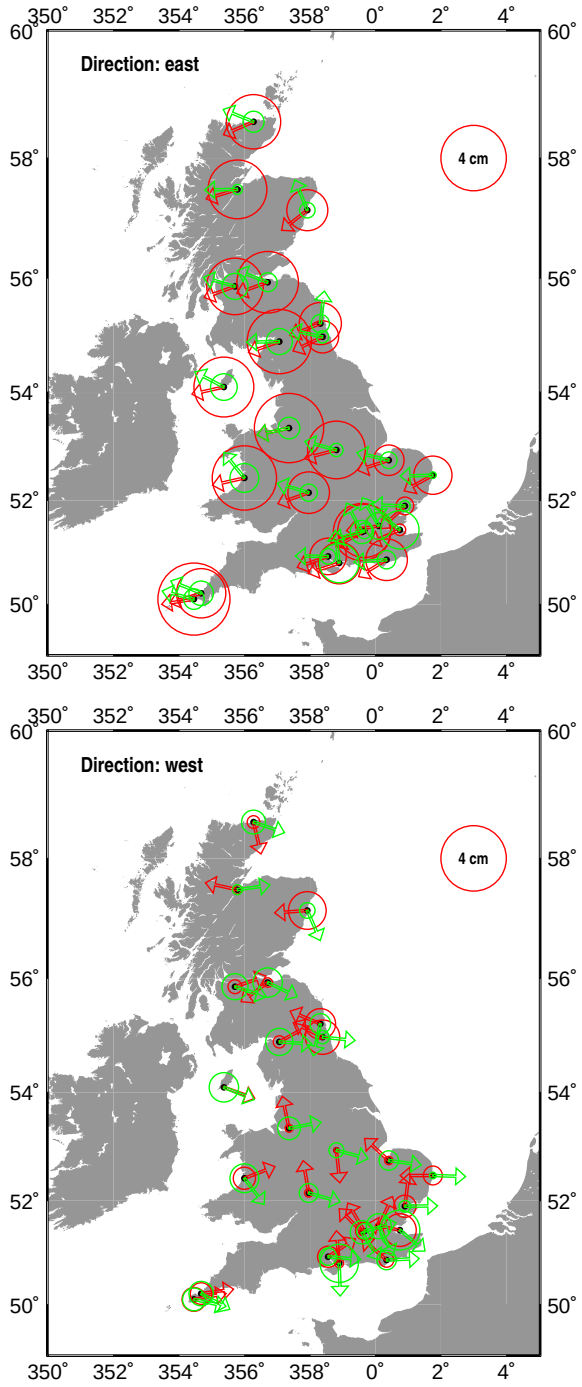

Figure 6.15: Amplitude and phase of the annual signal found in the azimuthal tropospheric asymmetry evaluated at 5 degrees elevation for the east (top) and west (bottom) directions. Red: using the azimuth dependent OMF; Green: estimating horizontal gradients.

The amplitude of the annual signal in the north direction obtained when using the AMF is much larger than the one obtained from the gradients, with 23 ± 8 mm versus 7 ± 9 mm. Big amplitudes are found for coastal sites, but this is not systematic. The phase, on the other hand, is very consistent. It reveals a regular pattern over the UK, possibly due to a misleading (filtering/smoothing) representation of the true climatology. Amplitudes for the south direction are smaller, but still much more significant than the ones found from the gradients (with 18 ± 7 mm versus 7± 9 mm).

Considering Figure 6.15, there is a significant difference between the amplitudes in the east and in the west for the AMF inferred azimuthal asymmetry, which is much lower west direction than in the east one, with respective amplitudes for the annual signal of 10± 6 mm and 29± 10 mm. Looking at Figure 6.15 further, there is a clear pattern in the distribution of the amplitude of the annual signal: for the east azimuthal variability, the more the site is in the western part of the area, the greater the amplitude. There seems to be a similar but opposite pattern for the west azimuthal asymmetry, with sites with the highest annual signal amplitudes located on the eastern part of the area.

The phases for the east troposphere asymmetry are in a very good agreement between the two modelling techniques, which both show consistency over the area. Again, due to the quasi absence of a signal in the west direction, phases look more random.

Although not all amplitudes and phases were published by Meindl et al. [2004] for their processing (only CGPS stations Kootwijk and Villanfranca were given), they found gradients with greater amplitude in the east component than in the

north, which is in a good agreement with what was obtained here for CGPS stations in the UK. Meindl et al. [2004], however, made clear that annual and semi-annual signals were not as pronounced for all stations as they were for the two CGPS stations mentioned above.

6.5 The impact of Troposphere Azimuthal Variability on ZTD Estimation

In this section the impact of accounting for the troposphere azimuthal variations on ZTD estimates is quantified. Four solutions are considered here: symmetric OMF with ray traced hydrostatic a priori ZHD (OMFSHRT), the azimuth dependent version of the OMFSHRT (OMFAHRT), and the OMFSHRT with gradients being solved for on a 24 hour basis (OMFSHRTGRD) and on a 6 hour basis (OMFSHRTGRD06H). For simplicity the _OFF suffix was dropped, but all solutions are free of atmospheric pressure loading correction. From the previous sections, the closeness between the two gradient solutions was demonstrated and a time series of the difference between the two is given as Figure 6.16. This figure confirmed that there was no need to further include the two, therefore, only OMFSHRT, OMFAHRT and OMFSHRTGRD06H are included in the remaining discussion for this section.

Table 6.7 details, on a station basis, the bias and standard deviation found in each possible difference between the three different solutions, computed over 3.8 years. Overall, the biases found are usually below 0.5 mm, which is well within the expected accuracy for the retrieval of ZTD using ground-based GNSS networks. Furthermore, the inter-solution noise (standard deviation of the differ-

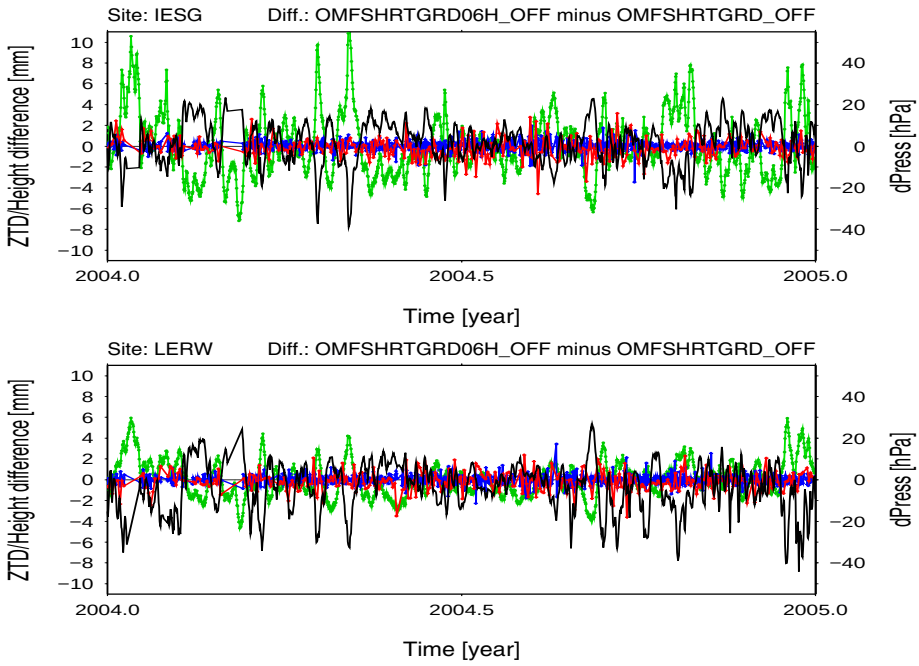

Figure 6.16: Time series of vertical coordinate (red) and ZTD (blue) difference based on different gradient estimation approaches for CGPS station IESG over year 2004.

ence) is in the region of 3 mm and is also below the precision attributed to the GNSS technique, which is still in the region of 1–1.5 cm (see e.g. Chapter 4).

6.6 Summary

Two approaches for handling the tropospheric asymmetry, either estimating gradients or using an azimuth dependent mapping function, were presented and compared. A study of the asymmetric contribution between the two approaches showed that overall, they are generally in agreement. Time series were found to be smoother for the gradients based estimates (as expected due to the contribution of all GPS data to the estimation of the gradients). Whereas, the use of an azimuth dependent mapping function clearly provided more consistent results on a station basis, as the GPS data at noisy stations does not contribute to the derivation of the mapping function.

Table 6.7: Bias and standard deviation of the difference between ZTD estimated using the azimuth dependent OMF mapping function and ZTD estimated using the symmetric OMF with and without gradients, for 30 CGPS stations in the UK over a 3.8 year period.

	OMFAHRT minus OMFSHRT			OMFSHRTGRD06 minus OMFSHRT			OMFSHRTGRD06 minus OMFAHRT		
Site	Bias (mm)	St.Dev (mm)	Sample Size	Bias (mm)	St.Dev (mm)	Sample Size	Bias (mm)	St.Dev (mm)	Sample Size
ABER	-0.7	2.9	3153	-0.3	3.4	3039	0.4	3.6	3038
ABYW	0.1	3.3	2694	1.8	3.1	2609	1.8	3.8	2609
BARK	-0.5	2.4	3114	-0.6	2.5	3004	-0.0	3.0	2999
CAMB	-0.2	2.8	3122	-0.4	2.6	3007	-0.2	3.2	3005
CARL	-0.3	2.7	2567	-0.1	2.1	2462	0.2	2.9	2455
COLC	-0.0	3.0	3022	-0.2	2.1	2910	-0.1	3.1	2908
DARE	-0.2	2.5	3150	-0.1	2.0	3053	0.1	2.6	3038
EDIN	-0.2	2.7	2929	0.1	2.3	2850	0.3	3.1	2818
GLAS	-0.1	2.7	3093	-0.1	2.2	3007	0.1	2.9	2983
HERS	-0.4	2.9	3303	-0.2	2.2	3337	0.1	2.9	3303
IESG	-0.4	3.0	3270	0.3	2.5	3190	0.7	3.0	3153
INVE	-0.4	2.6	2903	-0.3	2.7	2825	0.2	3.2	2790
IOMS	-0.5	2.2	2388	-0.0	2.2	2317	0.5	2.5	2281
KING	-0.2	2.6	3109	-0.1	2.0	3049	0.2	2.8	2994
LEED	-0.5	2.7	3084	-0.3	2.3	3016	0.3	3.0	2971
LERW	-0.2	2.3	3234	-0.3	2.0	3186	0.0	2.3	3117
LIVE	-0.7	3.0	3023	-0.6	3.3	2963	0.1	3.6	2908
LOWE	-0.7	3.2	3181	-0.2	2.5	3130	0.4	3.1	3067
MORP	-1.1	3.0	2958	0.6	3.6	2912	1.7	3.7	2842
NEWC	-0.3	2.3	3006	-0.0	2.2	2971	0.3	2.6	2891
NEWL	-0.1	3.2	3144	0.0	3.4	3125	0.1	3.2	3037
NOTT	-0.5	2.8	2853	0.1	3.1	2754	0.6	3.6	2681
NPLD	-0.5	3.0	2147	-0.1	2.0	2212	0.4	3.0	2141
NSTG	-0.9	4.3	2919	0.9	8.1	2876	1.9	8.2	2796
OSHQ	-0.3	2.8	2861	-0.2	2.2	2842	0.0	2.9	2742
PERS	-0.5	3.3	3179	-0.4	2.6	3168	0.1	3.4	3052
PMTG	-0.4	3.1	2892	-0.6	3.4	2889	-0.3	4.1	2781
SHEE	-0.8	2.8	3008	-0.9	3.0	3045	-0.1	3.7	2930
SUNB	-0.6	2.4	3049	-0.0	3.1	3050	0.6	3.5	2926
THUR	-0.2	2.1	2288	-0.1	2.0	2270	0.1	2.3	2165
Average	-0.4	2.8	30	-0.1	2.7	30	0.3	3.3	30

Chapter 7

Correlation Between Troposphere Modelling and Atmospheric Pressure Loading

This chapter details some results partly presented in [Orliac et al., 2007a] and [Orliac et al., 2007b] where the mapping function, together with the a priori zenith hydrostatic delay used in GPS processing, was found to influence the inferred vertical component by an amount which can be almost similar to the predicted atmospheric pressure loading induced effect.

7.1 Introduction

All solutions presented so far in this thesis are used again in this chapter. Apart from the OMF developed in this thesis, the NMF ([Niell, 1996]), GMF ([Boehm et al., 2006a]), and (gridded) VMF1 (VMF1G) ([Boehm et al., 2006b]) are used. For the sake of clarity, a brief recap on those various solutions is given here:

NMF	...	NMF used with standard a priori ZHD
GMF	...	GMF used with standard a priori ZHD
VMF1G	...	VMF1 used with standard a priori ZHD
VMF1GHRT	...	VMF1G used with consistent ray traced a priori ZHD.
OMFS	...	Azimuthally symmetric OMF (see Chapter 3 used with standard a priori ZHD)
OMFSHRT	...	Azimuthally symmetric OMF used with consistent ray traced ZHD
OMFSHRTGRD	...	OMFSHRT with daily horizontal gradients estimated
OMFAHRT	...	Azimuth dependent OMF with consistent ray traced ZHD
OMTS	...	Azimuthally symmetric Total OMF - Independent from a priori ZHD type

While comparing the impact of the different mapping functions on estimated positions and ZTD, it was found that the impact of the troposphere delay, in the sense of a mapping function plus a priori zenith delay, could influence the retrieved time series by an amount that would almost match that of the predicted atmospheric pressure loading induced displacement (APL) ([Orliac et al., 2007a] and [Orliac et al., 2007b]). This chapter shows how the choice of the mapping function, and of that of the a priori ZHD, influence the retrieved coordinate time series in a fashion that can almost perfectly match the predicted APL.

7.2 Cross-Correlation Between Height Time Series and Atmospheric Pressure Loading

The cross correlation between position height time series and predicted APL is examined here. The resolution of the time shift is the same as the estimated coordinates, i.e. one day. The range examined is -10 to $+10$ days. Ideally, time series with 6 hourly resolution would be examined, but coordinates were only estimated on a daily basis. The cross correlation was estimated for detrended height time series (periodic signals were left untouched, only the offset and linear trend were removed). The time series were detrended assuming the coordinate estimates stochastic model is best represented by a combination of white noise plus Flicker noise, following Williams et al. [2004].

The results are presented in Figure 7.1. It is stressed that no APL of any kind was applied. Admittedly, the correlation between predicted APL signal and coordinate time series is very weak and it cannot be pretended that the APL signal could be recovered from the coordinate time series analyzed here. The standard deviation is quite large, indicating strong station wise behavior as depicted on Figure 7.1 by the vertical error bars (1 sigma error). There are however three groups that can be identified on this plot: (*i*) those showing a positive correlation, which includes all the solutions that have ray traced ZHD as a priori information, instead of a ZHD derived from a standard model; (*ii*) those with no correlation, i.e. the VMF1G_OFF and the OMFS_OFF solutions; (*iii*) those with a negative correlation, i.e. the NMF_OFF and GMF_OFF solutions, the only two based on global models.

Of great interest, is the role played by the a priori ZHD in the attempt to

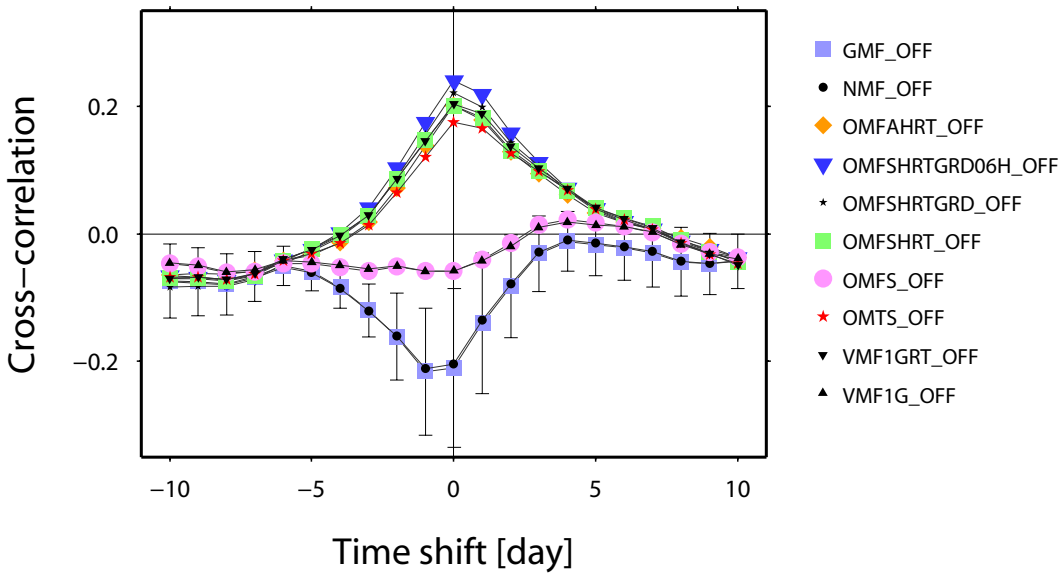

Figure 7.1: Average cross-correlations between the predicted atmospheric pressure loading induced displacements and height time series computed over a set of CGPS 27 stations in the UK. Error bars represent the standard deviation associated with the plotted value (only represented for the first solution plotted for clarity, as rather constant over the different solutions).

recover the APL signal. Those weak correlations do explain why when correcting for APL, generally worse solutions are obtained, as the signal cannot be recovered from any solution, accounting for it only adds noise. It is clear that switching from the OMFS_OFF to the OMFSHRT_OFF or from VMF1G_OFF to VMF1GRT_OFF, a better correlation to the APL is found. Although it is not possible, nor correct, to compute APL based on local pressure variation only, it was acknowledged e.g. by Petrov and Boy [2004] that it generally works. Therefore, as the ZHD, although ray traced from a complete NWM vertical profile, essentially depends only on the ground pressure, a better correlation to the APL is found.

7.3 Cross Correlation Between Differential Height Time Series and Atmospheric Pressure Loading

This section evaluates the impact of the mapping function on the coordinate estimates. To do so, various differential time series were formed, simply by differencing daily height estimates obtained with two different mapping functions. In a similar fashion, the impact of ray traced a priori zenith delay in place of a standard one is also assessed.

7.3.1 Impact of the Mapping Function

A series of differential solutions were obtained by taking the NMF_OFF solution as the reference one, that is, subtracting it from all other solutions. Cross-correlations with the APL are presented in Figure 7.2.

The importance of the choice of the mapping function in an attempt of recovering the APL is clearly demonstrated from these results. The differences for VMF1GRT_OFF, OMFSHRT_OFF, and OMTS_OFF show degrees of correlation above 0.6 (0.65±0.059, 0.63±0.057 and 0.62±0.054 respectively). Following this, the differences for OMFSHRTGRD_OFF were 0.56±0.085, for OMFAHRT_OFF were 0.48±0.076, for VMF1G_OFF were 0.42±0.027, and for OMFS_OFF were 0.40±0.025. Contrary to this, showing a constant but low correlation was the difference for GMF_OFF at 0.16±0.048.

The case of the GMF minus NMF difference is explained by the similitude of the two mapping functions. The main difference is the fit of the a coefficients.

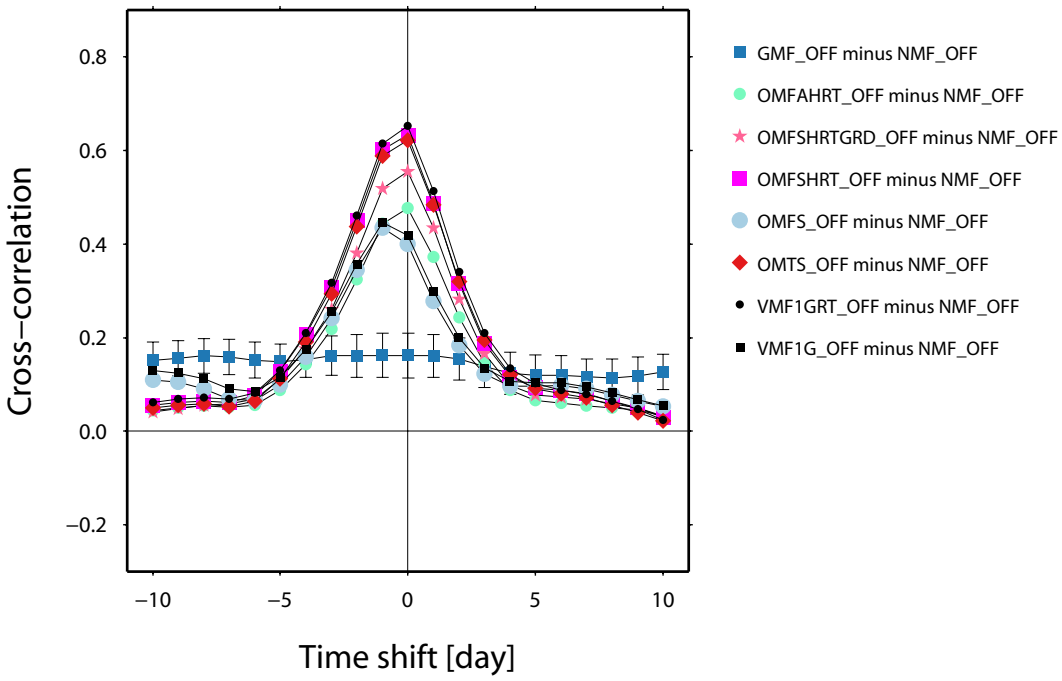

Figure 7.2: Average cross-correlations between the predicted atmospheric pressure loading induced displacements and differential height time series computed over a set of 27 CGPS stations in the UK. Error bars represent the standard deviation associated with the plotted value (only represented for the first solution plotted, for clarity, as rather constant over the different solutions).

It translates in this case into a large annual signal in the differential time series (partly illustrated on Figure 7.5). As the signal is smooth, it is no surprise that the value for the cross correlation is constant when shifting the two signals by minus to plus ten days. Both the NMF and the GMF, as empirical models, are not expected to handle short time scale variations of the atmosphere whereas all of the other mapping functions used here are based on NWM data and, especially when used in conjunction with ray traced a priori ZHD, the atmospheric modelling realism is expected to be much higher.

Two other figures are presented to complete the illustration of the impact of the mapping function itself. The first (Figure 7.3) has OMFS_OFF as a reference and only includes solutions based on a standard a priori ZHD, whereas the second

(Figure 7.4) is based on OMFSHRT_OFF as reference and only includes solutions with ray traced ZHD. In view of retrieving the APL signal, choosing between OMFS and VMF1 would not give different results overall; similar remark applies to all mapping functions when used together with ray traced a priori ZHD.

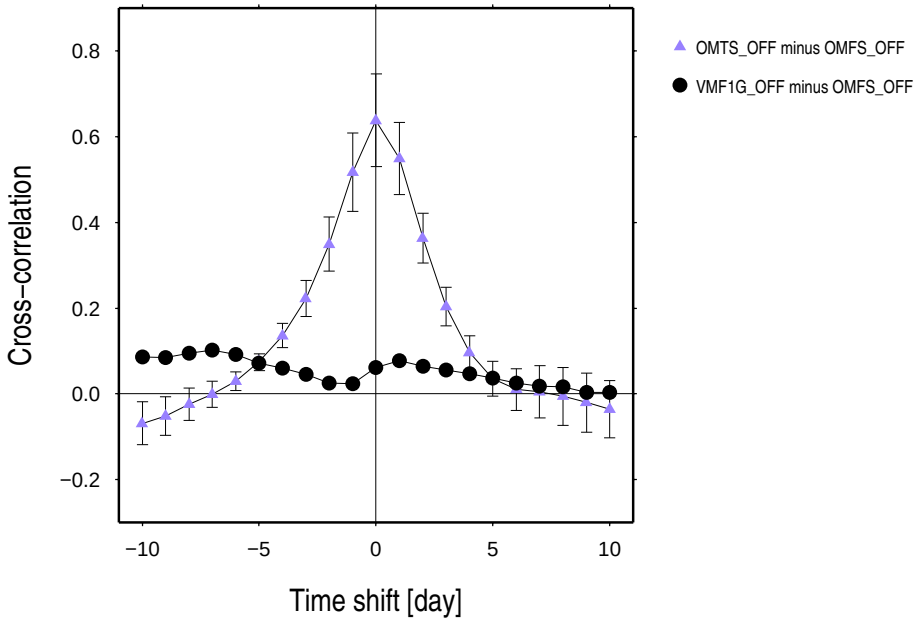

Figure 7.3: Average cross-correlations between the predicted atmospheric pressure loading induced displacements and differential height time series computed over a set of 27 CGPS stations in the UK with OMFS_OFF as the reference solution. Error bars represent the standard deviation associated with the plotted value (only represented for the first solution plotted, for clarity, as rather constant over the different solutions). Only solutions with standard a priori ZHD considered.

Six month coordinate and ZTD time series are presented for selected differences for CGPS station HERS in Figures 7.5 and 7.6 respectively. Further plots can be found in Appendices 11 and 12. Both figures clearly illustrate the fact that the choice of the mapping function can influence the inferred coordinate by an amount that can correlate almost perfectly with the predicted APL. This is most striking for the difference OMTS minus OMFS and, but not as much pronounced, for the difference OMTS minus NMF whereas, the difference between the GMF and NMF time series is characterized by a large annual signal which does not

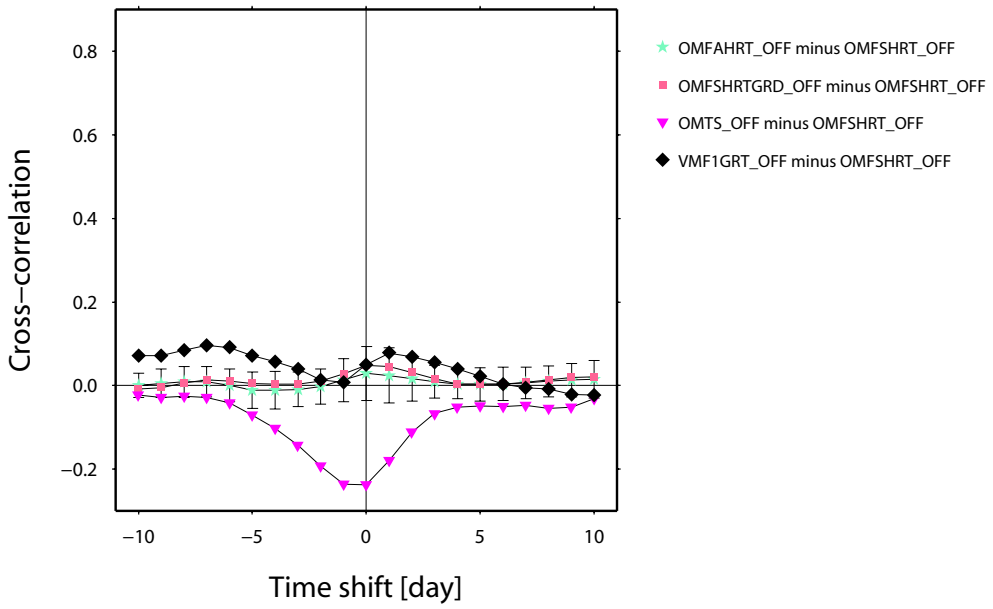

Figure 7.4: Average cross-correlations between the predicted atmospheric pressure loading induced displacements and differential height time series computed over a set of 27 CGPS stations in the UK with OMFSHRT_OFF as the reference solution. Error bars represent the standard deviation associated with the plotted value (only represented for the first solution plotted, for clarity, as rather constant over the different solutions). Only solutions with ray traced a priori ZHD considered.

correlate at all with the APL signal.

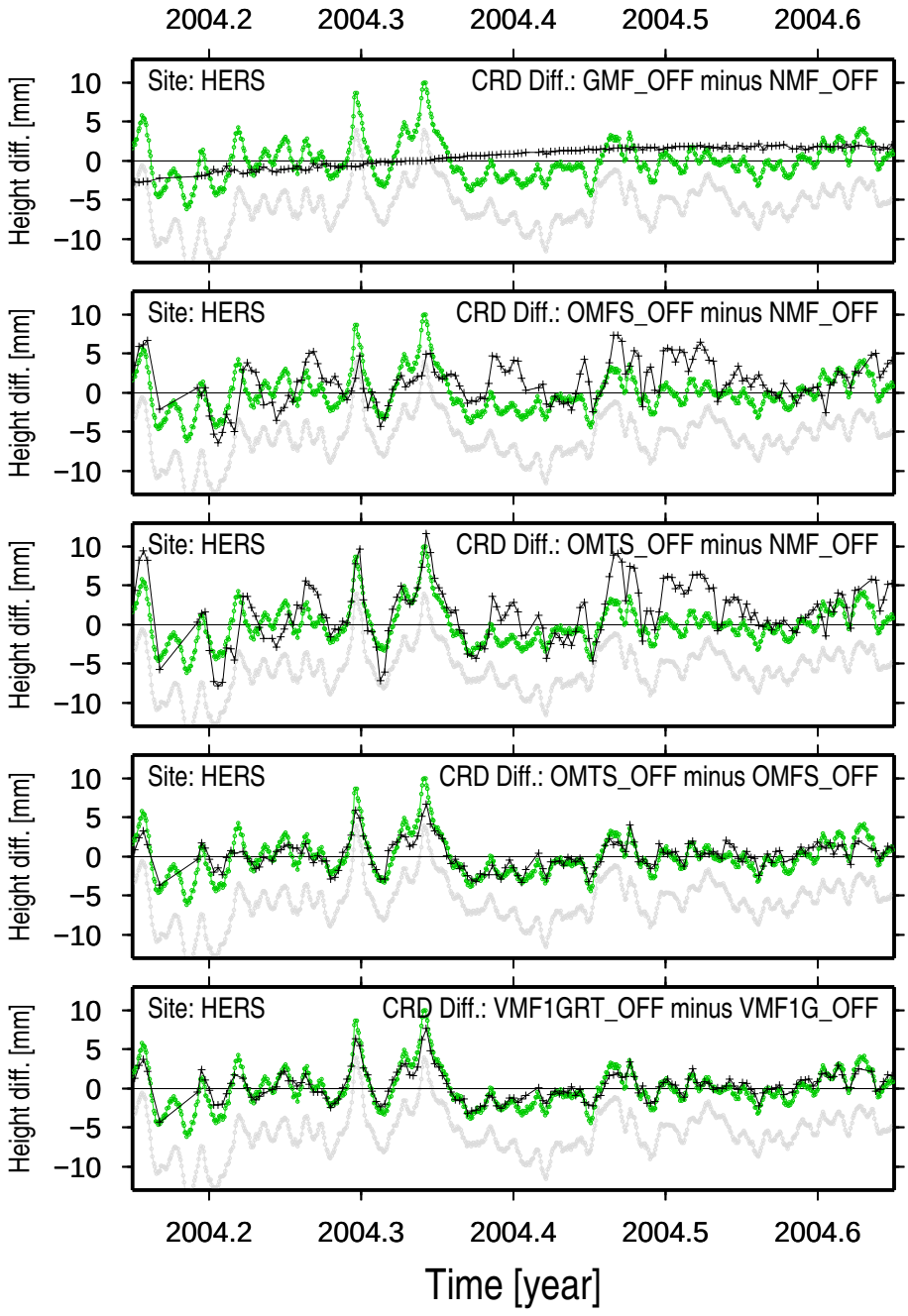

Figure 7.5: Differential height time series for CGPS station HERS. From top to bottom: GMF minus NMF, OMFS minus NMF, OMTS minus NMF, OMTS minus OMFS, and VMF1GRT minus VMF1G. Plotted on the same scale are the vertical displacement induced by atmospheric pressure loading as predicted by two models: in green a model run by T. van Dam (pers. comm.) and in light gray by aplo [Petrov, 2008]. No artificial offset was introduced.

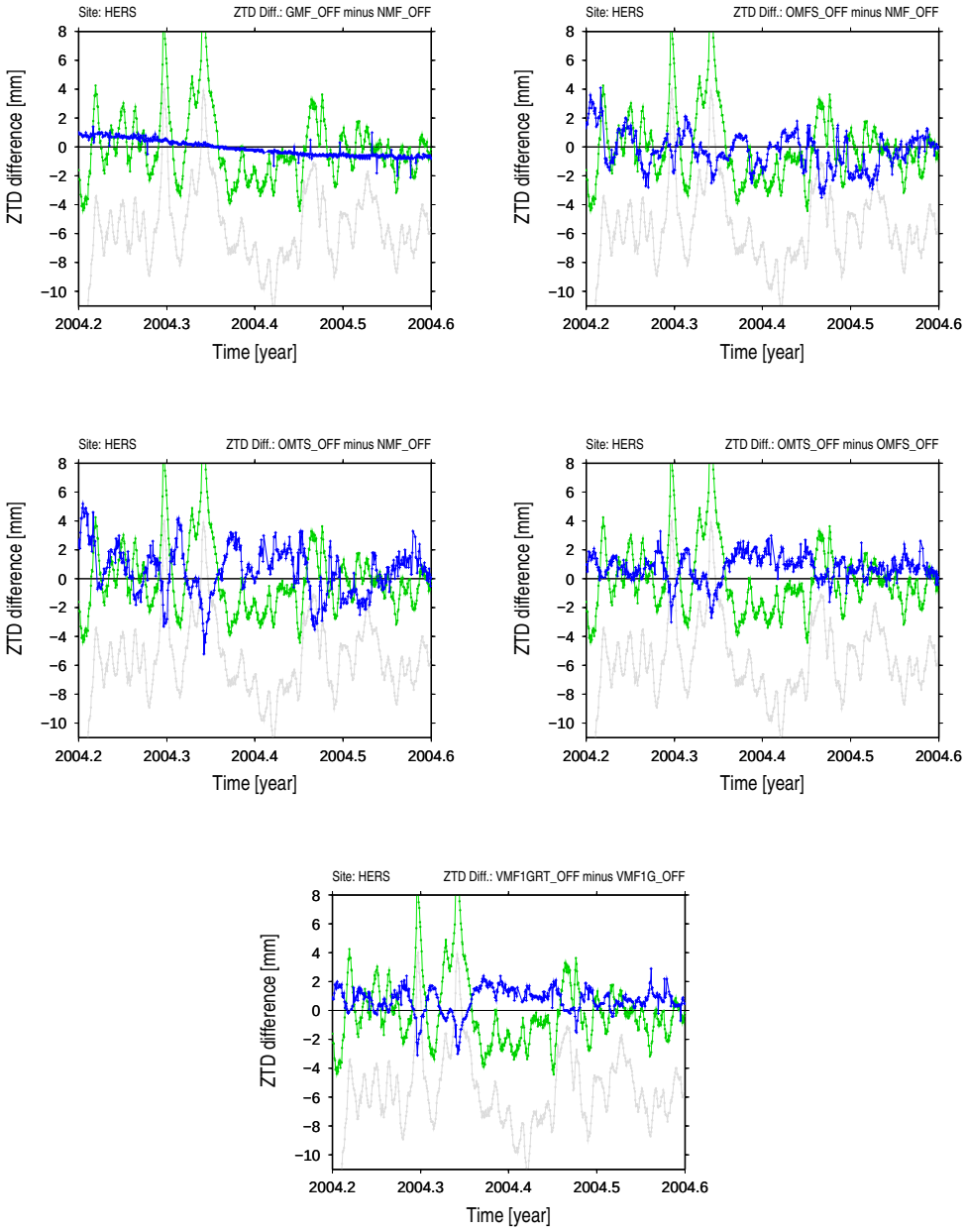

Figure 7.6: Differential ZTD time series for CGPS station HERS. Top left: GMF minus NMF; Top right: OMFS minus NMF; Middle left: OMTS minus NMF; Middle right: OMTS minus OMFS; Bottom: VMF1GRT minus VMF1G. Plotted on the same scale are the vertical displacement induced by atmospheric pressure loading as predicted by two models: in green a model run by T. van Dam (pers. comm.) and in light gray by aplo [Petrov, 2008]. No artificial offset was introduced.

7.3.2 A Priori Zenith Delay Impact

The effect of the a priori ZHD information on the retrieval of the APL can also be examined. Not all possible variants were produced for this thesis, given the significant amount of data processed, however, three differences can be formed to investigate the impact of using a ray traced a priori ZHD instead of a standard one: VMF1GRT_OFF minus VMF1G_OFF, OMFSHRT_OFF minus OMFS_OFF, and the OMTS_OFF minus OMFS_OFF. The consideration of the third one is not as trivial as the first two, but as the total mapping function renders the solution independent of any a priori information, it can be considered as perfect.

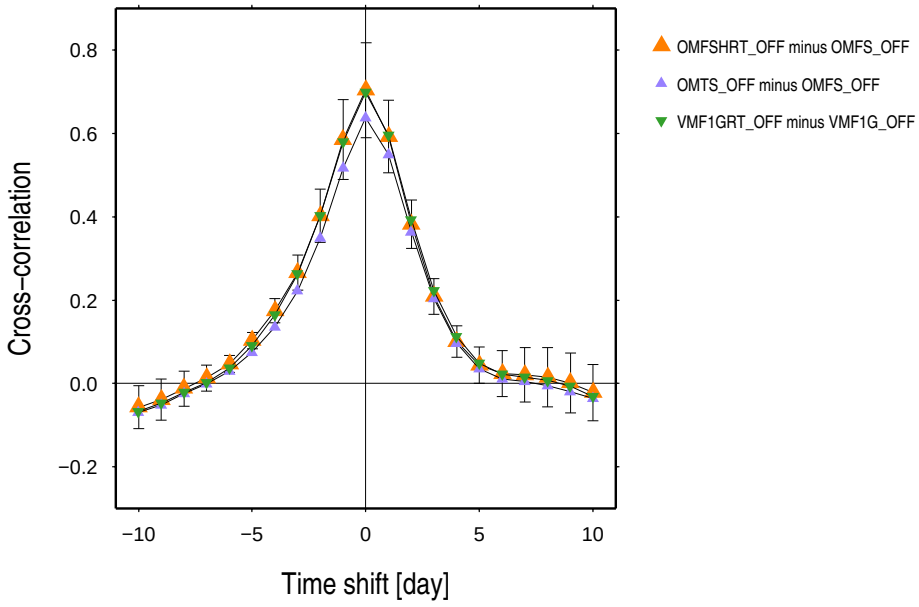

Figure 7.7: Average cross-correlations between the predicted atmospheric pressure loading induced displacements and differential height time series computed over a set of 27 CGPS stations in the UK with OMFSHRT_OFF as the reference solution. Error bars represent the standard deviation associated with the plotted value (only represented for the first solution plotted, for clarity, as rather constant over the different solutions). Only solutions with ray traced a priori ZHD considered.

The impact is clear and very similar for the three differences, especially for the VMF1GRT_OFF minus VMF1GRT_OFF and OMFSHRT_OFF minus OMFS_OFF ones. This emphasizes furthermore the need for realistic tropospheric

modelling if APL is to be corrected for. If not, as proven by the figures in Table 5.5, applying corrections for something not observed, basically makes things worse.

7.4 Summary

Evidence was presented that the troposphere modelling strategy, as a combination of an a priori delay and mapping function(s), can affect coordinates and zenith total delays (ZTD) time series, by an amount that highly correlates in time with the predicted atmospheric pressure loading (APL) induced displacement - up to a level of 0.7. The evidence is based on differential time series of height and ZTD obtained from comparing two different tropospheric modelling strategies.

Those results clearly show that the troposphere modelling can influence the time series by a signal that correlates very well with the APL. In other words, the APL can almost be accounted for depending on the troposphere modelling chosen and care should be taken not to correct for it if already handled by the troposphere modelling itself, that is the choice of the mapping functions themselves, e.g. the difference between VMF1G and the NMF or GMF, or the type of a priori ZHD, e.g. the difference between VMF1GRT and VMF1.

Chapter 8

Conclusions and Recommendations for Future Work

8.1 Conclusions

In this thesis, two new mapping functions were derived from a high resolution mesoscale numerical weather model (NWM) for the UK. One assuming azimuth symmetry (SMF), as in all mapping functions actually in use in geodetic data processing, and a second, which is azimuth dependent (AMF).

The development of an AMF required the implementation of a three dimensional ray tracing algorithm. For each site processed, to handle the troposphere's asymmetry, the NWM was ray traced on twelve different azimuths and 20 elevation angles. The selection of the elevation angles to be ray traced was treated with care. The Marini model, commonly used in the most accurate mapping functions, had to be left in favor of a cubic spline interpolation (CSI). It was also found

in this research that, when using CSI for interpolating on the elevation angle, it was by far more efficient to interpolate mapping function corrections to a 'base' mapping function, as opposed to mapping function ray traced values themselves.

A significant amount of work was put into trying to develop a procedure to assess the quality of the models used to vertically interpolate the pressure (P), the temperature (T) and the humidity (U) between two successive pressure levels of the NWM. To do so, several years of high resolution (hiRes) radiosonde (RS) data, available at five hiRes RS sites in the UK were used. These profiles, with data recorded every 2 s ascent (roughly 10 metres), allowed a comparison of interpolated values to measured values, therefore enabling realistic estimates of the uncertainties to be derived for the input to the refractivity model. Such values were derived on a pressure layer basis. Regarding the total refractivity for example, it was found that the model used for interpolating the total pressure induces a small negative bias of -0.075± 0.0093 %; that the model used for interpolating the temperature induces a positive bias of 0.02± 0.106 %; whereas the model used for interpolating the humidity (water vapour pressure in this thesis) induced a negative bias of -3.42± 9.42%.

Seven different ways of interpolating humidity with respect to height were tested and it was found that linearly interpolating the relative humidity on height was the best. Also, two approaches for integrating the delays were compared and differences identified. The best method for the ray tracing of the ZTD lead to agreement between hiRes RS data and NWM ray tracings of -0.6 ± 9.9 mm to 2.5 ± 12.8 mm (statistic computed on average over 2235 profiles per station).

A positioning performance analysis was first conducted using the azimuthally

symmetric OMF (OMFS) in order to compare it, above all, to what is considered the best mapping function currently available, the VMF1. The comparison was carried out on a set of 30 CGPS stations in the UK using a period of 3.8 years of data. The OMFS was found to perform the same as the VMF1 when comparing weighted RMS, with a value in the vertical component of 5.41 mm for both (when using ray-traced a priori ZHD). An average vertical offset of 0.7 mm was, however, found between the two. In view of those results, the azimuthally symmetric OMF were considered validated, and therefore the design of the azimuth dependent OMF, was considered valid as well. To the best knowledge of the author, the comparison of the OMF is the first independent test on the VMF1.

The azimuth dependent OMF (OMFA) was then tested against the azimuthally symmetric one, with and without estimating horizontal tropospheric gradients. It was found that using the OMFA slightly degraded the WRMS in the vertical component (5.69$\pm$0.33 mm against 5.35 $\pm$ 0.45mm) but made the results more consistent over the stations. Estimating gradients lead to the best overall results, in both the horizontal and vertical components; however, estimating gradients clearly failed for some stations, where using an azimuth dependent mapping function such as OMFA did not, as it is a priori information and not estimated from GPS data. Overall the consistency between the two approaches appeared satisfactory, emphasizing the realistic and physical aspects of the estimated gradients. The OMFA therefore offers an assessment of the validity of using horizontal tropospheric gradients for modelling the troposphere azimuthal variability.

This work also permitted the demonstration that the combination of mapping function plus a priori zenith hydrostatic delay in the processing of GPS data

can impact the inferred coordinate by an amount that matches the predicted atmospheric pressure loading (APL) induced displacement. Evidence was presented in the form of various differential coordinate (and ZTD) time series. A correlation of 0.7 was found between APL and the difference between the azimuthally symmetric OMF using either consistent ray-traced ZHD or standard a priori ZHD. This is an important consideration as modern mapping functions based on a NWM are used more in GNSS data processing as suggested in the IGS recommendations. The results presented in Chapter 7 suggest that when using the VMF1 (at least for the UK) one does not need to correct for APL.

Overall, this work has shown that a NWM can be used to derive azimuth dependent mapping functions which avoid to include the estimation of gradients which physical validity is still discussed, although positioning performances are improved. The work on the correlation between mapping functions and APL has a direct impact on all processing of GNSS (ground) data in geodetic applications.

8.2 Recommendations for future work

Several aspects of the work carried out for this thesis could be further developed and improved but there are four clear recommendations for future work:

- The development of more appropriate, better models for the meteorological data interpolation. It was shown in this work for example that the model used for interpolating the total pressure lead to a general underestimation of the quantity. However, the impact could be limited if the pressure layers' thickness is generally smaller than the ones offered by the MESO which contains only 13 pressure levels.

- The datasets used throughout this thesis were limited to the UK, limita-

tion imposed by the geographical coverage of the high resolution numerical weather model employed. The use of a global dataset could be considered. This would, for the wet specially, depend on the spatial and temporal resolution of the NWM available.

- Regarding the mapping functions developed here, some more understanding of the NWM may help to identify the reason for the slightly noisier results obtained when using an azimuth dependent mapping function rather than estimating gradients.

- In depth time series analysis over the 3.8 years of data could be carried out in order to study the impact of the various troposphere modelling approaches on velocities for example, or to study the nature of the noise contained in the time series.

References

Agnew, D. C. and Larson, K. M. [2007]. Finding the repeat times of the GPS constellation, *GPS Solutions* **11**: 71–76.

Baker, T. F., Curtis, D. J. and Dodson, A. H. [1995]. Ocean tide loading and GPS, *GPS World* pp. 54–59.

Bar-Sever, Y. E., Kroger, P. M. and Borjesson, J. A. [1998]. Estimating horizontal gradients of tropospheric path delay with a single GPS receiver, *Journal of Geophysical Research* **B3**: 5019–5035.

Bassiri, S. and Hajj, G. A. [1993]. Higher-order ionospheric effect on the global positioning system observables and means of modeling them, *Manuscripta Geodetica* **18**: 280–289.

Battaglia, A., Boudouris, G. and Gozzini, A. [1957]. Sur l'indice de refraction de l'air humide en microondes, *Ann. Telec* **12**: 47–50.

Bean, B. and Dutton, E. [1966]. *Radio Meteorology*, number 6021.2, National Bureau of Standards Monograph 92, Boulder, Colorado.

Berg, H. [1948]. *Allgemeine meteorologie*, Duemmler, Bonn.

Birnbaum, G. and Chatterjee, S. K. [1952]. The dielectric constant of water vapor in the microwave region, *J. Applied Phys.* **23**(220-223).

Birnbaum, G., Kryder, S. J. and Lyons, H. [1951]. Microwave measurements of the dielectric properties of gases, *J. Applied Phys.* **22**: 95–102.

Black, H. D. and Eiser, A. [1989]. Correcting satelling Doppler data for tropospheric effects, *Journal of Geophysical Research* **89**(D2): 2616–2626.

Blewitt, G. [1989]. Carrier phase ambiguity resolution for the global positioning system applied to geodetic baselines up to 2000 km, *Journal of Geophysical Research* **94**(B8): 1018710203.

Blewitt, G. and Lavallee, D. [2002]. Effect of annual signals on geodetic velocity, *Journal of Geophysical Research* **107**(B7).

Boehm, J. [2008 (last accessed July 5, 2009)]. Vienna Mapping Functions 1 VMF1, TU Wien, `http://www.hg.tuwien.ac.at/~ecmwf1/`.

Boehm, J., Heinkelmann, R. and Schuh, H. [2007]. Short note: A global model of pressure and temperature for geodetic applications, *Journal of Geodesy* **81**(10): 679–783.

Boehm, J., Niell, A. E., Tregoning, P. and Schuh, H. [2006b]. Global Mapping Function (GMF): A new empirical mapping function based on numerical weather model data, *Geophysical Research Letters* **33**: L07304, doi:10.1029/2005GL025546.

Boehm, J. and Schuh, H. [2003]. Vienna mapping functions, *Proceedings of the 16th Working Meeting on European VLBI for Geodesy and Astrometry*, Verlag des Bundesamtes fur Kartographie und Geodaesie, pp. 131–143.

Boehm, J. and Schuh, H. [2004]. Vienna mapping functions in VLBI analyses, *Geophysical Research Letters* **31**: L01603, doi:10.1029/2003GL018984.

Boehm, J., Werl, B. and Schuh, H. [2006a]. Troposphere mapping functions for GPS and Very Long Baseline Interferometry from European Centre for Medium-Range Weather Forecasts operational analysis data, *Journal of Geophysical Research* **111**: B02406, doi:10.1029/2005JB003629.

Born, M. and Wolf, E. [1999]. *Electromagnetic theory of propagation, interference and diffraction of light*, Seventh (expanded) edn, Cambridge University Press.

Boudouris, G. [1963]. On the index of refraction of air, the absorption and dispersion of centimeter waves by gases, *Journal of Research of the National Bureau of Standards-D. Radio Propagation* **67**(D): 631–684.

Bueche, F. [1986]. *Introduction to physics for scientists and engineers*, fourth edition edn, McGraw-Hill Book Company.

Byers, H. R. [1959]. *General Meteorology*, fourth edition edn, McGraw-Hill Publishing Company.

Chao, C. [1972]. A model for tropospheric calibration from daily surface and radiosonde balloon measurement, *Technical Memorandum 391-350*, Jet Propulsion Laboratory, Pasadena, California.

Chao, C. [1974]. The tropospheric calibration model for Mariner Mars 1971, *Technical Report 32-1587*, Jet Propulsion Laboratory, California Institute of Technology, Pasadena, California, pp. 61–76.

Chen, G. and Herring, T. A. [1997]. Effects of atmospheric azimuthal asymmetry on the analysis of space geodetic data, *Journal of Geophysical Research* **B9**: 20,489–20,502.

Dach, R., Hugentobler, U., Fridez, P. and Meindl, M. [2007]. *Bernese GPS Software*, Astronomical Institute University of Bern, Bern, Switzerland.

Darwin, G. [1882]. On variations in the vertical due to elasticity of the Earth's surface, *Philos. Mag.* **Ser. 5, 14**(90): 409–427.

Davis, J. L., Elgered, G., Niell, A. E. and Kuehn, C. E. [1993]. Ground-based measurement of gradients in the "wet" radio refractivity of air, *Radio science* **28**(6): 1003–1018.

Davis, J. L., Herring, T. A., Shapiro, I. I., Rogers, A. E. E. and Elgered, G. [1985]. Geodesy by radio interferometry: Effects of atmospheric modeling errors on estimates of baseline length, *Radio Science* **20**(6): 1593–1607.

Debye [1929]. *Polar Molecules*, Dover Publ. Co., New York, N.Y.

Essen, L. [1953]. The refractive indices of water vapour, air, oxygen, nitrogen, hydrogen, deuterium, and helium, *Proc. Phys. Soc (London)* **B66**: 189–193.

Essen, L. and Froome, K. D. [1951]. The refractive indices and dielectric constants of air and its principal constituents at 24,000 mc/s., *Communication from the National Physical Laboratory* .

Farrell, W. E. [1972]. Deformation of the earth by surface loads, *Rev. Geophys.* **10**: 751–797.

Gabriel, W. [1952]. *Proc. Inst. Radio Engrs* **40**: 940.

Gardner, C. S. [1976]. Effects of horizontal refractivity gradients on the accuracy of laser ranging to satellites, *Radio Science* **11**(12): 1037–1044.

Gardner, C. S. [1977]. Correction of laser tracking data for the effects of horizontal refractivity gradients, *Applied Optics* **16**(9): 2427–2432.

Ge, M., Gendt, G., Rothacher, M., Shi, C. and Liu, J. [2008]. Resolution of GPS carrier-phase ambiguities in Precise Point Positioning (PPP) with daily observations, *Journal of Geodesy* **82**: 82:389399, DOI 10.1007/s00190–007–0187–4.

Gleuckauf, E. [1951]. The composition of the atmosphere, *in* T. F. Malone (ed.), *Compendium of Meteorology*, American Meteorological Society, Boston, Mass., pp. 3–10.

Goff, J. A. [1957]. Saturation pressure of water on the new Kelvin temperature scale, *Transactions of the American Society of Heating and Ventilating Engineers*, pp. 347–354. presented at the semi-annual meeting of the American Society of Heating and Ventilating Engineers, Murray Bay, Que. Canada.

Goff, J. A. and Gratch, S. [1946]. Low-pressure properties of water from -160 to 212 °F, *in Transactions of the American Society of Heating and Ventilating Engineers*, pp. 95–122. Presented at the 52nd annual meeting of the American Society of Heating and Ventilating Engineers, New York, 1946.

Groves, I. and Sugden, S. [1935]. Dipole moments of vapors, part 2, *J. Chem. Soc (London)* pp. 971–974.

Haase, J., Ge, M., Vedel, H. and Calais, E. [2003]. Accuracy and variability of GPS tropospheric delay measurements of water vapor in the western mediterranean, *Journal of Applied Meteorology* **42**: 1547–1568.

Haltiner, G. J. and Martin, F. L. [1957]. *Dynamical and Physical Meteorology*, McGRAW-HILL BOOK COMPANY, INC.

Heineken, F. and Bruin, F. [1954]. -, *Physica* **20**: 350–360.

Herring, T. A. [1992]. Modeling atmospheric delays in the analysis of space geodetic data, *in* J. C. DeMunk and T. A. Spoelstra (eds), *Symposium on Refraction of Transatmospheric Signals in Geodesy*, Netherlands Geod. Commis. Ser. *36*, Ned. Comm. voor Geod, pp. 157–164.

Hill, R., Lawrence, R. and Priestley, J. [1982]. Theoretical and calculational aspects of the radio refractive index of water vapour, *Radio Science* **17**(5): 1251–1257.

Hopfield, H. S. [1969]. Two-quadratic tropospheric refractivity profile for correcting satelling data, *Journal Geophysical Research* **74**: 4487–4499.

Hugentobler, U., Meindl, M., Beutler, G., Dach, R., Jaggi, A., Urschl, C., Mervart, L., Rotacher, M., Schaer, S., Brockmann, E., Ineichen, D., Wiget, A., Wild, U., Weber, G., Habrich, H. and Boucher, C. [2005]. CODE IGS analysis center technical report 2003/2004, *Technical report*, CODE.

Hurdis, E. and Smyth, C. [1942]. Dipole moment induction and resonance in nitroethane and some chloronitroparaffins, *J. Am. Chem. Soc.* **64**: 2829–2834.

Ifadis, I. [1986]. *The atmospheric delay of radio waves: Modeling the elevation dependence on a global scale*, Tech. Rep. 38L, School of Electrical and Comput. Eng., Chalmers Univ. of Technol., Gothenburg, Sweden.

IGS Mail 2320 [1999]. J. Ray and H. Dragert and and J. Kouba, Handling mixed receiver types, IGS Mail 2320.

IGS Mail 4913 [2004]. CODE AC Team, CODE high rate clocks, IGS Mail 4913.

IGS Mail 5438 [2006]. G. Gendt, IGS switch to absolute antenna model and ITRF 2005, IGS Mail 5438.

Iribarne, J. and Godson, W. [1973]. *Atmospheric Physics*, D. Reidel Publishing Company, Dordrecht, Holland.

Kalnay, E., Kanamitsu, M., Kistler, R., Collins, W., Deaven, D., Gandin, L., Iredell, M., Saha, S., White, G., Woollen, J., Zhu, Y., Leetmaa, A., Reynolds, B., Chelliah, M., Ebisuzaki, W., Higgins, W., Janowiak, J., Mo, K., Ropelewski, C., Wang, J., Jennea, R. and Joseph, D. [1996]. The NCEP/NCAR 40-year reanalysis project, *Bull. Amer. Meteor. Soc* **77**: 437–471.

Kedar, S., Hajj, G. A., Wilson, B. D., and Heflin, M. B. [2003]. The effect of the second order GPS ionospheric correction on receiver positions, *Geophys. Res. Lett.* **30**(16): 1829, doi:10.1029/2003GL017639.

Kouba, J. [2008]. Implementation and testing of the gridded Vienna Mapping Function 1 (VMF1), *Journal of Geodesy* **82**(4-5). 10.1007/s00190-007-0170-0.

Kouba, J. and Heroux, P. [2001]. Precise point positioning using IGS orbit and clock products, *GPS Solutions* **5**(2): 12–28.

Lanyi, G. [1984]. Tropospheric delay effects in radio interferometry, *TDA Prog. Rep. 42-78* pp. 152–159. Jet Propul. Lab., Pasadena, Calif., Aug. 15.

Larson, K. M. and Levine, J. [1999]. Carrier phase time transfer, *IEEE transactions on ultrasonics, ferroelectrics, and frequency control* **46**(4).

Liebe, H., Gimmestad, G. and J.D.Hopponen [1977]. Atmospheric oxygen microwave spectrum - experiment versus theory, *IEEE Trans. on Antenna and Propagation* **AP-26**(3): 327–335.

List, R. J. [1966]. Smithsonian meteorological tables, *Smithsonian Miscellaneous Collections* **114**. 6th rev. ed., Smithsonian Institution Press, Washington, D.C.

Lyard, F., Lefvre, F., Letellier, T. and Francis, O. [2006]. Modelling the global ocean tides: a modern insight from FES2004, *Ocean Dynamics* **56**: 394–415.

MacMillan, D. S. [1995]. Atmospheric gradients from Very Long Baseline Interferometry observations, *Geophysical Research Letters* **9**: 1041–1044.

Mader, G. L. [1999]. GPS antenna calibration at the National Geodetic Survey, *GPS Solutions* **3**(1): 50–58.

Marini, J. W. [1971]. Closed form satellite tracking data corrections for an arbitrary tropospheric profile, *Goddard Space Flight Center Rep.* **X-551-71-122**.

Marini, J. W. [1972]. Correction of satellite tracking data for an arbitrary tropospheric profile, *Radio Science* **7**(2): 223–231.

Marini, J. W. and Murray, C. [1973]. Correction of laser tracking data for atmospheric refraction at elevations above 10 degrees, *Technical Report X-591-73-351*, NASA.

McCarthy, D. D. and Petit, G. [2003]. IERS CONVENTIONS (2003), IERS Technical Note No.32, *Technical report*, International Earth Rotation and Reference Systems Service (IERS).

Meindl, M., Schaer, S., Hugentobler, U. and Beutler, G. [2004]. Tropospheric gradient estimation at CODE: Results from global solutions, *in* R. A. Anthes et al. (ed.), *Applications of GPS Remote Sensing to Meteorology and Related Fields*, Vol. 82 of *Journal of the Meteorological Society of Japan*, pp. 331–338.

Mendes, V. B. [1999]. *Modeling the neutral-atmosphere propagation delay in radiometric space techniques*, Technical report no. 199, Department of Geodesy and Geomatics Engineering, University of New Brunswick, Fredericton, New Brunswick, Canada, 353 pp.

Mendes, V. B., Prates, G., Pavlis, E. C., Pavlis, D. E. and Langley, R. B. [2002]. Improved mapping functions for atmospheric refraction correction in SLR, *Geophysical Research Letters* **29**(10). doi 10.1029/2001GL014394.

Misra, P. and Enge, P. [2001]. *Global Positioning System. Signals, Measurements, and Performance*, Ganga-Jamuna Press.

Moffett, J. [1973]. Program requirements for two-minute integrated Doppler satellite navigation solution, *Technical memorandum tg 819-1 (rev. 2)*, The Johns Hopkins University, Applied Physics Laboratory, Silver Spring, Md.

Newell, A. and Baird, R. [1965]. Absolute determination of refractive indices of gases at 47.7 GHz, *Journal of Applied Physics* **36**(12): 3751–3759.

Niell, A. E. [1996]. Global mapping functions for the atmosphere delay at radio wavelengths, *Journal of Geophysical Research* **101**(B2): 3227–3246. Equations 4 and 5 corrected.

Niell, A. E. [2000]. Improved atmospheric mapping functions for VLBI and GPS, *Earth Planets Space* **52**: 699–702.

Niell, A. E. [2001]. Preliminary evaluation of atmospheric mapping functions based on numerical weather models, *Phys. Chem. Earth* **26**(6-8): 476–480.

Niell, A. E., Coster, A. J., Solheim, F. S., Mendes, V. B., Toor, P. C., Langley, R. B. and Upham, C. A. [2001]. Comparison of measurements of atmospheric wet delay by radiosonde, water vapor radiometer, GPS, and VLBI, *Journal of Atmospheric and Oceanic Technology* **18**: 830–850.

Niell, A. E. and Petrov, L. [2003]. Using a numerical weather model to improve geodesy, *in* T. van Dam and O. Francis (eds), *The State of GPS Vertical Positioning Precision: Separation of Earth Processes by Space Geodesy*, European Center for Geophysics and Seismology, Luxembourg, Belgium.

Orliac, E. J., Dodson, A. H., Bingley, R. M. and Teferle, F. N. [2007a]. Total mapping function, *Twenty fourth assembly of IUGG* .

Orliac, E. J., Dodson, A. H., Bingley, R. M. and Teferle, F. N. [2007b]. Correlation between mapping functions and atmospheric pressure loading in the processing of GNSS data, *Eos Transactions* **88**(52).

Owens, J. [1967]. Optical refractive index of air: dependence on pressure, temperature and composition, *Applied Optics* **6**(1): 51–59.

Penna, N. and Baker, T. [2002]. Ocean tide loading considerations for GPS processing around Australia, *Geomatics Research Australasia* **77**: 1–26.

Petrov, L. [2008]. Atmospheric pressure loading service, available online at http://gemini.gsfc.nasa.gov/results/aplo/ (last accessed July 2009).

Petrov, L. and Boy, J.-P. [2004]. Study of the atmospheric pressure loading signal in Very Long Baseline Interferometry observations, *Journal of Geophysical Research* **109**(B03405).

Ponte, R. M. and Ray, R. D. [2002]. Atmospheric pressure corrections in geodesy and oceanography: A strategy for handling air tides, *Geophysical Research Letters* **29**(24).

Ray, J., Altamimi, Z., Collilieux, X. and van Dam, T. [2008]. Anomalous harmonics in the spectra of GPS position estimates, *GPS Solutions* **12**(1). doi:10.1007/s10291-007-0067-7.

Remondi, B. W. [1985]. Global Positioning System carrier phase, description and use, *Bulletin Geodesique* **59**: 361–377.

Rocken, C., Sokolovskiy, S., , Johnson, J. M. and Hunt, D. [2001]. Improved mapping of tropospheric delay, *J. Atmospheric and Oceanic Tech.* **18**: 1205–1213.

Rüeger, J. M. [2002]. Refractive indices of light, infrared and radio waves in the atmosphere, *Unisurv S-68*, University of New South Wales.

Saastamoinen, J. [1972]. Atmospheric correction for the troposphere and stratosphere in radio ranging of satellites, *in* S. W. Henriksen, A. Mancini and B. H. Chovitz (eds), *The Use of Artificial Satellites for Geodesy*, Vol. 15 of *Geophys. Monogr. Ser*, AGU, Washington, D. C.

Saastamoinen, J. [1973]. Contributions to the theory of atmospheric refraction, *Bulletin Géodesique* (105-107): 279–298; 383–397; 13–34. In three parts.

Salby, M. L. [1995]. *Fundamentals of atmospheric physics*, Academic Press Limited.

Sass, B. H., Nielsen, N. W., Jorgensen, J. U., and Ammstrup, B. [1999]. The operational HIRLAM system at DMI, *DMI Tech. Rep.* (99-21): 43.

Schaer, S. and Steigenberger, P. [2006]. Determination and use of GPS differential code bias values. Paper presented at IGS Workshop, Darmstadt 8−11 May 2006.

Scherneck, H.-G. [1991]. A parameterized solid earth tide model and ocean tide loading effects for global geodetic baseline measurements, *Geophys. J. Int.* **106**: 677–694.

Schmid, R. and Rothacher, M. [2003]. Estimation of elevation-dependent satellite antenna phase center variations of GPS satellites, *Journal of Geodesy* **77**: 440–446,DOI:10.1007/s00190–003–0339–0.

Schmid, R., Steigenberger, P., Gendt, G., Ge, M. and Rothacher, M. [2007]. Generation of a consistent absolute phase center correction model for GPS receiver and satellite antennas, *Journal of Geodesy* **81**: 781–798, DOI 10.1007/s00190–007–0148–y.

Schupler, B., Allshouse, R. and Clark, T. [1994]. Signal characteristics of GPS user antennas, *J Inst Navigation* **41**: 277–295.

Staniforth, A., White, A., Wood, N., Thuburn, J., Zerroukat, M., Cordero, E. and Davies, T. [2006]. The joy of u.m. 6.3 - model formulation, unified model documentation paper no. 15, available online at http://www.metoffice.com/research/nwp/publications/papers/unified_model/index.html (last accessed July 2009).

Stranathan, J. D. [1935]. Dielectric constant of water vapor, *Phys. Rev.* **48**: 538–544.

Tans, P. [2009]. Noaa/esrl, trends in atmospheric carbon dioxide, www.esrl.noaa.gov/gmd/ccgg/trends (last accessed July 2009).

Teferle, F., Orliac, E. J. and Bingley, R. M. [2007]. An assessment of Bernese GPS software Precise Point Positioning using IGS final products for global site velocities, *GPS Solutions* **11**: 205–213,DOI 10.1007/s10291–006–0051–7.

Thayer, G. D. [1974]. An improved equation for the radio refractive index of air, *Radio Science* **9**(10): 803–807.

Tregoning, P. and Herring, T. A. [2006]. Impact of a priori zenith hydrostatic delay errors on GPS estimates of station heights and zenith total dealys, *Geophysical Research Letters* **33**(L23303).

Tregoning, P. and van Dam, T. [2005]. Atmospheric pressure loading corrections applied to GPS data at the observation level, *Geophysical Research Letters* **32**(L22310).

USSA [1976]. *U.S. Standard Atmosphere, 1976*, National Oceanic and Atmospheric Administration, National Aeronautics and Space Administration, United States Air Force.

Vaisala [1998]. *Sounding Data File Formats for PC-based Systems*.

van den Dool, H. M., Saha, S., Schemm, J. and Huang, J. [1997]. A temporal interpolation method to obtain hourly atmospheric surface pressure tides in Reanalysis 1979-1995, *Journal of Geophyiscal Research* **102**(D18): 22013–22024.

Vanicek, P. and Krakiwsky, E. J. [1982]. Geodesy: The concepts, North-Holland, Amsterdam.

Vedel, H., Mogensend, K. S. and Huang, X.-Y. [2001]. Calculation of zenith delays from meteorological data comparison of NWP model, radiosonde and GPS delays, *Physics and Chemistry of the Earth* **26**(6-8): 497–502.

Vey, S., Dietrich, R., Fritsche, M., Rlke, A., Rothacher, M. and Steigenberger, P. [2006]. Influence of mapping function parameters on global GPS network analyses: Comparisons between NMF and IMF, *Geophys. Res. Lett.* **33**. L01814, doi:10.1029/2005GL024361.

Wallace, J. and Hobbs, P. V. [1977]. *Atmospheric Science: An Introduction Survey*, Academic Press.

Wexler, A. [1976]. Vapor pressure formulation for water in range 0° to 100°c – a revision, *J. Res. Natl. Bur. Stand.* **80**(A): 777 ff.

Wexler, A. [1977]. Vapor pressure formulation for ice, *J. Res. Natl. Bur. Stand.* **81**(A): 5–20.

Williams, S. D. P. [2008]. CATS : GPS coordinate time series analysis software, *GPS Solutions* **12**(2): 147–153.

Williams, S. D. P., Bock, Y., Fang, P., Jamason, P., Nikolaidis, R. M., Prawirodirjo, L., Miller, M. and Johnson, D. J. [2004]. Error analysis of continuous GPS position time series, *Journal of Geophysical Research* **109**(B03412). doi:10.1029/2003JB002741.

Wu, J., Wu, S., Hajj, G., Bertiger, W. and Lichten, S. [1993]. Effects of antenna orientation on GPS carrier phase, *Manuscripta Geodaetica* **18**(2): 91–98.

Zieman, C. [1952]. Dielectric constants of various gases at 9740 mc, *J. Appl. Phys.* **23**: 154.

Zumberge, J. F., Heflin, M. B., Jefferson, D. C., Watkins, M. M. and Webb, F. H. [1997]. Precise Point Positioning for the efficient and robust analysis of GPS data from large networks, *Journal of Geophysical Research* **102**(B3): 5005–5017.

Chapter 9

Coordinate Time Series

This appendix presents all time series obtained with the GMF mapping function to illustrate the offset selection for each CGPS station and the general aspect of the coordinate time series. The offset is site dependent and is the same for all solutions.

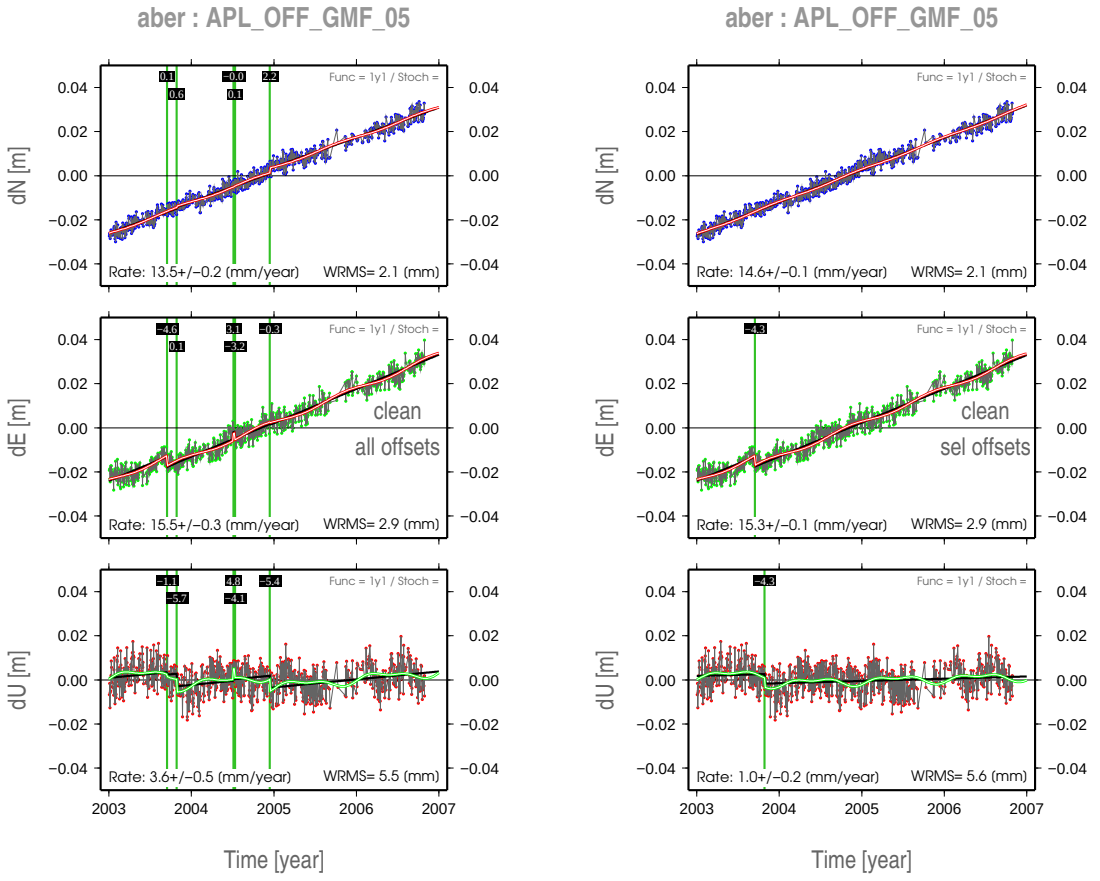

(a) All Offsets

(b) Selected Offsets

Figure 9.1: Example offset selection for CGPS station ABER. **Left plot**: all potential global offsets induced by changes in product generation, local offsets due to hardware changes (receiver/antenna) and visually identified offsets included. **Right plot**: only offsets identified as significant included. Green bars represent "global" offsets (from product generation). Light grey bars represent receiver changes. Pink bars represent antenna changes. Black bars are simultaneous receiver plus antenna changes. Orange bars indicate where an offset was not attributed to a hardware change nor a change in the processing strategy of the analysis center who generated the products but was manually added. Yellow areas are bad periods which were taken away from the analysis. Black lines represent (broken) linear variations whereas white on red lines (East and North) and white on green (Up) represent (broken) linear plus annual plus semi-annual signals as estimated using MLE using respectively all offsets (left) and selected only (right) offsets.

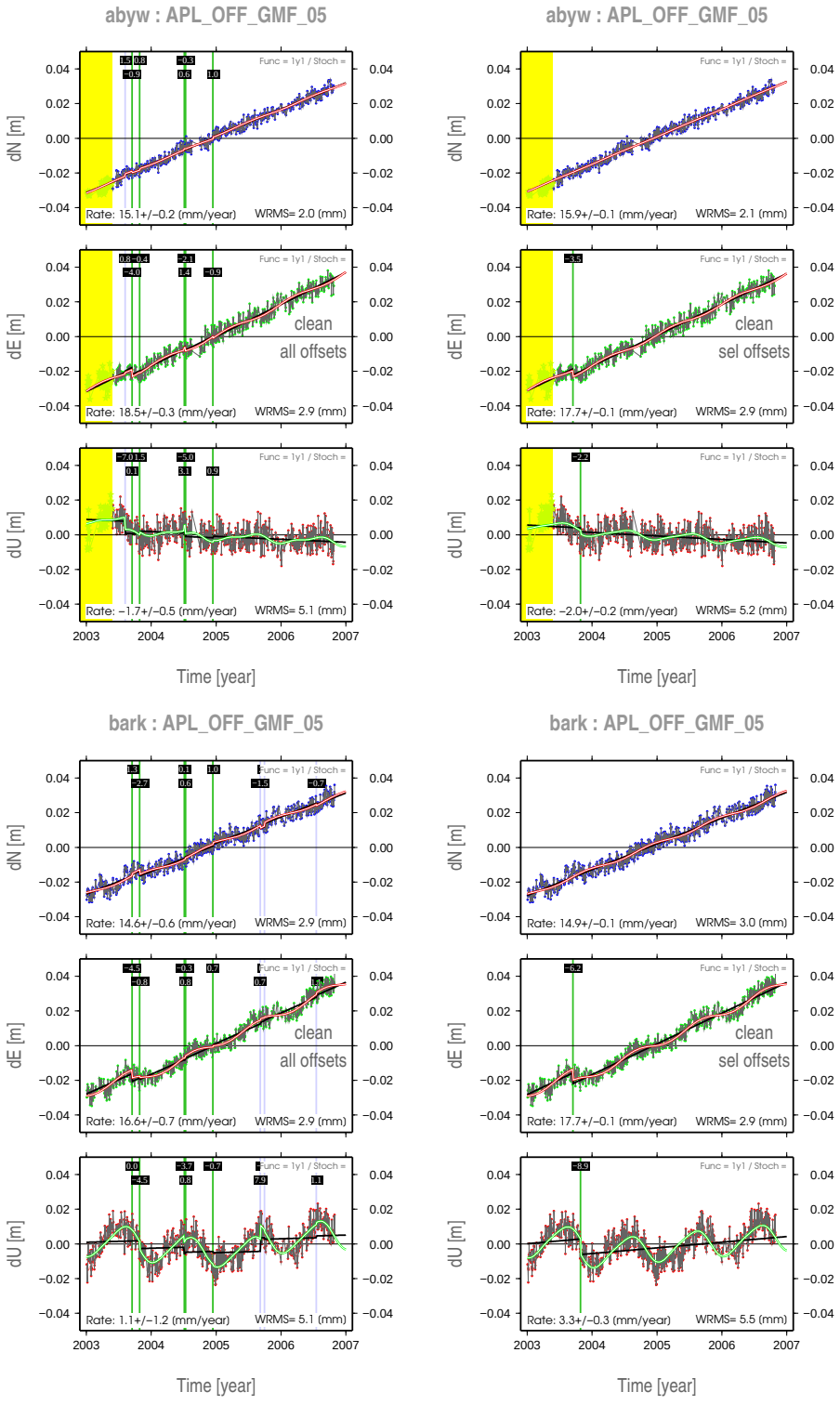

Figure 9.2: Same as Figure 9.1 for CGPS stations ABYW (top) and BARK (bottom). Left: all offsets; right: selected offsets.

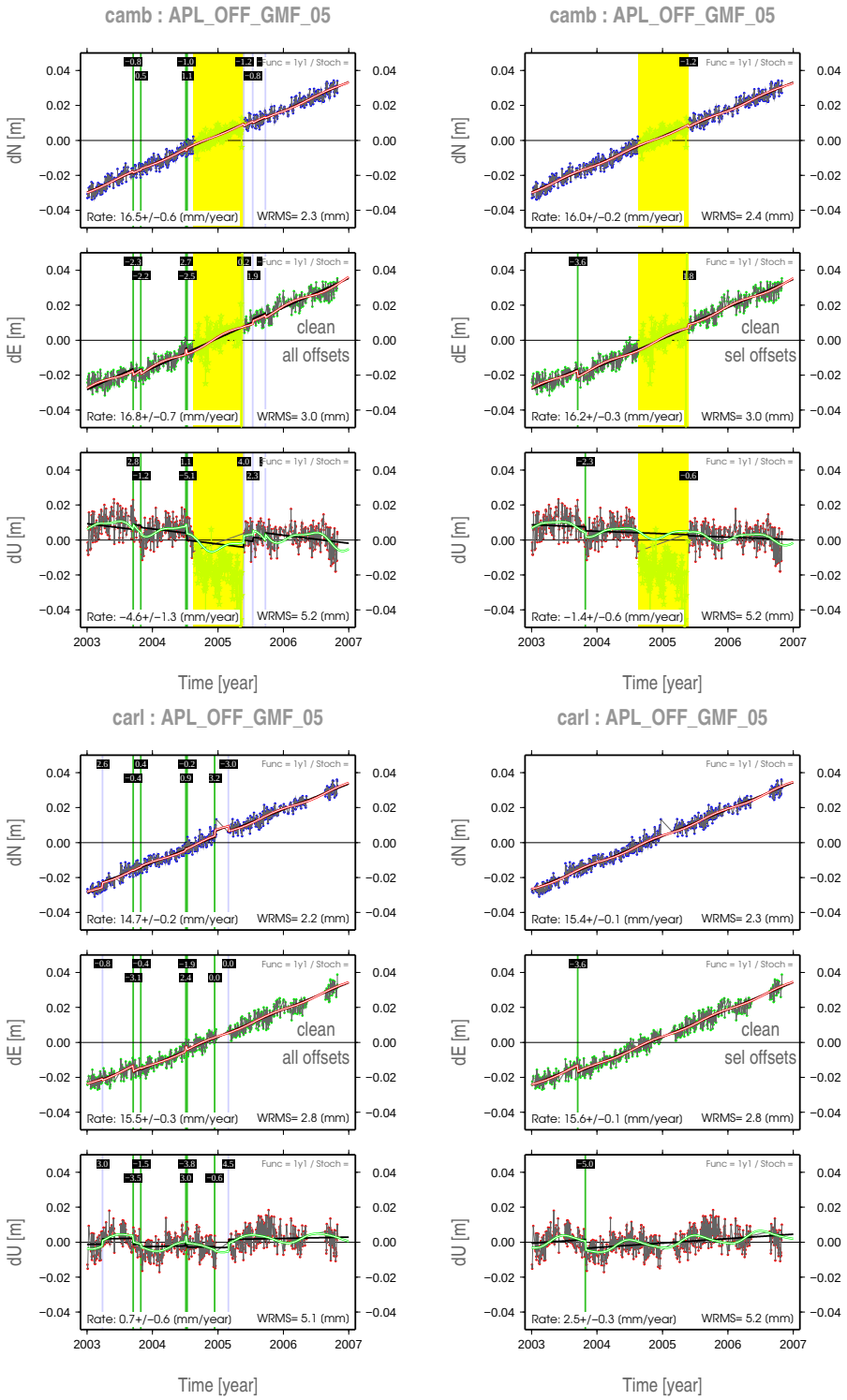

Figure 9.3: Same as Figure 9.1 for CGPS stations CAMB (top) and CARL (bottom). Left: all offsets; right: selected offsets.

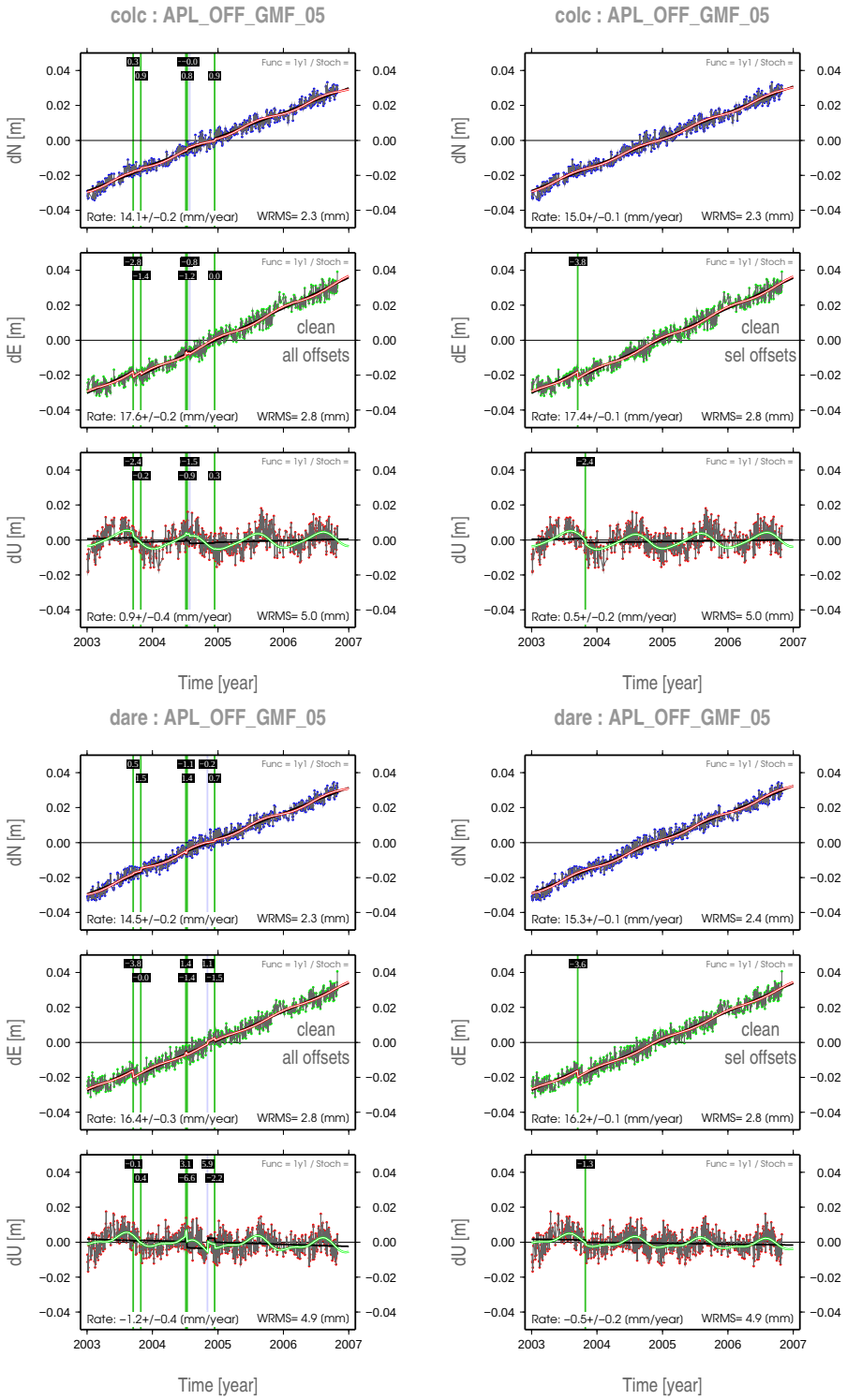

Figure 9.4: Same as Figure 9.1 for CGPS stations COLC (top) and DARE (bottom). Left: all offsets; right: selected offsets.

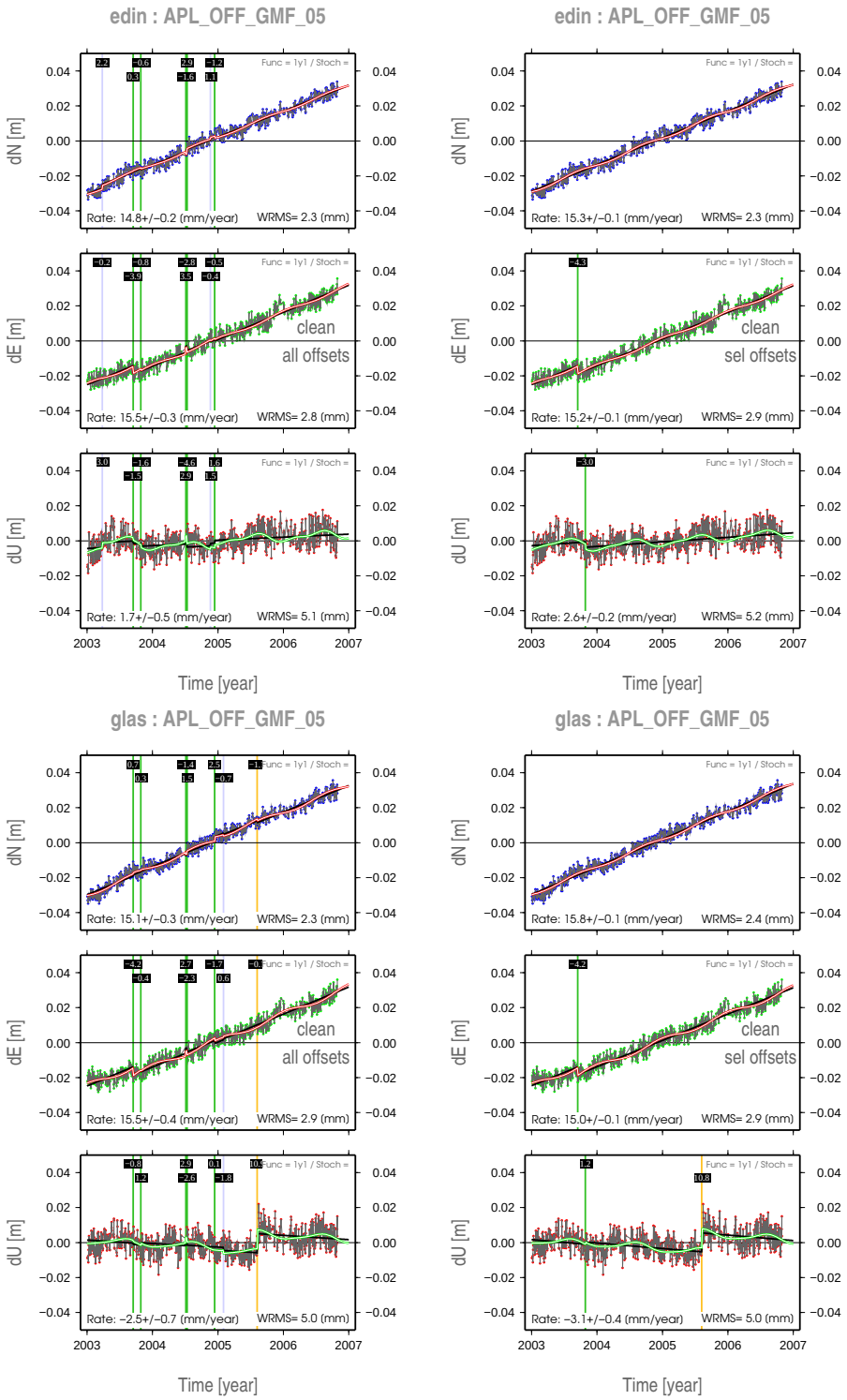

Figure 9.5: Same as Figure 9.1 for CGPS stations EDIN (top) and GLAS (bottom). Left: all offsets; right: selected offsets.

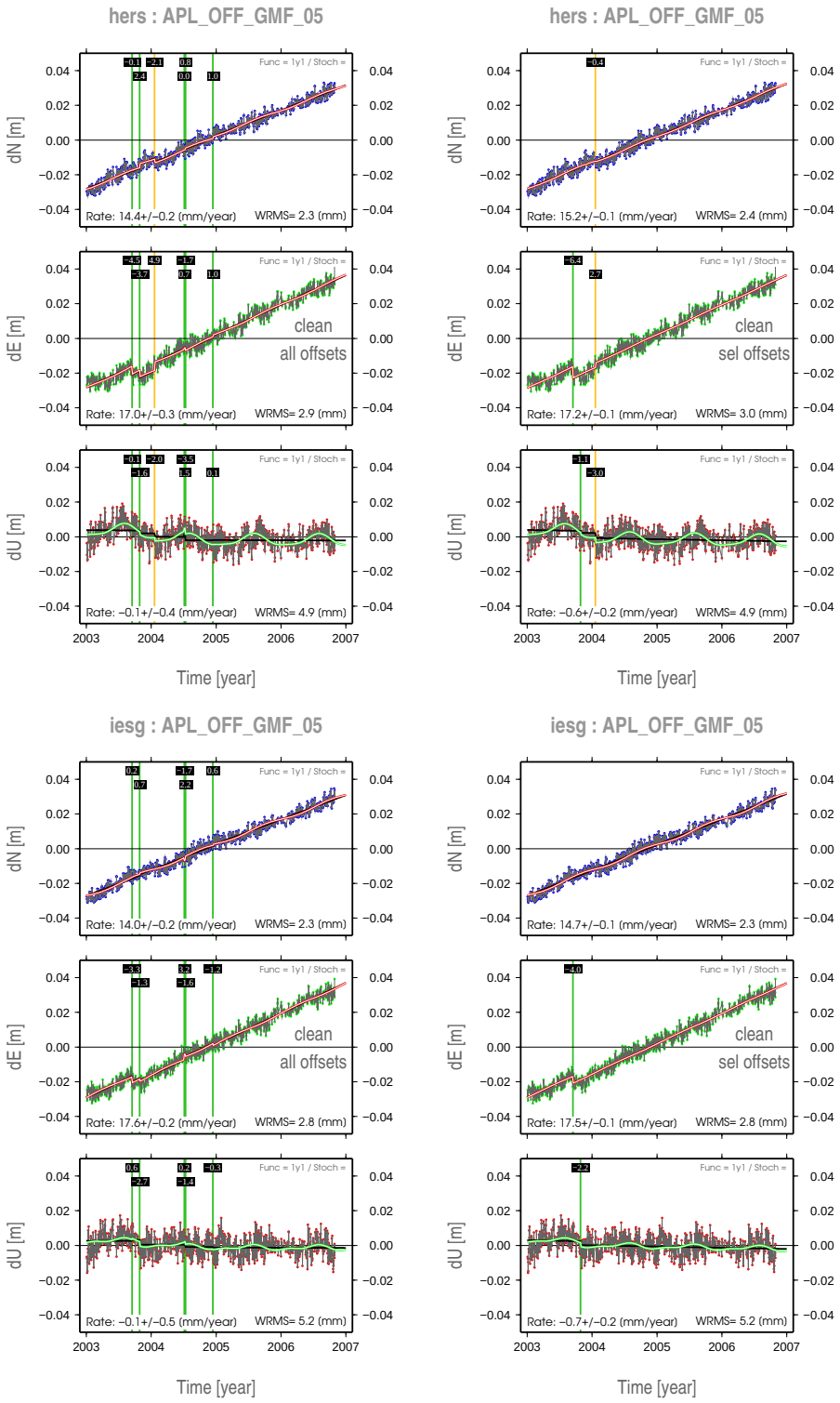

Figure 9.6: Same as Figure 9.1 for CGPS stations HERS (top) and IESG (bottom). Left: all offsets; right: selected offsets.

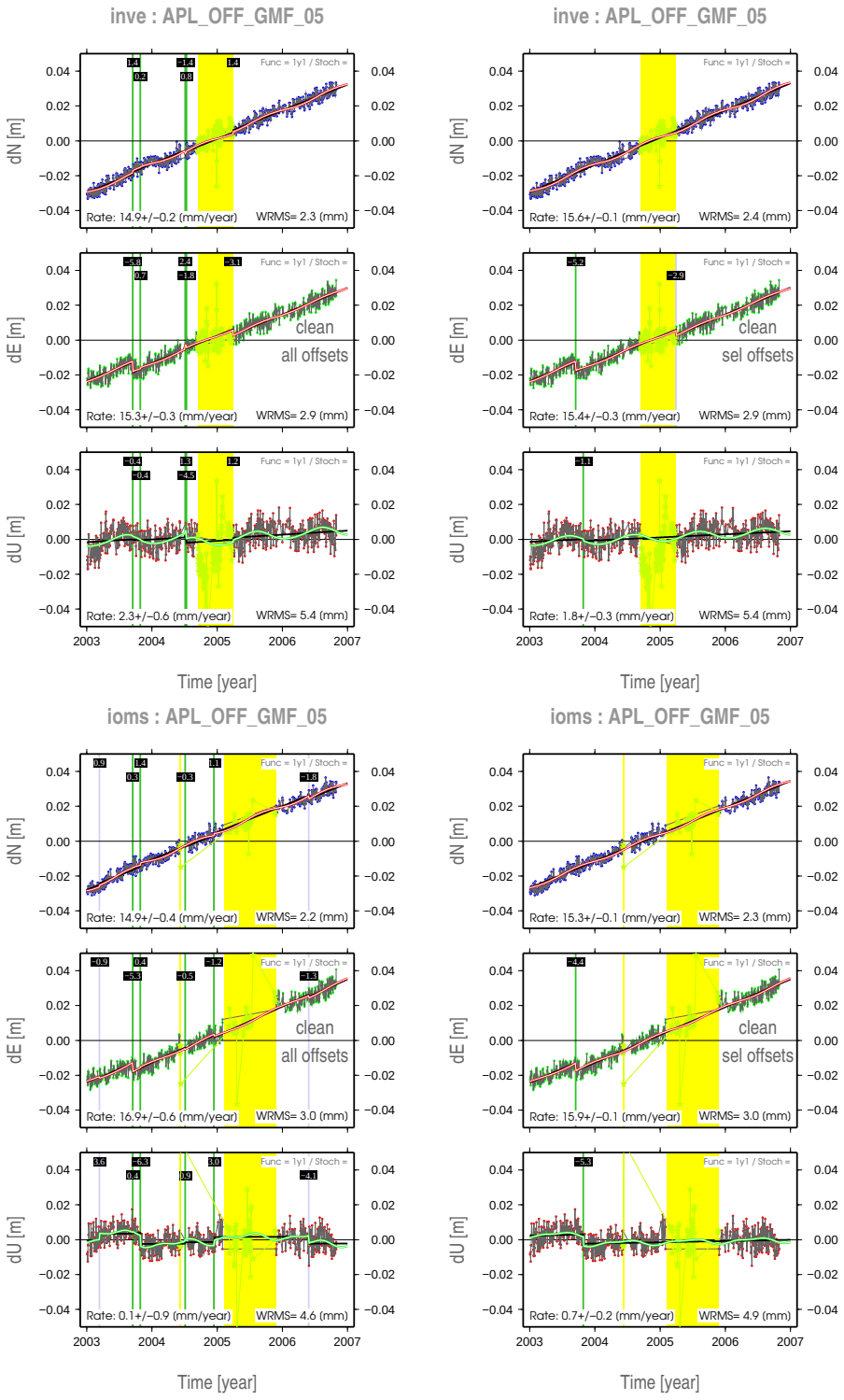

Figure 9.7: Same as Figure 9.1 for CGPS stations INVE (top) and IOMS (bottom). Left: all offsets; right: selected offsets.

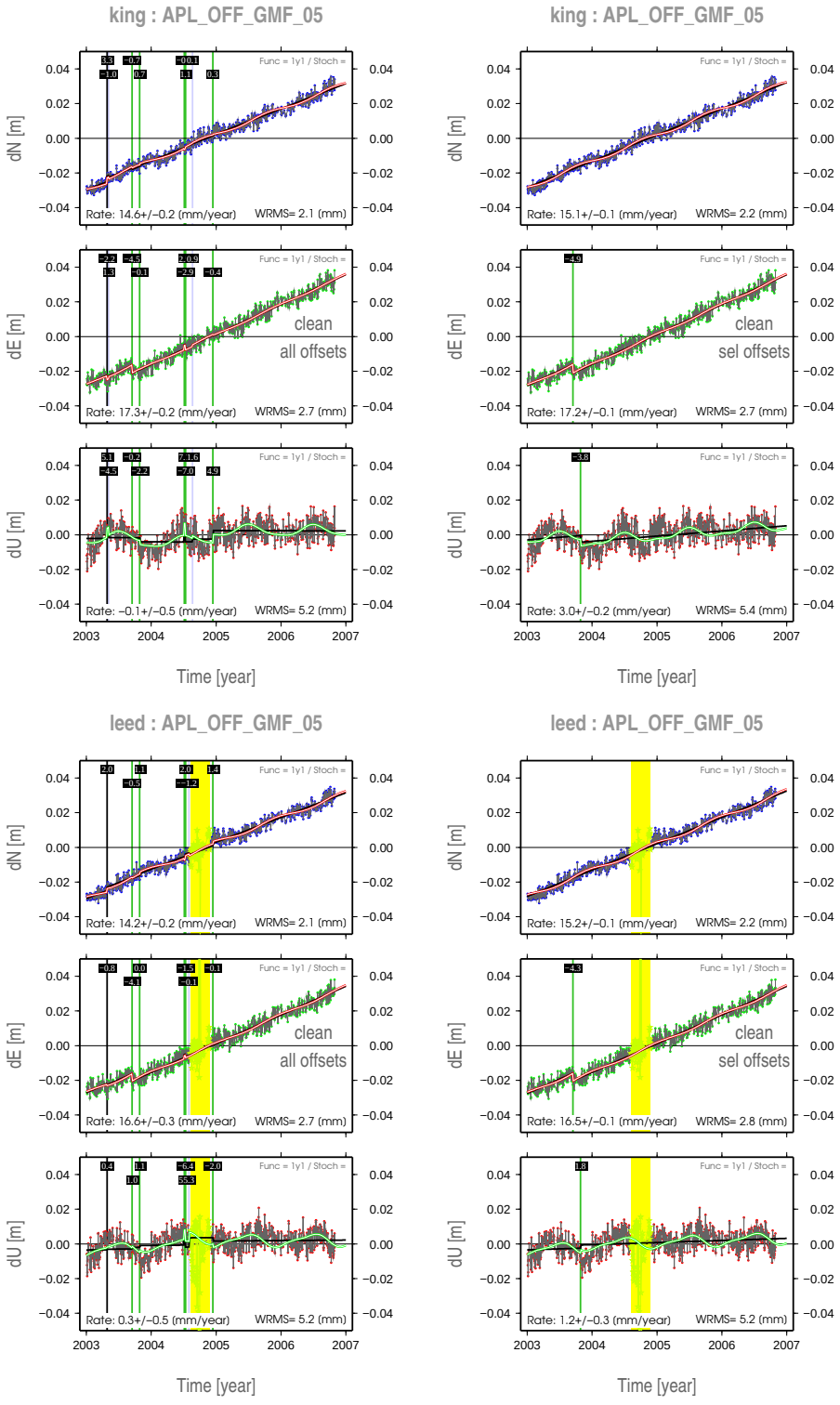

Figure 9.8: Same as Figure 9.1 for CGPS stations KING (top) and LEED (bottom). Left: all offsets; right: selected offsets.

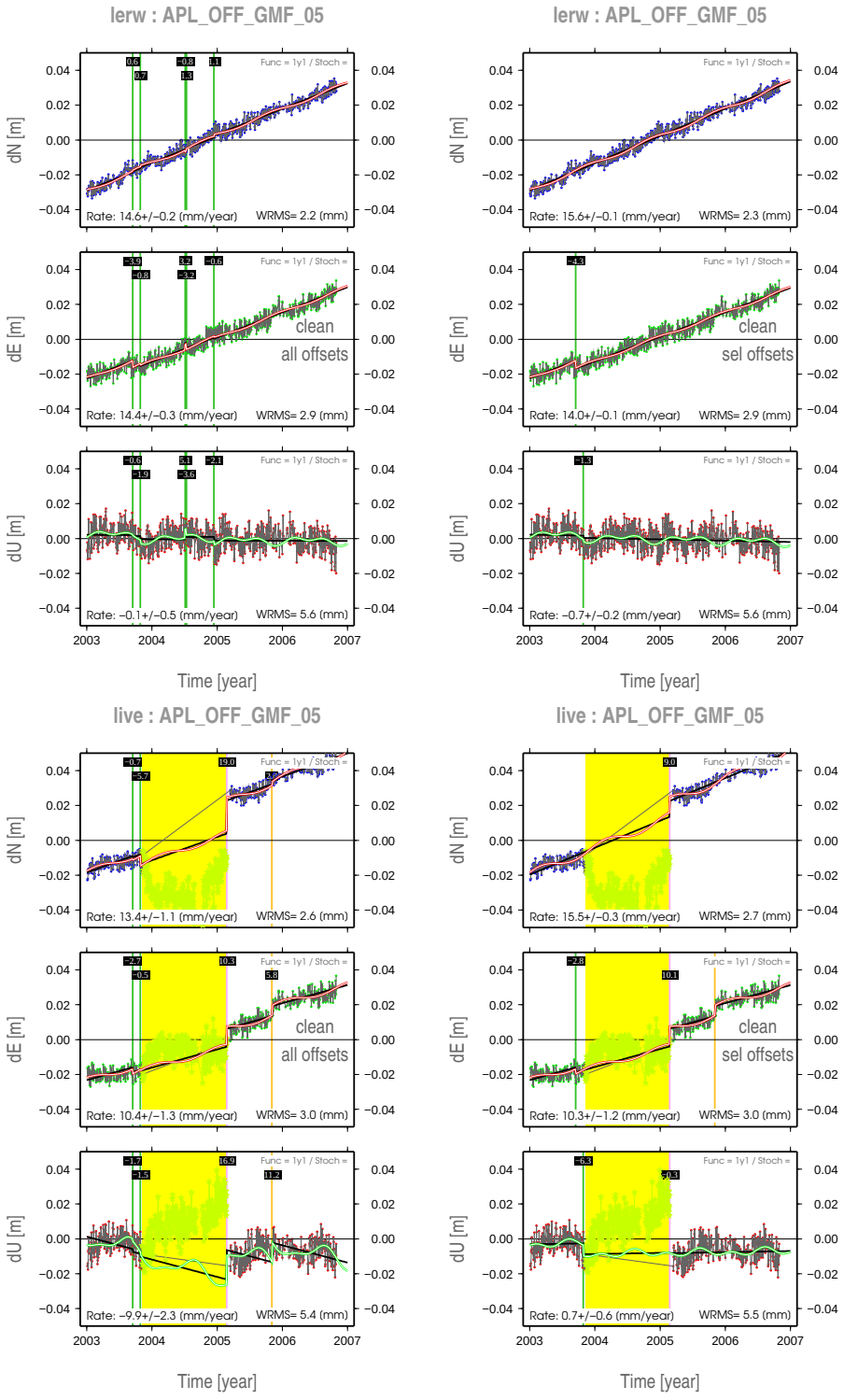

Figure 9.9: Same as Figure 9.1 for CGPS stations LERW (top) and LIVE (bottom). Left: all offsets; right: selected offsets.

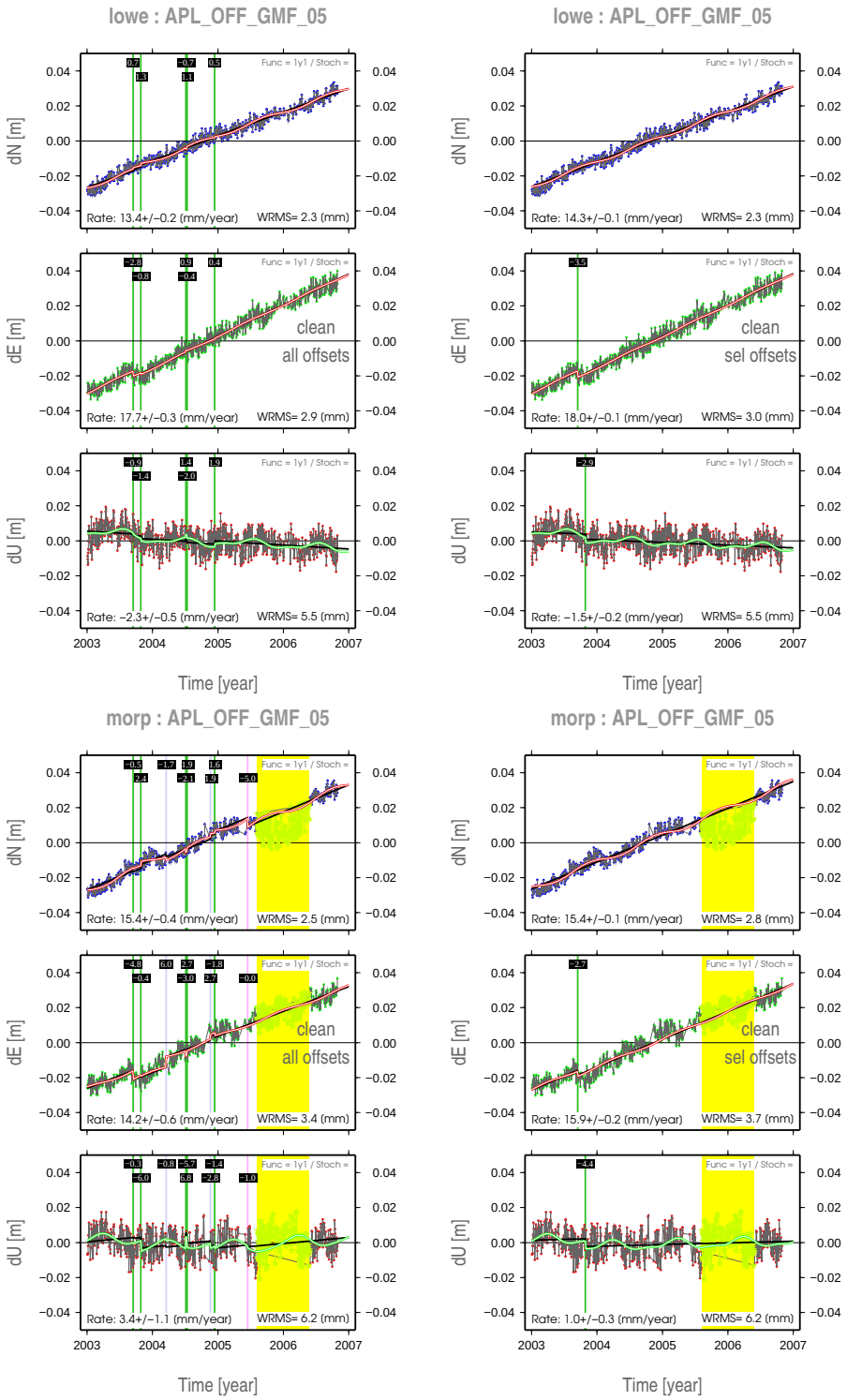

Figure 9.10: Same as Figure 9.1 for CGPS stations LOWE (top) and MORP (bottom). Left: all offsets; right: selected offsets.

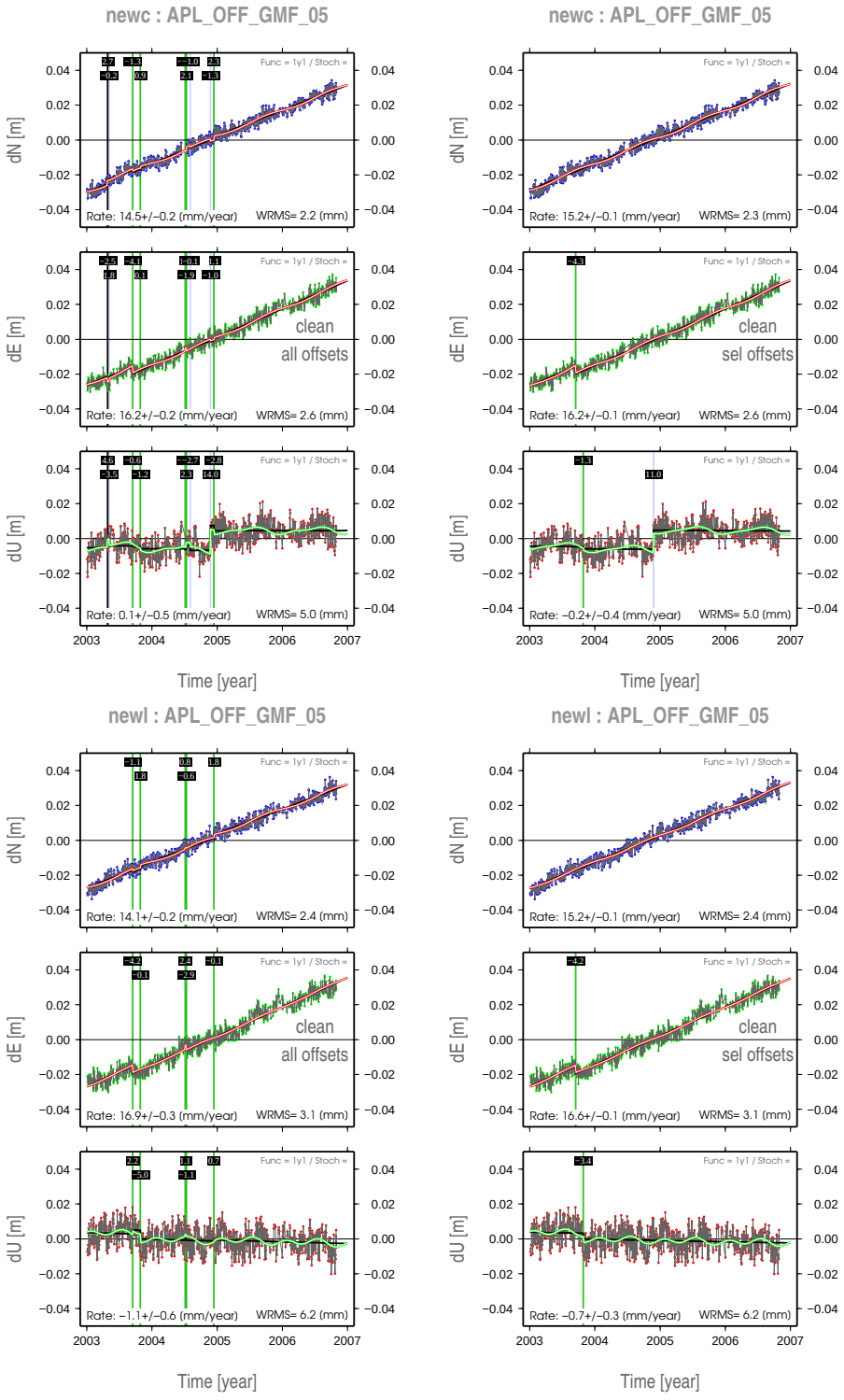

Figure 9.11: Same as Figure 9.1 for CGPS stations NEWC (top) and NEWL (bottom). Left: all offsets; right: selected offsets.

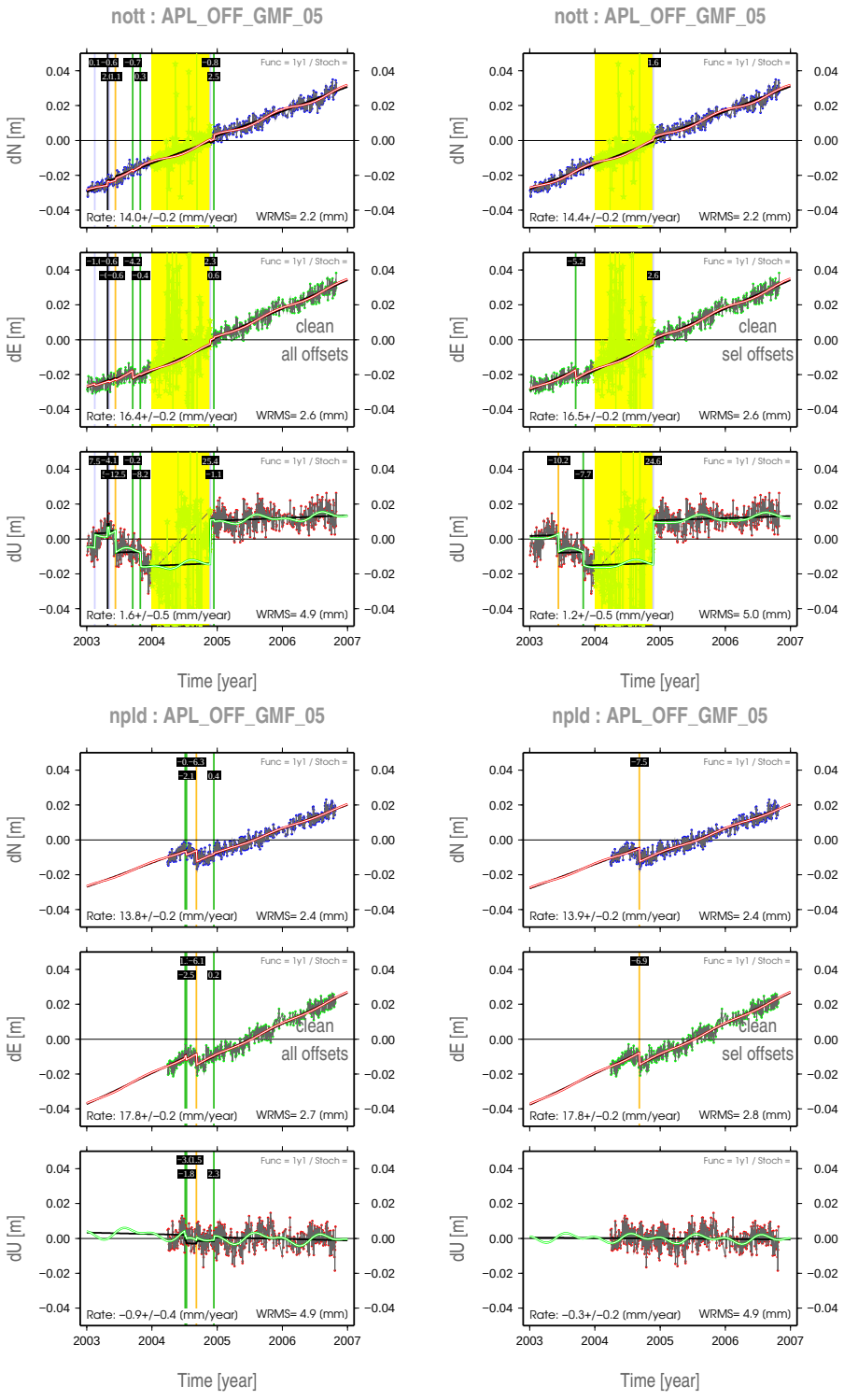

Figure 9.12: Same as Figure 9.1 for CGPS stations NOTT (top) and NPLD (bottom). Left: all offsets; right: selected offsets.

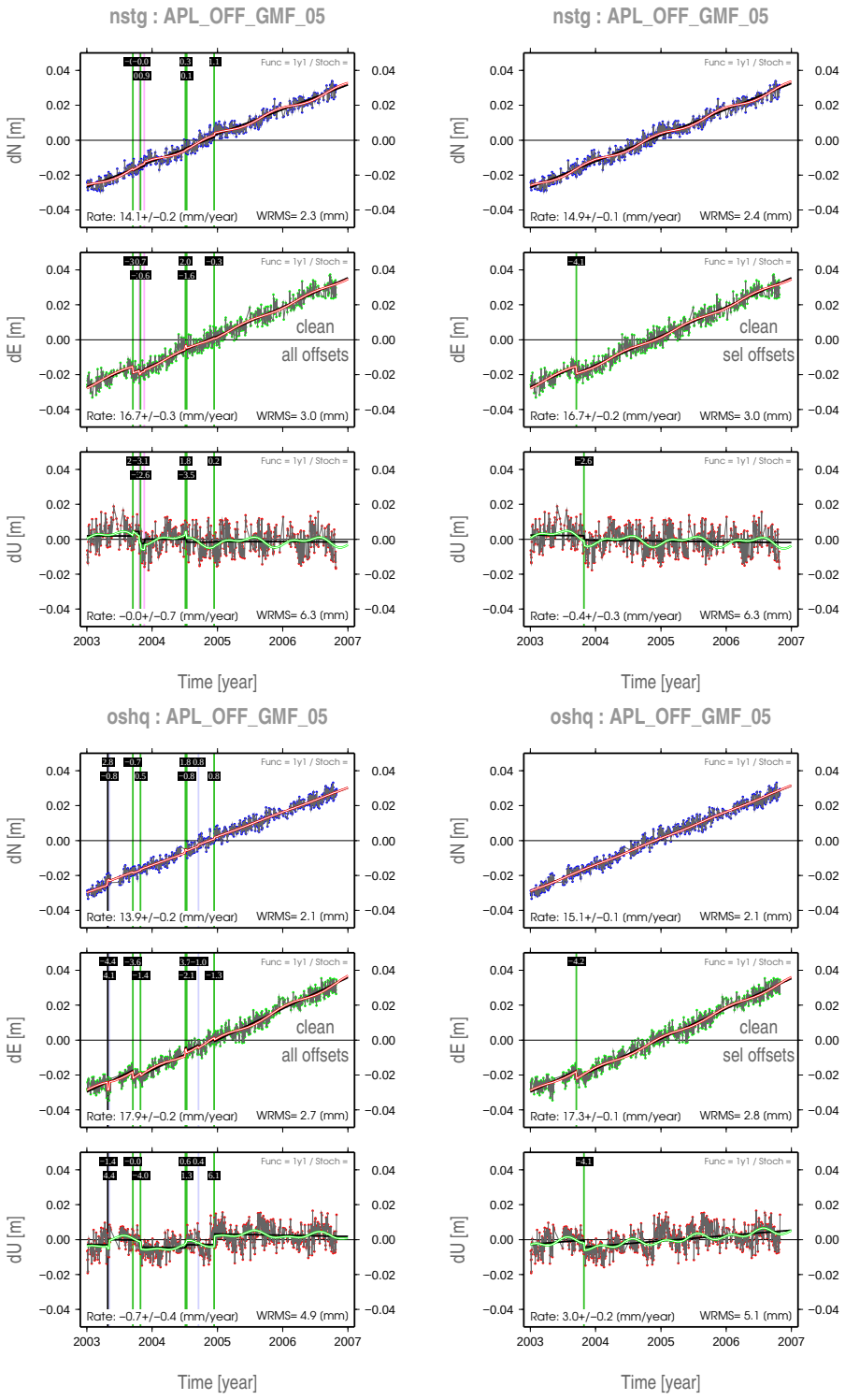

Figure 9.13: Same as Figure 9.1 for CGPS stations NSTG (top) and OSHQ (bottom). Left: all offsets; right: selected offsets.

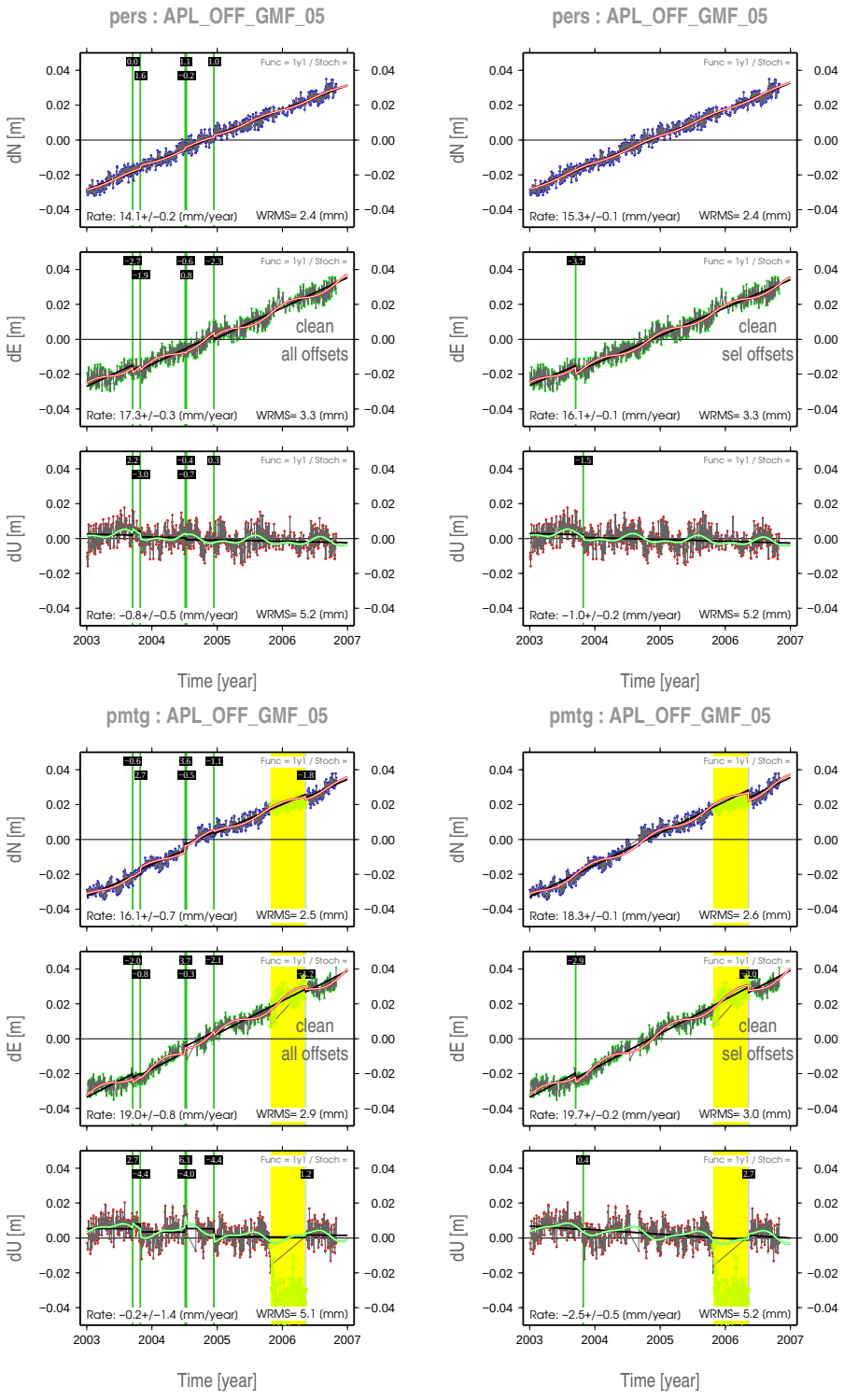

Figure 9.14: Same as Figure 9.1 for CGPS stations PERS (top) and PMTG (bottom). Left: all offsets; right: selected offsets.

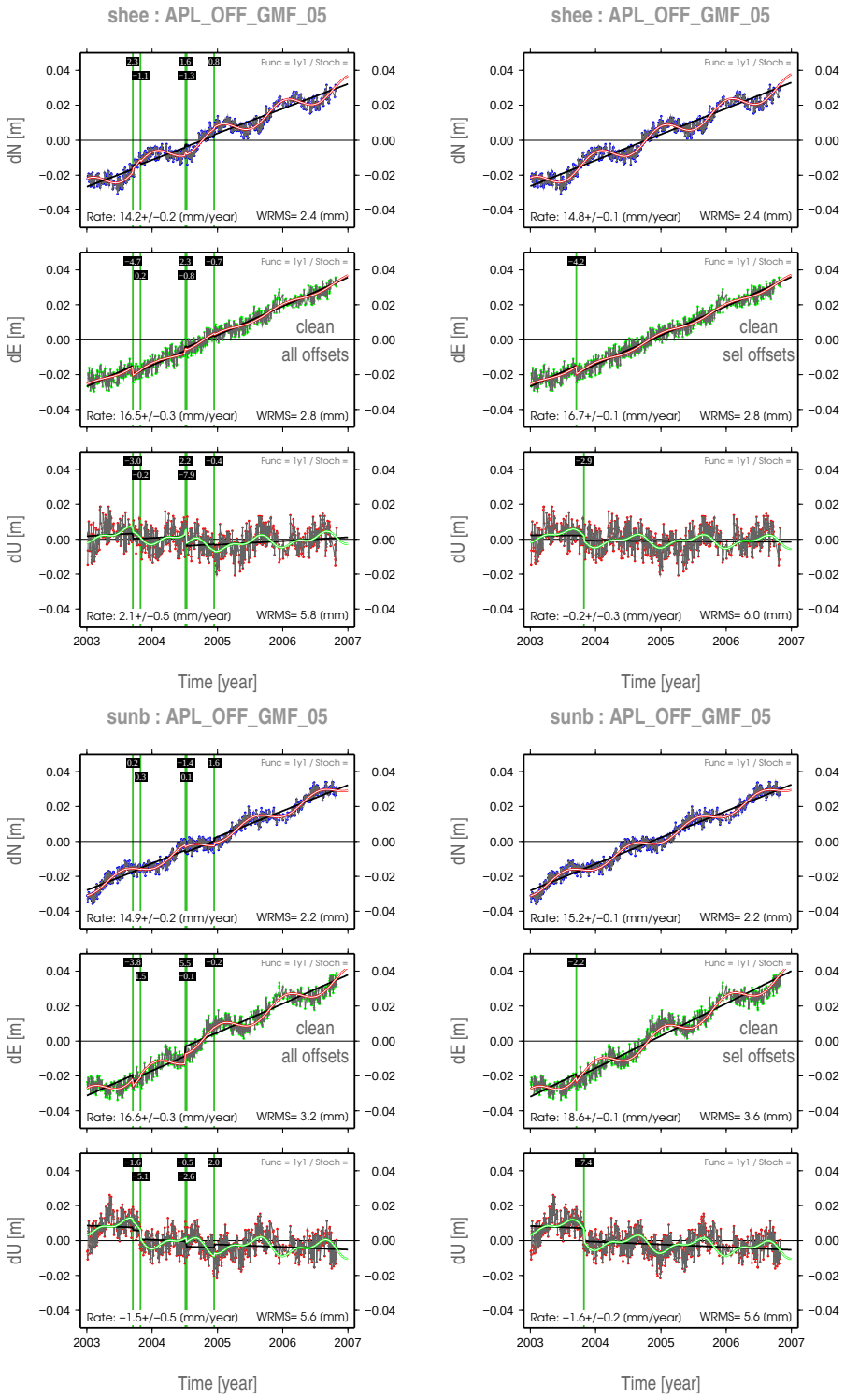

Figure 9.15: Same as Figure 9.1 for CGPS stations SHEE (top) and SUNB (bottom). Left: all offsets; right: selected offsets.

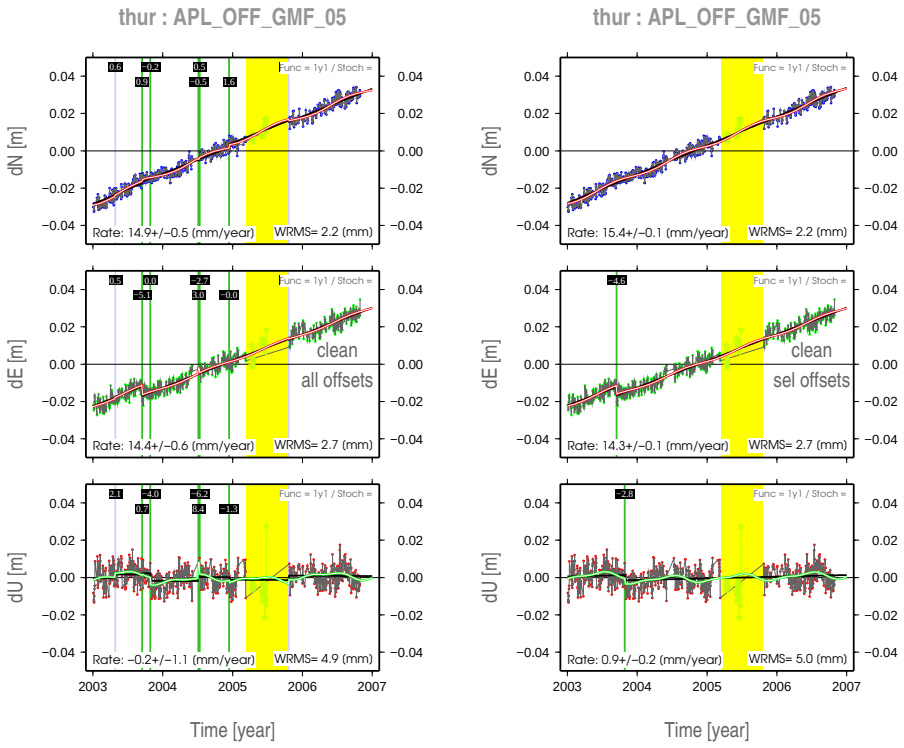

Figure 9.16: Same as Figure 9.1 for station THUR. Left: all offsets; right: selected offsets.

Chapter 10

Azimuthal Asymmetry in the OMF

This appendix presents for five CGPS stations well distributed over the UK, two days of six hourly plots representing the asymmetry of the azimuth dependent version of the OMF. It was chosen to present the asymmetry in term of slant range differences for standard hydrostatic and wet zenith delays of 2300 and 100 mm respectively, with the 'base' mapping function of the OMF, i.e. the NMF, hydrostatic and wet.

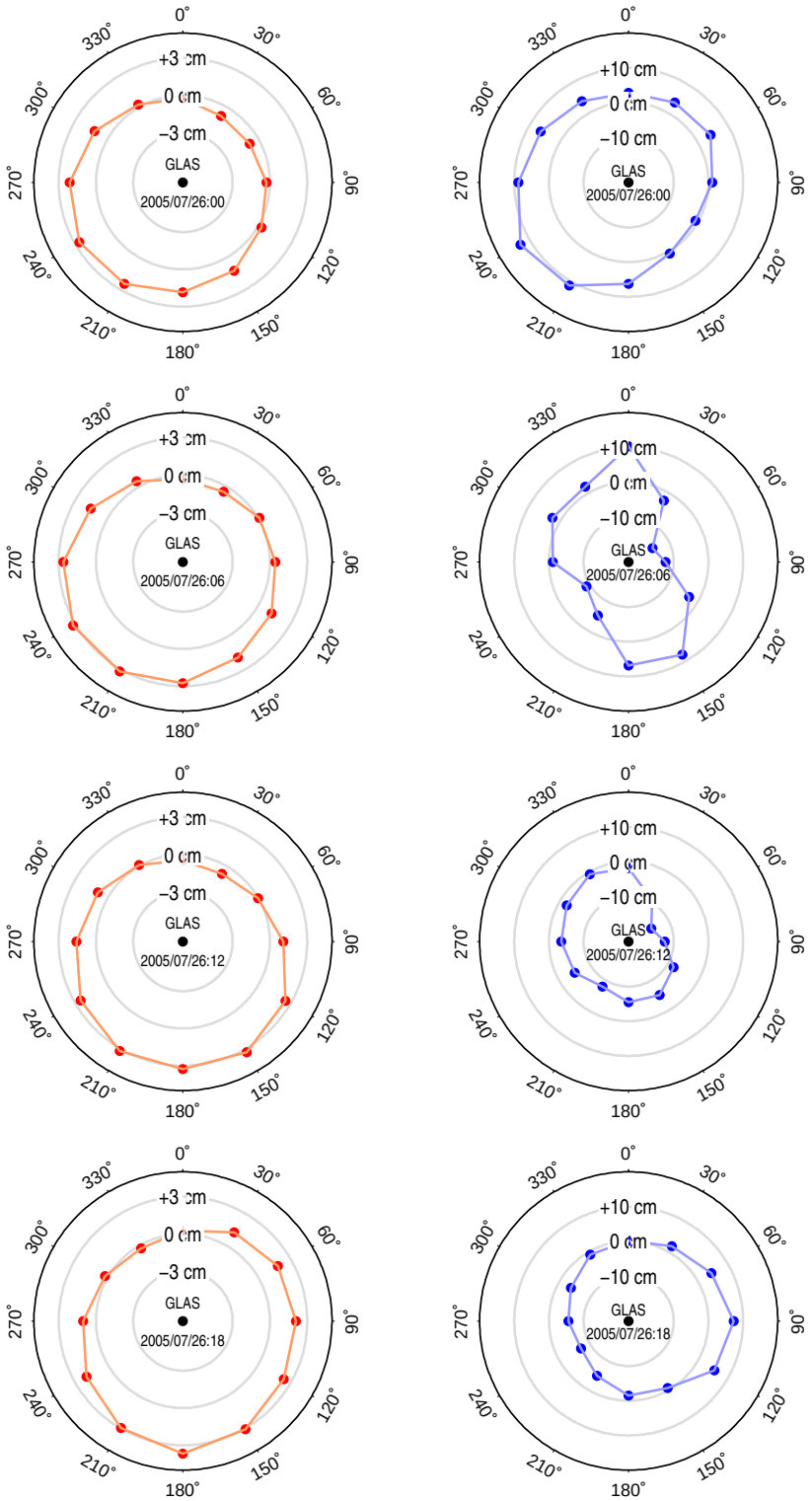

Figure 10.1: Slant atmospheric delay difference for CGPS station GLAS between the azimuth dependent mapping function OMF_AZI and the NMF at 5 degrees elevation for a standard ZHD of 2300 mm (left column) and ZWD 100 mm (right column) for 26 July, 2006.

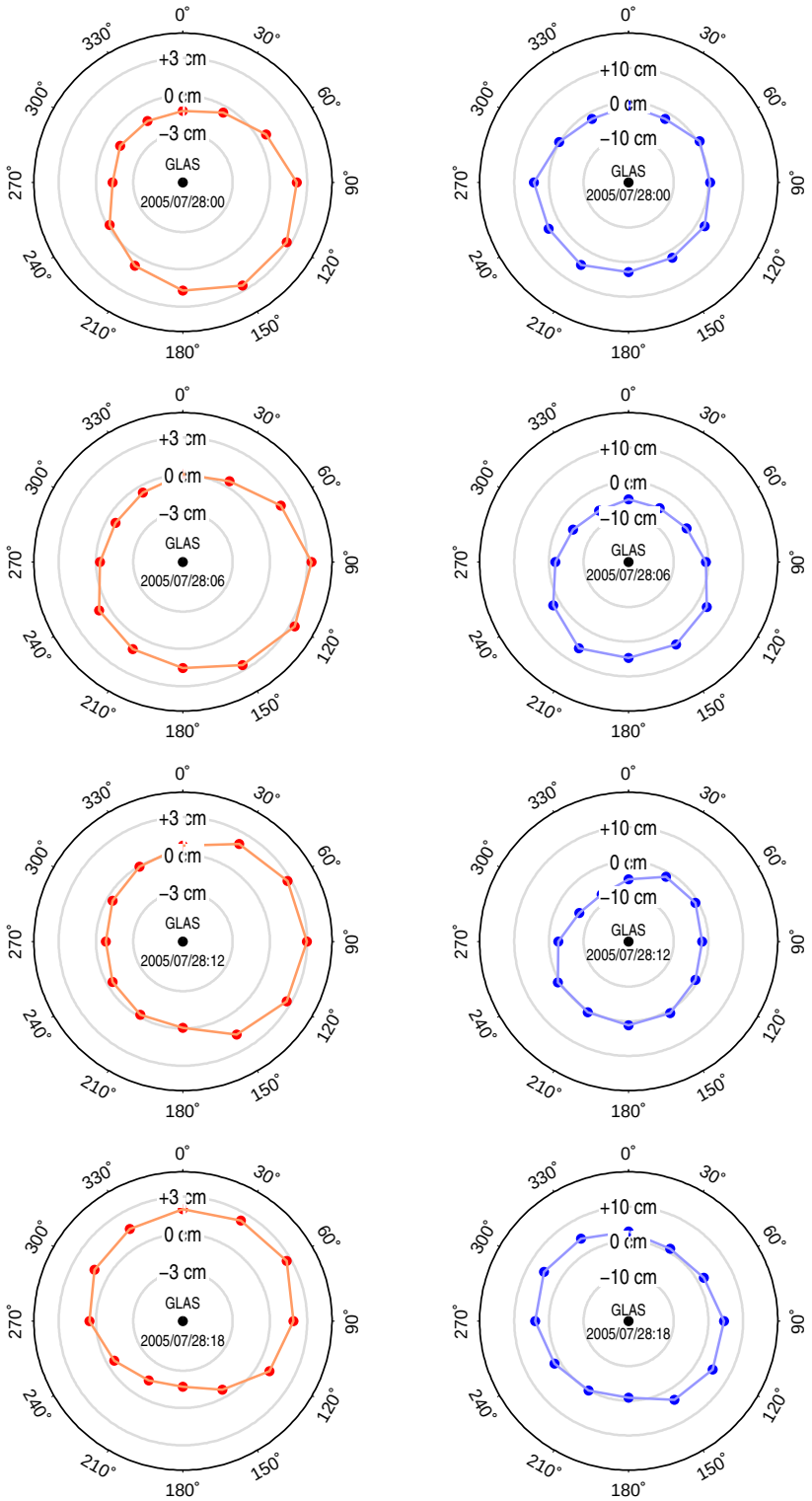

Figure 10.2: Slant atmospheric delay difference for CGPS station GLAS between the azimuth dependent mapping function OMF_AZI and the NMF at 5 degrees elevation for a standard ZHD of 2300 mm (left column) and ZWD 100 mm (right column) for 28 July, 2006.

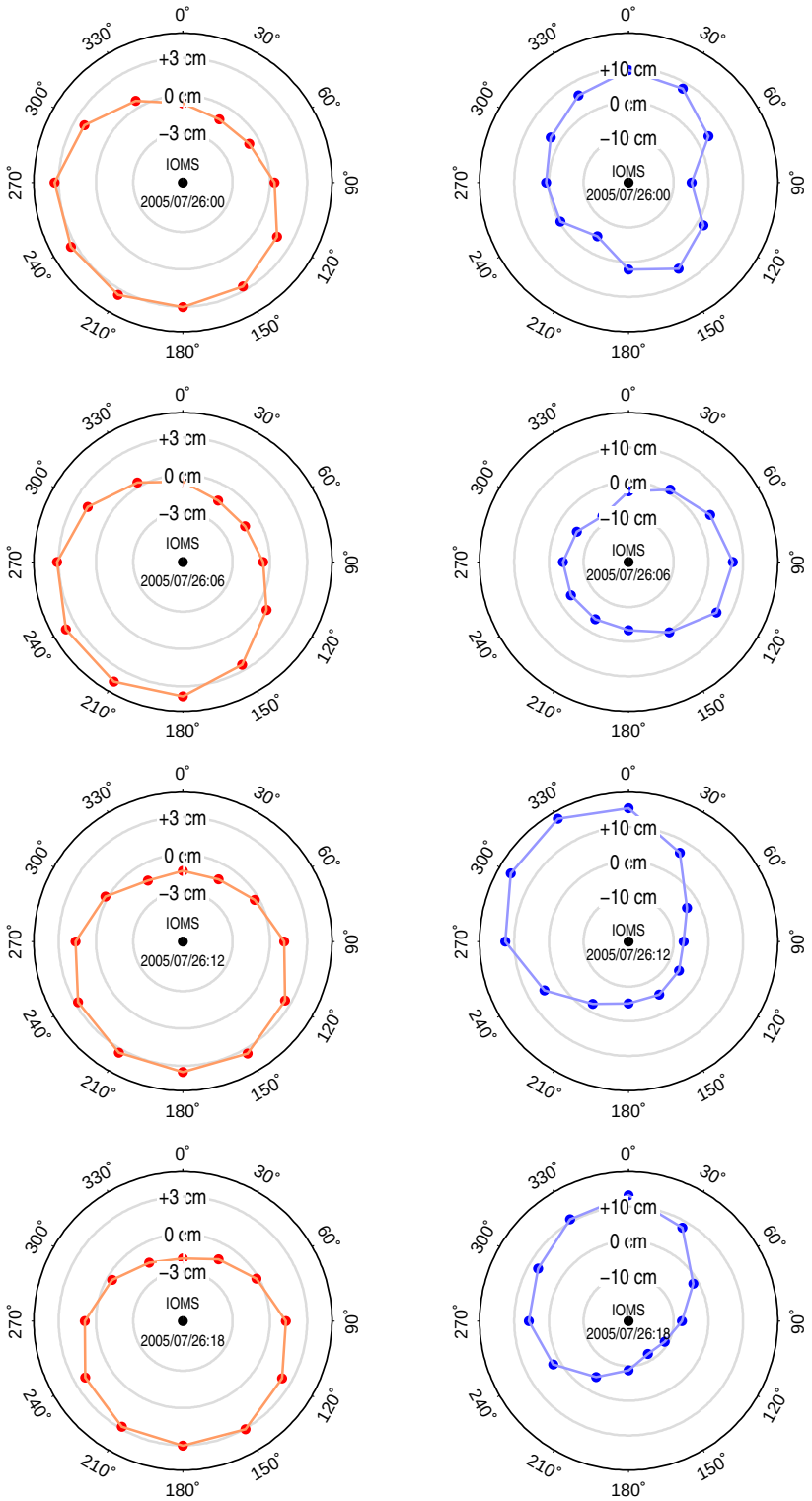

Figure 10.3: Slant atmospheric delay difference for CGPS station IOMS between the azimuth dependent mapping function OMF_AZI and the NMF at 5 degrees elevation for a standard ZHD of 2300 mm (left column) and ZWD 100 mm (right column) for 26 July, 2006.

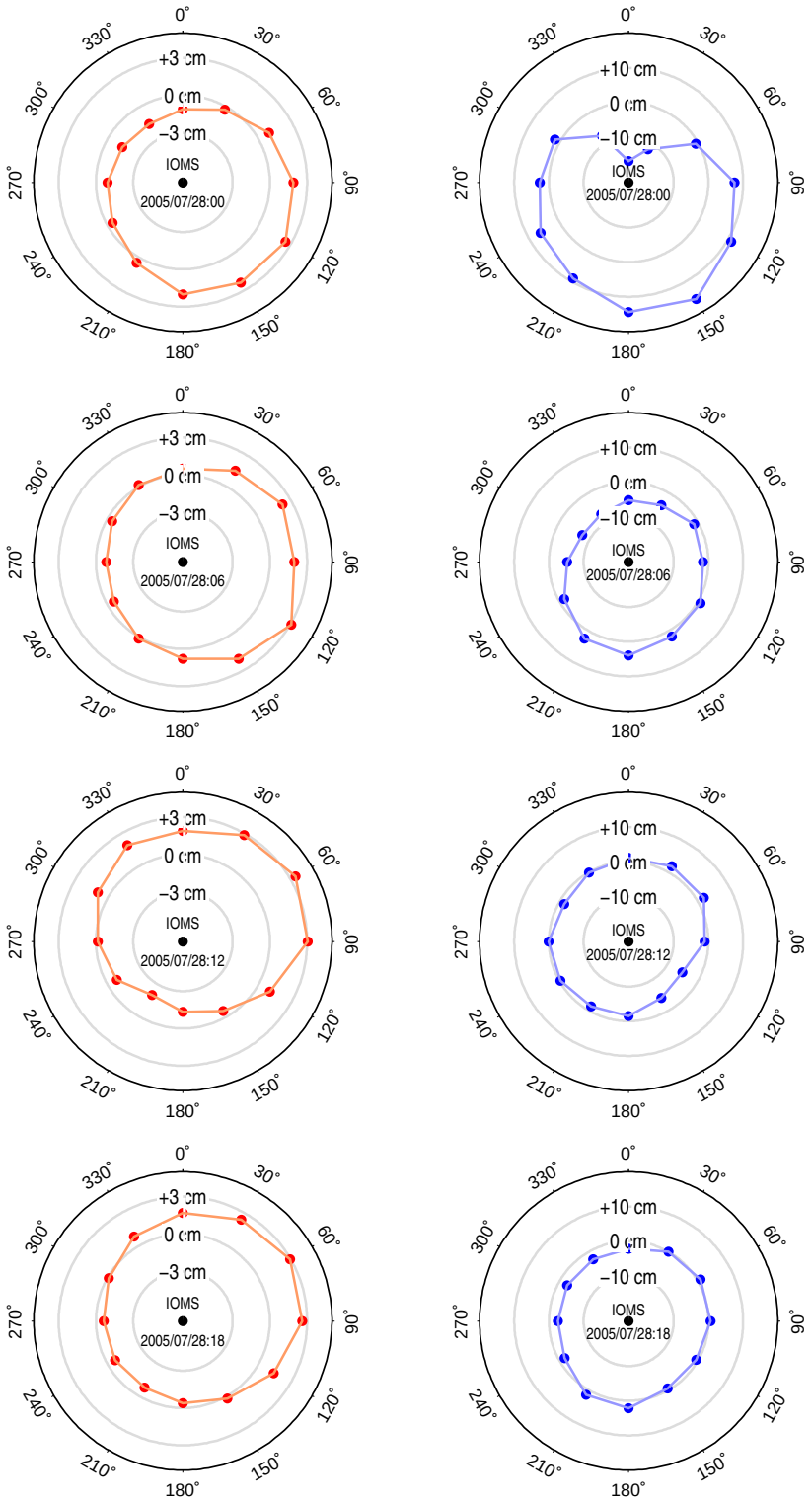

Figure 10.4: Slant atmospheric delay difference for CGPS station IOMS between the azimuth dependent mapping function OMF_AZI and the NMF at 5 degrees elevation for a standard ZHD of 2300 mm (left column) and ZWD 100 mm (right column) for 28 July, 2006.

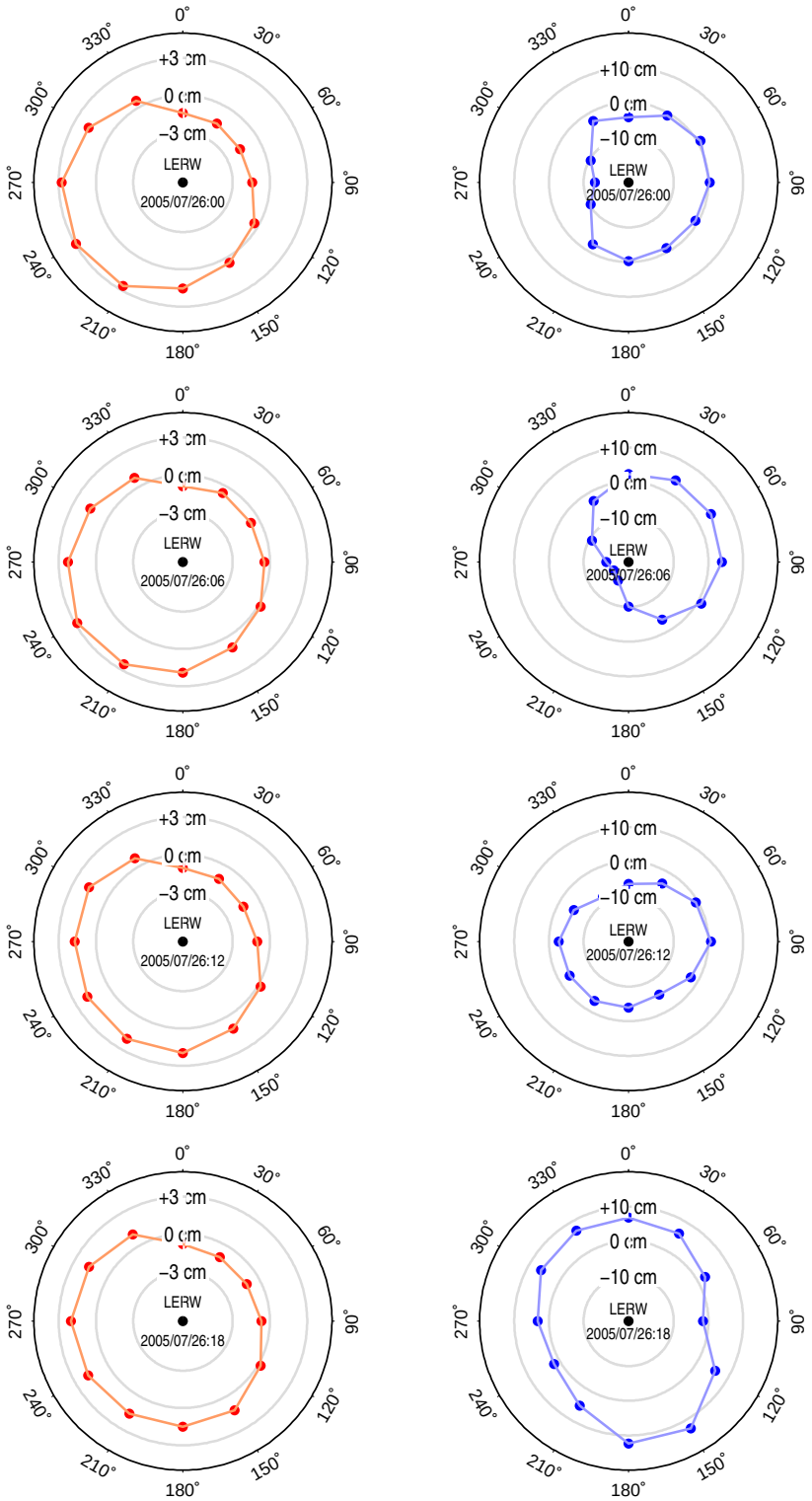

Figure 10.5: Slant atmospheric delay difference for CGPS station LERW between the azimuth dependent mapping function OMF_AZI and the NMF at 5 degrees elevation for a standard ZHD of 2300 mm (left column) and ZWD 100 mm (right column) for 26 July, 2006.

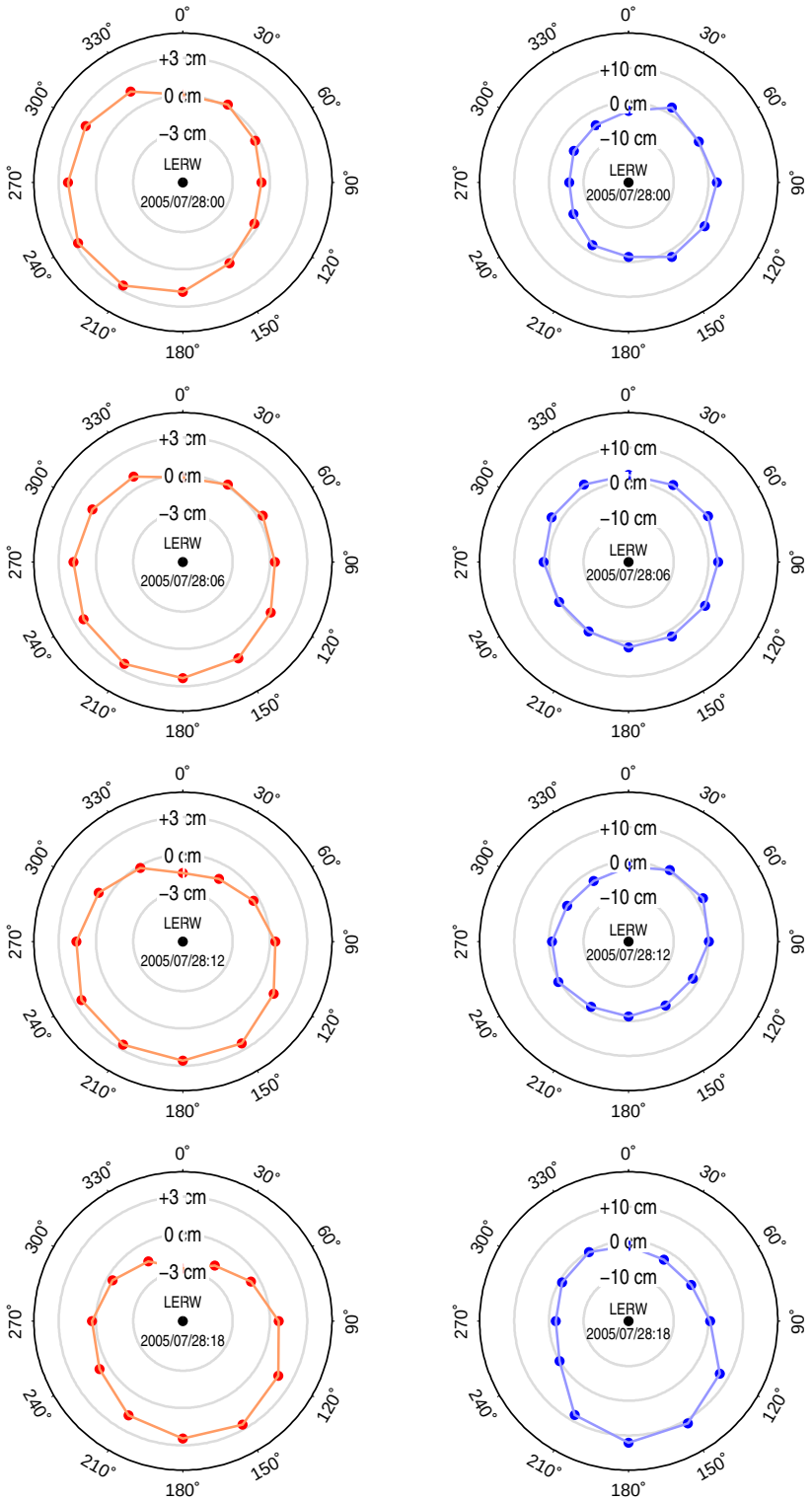

Figure 10.6: Slant atmospheric delay difference for CGPS station LERW between the azimuth dependent mapping function OMF_AZI and the NMF at 5 degrees elevation for a standard ZHD of 2300 mm (left column) and ZWD 100 mm (right column) for 28 July, 2006.

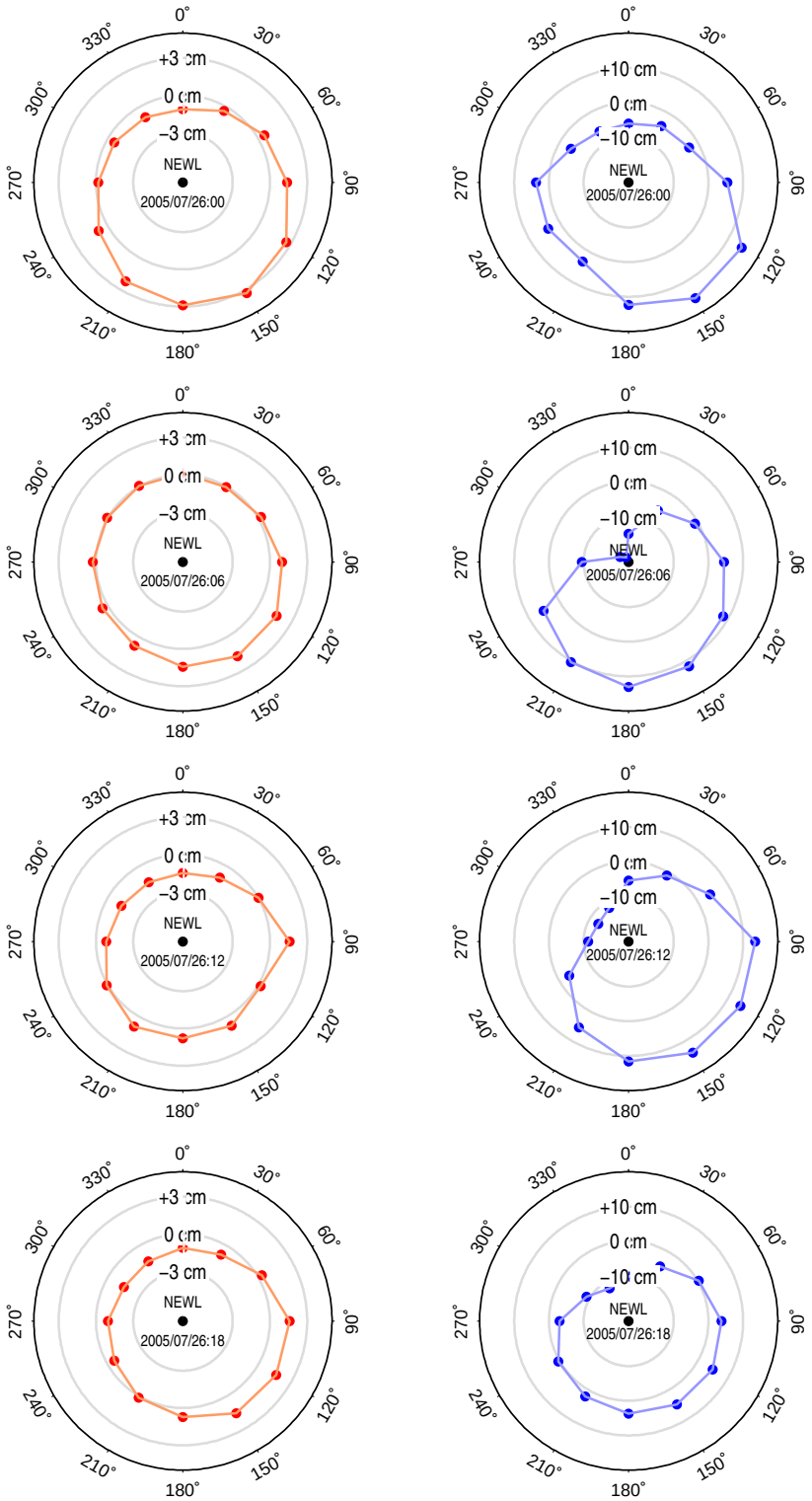

Figure 10.7: Slant atmospheric delay difference for CGPS station NEWL between the azimuth dependent mapping function OMF_AZI and the NMF at 5 degrees elevation for a standard ZHD of 2300 mm (left column) and ZWD 100 mm (right column) for 26 July, 2006.

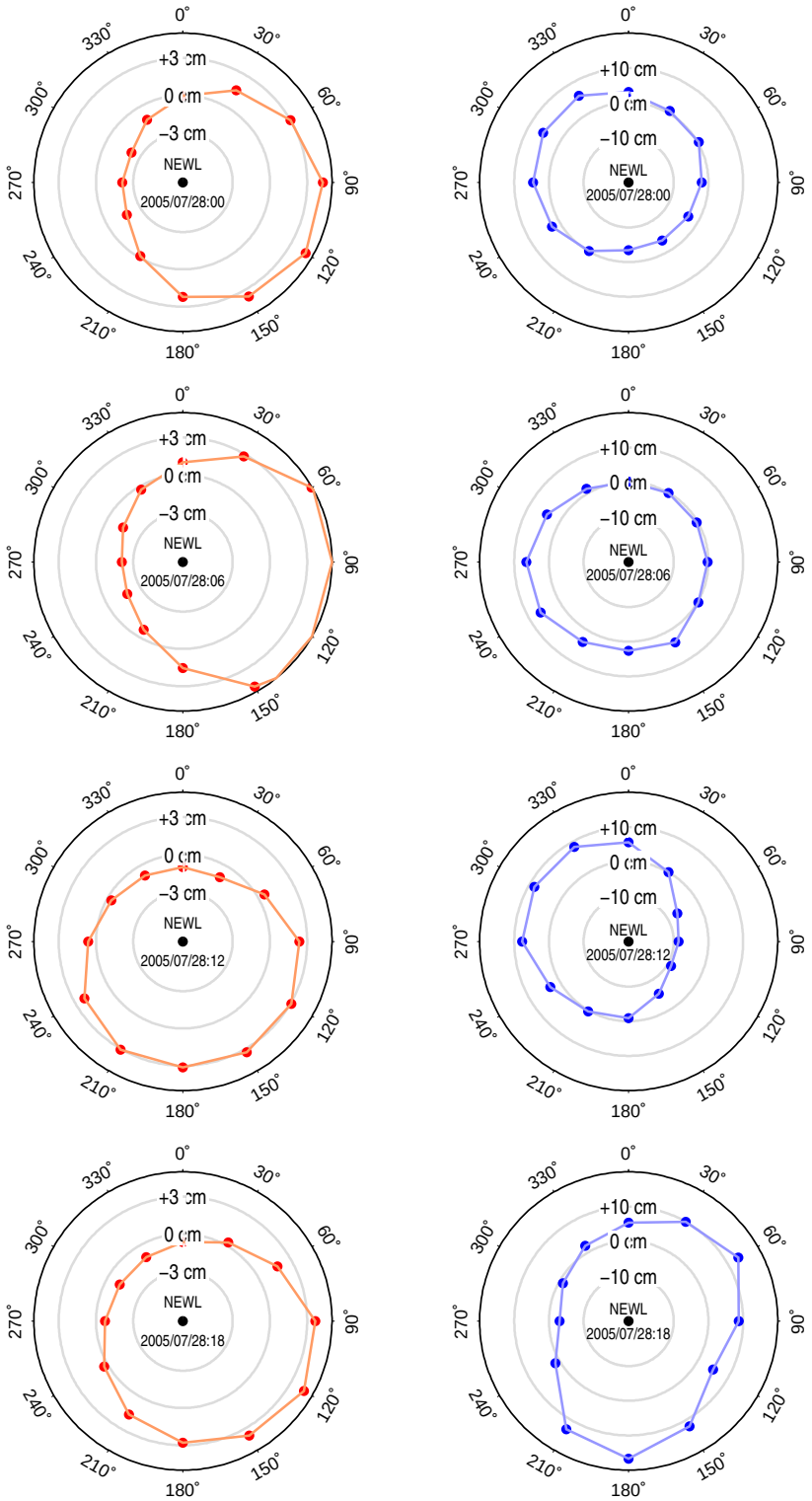

Figure 10.8: Slant atmospheric delay difference for CGPS station NEWL between the azimuth dependent mapping function OMF_AZI and the NMF at 5 degrees elevation for a standard ZHD of 2300 mm (left column) and ZWD 100 mm (right column) for 28 July, 2006.

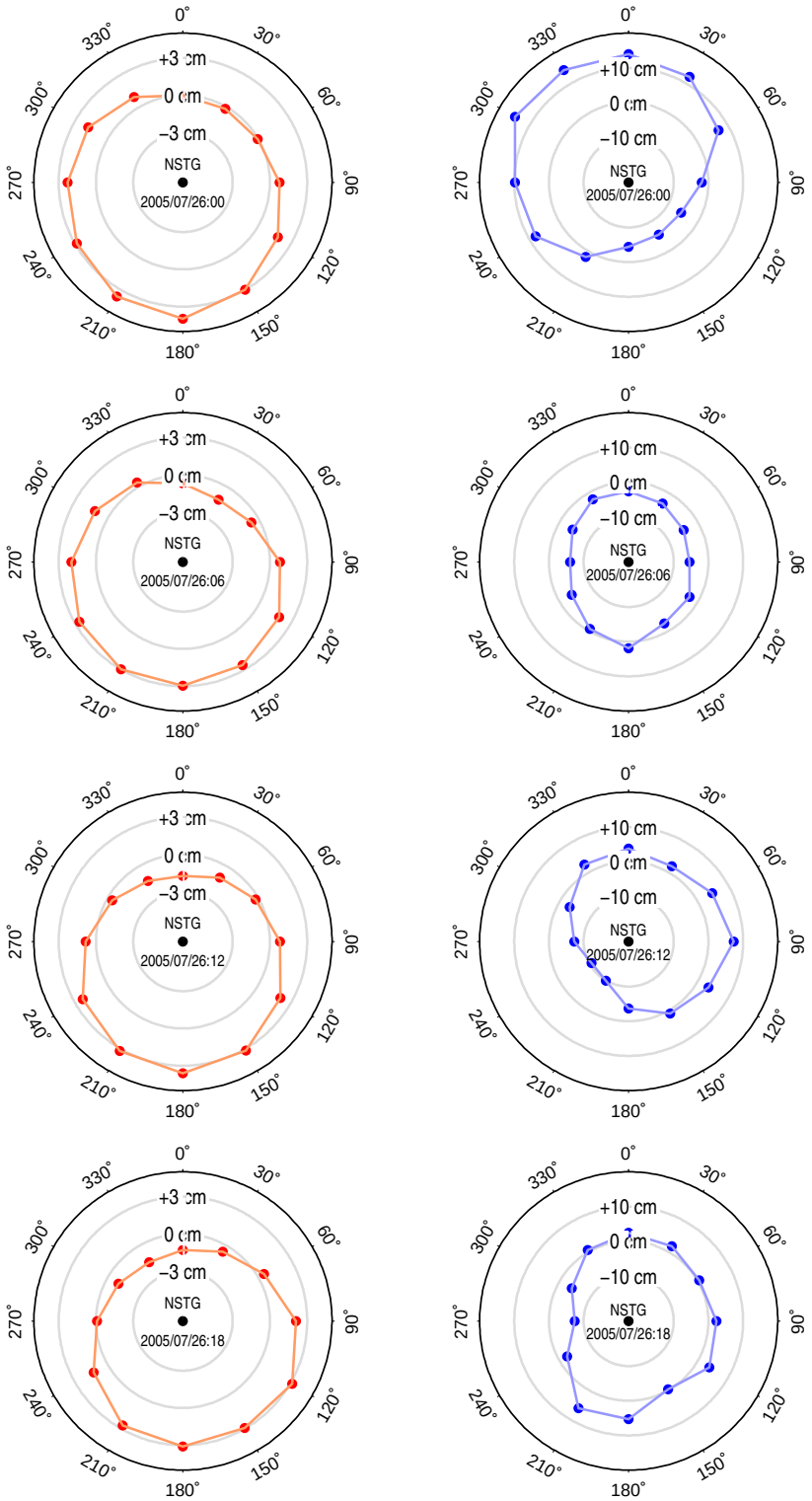

Figure 10.9: Slant atmospheric delay difference for CGPS station NSTG between the azimuth dependent mapping function OMF_AZI and the NMF at 5 degrees elevation for a standard ZHD of 2300 mm (left column) and ZWD 100 mm (right column) for 26 July, 2006.

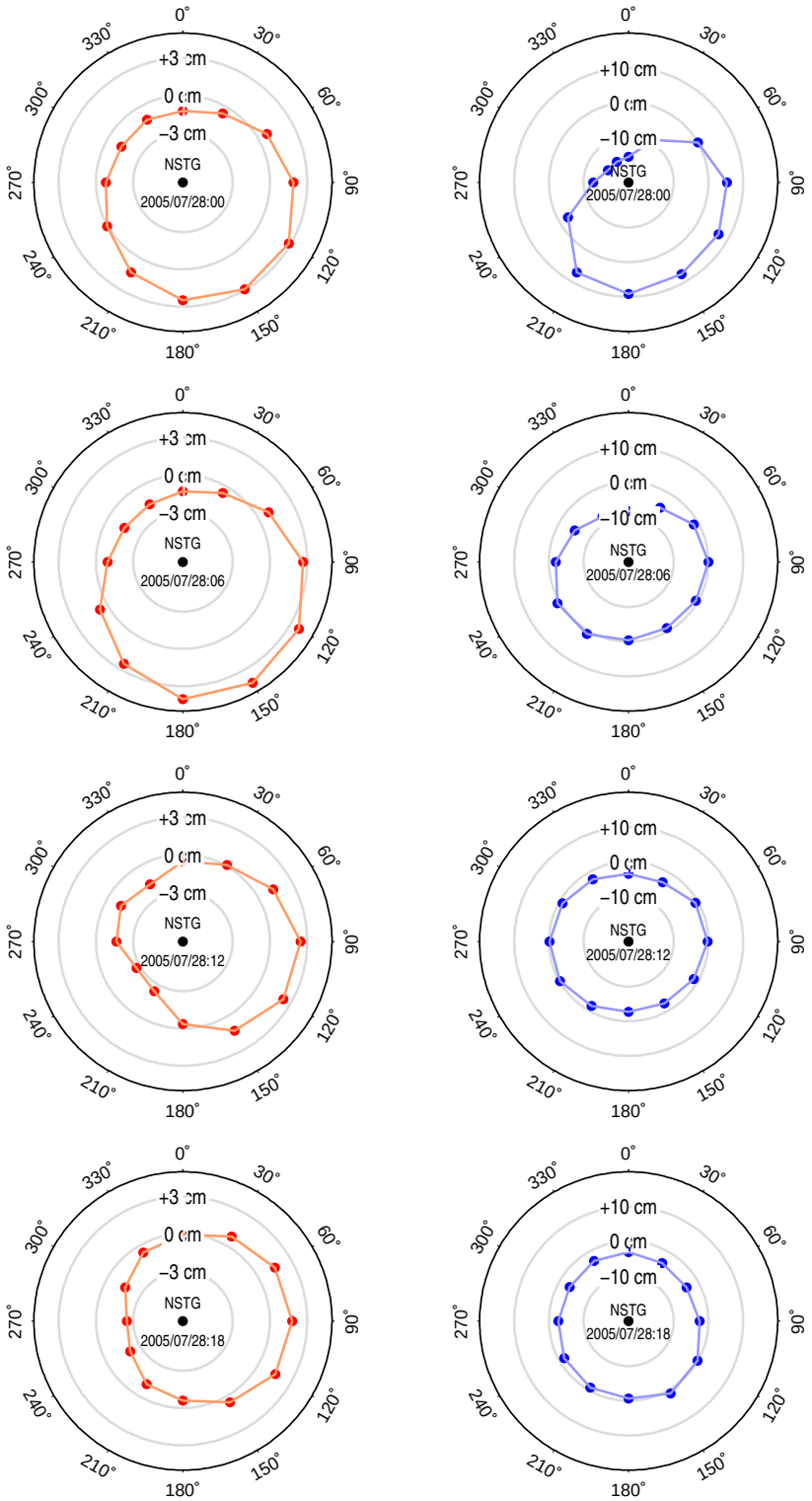

Figure 10.10: Slant atmospheric delay difference for CGPS station NSTG between the azimuth dependent mapping function OMF_AZI and the NMF at 5 degrees elevation for a standard ZHD of 2300 mm (left column) and ZWD 100 mm (right column) for 28 July, 2006.

Chapter 11

APL and Differential Coordinate Time Series

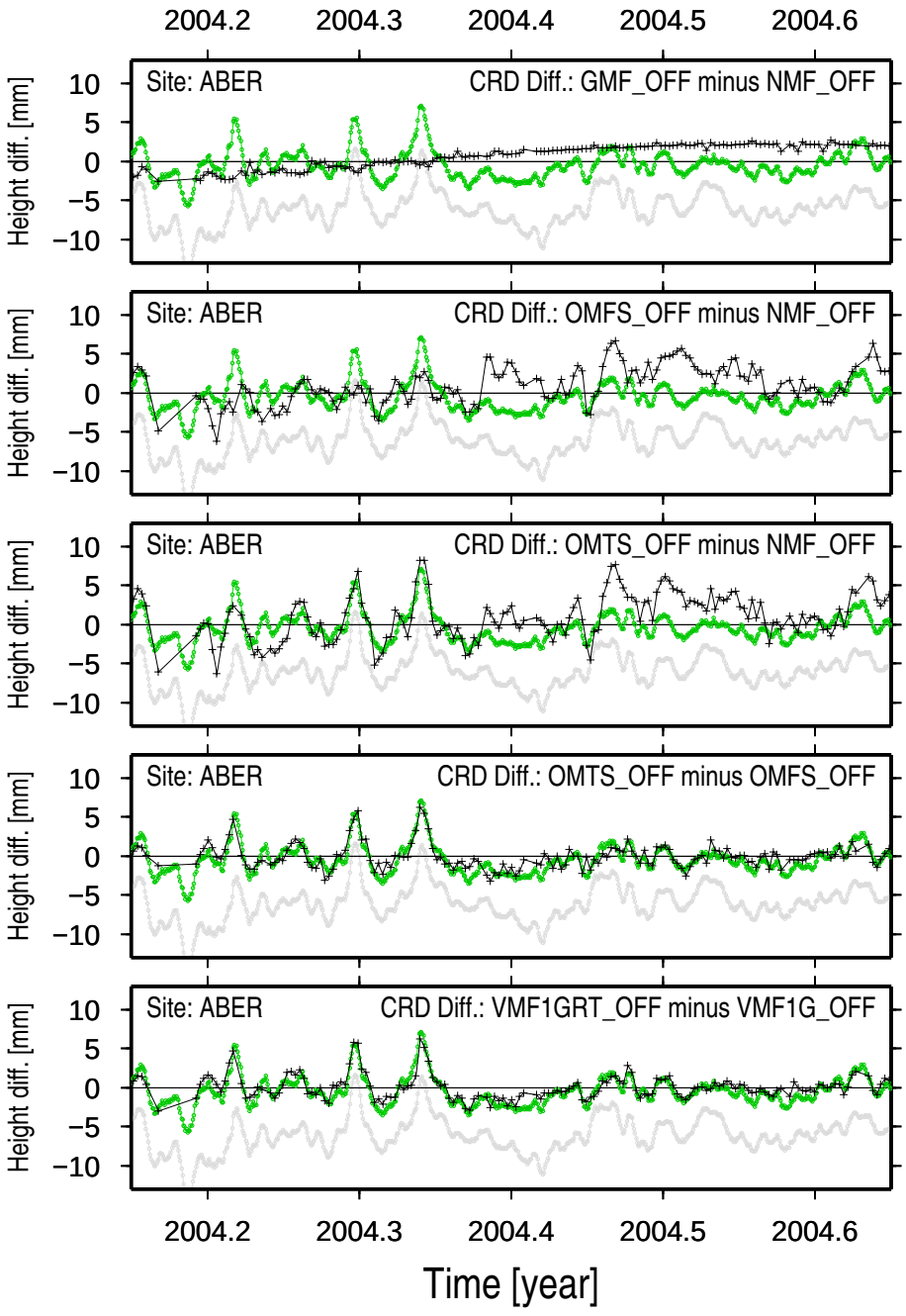

Figure 11.1: Differential height time series for CGPS station ABER. From top to bottom: GMF minus NMF, OMFS minus NMF, OMTS minus NMF, OMTS minus OMFS, and VMF1GRT minus VMF1G. Plotted on the same scale are the vertical displacement induced by atmospheric pressure loading as predicted by two models: in green a model run by T. van Dam (pers. comm.) and in light gray by aplo, L. Petrov's package available from url. No artificial offset was introduced.

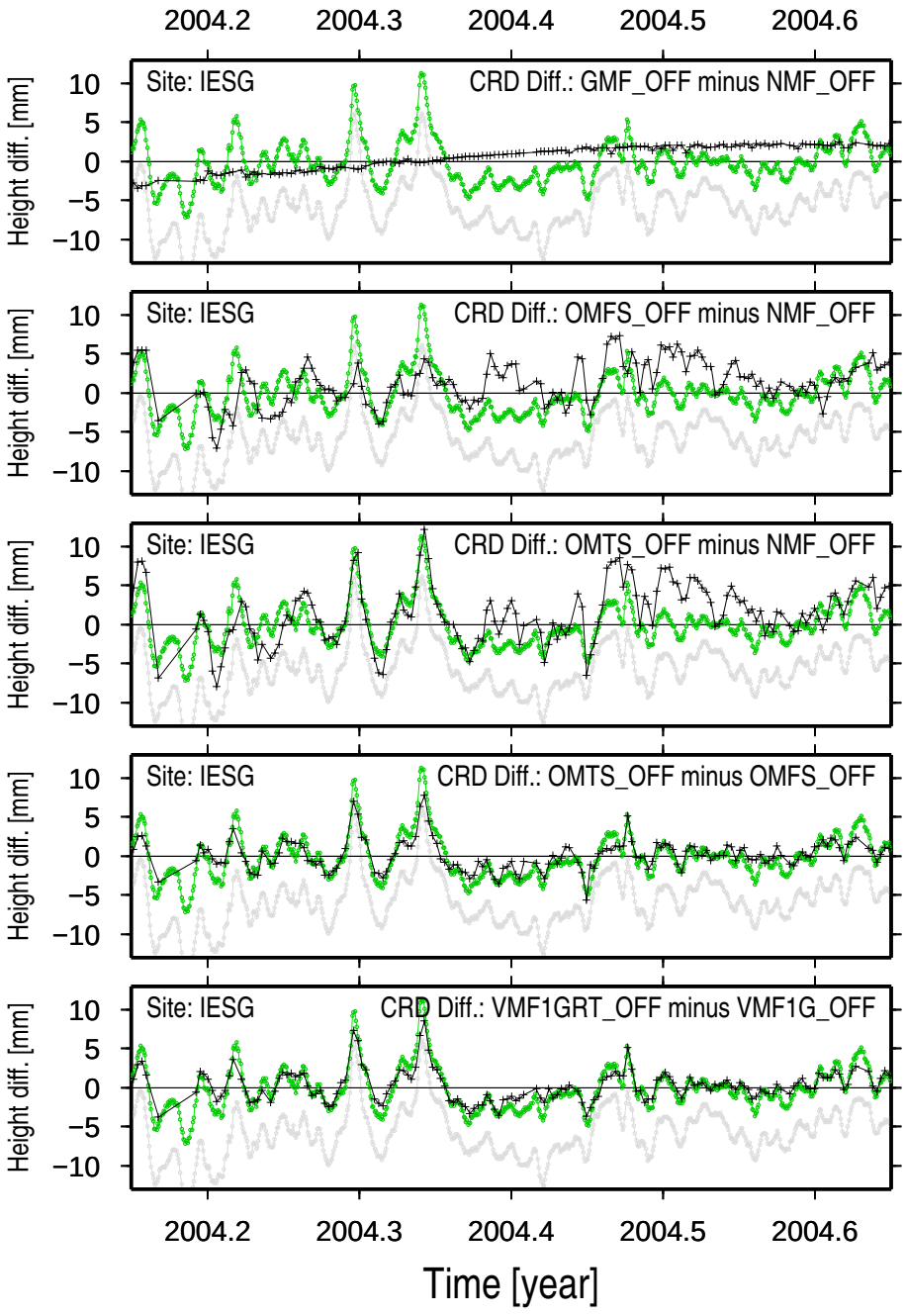

Figure 11.2: Differential height time series for CGPS station IESG. From top to bottom: GMF minus NMF, OMFS minus NMF, OMTS minus NMF, OMTS minus OMFS, and VMF1GRT minus VMF1G. Plotted on the same scale are the vertical displacement induced by atmospheric pressure loading as predicted by two models: in green a model run by T. van Dam (pers. comm.) and in light gray by aplo, L. Petrov's package available from url. No artificial offset was introduced.

Chapter 12

APL and Differential ZTD Time Series

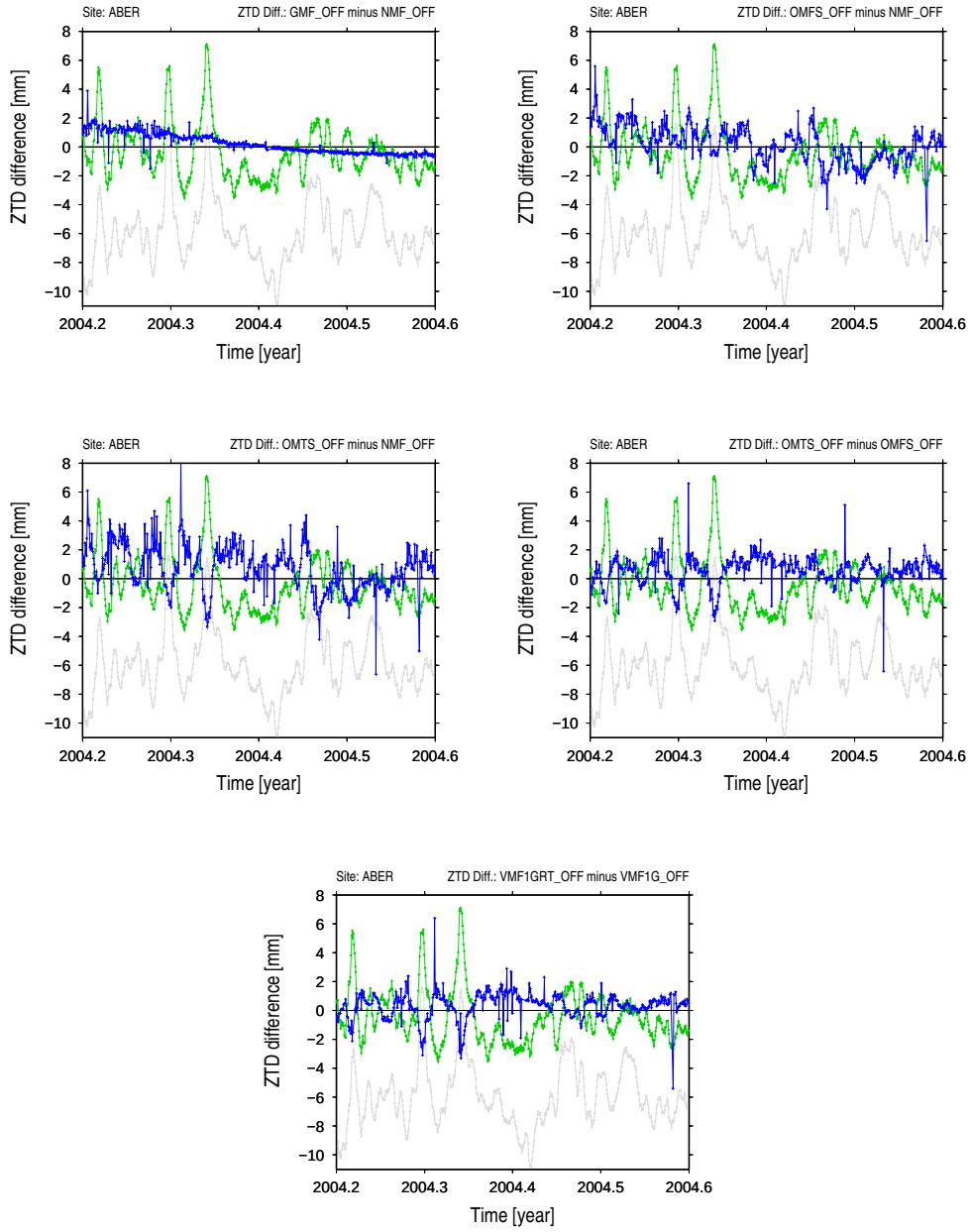

Figure 12.1: Differential ZTD time series for CGPS station ABER. Top left: GMF minus NMF; Top right: OMFS minus NMF; Middle left: OMTS minus NMF; Middle right: OMTS minus OMFS; Bottom: VMF1GRT minus VMF1G. Plotted on the same scale are the vertical displacement induced by atmospheric pressure loading as predicted by two models: in green a model run by T. van Dam (pers. comm.) and in light gray by aplo, L. Petrov's package available from url. No artificial offset was introduced.

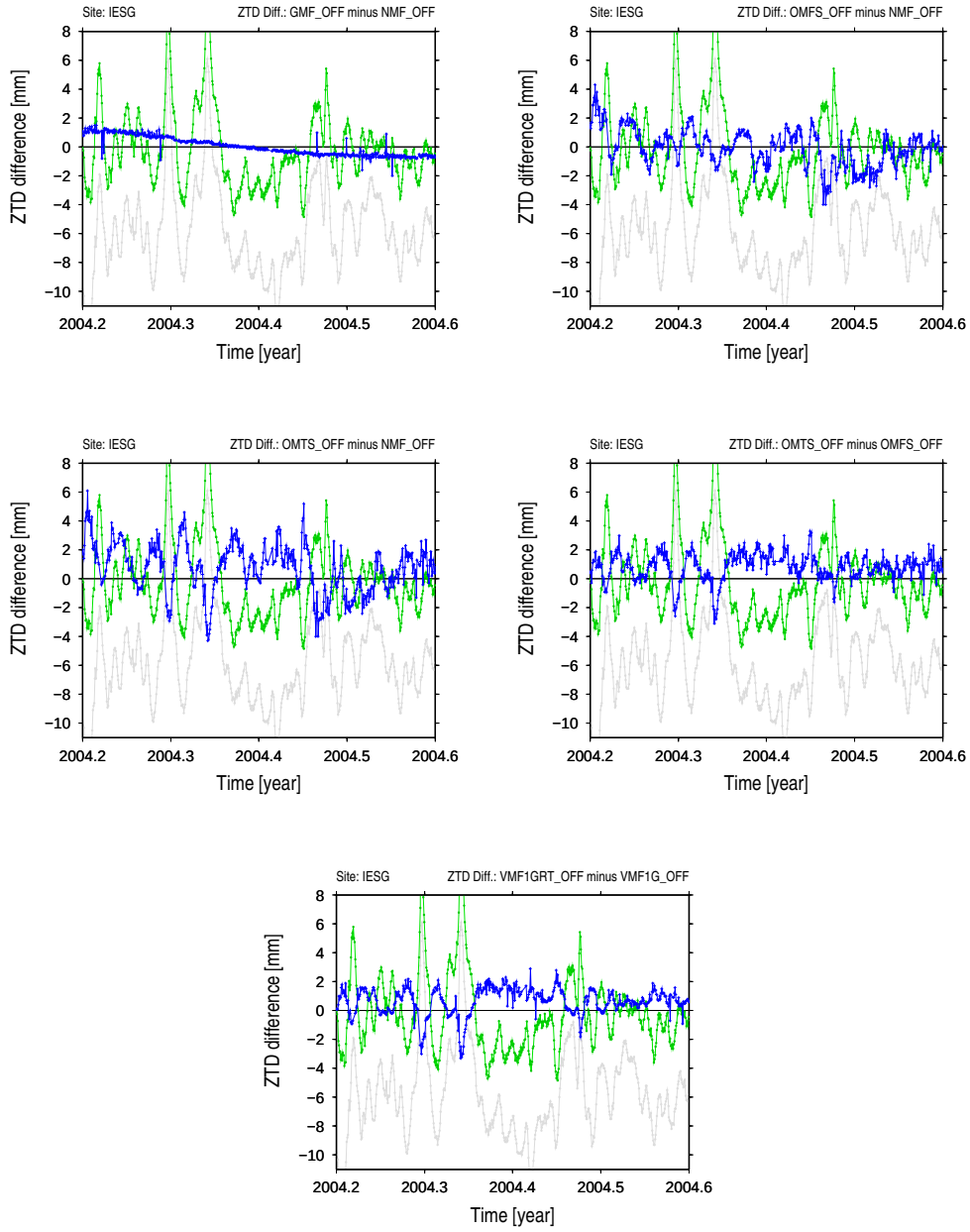

Figure 12.2: Differential ZTD time series for CGPS station HERS. Top left: GMF minus NMF; Top right: OMFS minus NMF; Middle left: OMTS minus NMF; Middle right: OMTS minus OMFS; Bottom: VMF1GRT minus VMF1G. Plotted on the same scale are the vertical displacement induced by atmospheric pressure loading as predicted by two models: in green a model run by T. van Dam (pers. comm.) and in light gray by aplo, L. Petrov's package available from url. No artificial offset was introduced.